

Università degli Studi di Napoli “Federico II”

SCUOLA POLITECNICA E DELLE SCIENZE DI BASE

DIPARTIMENTO DI INGEGNERIA INDUSTRIALE

Corso di Dottorato in Ingegneria Industriale

XXXIV Ciclo



TESI DI DOTTORATO

**Experimental investigation of wingtip vortices
control with synthetic jets**

MIRKO ZACCARA

Tutori:

Prof. Ing. Gennaro Cardone
Prof. Ing. Carlo Salvatore Greco

Coordinatore:

Prof. Ing. Michele Grassi

Marzo 2022

*Let your dreams be bigger than your fears,
and your actions be louder than your words.*

M. Scott Peck

ABSTRACT

Wingtip vortices are proven to be detrimental to both aircraft efficiency and safety due to their adverse effects such as wake hazard, blade vortex interaction (BVI) noise, and induced drag. Despite the extensive literature on the subject, the number of experimental works featuring far field velocity measurements under active control are very limited. The present thesis presents the experimental investigation of the effectiveness of synthetic jet actuation control on the wingtip vortices and their wake hazard. In order to preserve the mutual induction of the counter-rotating vortices during their evolution, an unswept, low aspect ratio, squared-tipped, finite-span wing is employed. The synthetic jet actuation is based on triggering the inherent instabilities of Crow and Widnall at different momentum coefficient C_μ with the goal to reduce the vortices strength, the induced circumferential velocity, and to obtain an anticipated vortices break up. Different exit geometries of the synthetic jet have been tested to analyze the effects of the jet velocity and jet position changes on the wingtip vortices. A proper phase-locked stereoscopic particle image velocimetry setups have been designed to carry out such a parametric study in the near and far wake at a distance from the wing trailing edge up to 2 and 80 chord lengths, respectively. The effects of blowing at high momentum coefficient $C_\mu = 1\%$ are demonstrated to be remarkable on the wingtip vortices mitigation but the implementation of this control configuration on a real-scaled wing could be unfeasible. On the other hand, both the time and phase-averaged results suggest that, at relatively low value of $C_\mu = 0.2\%$, using a larger synthetic jet exit section area allows to greatly affect the wingtip vortices features causing a striking alleviation of the vorticity distribution up to 90% with respect to the baseline reference case. As a matter, due to the actuation at low frequency, the vortices instability is prematurely risen up and amplified, leading to an early vortices linking and their consequent dissipation.

CONTENTS

List of symbols	ix
1 Introduction	1
1.1 Adverse effects of trailing vortices	4
1.1.1 Wake-hazard	5
1.1.2 Induced drag	6
1.1.3 Blade vortex interaction noise	8
1.2 Wingtip vortices instabilities	9
1.2.1 Crow Instability	10
1.2.2 Widnall Instability	13
1.3 Control strategies	15
1.3.1 Passive control	15
1.3.2 Active control	16
1.4 Synthetic jets	19
1.5 Motivation of the work	21
2 Stereoscopic Particle Image Velocimetry	23
2.1 Principle of Particle Image Velocimetry	23
2.1.1 Imaging and optical system	24
2.2 Stereoscopic Particle Image Velocimetry	26
2.2.1 S-PIV algorithm	28
2.2.2 Optical calibration procedure	28
2.2.3 Image dewarping	29
2.2.4 Disparity correction	30
2.2.5 3C displacement reconstruction	31
3 Feasibility test on wingtip vortices alleviation	37
3.1 Experimental apparatus and operating conditions	37
3.1.1 Experimental rigs	37
3.1.2 Stereoscopic particle image velocimetry setup	39
3.1.3 Operating conditions	40
3.2 Results and discussions	41
3.2.1 Time-averaged analysis	41
3.2.2 Phase-averaged analysis	43
3.3 Conclusions and perspectives	48

4	Experimental rigs	51
4.1	Near-field measurements setup	51
4.1.1	D3M wind tunnel	51
4.1.2	Wing model and synthetic jet device	52
4.1.3	S-PIV setup and image processing	56
4.2	Far-field measurements setup	57
4.2.1	LMFL Boundary Layer Wind Tunnel	57
4.2.2	Wing model and synthetic jet device	58
4.2.3	S-PIV setup and image processing	63
4.3	Data processing and metrics	65
4.3.1	Vortex identification method.	65
4.3.2	Vortex model.	66
4.3.3	Metrics.	67
5	Time-averaged results	69
5.1	Near-field analysis	69
5.1.1	Streamwise vorticity and geometrical features	69
5.1.2	Circumferential velocity	73
5.1.3	Circulation.	76
5.2	Far-field analysis	77
5.2.1	Streamwise vorticity and geometrical features	79
5.2.2	Circumferential velocity	84
5.2.3	Circulation.	89
6	Phase-averaged results	93
6.1	Near-field analysis	93
6.1.1	Streamwise vorticity and geometrical features	93
6.1.2	Circumferential velocity	103
6.1.3	Circulation.	104
6.2	Far-field analysis	106
6.2.1	Streamwise vorticity and geometrical features	106
6.2.2	Circumferential velocity	125
6.2.3	Circulation.	128
7	Conclusions and outlooks	133
	Bibliography	137
	List of Publications	145
	Acknowledgements	147

LIST OF SYMBOLS

Acronyms

3C	Three Components
2D	Two Dimensional
3D	Three Dimensional
ATC	Air Traffic Control
BC	Baseline Case
BCr	Rounded wing Baseline Case
BCs	Squared wing Baseline Case
BVI	Blade Vortex Interaction
CC	Control Case
CCD	Charge-Coupled-Device
CMOS	Complementary Metal-Oxide-Semiconductor
FOV	Field Of View
ICAO	International Civil Aviation Organization
LMFL	Laboratoire de Mécanique des Fluides de Lille
MJF	Multi Jet Fusion
MTF	Modulation Transfer Function
MTOW	Maximum Take-Off Weight
PIV	Particle Image Velocimetry
sCMOS	scientific Complementary Metal-Oxide-Semiconductor
Rhc	Rounded wing with one hole in the chord-plane as SJ exit section
Sh4	Squared wing with four holes as SJ exit section
SJ	Synthetic Jet
SLS	Selective Laser Sintering
S-PIV	Stereoscopic Particle Image Velocimetry
Ss01	Squared wing with synthetic jet slot height of 1% of the chord length
Ss02	Squared wing with synthetic jet slot height of 2% of the chord length
Ss04	Squared wing with synthetic jet slot height of 4% of the chord length
ZNMF	Zero-Net-Mass-Flux

Roman letters

A_c	vortex core area, m^2
A_{Crow}	signal amplitude of the Crow instability control case, V
A_j	synthetic jet exit section area, m^2

$A_{Widnall}$	signal amplitude of the Widnall instability control case, V
$A_{w/2}$	half-wing surface area, m^2
b	wing span, m
b_0	vortices distance at a generic station downstream of the wing, m
C_{D_i}	induced drag coefficient of the wing
C_L	lift coefficient of the wing
c	wing chord, m
C_l	lift coefficient of the airfoil
D	synthetic jet orifice diameter, m
D_e	equivalent hydraulic diameter, m
D_i	induced drag force, N
D_{max}, D_{min}	Major and minor axes of the vortex, m
D_u	disparity vector, m
d_{diff}	diffraction image particle diameter, m
d_{geom}	geometric image particle diameter, m
d_p	physical particle diameter, m
d_τ	particle diameter in the image sensor, m
$d\underline{X}_c$	infinitesimal displacement vector in the image plane relative to camera c , pixels
dX_c, dY_c	2C infinitesimal displacement in the image plane relative to camera c , pixels
$d\underline{x}$	infinitesimal displacement vector in object space, mm
dx, dy, dz	3C infinitesimal displacement in object space, mm
e	span efficiency factor of the wing
$\underline{F}^{(c)}$	vectorial mapping function relative to camera c , pixels/mm
f	frequency, Hz
f_a	actuation frequency, Hz
f_{acq}	acquisition frequency, Hz
k_a	axial wave number, rad/m
L	lift force, N
L_0	stroke length of the synthetic jet, m
L_e	equivalent length, m
m	azimuthal wave number
M_f	magnification factor
N_{Div}	number of division of the synthetic jet signal
n_p	number of periods of the synthetic jet signal
$Oxyz$	Physical reference frame
$O'x'y'$	Vortex centered reference frame
P_j	synthetic jet rms electrical power, W
p'	pressure fluctuation for a kelvin wave, Pa
\hat{p}	pressure disturbance eigenvector, Pa
p_j	synthetic jet exit section perimeter, m
R	radius, m
r_c	vortex core radius, m
S	wing surface area, m^2
T	synthetic jet actuation period, s

t_0	time scale of wake vortex downward movement, s
U_0	characteristic velocity of the synthetic jet, m/s
U_θ	circumferential velocity, m/s
$U_{\theta,m}$	maximum circumferential velocity, m/s
v_c	transverse velocity of the vortex center, m/s
U_∞	free-stream flow velocity, m/s
u_c	spanwise velocity of the vortex center, m/s
u_e	velocity along the jet centerline at the exit section, m/s
u, v, w	velocity component in the Cartesian reference frame, m/s
u_c, v_c	2C displacement relative to camera c , mm
V'_x, V'_r, V'_θ	velocity fluctuations for a kelvin wave, m/s
$\hat{V}_x, \hat{V}_r, \hat{V}_\theta$	velocity disturbance eigenvectors, m/s
w	induced downwash velocity, m/s
$W(t)$	synthetic jet actuation signal, V
X_c, Y_c	coordinates relative to camera c in the image plane, pixels
$X^{(c)}$	mapping function of the image coordinates X_c , pixels/mm
$Y^{(c)}$	mapping function of the image coordinates Y_c , pixels/mm
x, y, z	coordinates in object space, mm
x_0, y_0	Vortex center coordinates, m

Greek letters

α	geometrical angle of attack, $^\circ$
α_c	angle between the viewing ray of the camera c and the plane yz measured in the xz plane, rad
α_e	effective angle of attack, $^\circ$
α_i	induced angle of attack, $^\circ$
$\alpha_{L=0}$	zero lift angle of attack, $^\circ$
β_c	angle between the viewing ray of the camera c and the plane xz measured in the yz plane, rad
Γ	vortex circulation, m^2/s
Γ^{BC}	vortex circulation of the baseline case, m^2/s
Γ_b	initial vortex bound circulation, m^2/s
Γ_c	vortex core circulation, m^2/s
Γ_0	vortex circulation at a generic station downstream of the wing, m^2/s
γ	vorticity distribution of the vortex sheet, $1/s$
Δt	time separation between laser pulses, μs
$\Delta \tau$	time delay between the acquisition system and the SJ signal, μs
δ_z	depth of field, m
ε_r	radial deformation/shear rate, s^{-1}
ζ_z	streamwise vorticity, $1/s$
$\zeta_{z,max}$	maximum streamwise vorticity, $1/s$
$\zeta_{z,max}^{BC}$	maximum streamwise vorticity of the baseline case, $1/s$
θ_0	inclination angle of instability propagation plane, rad
λ	wavelength, m

λ_{Crow}	Crow instability wavelength, m
λ_{Widnall}	Widnall instability wavelength, m
μ	dynamic viscosity, Pa · s
μ_{∞}	free-stream dynamic viscosity, Pa · s
μ_j	jet dynamic viscosity, Pa · s
ρ_{∞}	free-stream flow density, kg/m ³
ρ_j	jet density, kg/m ³
ρ_p	particle density, kg/m ³
σ_{Crow}	Crow instability growth rate, s ⁻¹
σ_{Widnall}	Widnall instability growth rate, s ⁻¹
τ	non-dimensional time, convective time $3c/U_{\infty}$
τ_s	relaxation time, s
Φ	vortex inclination angle, °
ϕ	phase of the synthetic jet signal, °
ω	angular frequency, rad/s

Other symbols

\mathcal{R}	wing aspect ratio
$f_{\#}$	f-number
Δ_x, Δ_y	local displacement components in the image plane, pixels
Δ_z	local misalignment of the laser sheet, m

Operators

∇	gradient, m ⁻¹
$\overline{(\cdot)}$	time-averaged value
$\langle \cdot \rangle$	phase-averaged value
$(\cdot)_x, (\cdot)_y, (\cdot)_z$	spatial derivative, m ⁻¹

Dimensionless parameters

C_{μ}	momentum coefficient, $(A_j \rho_j U_0^2) / (A_w / 2 \rho_{\infty} U_{\infty}^2)$
η	self-similar variable, r / r_c
F^+	dimensionless frequency, $f_a c / U_{\infty}$
Re_j	synthetic jet Reynolds number, $(\rho_j U_0 D) / \mu_j$
Re_c	chord Reynolds number, $(\rho_{\infty} U_{\infty} c) / \mu_{\infty}$
Sr_j	synthetic jet Strouhal number, $(f_a D) / U_0$
St	Stokes number, $(\tau_s U_{\infty}) / d_p$
σ_{Crow}^*	non-dimensional Crow instability growth rate, $(\sigma_{\text{Crow}} 2\pi b_0^2) / \Gamma_0$
$\sigma_{\text{Widnall}}^*$	non-dimensional Widnall instability growth rate, $(\sigma_{\text{Widnall}} 2\pi b_0^2) / \Gamma_0$

1

INTRODUCTION

WINGTIP vortices are a menacing byproducts of finite-span lifting wings. The long-lasting nature of the wingtip vortices have been proven to be detrimental to both aircraft efficiency and safety due to their adverse effects. In fact, the aviation industry has been concerned for decades because of they drawbacks such as wake hazard, blade vortex interaction (BVI) noise, and induced drag. With regard to the first one, if a smaller aircraft encounters the strong vortices shed from a larger plane, the angular momentum from the vortices may induce a large destabilizing moment, which can cause an irrecoverable loss of control (Spalart, 1998). To overcome this, aviation regulations mandate strict following distances that is dependent on both the leading and trailing aircraft. In the case of rotors, the interaction of the blade tip vortices with the following blade represents the major source of noise and vibration in descending and maneuvering flight (Yu, 2000). The unacceptable noise level produced by helicopters prevents them from spreading for commercial use and passenger carrier. Lastly, the induced drag caused by the downwash of the wingtip vortices account for up to 40% of the aircrafts drag (Kroo, 2001). The adverse effects of the wingtip vortices are discussed later in the present introduction in section 1.1.

The long time research over the trailing vortices, primarily due to the previously mentioned hazard they present, is related to one of the oldest topics in fluid mechanics: the study of flows with concentrated vorticity in free motion (S. E. Widnall, 1975). In fact, the counter-rotating vortex pair resulting from the wing wake represents one of the simplest flow configurations for understanding elementary flow which can yield useful information about the physics of more complex turbulent flows (Leweke et al., 2016). With respect to the first attempts to analyze and assess this phenomenon and its related consequences, when scientists at the US National Advisory Committee for Aeronautics claimed that *the rolling up of the trailing vortices associated with high-aspect-ratio wings is of little practical importance* (Spreiter and Sacks, 1951), a complete awareness of the complexity and riskiness of trailing vortices has been reached.

It is well known that, given a lifting finite wing, the spanwise distribution of lift $L(y)$ ob-

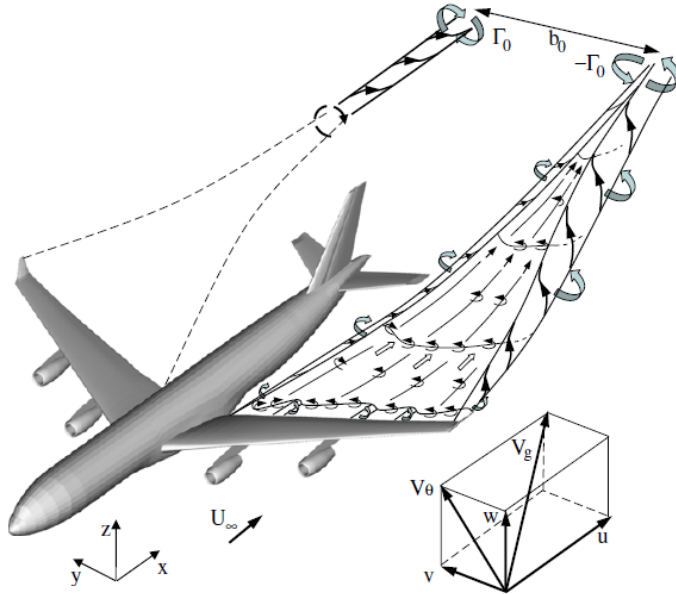


Figure 1.1: Vortex wake generation and roll-up process. Image taken from Breitsamter, 2011.

tained by a lifting-line analysis is related to the flight speed U_∞ , fluid density ρ_∞ , and bound circulation $\Gamma(y)$ as

$$L(y) = \rho_\infty U_\infty \Gamma(y) \quad (1.1)$$

Moreover, according to Helmholtz' theorem, a trailing vortex sheet of strength $\gamma(y) = \frac{d\Gamma}{dy}$ is created as the circulation changes along the span. From a physical point of view, the occurrence of wingtip vortices is often misrepresented as it can be explained by three distinctive and complimentary ways (Green, 1995). The first and commonly adopted considers the pressure differential between the pressure and the suction side of the wing. Due to its curvature, the flow is bent generating centripetal forces which result in a normal and outward acceleration balanced by an inward pressure drop leading to a pressure reduction on the upper/lower surface relative to the lower/upper surface with a positive/negative angle of attack. Along the entire span of the wing, the streamlines on the upper surface turn inboard, while the lower surface streamlines turn outboard. When reaching the trailing edge of the wing, the spanwise velocity discontinuity produces a vortex sheet shed from the trailing edge (see Figure 1.1). For finite wings, the boundary condition at the wingtip physically requires the upper and lower pressures to be equal. Therefore, the resulting pressure differential at the wingtip produces a net flow which curls and creates a strong vortical flow referred to as a wingtip vortex.

A second and more schematic explanation involves Helmholtz's vortex theorems which impose that a vortex tube can not end in free space. Considering a finite wing at rest, the net circulation is null. When it impulsively accelerates forward, according to the Kutta-Joukowski law (Bertin & Cummings, 2021), if the wing generates lift a net circulation

exists referred to as the "bound vortex". Kelvin's theorem dictates that this circulation must be matched by an equal and opposite spanwise circulation shed from the trailing edge (the so-called "starting vortex"). Finally, because of the second Helmholtz's law, both the bound and the starting vortex lines can not end in a fluid, thus two wingtip vortices are generated to connect them.

A third way to explain the presence of wingtip vortices is related to the shear layer that exists near the tip. It is important to recall that if a gradient is present in a velocity field, a vorticity fields must exists too. By considering a crosswise plane some spanwise distance away from the wing (undisturbed flow), the streamlines are horizontal, while they are following the wing curvature in a parallel slice just inboard the wingtip. The non-parallelism of the wing surface and free-stream velocity vectors implies a net streamwise vorticity oriented between the two directions. It is worth noting that, even for wing equipped with a symmetric airfoil at zero degree angle of attack, two weak counter-rotating trailing vortices shed from the upper and lower surface exist as a result of this phenomenon.

Although some attempts have been made to design vortex sheets in a different way, under most conditions the vortex sheet will roll up, and the wake structure will be established within a few wing spans. Therefore, the problem has shifted to the analysis of the wake: given the distribution of vorticity $\gamma(y)$ in the initial flat trailing vortex sheet, the final structure of the wake must be obtained. Especially for lightly loaded wings at high Reynolds numbers, roll-up takes place gradually enough to justify the use of a local two-dimensional model of the wake flow and yet rapidly enough to use an inviscid model of the flow. The resulting structure could be used as initial conditions in the wake analysis, dissipation and instabilities development. Two different approaches are usually employed to compute the wake structure: the first one concerns the step-by-step calculation of the roll-up process itself, while the second approach employs direct calculation of the trailing vortices structure neglecting the roll-up process. In the latter case, a final configuration is assumed and imposed for the flow requiring the conservation of some quantities such as the initial vorticity distribution over the wing, circulation, impulse, moment of impulse (Betz, 1932; Donaldson, 1971), and kinetic energy (Moore & Saffman, 1973; Spreiter & Sacks, 1951). Further details about the roll up calculations and far field structure of trailing vortices can be found in S. E. Widnall, 1975 and Spalart, 1998. However, what is observed is that the trailing vortex is more complex than the aforementioned mechanisms and the flow at the wingtip involves development and interactions of multiple vortical structures, shear layer instabilities, three-dimensional separations and reattachment; in the wake, rolling-up of the vorticity sheet, vortex instabilities, decay and diffusion, vortices interaction and merging are observed. Furthermore, the formation and development are strongly affected by several factors such as wing geometry, tip geometry, wing load distribution, vortex circulation, nature of the boundary layer on the wing, atmosphere stratification, wind, and turbulence (S. E. Widnall, 1975). Considering the downstream development, a vortex wake can be divided into four regions (Breitsamter, 2011), reported schematically in Figure 1.2:

1. the *near field*, $z/b \leq 0.5$, which is characterized by the formation of highly concentrated vortices shed at all surface discontinuities (i.e. control surface deflected, flap, wing-fuselage junction among the others);

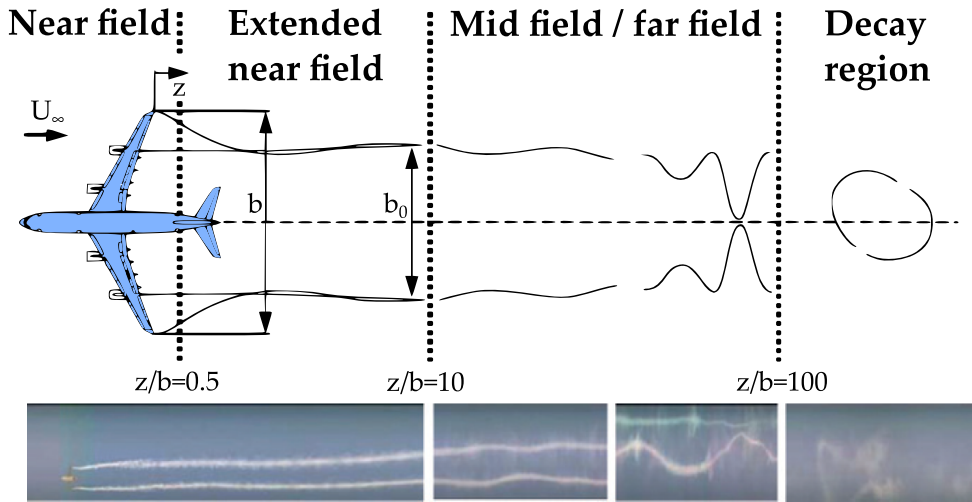


Figure 1.2: Stages of wake vortex lifespan. Adapted from Breitsamter, 2011.

2. the *extended near field*, $0.5 < z/b \leq 10$, where the wake roll up process takes place and the merging of dominant vortices (i.e. shed at flap edge, wing tip, etc.) occurs, leads gradually to two counter-rotating vortices;
3. the *mid and far field*, $10 < z/b \leq 100$, where the wake is descending in the atmosphere and linear instabilities emerge;
4. the *dispersion* region, $z/b > 100$, where fully developed instabilities cause a strong interaction between the two vortices until they collapse.

With the origin of trailing vortices explained, the following sections 1.1 and 1.2 describe their adverse effects and instabilities. The latter is a precursory topic necessary for the design of the best control strategies which are discussed in section 1.3. Finally, the basic principles of the synthetic jets, which is the device employed in the present thesis to actively control the wingtip vortices, are reported in section 1.4 followed by the motivation of the present work (section 1.5).

1.1. ADVERSE EFFECTS OF TRAILING VORTICES

As already mentioned, the trailing vortices are produced as a result of lift generation and they come with many adverse effects spanning various applications. In aeronautical applications, the wingtip vortices cause wake hazards during take off and landing and induced drag during cruise. The fluid-structure interaction with the vortices generated by a rotor blade (blade vortex interaction), is the main responsible of the helicopter noise. Moreover, the vortices reduce the efficiency in turbine blades (Green, 1995). In maritime applications, trailing vortices are produced from sails and rudders. The long-lived and stable vortex shed from a sail increases detectability in maritime vessels that desire a small footprint (Reed & Milgram, 2002; Wren, 1997). Further, trailing

vortices cause cavitation on propellers increasing structural fatigue, maintenance costs, noise, and potential of propeller failure (Asnaghi et al., 2021; Lee et al., 2017; Sezen & Bal, 2020).

In the following, only the aeronautical adverse effects will be discussed.

1.1.1. WAKE-HAZARD

DUE to the durable nature of the wingtip vortices which travel far downstream of the wing and dissipate slowly over time (Spalart, 1998), the main adverse effect is represented by the wake hazard. The relative position of the following aircraft with respect to the vortex wake can lead the airplane to experience an upwind field, a downwind field (i.e. a loss of lift) or a rolling moment, together with an increase of turbulence and structural dynamic loads being the vortex wake cross flow velocities of hundreds of km/h and extended up to tens of km (Figure 1.3). The possibility of an encounter is greater in the vicinity of airports since all the aircraft are limited to fly in specific air corridors during takeoff and landing. The severity of wake hazard depends not only on the size, weight,

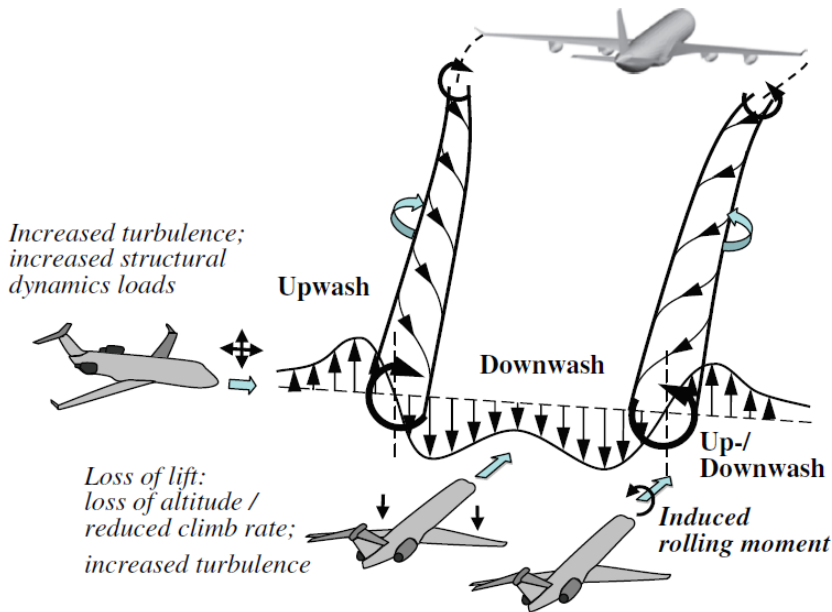


Figure 1.3: Wake vortex hazard for an aircraft crossing the vortex wake of the preceding one. Image taken from Breitsamter, 2011.

distance between the two aircraft, and the probability of wake encounter, but it varies also for a given local atmospheric condition (i.e. wind flowfield, stratification, turbulence) that influences the position, merging, strength, and decay of vortices. Due to the non-deterministic combination effects of these factors, the fundamental nature of wake vortices and their attenuation have been a difficult problem since the early operation of commercial flights.

To avoid the wake hazard, the Air Traffic Control (ATC) obeys to the International Civil Aviation Organization (ICAO) regulations which require aircraft to respect a separation distance with dependence on the Maximum Take-Off Weight (MTOW). This criterion is based on the introduction of three weight categories, *light* (< 7000 kg), *medium* (> 7000 kg and < 136000 kg), *heavy* (> 136000 kg), and *super* (up to 560000 kg) and prescribes a distance between the airplanes that can range from 3 up to 8 nautical miles. This increases air-traffic congestion, particularly at major airport hubs, forcing aircraft to circle in fuel-wasting and time-consuming holding patterns while the flow field returns to ambient conditions. The delays and wasted fuel increase cost to both the industry and the consumer. If the trailing vortex dissipated at an accelerated rate, air-traffic congestion would reduce, holding patterns would become unnecessary, and fuel would be saved, making airline travel more affordable, with the possibility to increase the number of take off and landing operations per unit time managed by a single airport and, therefore, the number of flights.

1.1.2. INDUCED DRAG

LIFT induced drag is well known to be a natural byproduct of a lifting wing in three-dimensional flow fields and it can represent up to the 40% of the aircraft total drag at cruise (Kroo, 2001). Due to the presence of the wingtip vortices, the streamwise kinetic energy is transferred into rotational one producing downwash in the wake of the wing. In a more schematic way (see Figure 1.4), by considering an airfoil section of a finite wing at the spanwise location y_0 , the downwash w tilts the lift vector aft by reducing the geometric angle of attack α , by an induced angle of attack $\alpha_i(y_0)$, obtaining an effective angle of attack $\alpha_e(y_0) = \alpha - \alpha_i(y_0)$ which generally can vary across the wing span. The result is a reduction of lift and the generation of a component of drag referred to as induced drag. By recalling the lifting-line theory of Prandtl (Anderson, 2007), the induced angle of attack at the location y_0 can be expressed as a function of the circulation spanwise distribution $\Gamma(y)$ via the Biot-Savart law and geometrical inspection of Figure 1.4 as

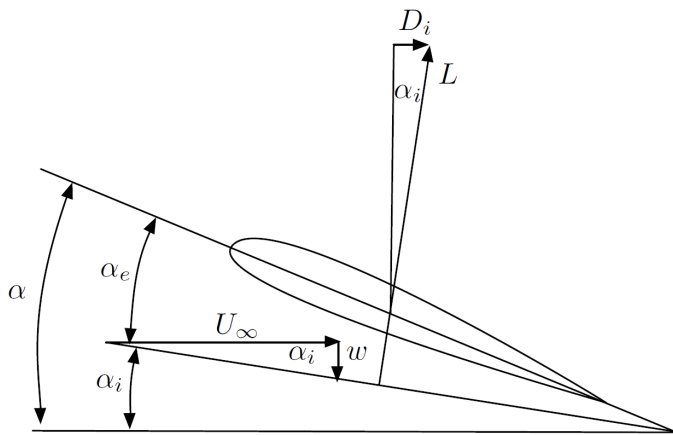


Figure 1.4: Schematic of the downwash effect on the local flow over the airfoil. Adapted from Anderson, 2007.

follows:

$$\alpha_i(y_0) = \tan^{-1}\left(\frac{w}{U_\infty}\right) \approx \frac{w}{U_\infty} = \frac{1}{4\pi U_\infty} \int_{-b/2}^{b/2} \frac{d\Gamma/dy}{y_0 - y} dy \quad (1.2)$$

where b is the wing span. The lift coefficient for the airfoil section located at $y = y_0$ is

$$c_l(y_0) = 2\pi(\alpha_e(y_0) - \alpha_{L=0}(y_0)) \quad (1.3)$$

where the local section lift slope has been assumed equal to $2\pi \text{ rad}^{-1}$ from the thin airfoil theory. If the wing has no aerodynamic twist, the angle of zero lift $\alpha_{L=0}$ is constant across the span. By recalling the definition of lift coefficient and the Kutta-Joukowski theorem, it is possible to express the local lift coefficient as a function of the circulation $\Gamma(y_0)$ as

$$c_l(y_0) = \frac{2\Gamma(y_0)}{U_\infty c(y_0)}. \quad (1.4)$$

Substituting Eq. (1.4) in Eq. (1.3), and solving for $\alpha_e(y_0)$, it derives the following expression

$$\alpha_e(y_0) = \frac{\Gamma(y_0)}{\pi U_\infty c(y_0)} + \alpha_{L=0}(y_0). \quad (1.5)$$

Finally, it is possible to obtain the fundamental equation of Prandtl's lifting-line theory which simply states that the geometric angle of attack is equal to the sum of the effective angle plus the induced angle of attack as

$$\alpha(y_0) = \frac{\Gamma(y_0)}{\pi U_\infty c(y_0)} + \alpha_{L=0}(y_0) + \frac{1}{4\pi U_\infty} \int_{-b/2}^{b/2} \frac{d\Gamma/dy}{y_0 - y} dy. \quad (1.6)$$

Equation (1.6) is an integro-differential equation in which the only unknown is the circulation distribution Γ . By making some maths, it is possible to express the lift and the induced drag as a function the solution $\Gamma = \Gamma(y_0)$:

$$L = \rho_\infty U_\infty \int_{-b/2}^{b/2} \Gamma(y) dy \implies C_L = \frac{2}{U_\infty S} \int_{-b/2}^{b/2} \Gamma(y) dy \quad (1.7)$$

$$D_i = \rho_\infty U_\infty \int_{-b/2}^{b/2} \Gamma(y) \alpha_i(y) dy \implies C_{D_i} = \frac{2}{U_\infty S} \int_{-b/2}^{b/2} \Gamma(y) \alpha_i(y) dy. \quad (1.8)$$

The general solution $\Gamma(y)$ of Eq. (1.6) can be approximated by a Fourier series, thus providing the coefficients C_L and C_{D_i} in terms of Fourier coefficients (Anderson, 2007; Glauert, 1983). Finally, the induced drag coefficient can be written as follows:

$$C_{D_i} = \frac{C_L^2}{\pi \mathcal{R}e} \quad (1.9)$$

where $e \leq 1$ is the span efficiency factor (also named Oswald's factor) and $\mathcal{R} = b^2/S$ is the wing aspect ratio. It is worth noting that the minimum induced drag is obtained for an elliptical lift distribution ($e = 1$), which justify the practical interest it had over the years.

As a result, the ideal configuration is represented by a wing with an elliptical plan form with no aerodynamic and/or geometric twist. Unfortunately, they are really expensive to manufacture, thus the aviation industries found a compromise in the tapered wing whose lift distribution is close to the elliptic case. Looking at the Eq. (1.9), since reducing lift would be counterproductive, the other option to reduce the induced drag is to increase the wing aspect ratio although it is limited by structural constraints. As such, since the Seventies many wings mount on their tips the vertical end-plates called winglet. The installation of this structure is aimed to deceive the flow field, making the wings appear longer than they are without compromising structural integrity and to physically hinder the creation of wingtip vortex. Satisfactory results have been achieved since this technology introduction, considering that it is possible to reach a decrease of the induced drag up to the 20% and with a consequent increase in wing efficiency of roughly 9% (Whitcomb, 1976). On the other hand, the introduction of a new surface leads unavoidably to a skin friction drag increase.

1.1.3. BLADE VORTEX INTERACTION NOISE

HELICOPTER main rotor blades represent another area where vortex-structure interaction could compromise the structural integrity of the blades. During the rotation, each rotor blade sheds a tip vortex which can interact with the following blades and the tail-rotor blades, as shown in Figure 1.5 (Leishman, 2000). This interaction results in

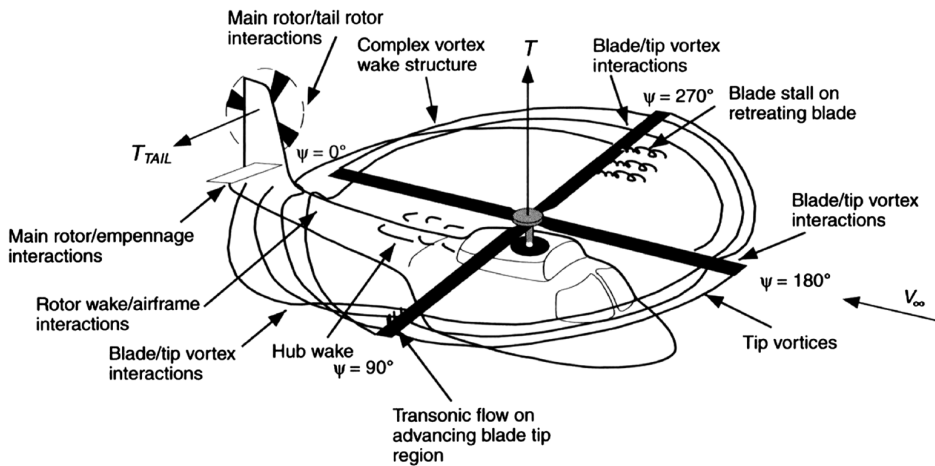


Figure 1.5: Different noise sources in helicopters. Image taken from Chae et al., 2010.

large unsteady forces due to rapid changes in local velocity around the blades, resulting in a premature rotor-blade fatigue and excessive noise (Schmitz, 1991; Yu, 2000). This type of noise is large and impulsive in nature and it is therefore significant for both military and civilian applications. As a matter, the rotor blade can intersect a trailing vortex at different angles depending on the blade's azimuth position and the vortex age. In particular, the most prominent Blade-Vortex-Interaction (BVI) event is the one where the trailing vortex is nearly parallel to the blade, usually occurring near azimuth angles of 70

to 80 deg and during low speed descent. Parallel-BVI is known to be the strongest and most important event for acoustics because of the brief and dramatic pressure changes the blade experiences along its entire span as it travels through the vortex flow field (Yu, 2000). In general, three ways are conceivable to reduce the BVI noise: increase the miss distance between the tip vortex and the blade; reduce the loading on the blade when the vortex interaction occurs; decrease the tip vortex strength. In this framework, researchers proposed innovative blade tip design (Brocklehurst & Barakos, 2013) trying to deflect the vortex avoiding the impact with the following blade and the use of wingtip devices to weaken the tip vortex such as sub-wing (Bhagwat et al., 1999; Hoad, 1980; Tangler, 1975), end-plate tip (Hoad, 1980), vane tip (Brocklehurst & Pike, 1994), tip spoiler (McAlister et al., 2001), canard tip (Ota et al., 2001), and wingtip blowing (Han & Leishman, 2004; Liu et al., 1999, 2000; Vasilescu & Dancila, 2006).

1.2. WINGTIP VORTICES INSTABILITIES

IT is well known that trailing vortices do not decay by simple diffusion, indeed they undergo to a nearly sinusoidal instability until they join together to form a train of vortex rings and then dissipate (Crow, 1970). The development of a three-dimensional instability requires the presence of both temporal and spatial disturbances, superimposed on the mean flowfield of a vortex system (Lessen & Paillet, 1974; Lessen et al., 1974). Kelvin waves propagating along the vortex are always introduced in the accurate analysis of this phenomenon (Jacquin et al., 2003)¹. The corresponding initial disturbances, that can consist of velocity and pressure fluctuations, can be expressed as

$$(V'_x, V'_r, V'_\theta, p') = (\hat{V}_x, \hat{V}_r, \hat{V}_\theta, \hat{p}) e^{i(k_a x + m\theta - \omega t)} \quad (1.10)$$

where $V'_x, V'_r, V'_\theta, p'$ represent the velocity fluctuation in the axial, radial and azimuthal direction in the co-moving reference frame of the vortex and the pressure fluctuation respectively. The disturbance is characterized by $k_a = \frac{2\pi}{\lambda}$, the axial wave number, m , the azimuthal wave number and $\omega = 2\pi f$, the angular frequency. In particular, the frequencies ω related to a discrete spectrum are the eigenvalues while the components $(\hat{V}_x, \hat{V}_r, \hat{V}_\theta, \hat{p})$ are the eigenvectors (i.e. disturbance amplitudes). Furthermore, the disturbance mode shape depends on the value of m leading to an axially mode shape for $m = 0$, a helical shape for $m = \pm 1$ (the so-called bending mode), and a multiple helix form for $|m| > 1$.

For a counter-rotating vortex pair, two different inherent mechanisms can lead to three-dimensional instability (Lewke et al., 2016). The first produces the long-wave Crow instability (Crow, 1970) involving perturbations which displace the vortices locally as a whole without changing their core structure. The second mechanism is related to the development inside the vortex core of short-wave perturbations amplification which growth is linked to the strain field induced by the neighboring vortex. The latter phenomena modifies the vortex core structure due to the combination of strain and rotation which causes the elliptic streamlines to be oriented at 45° to the principal stretching axis.

¹Any perturbation in a rotating flow leads to the propagation of dispersive waves, called inertia waves. These waves are equivalent to gravity waves in a stably stratified medium. The inertia waves propagating along a vortex are named Kelvin waves (Jacquin et al., 2003)

These effects produce the elliptic instability (Kerswell, 2002), also referred to as Widnall instability (Sipp & Jacquin, 2003).

In the following, the major characteristics of the Crow and Widnall instability are outlined.

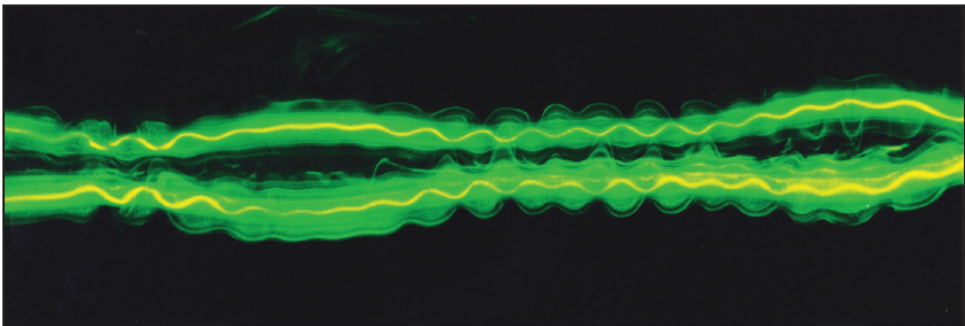
1.2.1. CROW INSTABILITY

THE Crow instability produces a periodic long-wave deformation which is the mainly responsible for wake vortex dissipation. It is frequently observed in the sky through the *contrails* (the pressure drop in the vortex core and jet-vortex interaction lead to condensation of water vapor and formation of ice crystals, respectively, over suitable nucleation sites, like soot particles and sulfur aerosols, emitted by aircraft engines), indicating sinusoidal deflections of the vortex trajectory (Figure 1.6).

The long-wave instability was first described by Crow (Crow, 1970) with a filament approach for the case of a counter-rotating Rankine vortex pair of equal strength $-\Gamma_1 = \Gamma_2 = \Gamma_b$, with Γ_b indicating the initial bounded circulation on the wing. Given a sinusoidal disturbance of the initial vortices, it is subjected to three different mechanisms shown in Figure 1.7. First, there is its self-induced rotation, in the direction opposite the rotation of the core fluid, whose rate is a function of the core radius r_c and the axial



(a) Photograph of the jet condensation trails from a Boeing 747 at $Re \approx 6 \times 10^7$. The field of view is approximately $150\text{m} \times 520\text{m}$.



(b) Dye visualization in a water tank at $Re = 2750$. The field of view is approximately $14\text{cm} \times 42\text{cm}$.

Figure 1.6: Visualizations of long-wave and short-wave instabilities developing in counter-rotating pairs of equal strength. Image taken from Leweke et al., 2016.

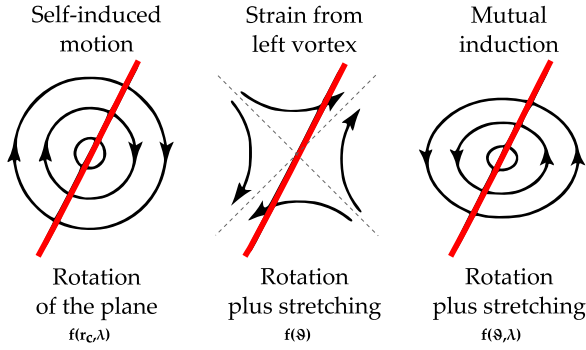


Figure 1.7: Schematic of different mechanisms acting to rotate and stretch the plane containing the wavy perturbation. Adapted from Leweke et al. (2016).

perturbation wavelength λ . Second, by considering the frame moving with the vortex pair, the motion induced by the opposite vortex, assumed unperturbed, consists of a plane stagnation point flow with maximum stretching in the $\theta = 45^\circ$ direction. Finally, there is the motion due to the perturbations combination of the two vortices which induces a rotation and radial stretching on the perturbation plane (the plane containing the waviness), but it also depends on λ . Instability occurs when, for a given combination (r_c, θ, λ) , the three rotation effects cancel each other and the wave is held at a constant angle θ for which the total radial stretching rate is positive.

The induced downward velocity at the vortex centers is

$$w_1 = w_2 = \frac{\Gamma_0}{2\pi b_0} \quad (1.11)$$

where b_0 is the mean distance between the vortices at a generic station downstream of the trailing edge, being a certain fraction of the initial span b , while the vertical distance between the vortex centers is null. Inside the vortex core circular streamlines exist, considering a reference frame moving with the "sinking" vortex pair, while the streamlines outside the cores assume elliptical shape. Taking into account one vortex per time, because of its downward movement with a velocity $w_{1,2}$, a stagnation point will be present at the center of the other vortex. These stagnation flows cause a radial deformation of each vortex core. The axes of maximum deformation will be the locations where the circumferential velocity vanishes ($U_\theta = \sqrt{u^2 + v^2} = 0$). The expression of the inclination of these axes with respect to the lateral direction (i.e. spanwise direction), in the case of counter-rotating vortices, is given by

$$\theta_0 = \arccos\left(\pm \sqrt{\frac{-\Gamma_2}{2\Gamma_1}}\right) \quad (1.12)$$

where Γ_1 and Γ_2 indicate interchangeably circulation of the two vortices. In the particular case of counter-rotating vortices of equal strength ($-\Gamma_1 = \Gamma_2$) the inclination angle is $\theta_0 = \pm 45^\circ$ as shown in Figure 1.8.

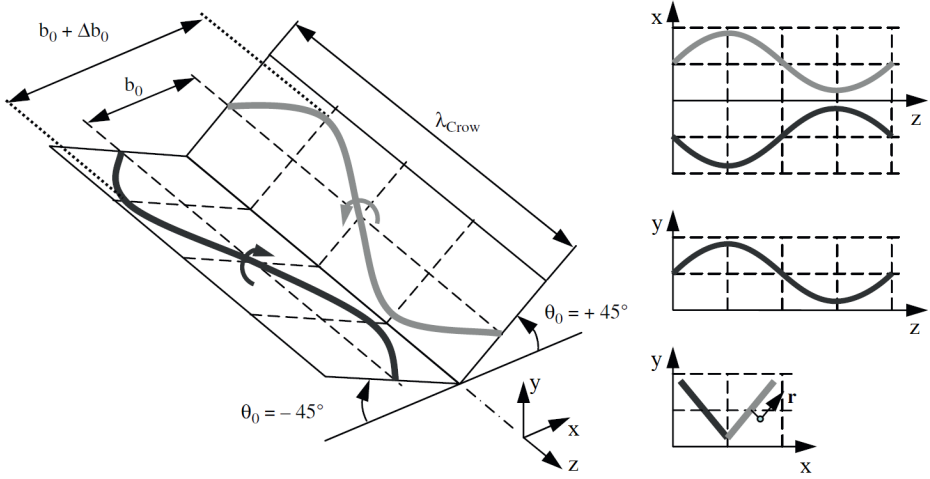


Figure 1.8: Schematic representation of the long wave Crow instability. Image taken from Breitsamter (2011).

Generally, the superposition of two Kelvin waves may cause the sinusoidal initial disturbance that triggers the instability. This is the case if the two Kelvin waves move in opposite directions ($m_{KW1} = -m_{KW2}$), have helical shape ($\|m_{KW1}\| = \|m_{KW2}\|$), stationary ($\omega_{KW1} = \omega_{KW2}$), and with the same axial wave numbers, i.e. $k_{a,KW1} = k_{a,KW2}$ (KW1,2 stands for *Kelvin Wave 1,2*). The stability analysis provides both a symmetric mode and an anti-symmetric mode. As a matter, only the symmetric one leads to a strong interaction between the two trailing vortices. The projection of the trajectory deflections of the two trailing vortices on the xz -plane shows the symmetric behavior with respect to the z -axis (Figure 1.8), while the projection on the yz -plane reports that they are in phase. With increase in time and distance, the deflection amplitude Δb_0 grows exponentially with the amplification rate σ_{Crow} , reducing the distance between the trailing vortices

$$\Delta b_0(t) = \Delta \hat{b}_0 e^{\sigma_{Crow} t} = \Delta \hat{b}_0 e^{\sigma_{Crow}^* \tau} \quad (1.13)$$

where τ is the dimensionless time, obtained dividing the time t by the interval t_0 at which the vortex pair moves downward by a distance equal to the vortex spacing b_0

$$\tau = \frac{t}{t_0} = t \frac{\Gamma_0}{2\pi b_0^2} \quad (1.14)$$

The amplification rate σ_{Crow} has been considered non-dimensional as σ_{Crow}^* by means of the shear rate $\varepsilon_r = \frac{\Gamma_0}{2\pi b_0^2}$ at the vortex centers

$$\sigma_{Crow}^* = \frac{\sigma_{Crow}}{\varepsilon_r} = \frac{2\pi b_0^2}{\Gamma_0} \sigma_{Crow} \quad (1.15)$$

Typical values of σ_{Crow}^* and wavelength λ , related to the ratio between the vortex core

radius r_c and b_0 , are, according to Breitsamter, 2011

$$\sigma_{\text{Crow}}^* = 0.825 \pm 0.025; \quad \frac{\lambda_{\text{Crow}}}{b} = 7.0686 \pm 0.7854 \quad (1.16)$$

As already mentioned, the amplitude exponential growth eventually leads to the cores touch and overlap at oscillation troughs, causing an exchange of vorticity of opposite sign. It is this periodical re-connection at the nearest points that causes vortex tubes to break up and turns them in a series of three-dimensional vortex rings (Figure 1.9). These peculiar structures dissolve faster and finally decay.

S. E. Widnall et al., 1974 extended the stability analysis considering a more general vortex velocity profiles including both an axial component and the case of two vortices with no equal and opposite circulations. Finally, in the framework of the filament approach, Klein et al., 1995 demonstrated that all counter-rotating pairs are unstable according to the Crow mechanism.

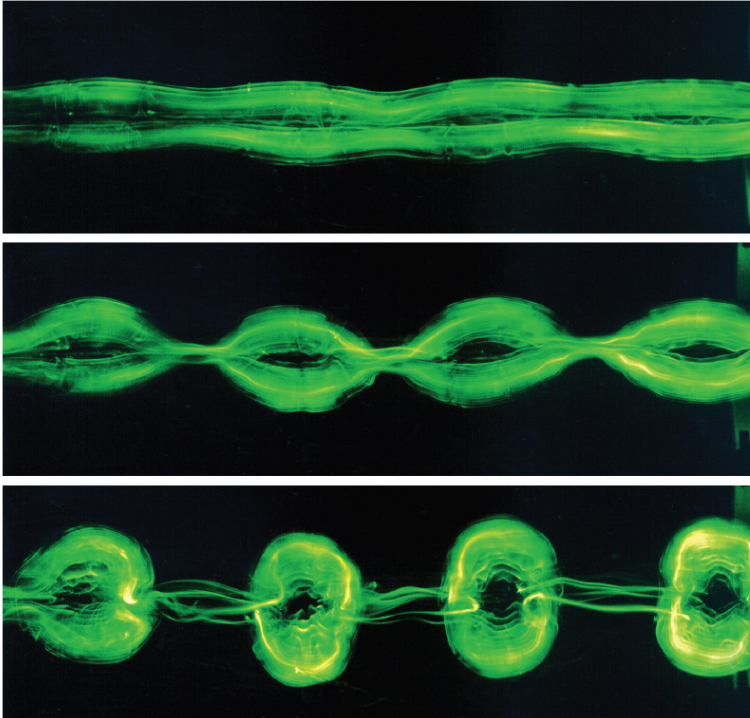


Figure 1.9: Vortex rings formation. Image taken from Leweke et al., 2016.

1.2.2. WIDNALL INSTABILITY

IN addition to the long-wave instability, short-wave instability develops too. The two instabilities occur together and interact with each other (Thomas & Auerbach, 1994).

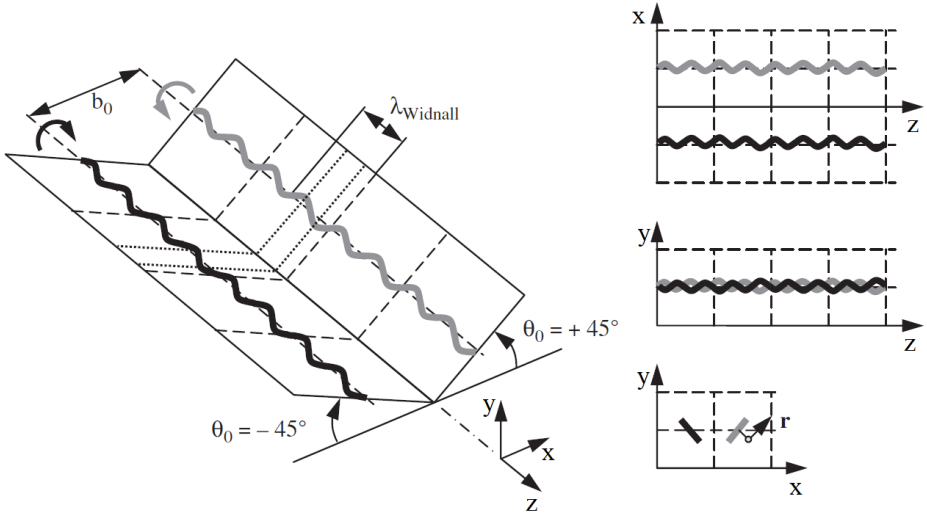


Figure 1.10: Schematic representation of the short wave Widnall instability. Image taken from Breitsamter, 2011.

The description of this kind of instability depends on the detailed vortex core structure since shortwave perturbations wavelength is of the same order of magnitude of the core size. The mechanism generating this oscillation was firstly explained by Tsai and Widnall, 1976, that revealed how it is caused by the resonance between perturbation waves (Kelvin waves) of the axisymmetric structure of the vortices and the modification of the core caused by the strain from the other vortex (S. E. Widnall et al., 1974). The instability of the vortex is in fact caused by the exponential amplification of these perturbations. A resonance with two Kelvin modes is obtained if the following conditions are satisfied

$$k_{a,KW1} = k_{a,KW2} \quad \|m_{KW1} - m_{KW2}\| = 2 \quad \omega_{KW1} = \omega_{KW2}. \quad (1.17)$$

For a fixed m_{KW1} and m_{KW2} pair, the previous conditions can be satisfied in various combination. However, it has been observed that elliptic instability is strongest when the two modes have a similar radial structure. As for the Crow instability, the Widnall instability is also developing along the planes associated with maximum radial deformation of the vortex core inclined by $\theta_0 = \pm 45^\circ$ against the horizontal one (Figure 1.10). The projection of the trajectory deflections on the xz -plane shows an in-phase behavior, while the projection on the yz -plane indicates a phase shift of 180° .

Typical values of $\sigma_{Widnall}^*$ (Breitsamter, 2011), and wavelength $\lambda_{Widnall}$ (Dghim et al., 2016; Ortega et al., 2003; S. E. Widnall et al., 1971), are

$$\sigma_{Widnall}^* = 0.95 \pm 0.3; \quad \frac{\lambda_{Widnall}}{b} = 0.9 \pm 0.023 \quad (1.18)$$

As it is possible to notice, the amplification rate, in this case, is higher than the one for the Crow instability, as found out also by S. E. Widnall, 1975.

1.3. CONTROL STRATEGIES

SIGNIFICANT efforts have been devoted over the years trying to control the adverse effects of trailing vortices which are described in section 1.1. The most common alleviation schemes rely on altering the thickness, turbulence, and longitudinal velocities in the vortex sheet. It has been proven by Bailey and Tavoularis, 2008 that adding turbulence to the free-stream increases the vortex wandering and the rate of decay of the peak tangential velocity. Since creating upstream turbulence in the flight-path of an airplane is not a practical method, different methods have been extensively studied to inject turbulence into a wingtip vortex such as:

- use of structural modification of the wingtip (i.e. winglets) and/or along the trailing edge of the wings and flaps to enhance the three-dimensional features of the flow and turbulence in the shear layer after their roll-up;
- injection or suction in the vicinity of wingtip in an attempt to disrupt the developing vortex, and hasten its dissipation;
- excitation of the inherent vortices instabilities to amplify and accelerate their break up.

The control techniques implementing the aforementioned methods are generally distinguished between passive and active control strategies. The main difference lies in the use of time dependent forcing which is a prerogative of the second group. In the following, a review of the previous research of both control strategies is presented.

1.3.1. PASSIVE CONTROL

MOST of the early research into passively solving the wake vortex hazard involved modifying the structure of the wake before roll-up by changing the geometry of the wing, in turn changing the loading distribution. Rossow, 1975 performed theoretical studies using 2D inviscid computations to determine the optimized loading distribution which would result in a wake that would either not roll-up or be more diffused. Linear loading distributions from root to tip as well as with abrupt variation in lift resulted in a diffused vorticity field with a noticeable decrease in the induced rolling moment that would be encountered by the following aircraft. Also a notched loading distribution has been demonstrated to result in a more diffused wake by Graham et al., 2003. Corsiglia and Dunham, 1977 performed experiments both on ground-based facilities and flight tests on a full scale Boeing 747 showing that a less hazardous wake can be obtained by shifting the center of pressure inboard.

In addition to geometric modification of the wings, a variety of experiments were performed on adding static devices to already existing wing plan forms. Patterson, 1975 investigated splines mounted directly downstream of the wing tip such that their bluff body shape would interfere with the tip vortex. They were found to be effective in increasing the size of the vortex core but they also created a large drag penalty. Other splines as well as various wing tip shapes were reviewed in the work of Traub et al., 1998. Croom, 1977 performed wind tunnel experiments as well as flight tests installing spoilers on the suction side of wings typically used as air brakes on commercial aircraft and

observed a significant increase in the vortex core size.

A large amount of work has gone into the idea of using fins (i.e. winglets) mounted on the suction or pressure side of wings in order to modify the loading distribution and/or add another discrete vortex to the wake that might interact with the tip vortex in a beneficial way. Rossow, 1978 performed wind tunnel tests and attempted to determine an optimal placement and orientation for a fin founding that a fin on the wing suction side creates a counter-rotating vortex with respect to the tip vortex producing a most benign wake. Later, Schell et al., 2000 and Ozger et al., 2001 investigated the wake-vortex structure behind a flapped rectangular wing and a swept tapered wing with slats and flaps. They conducted a parametric study on both flap extensions and fin positions concluding that the maximum decrease of the induced rolling moment and the largest increase of the core size is obtained with the fins mounted at the outboard flap edge region. On the contrary, Schöll et al., 2006 reported that, for an aircraft wing set up in high lift configuration, the fins show no significant impact on the induced rolling moment after the roll-up phase. However, the fins lead to an increased meandering which decreases the hazard to following aircraft due to a reduction in the bank angle associated with a vortex encounter. Lastly, the vortex motion could act as a starting point for instabilities in the far-field. In this framework of natural instability excitation via turbulence injection, the use of vortex generators has been proven to be aiding to distribute circulation over an increased area thus reducing the rolling moment. In particular, cooperative instabilities in multiple vortex systems could be initiated due to the unsteadiness of the vortex generators flow in stall configuration which results in enhanced vorticity diffusion. Ortega et al., 2002 and Ortega et al., 2003 performed towing tank experiments with a rectangular wing equipped with triangular flaps at the tips to extend the trailing edge creating a pair of inboard vortices that are counter-rotating with respect to tip vortices. Different flap sizes were studied with the strength of the inboard vortices ranged from -40% to -70% of the outboard vortex strength. It was shown that introducing the oppositely signed inboard vortices near the wing tip vortices causes a rapidly growing instability to occur between the vortices on either side of the wake. This mechanism was numerically confirmed by RANS and LES simulations of Stumpf, 2004.

The main advantage in using passive techniques is that they can be easily implemented by the aircraft industries because they represents no complex modification to the wing structures. On the other hand, one should accept the performance penalties such as drag increase, lift inefficiencies, and additional fatigue on the plan form. In fact, these devices are optimized around cruise configuration because they primarily address the induced drag and they can not be retracted when not required. As the design requirement across the entire flight envelope varies significantly, combined with the stochastic nature of atmospheric flight conditions, trailing vortices are a prime candidate for active flow control technologies.

1.3.2. ACTIVE CONTROL

ACTIVE wake alleviation strategies rely upon some time-dependent forcing to perturb the aircraft wake and excite inherent instabilities for a faster decay. They can be divided into two groups which adopts the oscillation of the aircraft control surfaces and/or high-lift systems (i.e. flaps) or injection/suction of a jet in the vicinity of the wingtips.

Chevalier, 1973 was the first on performing flight tests to demonstrate that the dissipation of high-intensity vortices could be accelerated by elevator oscillations at a critical frequency. Lift distribution oscillation was experimented later by Crow and Bate, 1976 to move the vorticity centroid outboard and inboard along the wing while Bilanin and Widnall, 1973 adopted periodic flap oscillations to move a significant fraction of lift inboard and outboard keeping the lift to within $\pm 2\%$. They demonstrated that the instability excitation and vortices break up are achievable only with an excessive level of oscillations. Barber and Tymczyszyn, 1980 and Jordan, 1983 conducted flight tests and towing tank experiments on a large commercial aircraft with lateral-control oscillations to excite the Crow instability. Their results show that the wake could vanish within three nautical miles of the generating aircraft through oscillating spoiler deflections even though they have proven to be not feasible during take-off or landing because of their large amplitude. Rossow, 1986 considered the use of roll oscillations of the aircraft as a means for exciting the Crow instability. Although this could be achieved without large oscillations in lift, the passenger discomfort associated with roll oscillations is the main drawback of this strategy making it impracticable. Further studies evaluated the use of oscillating ailerons (Haverkamp et al., 2005) and segmented Gurney flaps (Matalanis & Eaton, 2007) to introduce spatial disturbances to a trailing vortex in both the spanwise and lift directions trying to minimize fluctuations of the lift coefficients. It is important to outline that introducing lift distribution oscillations could lead to bending mode resonance of the wing, thus structural problems need to be taken into account during the design process.

More up-to-date methods in the effort of instability excitation rely on expelling mass and momentum in the vicinity of the wingtip to control the trailing vortex start. The drawback is to harvest the mass injected, usually bleeding it from the engine, which could reduce its efficiency. However, this comes true only during take-off and cruise, as the engines are generally idling during landing approach. To overcome this shortcoming, zero-net-mass-flux (ZNMF) devices (e.g. synthetic jets, plasma actuators, etc.) for momentum injection may be implemented. On the other hand, these devices lack the control authority of net mass flux devices and therefore involves their own set of challenges (Cattafesta & Sheplak, 2011).

Recently, Edstrand and Cattafesta, 2015 performed PIV experiments on the effects of uniform and segmented steady blowing from the wing suction side. The jet was supposed to hinder the wingtip vortex via the Coanda effect but it was bent backward causing an early vortex formation with a lower vorticity and larger core size. In addition, they state that there is not a configuration outperforming the other one but it is possible to find an optimum blowing coefficient for all the considered metrics which is encouraging. Garcia-Ortiz et al., 2020 investigated the effects of continuous blowing through a small orifice up to 20 chord-lengths downstream. Although the wingtip vortex strength is highly decreased at a chord Reynolds number $Re_c = 7 \cdot 10^3$, the active flow control at higher Re_c values was demonstrated to fail. Using steady and pulsed jets from discrete ports on the wingtip, Heyes and Smith, 2004 studied the effect of blowing on the vortex position. They showed striking effects on the vortex structure resulting in a higher core size and a reduced induced velocity peak. The wingtip vortex moved upward and outboard becoming more diffuse due to an increased turbulence production. In addi-

tion, the vortex displacement and its growth rate were found to be related directly to the blowing rate with a different trajectory if an angle between the jet and the chord plane is present. This was the first work with the goal of introducing vortex perturbations tuned to the inherent instability frequencies, accelerating the vortex break up. Bearman et al., 2005 performed a far field PIV investigation on a counter-rotating vortex pair generated by two split wings up to 75 span-lengths downstream. They showed that the pulsed jets are able to decrease the vortices linking distance of about 37%. In their additional work, Bearman et al., 2007 pointed out that if the actuation wavelength is outside the range amplified by the Crow instability, it dies out and it is replaced by a preferred one within the range, which is a useful information when designing the control devices.

As already mentioned, the use of zero-net-mass-flux devices, such as synthetic jets (SJs), allows adding turbulence, momentum, and vorticity to the flow with a variable frequency tuned to the inherent instabilities on the wingtip vortices without bleeding air from the engine. In order to analyze the effectiveness of SJs actuation and for comparison purposes in the wingtip vortices literature, two dimensionless active control parameters are taken into account. More specifically, the SJ momentum coefficient is estimated as

$$C_\mu = \frac{A_j}{A_{w/2}} \frac{\rho_j U_0^2}{\rho_\infty U_\infty^2} \quad (1.19)$$

where A_j is the exit section area of the jet, $A_{w/2} = bc/2$ is the half-wing surface, ρ_j and U_0 are the density and the characteristic velocity of the jet. The dimensionless actuation frequency is defined as

$$F^+ = \frac{f_a c}{U_\infty} \quad (1.20)$$

where f_a is the jet actuation frequency and c is the wing chord-length.

Margaris and Gursul, 2006, 2010 conducted a parametric PIV investigation on the effect of both continuous and synthetic jets blowing from the leading and trailing edge slots of a NACA 0015 with both a squared and rounded wingtip. Two slots blew upward and downward vertically from the wingtip, while two other slots blew spanwise on the upper and lower surfaces of the wingtip. They observed that the jet produced one or more counter-rotating vortices that typically merged with the primary vortex, reducing its strength. The jet acted like a jet in crossflow due to the presence of the flow wrapping around the wingtip. In their best configuration ($C_\mu = 0.016\%$, $F^+ = 0.75$), the SJ demonstrates to be helpful in mitigating vorticity strength (-50%) with a relevant reduction of the tangential velocity and an increase of wandering levels and core radius, especially when it is located near the suction side. By comparing the result to the continuous jet, no clear favorite configuration can be determined. Dghim et al., 2018, 2020; Dghim et al., 2016 reported an exhaustive investigation of the effectiveness of SJ actuation in the near and mid-wake development of a wingtip vortex. They demonstrated that blowing with an actuation frequency in the range individuated by the Crow and Widnall instability frequencies leads to the best results in terms of decreased pressure coefficient distribution at the wingtip. With the actuation frequency set up, a meaningful impact on the wingtip vortex with a vorticity peak reduction up to 60% is obtained by increasing the values of the control momentum coefficient up to $C_\mu = 1\%$. They concluded that a lower

frequency allows a better entrainment and thus a faster dissipation because of the capability of a synthetic jet to travel further in the vortex core. Furthermore, they investigated the effects of the blowing slot shape with a spanwise straight and a curved nozzle. In both cases, the actuation results in a more diffused vortex with a reduction of the tangential velocity peak and an increased core size. As far as regards the latter metrics, the directed SJ presents better performance due to the larger turbulence level introduced by this particular nozzle.

In the following, the main features of the synthetic jets device are briefly reviewed to introduce the reader to the active control device employed in the present thesis.

1.4. SYNTHETIC JETS

SYNTHETIC jet actuators have become a widespread topic in the worldwide fluid dynamic community due to the potential applications in the flow control research field with relevant and beneficial results. As already mentioned, the major characteristic of these devices is a non-zero momentum rate production with a zero-net-mass flux. In addition, the jet does not require any continuous fluid supply to be generated, because it is synthesized directly from the surrounding fluid in which they are deployed and they are more efficient devices than fans requiring lower power consumption. Furthermore, control and design of SJ actuators are rather simple and their actuation frequency can range from few to several kHz. The main disadvantages are related to a maximum velocity achievable, mechanical failure due to fatigue mechanism, and noise problems (Lance & Aarts, 2008).

The first innovative zero-net-mass flux synthetic jet was proposed by Coe et al., 1994. As sketched in Figure 1.11, a synthetic jet device consists of a cavity bounded on a side by an oscillating boundary (commonly a loudspeaker, piezoelectric diaphragm or piston) and on the opposite side by an opening (orifice, slot, pipe or nozzle) acting as both inlet and outlet. Due to the oscillation of the moving boundary, a periodic cavity volume changes (i.e. pressure variations) is generated resulting to alternate ejection and suction of fluid across the opening. In this way, the device is able to transfer momentum to the external environment without net mass ejection. During the ejection stroke, the flow separates at the edges of the outlet and a vortex sheet rolls up. Under certain conditions discussed later in this section, a vortex ring is created and convects away under its own self-induced velocity. During the suction stroke, the surrounding fluid is entrained into the cavity from all directions. The jet formation is possible if the ejected fluid has enough momentum to overcome the call back forces, otherwise the vortex ring is ingested back through the orifice and no jet is generated. The time-periodic cycle induces a time-periodic formation, advection, and interactions of discrete vortical structures which ultimately become turbulent, slow down, and lose their coherence turning into a steady turbulent jet (Smith & Glezer, 1998). Furthermore, a stagnation point (i.e. saddle point), located on the jet centerline separates the suction flow directed towards the cavity from the established jet convecting away.

The flow characteristics of a synthetic jet can be described by two dimensionless param-

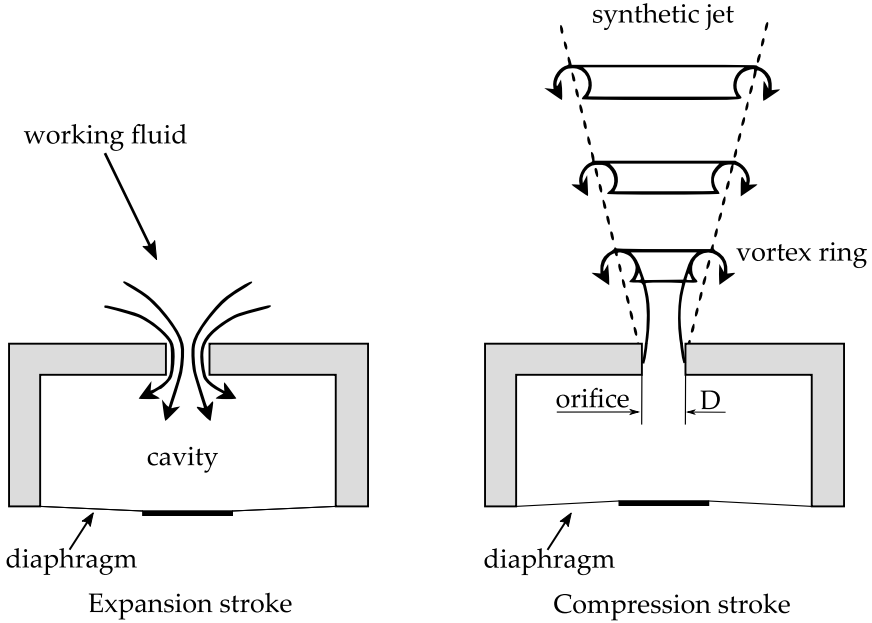


Figure 1.11: Sketch of a synthetic jet device. On the left: fluid ingestion phase; on the right: fluid expulsion phase and vortex ring formation.

eters, the Reynolds and Strouhal numbers, defined as

$$Re_j = \frac{\rho_j U_0 D}{\mu_j} \quad (1.21)$$

$$Sr_j = \frac{D}{L_0} = \frac{f_a D}{U_0} \quad (1.22)$$

where D is the characteristic length usually the orifice or nozzle diameter, μ_j is the jet dynamic viscosity, L_0 is the stroke length (defined as U_0/f_a) and f_a is the oscillating frequency of the membrane (i.e. actuation frequency). In the literature, it is possible to find several definitions of the characteristic velocity of the jet U_0 (Cater & Soria, 2002; Smith & Glezer, 1998). In the present work, accordingly to Smith and Glezer, 1998, U_0 is defined as the mean centerline velocity over the ejection half of the cycle

$$U_0 = \frac{1}{T} \int_0^{\frac{T}{2}} u_e(t) dt \quad (1.23)$$

where T is the actuation period and u_e is the velocity along the jet centerline at the exit section.

Shuster and Smith, 2007 investigated the effect of the dimensionless stroke length and Reynold number. In accordance with the previous works, in the near field, they found the flow dominated by the vortex ring formed during the ejection phase of the actuator

cycle, with the flow field scaled only with the actuator stroke length. At a distance from the orifice larger than the stroke length L_0 , the flow field first undergoes a transition from discrete vortex rings to a nominally steady turbulent jet and then resembles a conventional round turbulent jet. On the other hand, in the far field some differences were observed. The SJ had a faster spreading rate with a correspondingly more rapid decrease in the mean centerline velocity. More recently, McGuinn et al., 2013 have carried out high-speed PIV and hot-wire anemometry measurements to investigate the effect of varying stroke length on the flow morphology of SJs. Four free synthetic jet flow morphology regimes were identified, based on threshold values for the stroke length L_0/D , which are in good agreement with previously published findings for an impulsively started jet flow. No jet is formed for dimensionless stroke length below the formation threshold $L_0/D \leq 0.16$ (Holman et al., 2005). In agreement with Gharib et al., 1998, the strength of a vortex ring increases as the stroke length increases up to $L_0/D = 4$. For additional ejected fluid, $4 \leq L_0/D \leq 8$, the vortex ring shows a wider vortex core and a following trailing jet is created. For $8 \leq L_0/D \leq 16$, a maximum ejected velocity was observed in the trailing jet, which destabilizes the vortex and results in an increased flow mixing. Higher L_0/D exhibited a flow regime dominated by the trailing jet, which overtakes the vortex, resulting in a highly turbulent intermittent jet flow. Figure 1.12 shows a schematic illustration of the morphology of formation and evolution of the synthetic jet flow at different stroke lengths.

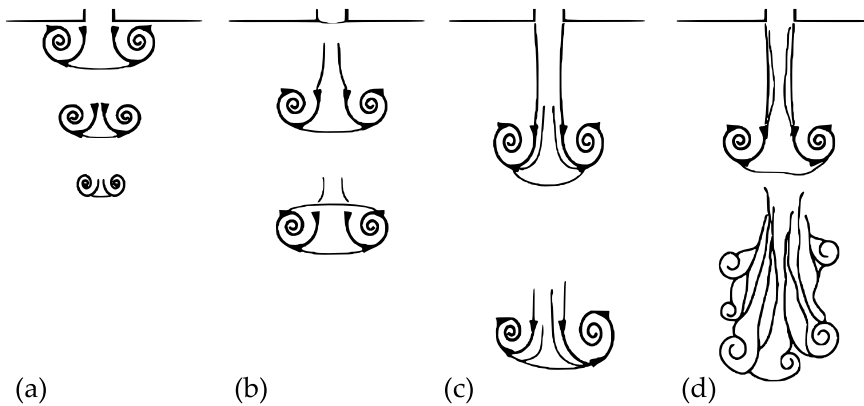


Figure 1.12: Flow morphology of vortex evolution at various stroke lengths (a) $L_0/D < 4$, (b) $4 \leq L_0/D < 8$, (c) $8 \leq L_0/D < 16$, and (d) $L_0/D \geq 16$. Adapted from McGuinn et al., 2013.

1.5. MOTIVATION OF THE WORK

MOST of the researches mentioned in the previous literature review performed a time-averaged analysis of the wake behavior studying the direct impact of blowing on the vortex dissipation by employing only a half-wing to generate one single wingtip vortex. The aim of the present thesis is to experimentally investigate the effectiveness of synthetic jet actuation on the wingtip vortices and wake hazard generated by a finite-span wing in order to preserve the mutual induction of the counter-rotating vortices

during their evolution. The active control has been focused on triggering the inherent instabilities of Crow and Widnall at different momentum coefficient C_μ with the goal to reduce the vortices strength, the induced circumferential velocity, and to obtain an early vortices break up and dissipation. In particular, a first feasibility test on the couple of wingtip vortices alleviation has been conducted by the author on a single measurement plane at three chord lengths downstream of the wing. A parametric study with two momentum coefficients and four actuation frequencies has been carried out to evaluate the best configurations to be further investigated in the present thesis work. As such, two different Stereo-PIV experimental campaigns have been conducted in the near and far field wake in order to analyze how the SJ perturbations affect the wingtip vortices and their development. To the author's knowledge, in the literature of wingtip vortices, the number of experimental works featuring far field velocity measurements under active control up to 75 span lengths is limited to Bearman et al., 2005, 2007. However, in none of these investigations the SJ technology was employed. Furthermore, in the present thesis, a phase-locked analysis has been conducted to give clear insight of the development of the wingtip vortices under the SJ actuation which has not been investigated in the literature except to the previous work of the author (Zaccara et al., 2022). Lastly, different exit geometries of the SJ have been tested to analyze the effects of the jet velocity and jet position changes on the wingtip vortices.

The remaining of this thesis is structured as follows. Stereoscopic Particle Image Velocimetry represents the measurement technique extensively employed in the present thesis and its working principles are reported in chapter 2. In chapter 3, the feasibility test on the wingtip vortices alleviation is reported including the experimental rigs employed and the results which have inspired the following investigation of the thesis. The experimental rigs involved in both the near and far field measurements are reported in chapter 4 where the wind tunnel facilities, the wing models, the synthetic jet devices, the operating conditions, and the image processing are described in details, together with the data processing and metrics employed to analyze the results. The physical behavior and geometrical characteristics of the wingtip vortices under the SJ actuation in the near and far field wake are reported in chapter 5 and 6 for the time-averaged and phase-averaged analysis respectively. Finally, in chapter 7, the conclusions are drawn and future perspective are proposed.

2

STEREOSCOPIC PARTICLE IMAGE VELOCIMETRY

THIS chapter introduces the principles of the measurement technique employed in the present experimental investigation which is the Stereoscopic Particle Image Velocimetry (S-PIV). As such, the general features of the Particle Image Velocimetry (PIV) are firstly outlined and the main aspects related to the stereoscopic configuration are discussed. More details can be found in Raffel et al., 2007.

2.1. PRINCIPLE OF PARTICLE IMAGE VELOCIMETRY

PARTICLE Image Velocimetry is a non-intrusive, laser-based anemometric whole-field technique for measuring the two instantaneous components of the velocity vector within a plane of complex flows. Figure 2.1 presents a typical setup for PIV recording in a wind tunnel. A seeding system inserts tracer particles which needs to accurately follow the flow and to present great light scattering properties. An illumination system, such as a pulsed-laser, creates a collimated light-sheet which illuminates the tracers at least twice within a short time interval. The light scattered is then recorded via high quality camera on a single or multiple frames. It is important to highlight that the PIV technique measures the local fluid velocity indirectly as a function of the tracers displacement occurring in the time interval between two laser pulses. A proper and sophisticated computer algorithm evaluates the local displacement vector for the PIV recordings (Raffel et al., 2007). The acquired images are divided in small subareas called interrogation windows, in which the local displacement vector of the tracer particles is determined using statistical auto-correlation (in case of double-exposure single-frame) or cross-correlation (in case of single-exposure double-frame). Most PIV systems ensure high spatial resolution, but at relative low frame rates. As a matter, the spatial resolution is related to the size of interrogation windows which have to be large enough to include a minimum number of particles which ensures reliable statistical values, but small enough

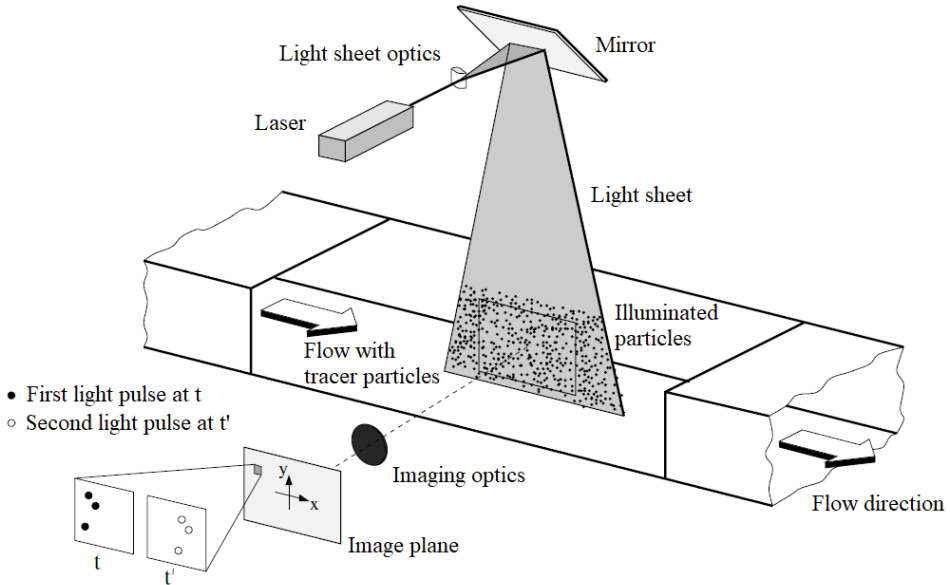


Figure 2.1: Typical experimental layout for particle image velocimetry.

to avoid that the velocity gradients have significant influence on the results. The spatial resolution determines also the number of independent velocity vectors. Finally, the velocity vector is evaluated as

$$\begin{pmatrix} u \\ v \end{pmatrix} = \frac{M_f}{\Delta t} \begin{Bmatrix} \Delta_x \\ \Delta_y \end{Bmatrix} \quad (2.1)$$

where u and v are the instantaneous local velocity components in the object plane, Δt is the time separation between the two laser pulses, Δ_x and Δ_y are the components of the local displacement vector in the image plane, and M_f is the magnification factor from the object plane to the image plane, which is constant in case of no aberrations and misalignment. The magnification factor is the ratio of the distance between the image plane and the lens to the distance between the object plane and the lens.

2.1.1. IMAGING AND OPTICAL SYSTEM

THE three main components of a PIV imaging and optical system are the seeding particles, the illumination source, and the recording system (i.e. digital cameras). Additional elements, such as lenses, mirrors, and filters, are used to shape the light beam in an appropriate pattern, and to enhance the particle imaging thus obtaining high contrast images (high signal-to-noise ratio).

SEEDING PARTICLES

As already said, the PIV technique determines the tracer particles velocity instead of the fluid velocity. Therefore, the particles should faithfully follow the motion of the fluid elements and such a condition requires small size of the same particles. In this

regard, the Stokes number has a primary importance: particles with a low Stokes number (< 0.1) tend to follow fluid elements, on the contrary the motion of particles with a large Stokes number is dominated by inertial effects and does not match that of the fluid (the particles move with their own advection velocities). The Stokes number may be expressed as

$$St = \frac{\tau_s U_\infty}{d_p} \quad (2.2)$$

where U_∞ is the free-stream flow velocity, d_p is the physical particle diameter, and τ_s is the relaxation time defined as

$$\tau_s = d_p^2 \frac{\rho_p}{18\mu_p} \quad (2.3)$$

where ρ_p and μ are the particles density and the dynamic viscosity of the fluid respectively. More details on the most appropriate seeding materials for liquid and gases can be found in Raffel et al., 2007.

In order to increase accuracy in measurements, the particles needs to be in focus throughout the illuminated region with an appropriate size on the sensor plane. The particle image is associated both to geometric effects (i.e. optical magnification) and to diffraction effects which are strictly related to the lens aperture area and the light wavelength. According to Adrian and Yao, 1985, the diameter of the particle in the image plane is given by:

$$d_\tau = \sqrt{d_{\text{geom}}^2 + d_{\text{diff}}^2} = \sqrt{(M_f d_p)^2 + [2.44 f_\# (1 + M_f) \lambda]^2} \quad (2.4)$$

being d_{geom} the geometric image diameter of the particle obtained with a magnification factor M_f (equal to the ratio d_{geom}/d_p), d_{diff} the diffraction image diameter obtained considering the intensity distribution as a Gaussian curve, λ the light wavelength, and $f_\#$ the f-number (ratio of the lens focal length to the aperture diameter). In most cases, $d_{\text{diff}} \gg d_{\text{geom}}$ and $d_\tau \sim f_\#$. As a general rule, d_τ should be not smaller than 2 pixels to avoid the "peak locking", a bias error in the displacement estimation (Westerweel et al., 1997). On the other hand, a larger particle size (>5 pixels) leads to higher uncertainty although it ensures a better light scattering, thus a compromise must be reached.

As far as the best focusing condition regards, it is obtained at the intersection position of the rays coming from the object, after passing through the lens. If the distance between the camera sensor and the lens is not accurately adjusted, the geometric image results blurred. Typically, the extent of the in-focus region is referred to as "depth of field" defined as the distance along the optical axis over which the particle image appears not significantly blurred. The depth of field is related to the diffraction diameter by means of the following expression (Raffel et al., 2007)

$$\delta_z = 2 f_\# d_{\text{diff}} \left(\frac{M_f + 1}{M_f^2} \right) = 4.88 f_\#^2 \lambda \left(\frac{M_f + 1}{M_f} \right)^2 \quad (2.5)$$

ILLUMINATION AND RECORDING SYSTEM

THE dual-cavity pulsed lasers represent the main illumination source in most PIV application to meet the requirement of high-energy density pulses. The duration of the illumination light pulse must be short enough to "freeze" the motion of the particles in

order to avoid blurring of the images ("no streaks"). On the other hand, the time delay between the stroboscopic illuminations, which is a function of the mean fluid velocity and magnification, needs to be short enough to avoid particles with an out-of-plane velocity component leaving the light sheet between subsequent illumination, but long enough to be able to detect the particles' displacements between the images with a sufficient resolution.

Generally, neodymium-doped yttrium aluminum garnet lasers (Nd:YAG lasers) guarantee high pulse energy between 100mJ/pulse and 800mJ/pulse only at low frequencies up to 15 Hz. For high-speed setups up to 10 kHz, Neodymium-doped yttrium lithium fluoride lasers (Nd:YLF lasers) are employed with a considerably lower pulse energy (15 mJ/pulse to 30 mJ/pulse). The wavelength of the emitted light is 532 nm for the Nd:YAG lasers and 527 nm for the Nd:YLF ones. Typically, the laser beam diameter is about 10 mm at the laser output, so a combination of spherical and cylindrical lenses is required to collimate the laser light in a thin sheet.

The images of the tracer particles are recorded by using PIV cameras equipped with CCD (charge-coupled device) and CMOS (complementary metal-oxide-semiconductor) sensors. The first ones offer higher dynamic range and higher resolution, but they are also slower, more expensive and more power-consuming. The second ones guarantee higher repetition rates up to few thousands per second, with a better anti-blooming behavior. The more recent sCMOS (scientific CMOS) technology combines the advantages of modern CCD and CMOS sensors to provide high performance and they have been used for the PIV experiments in the present thesis. Typical sensor sizes vary between 1 to 16 millions of pixels.

2.2. STEREOSCOPIC PARTICLE IMAGE VELOCIMETRY

THE PIV technique described so far presents a planar nature of recording, thus allowing to recover only the projection of the displacement vector into the plane of the light sheet. The out-of-plane velocity component is lost and, as a consequence, the signal-to-noise ratio is reduced together with the accuracy in detecting the correlation peak (Raffel et al., 2007). Moreover, the in-plane components are affected by an unrecoverable error due to the particle displacement in the laser thickness direction (i.e. perspective transformation error) which increases at the edge of the field of view (FOV). As a consequence, PIV can generate significant measurement errors of the local velocity vector when applied to highly three-dimensional flows. Such an error increases as the distance to the optical axis increases and so an advantageous choice is to select viewing distance much larger than the imaged area to keep the projection error to a minimum. This may be achieved using long focal length lenses. Anyway, it is often required to extract 3D information due to the complexity of the phenomenon.

In order to overcome these shortcomings, Stereoscopic Particle Image Velocimetry (S-PIV) has been developed. S-PIV employs two cameras to acquire two simultaneous views along different directions, thus allowing the out-of-plane velocity component to be measured as shown in Figure 2.2. The two components of velocity nominally perpendicular to the camera optical axis are measured from each camera perspective and combined, through appropriate geometric reconstruction formulas, to obtain the three-component velocity vector within the observed plane. The most accurate determination of the out-

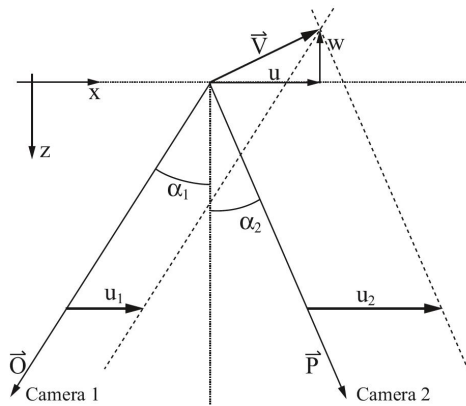


Figure 2.2: Stereo viewing geometry in the xz -plane. Adapted from Raffel et al., 2007.

of-plane displacement (i.e. velocity) is accomplished when the opening angle between the two cameras $\alpha_1 + \alpha_2$ is 90° . Among several optical arrangements of the two cameras, the Scheimpflug configuration was found to be the best layout and anyway necessary when small values of camera f-number (i.e. small depth of field) are required. According to the Scheimpflug condition, the object plane, image plane, and lens principle plane have to intersect at a common line, as shown in Figure 2.3. By tilting the image sensor plane and the lens plane to the Scheimpflug condition, it is possible to achieve a good focus over the entire plane of the light sheet. The drawback of an oblique view of the scene is the introduction of a perspective distortion that is further increased by the Scheimpflug imaging arrangement, resulting in a magnification factor that is no longer constant across the field of view and requires an additional means of calibration.

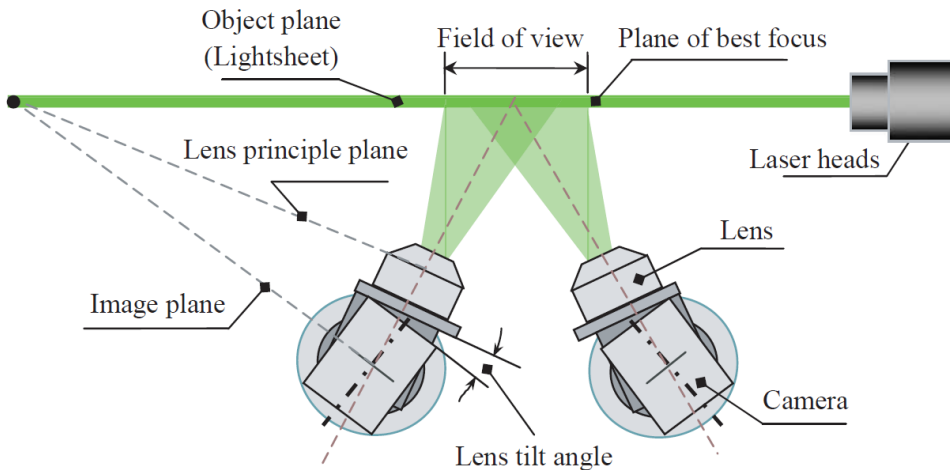


Figure 2.3: Scheimpflug stereoscopic camera configuration. Image taken from Liu et al., 2006.

2.2.1. S-PIV ALGORITHM

THE S-PIV algorithm employed in the present thesis is made of three main steps: the correction of the misalignment error between calibration and measurement planes (Figure 2.4), PIV cross-correlation, and 3C displacement reconstruction. In particular, the S-PIV steps are:

- Optical calibration: a mapping function, which transforms the object coordinates into the image coordinates of camera 1 and of camera 2, is computed.
- Image dewarping: the two dewarped images recorded at the same instant by the two cameras are compared with a PIV process based on the iterative image deformation method (Astarita, 2006).
- Disparity correction: the disparity map can be computed and used to evaluate the local misalignment by means of triangulation.
- Measurement plane determination: the equation of the measurement plane in the object space is computed by means of a regression method. The above steps are iterated to obtain a better accuracy in the determination of the measurement plane equation.
- PIV cross-correlation: the images of each camera are dewarped on the correct measurement plane onto a common grid in the physical space. A PIV cross-correlation algorithm, detailed in Astarita, 2008, is applied individually for each camera.
- Three component displacement reconstruction: finally, the three component displacement is obtained by using geometrical relations (Giordano & Astarita, 2009; C. Willert, 1997) or gradient based formulations (Soloff et al., 1997).

2.2.2. OPTICAL CALIBRATION PROCEDURE

THE optical calibration procedure is based on the determination of the mapping function $F^{(c)}$ between the object coordinates \underline{x} and image coordinates \underline{X}_c relative to each camera c :

$$\underline{X}_c = F^{(c)}(\underline{x}) . \quad (2.6)$$

A typical S-PIV calibration setup is based on recording images of planar calibration target which is placed coincident with the light sheet plane. The calibration target consists of a precise grid of high-contrasted known markers. In order to evaluate the camera orientation, a set of image-to-object correspondence points that are not co-planar are needed. Therefore, different images of the calibration target are recorded when it is slightly displaced at known positions in the direction normal to the light sheet plane.

Calibration comprises essentially three phases:

1. after recording images of the target at different positions, each of the two calibration grid images is cross-correlated with a proper correlation mask to evaluate the position of the marks which are fitted with the typical three-points (Gaussian) estimator with sub-pixel accuracy;

2. creation of a discrete correspondence between the physical and image plane coordinates of the detected marks;
3. a regression method based on a chosen mapping function F is applied to each of the two image-object point pair sets yielding a set of reconstruction coefficients for each camera view. One of the most adopted model for F is the pinhole camera model.

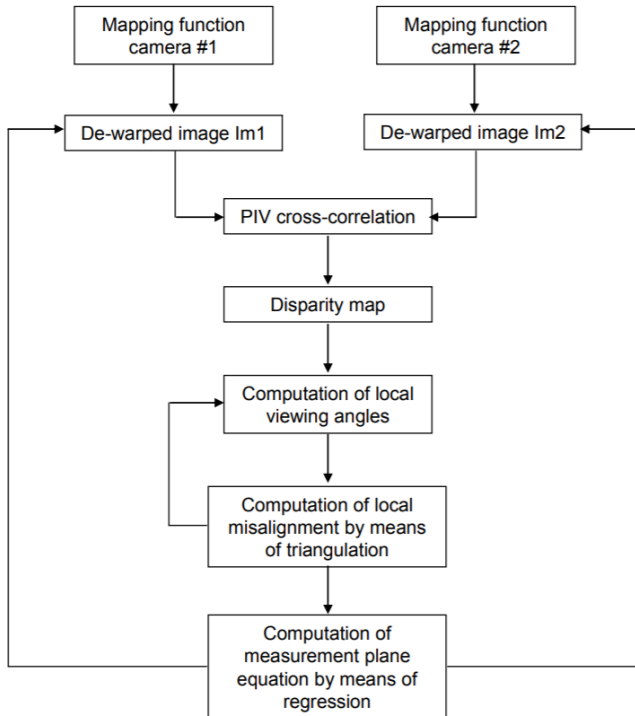


Figure 2.4: Scheme of the procedure used to correct the misalignment error between calibration and measurement planes. Adapted from Giordano and Astarita, 2009.

2.2.3. IMAGE DEWARPING

IN order to obtain the three component displacement, the data set must first be converted from the image plane to true displacements in the global coordinates system taking into account of all magnification issues. The first step is image dewarping, which consists in the removal of distortion (i.e. variation in the magnification factor) in the recorded image, in order to associate velocity vectors to the points in a common grid of the physical space (the effective area of interest) by using the mapping function F , as shown in Figure 2.5. A high-order interpolation scheme is required to increase the accuracy of the backprojection. Interpolation schemes based on B-spline functions are widely employed by the PIV community users. In this case it is possible to use square

interpolation grids with a linear dimension that is a function of the spline order. In particular, a spline of order two uses a stencil of 3×3 points, while a spline of order three uses 4×4 points. Details on implementation of the algorithm and on the relations of the B-spline interpolation schemes with the cardinal interpolation formula can be found in Unser et al., 1993a, 1993b and in Unser, 1999.

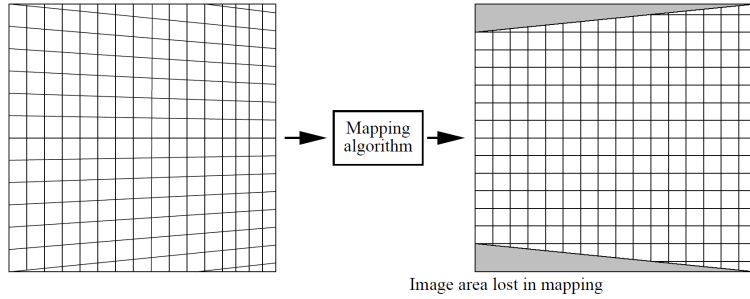


Figure 2.5: Mapping function between the image and the object plane. Adapted from C. Willert, 1997.

2.2.4. DISPARITY CORRECTION

ONE of the main source of errors in a S-PIV measurement setup is represented by the unavoidable misalignment that occurs between the calibration plane and the laser sheet, i.e. the measurement plane, as shown in Figure 2.6. It greatly affects the true position of the light sheet in space and the dewarping of images, thus a disparity correction based on cross-correlation between the images of the two cameras is applied.

The scheme of the whole correction procedure is reported in Figure 2.4. By comparing the two instantaneous dewarped images, the disparity map can be computed with a PIV cross-correlation process. In the case of a misalignment, as shown in Figure 2.6, a generic point P of the measurement plane is viewed in two different positions P_1 and P_2 by the two cameras in the dewarping process.

Using the disparity vector D_u and the local viewing angles of each camera α_c (angle between the viewing ray and the plane yz measured in the xz plane), it is possible to compute the local misalignment by means of triangulation:

$$\Delta z = \frac{D_u}{\tan \alpha_1 + \tan \alpha_2} . \quad (2.7)$$

Finally, the equation of the measurement plane in the object space is computed by means of a regression method. The whole procedure is iterated in order to obtain a better accuracy in the determination of the measurement plane equation. After the first iteration, the images are dewarped taking into account the measurement plane equation computed in the previous step. Obviously, in order to avoid extrapolation in the dewarping process, the mapping volume has to contain the measurement plane. Alternatively, it is also possible to recompute the mapping function Wieneke, 2005; in this way, the measurement plane has always the equation $z = 0$.

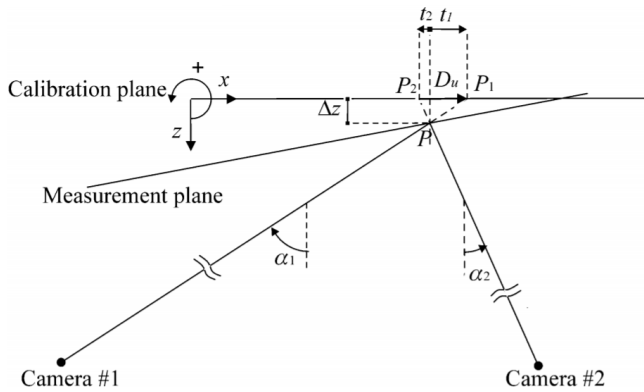


Figure 2.6: Sketch of a generic misalignment error between calibration and measurement planes. Image taken from Giordano and Astarita (2009).

2.2.5. 3C DISPLACEMENT RECONSTRUCTION

As already mentioned, the application of a stereoscopic reconstruction allows obtaining the 3C of the velocity vector from the two-dimensional views. There are several methods to perform the stereoscopic reconstruction and Prasad, 2000, in a review article, subdivided these methods into geometrical and calibration based. The former approach is not used anymore because the latter is normally more accurate.

Among the possible calibration-based approaches, the S-PIV community mainly adopts two alternative methods: geometrical (C. Willert, 1997) and gradient based (Soloff et al., 1997). In the former, the two images recorded from different angles are first dewarped and then processed with a standard PIV algorithm in order to obtain the two-dimensional maps of the displacements along the directions orthogonal to the camera axes. Finally, a geometrical reconstruction is used to obtain the 2D3C velocity vector in the laser sheet plane. Soloff et al., 1997 proposed to skip the dewarping step and to apply the PIV algorithm directly on the recorded images. In this case, the stereoscopic reconstruction is performed by using a gradient based formulation. The method proposed by Soloff et al., 1997 can only be applied by computing the two 2D displacement maps directly on the recorded images. On the other hand, Coudert and Schon, 2001 showed that the geometrical approach can be applied on both the dewarped and the raw images. In the present thesis, both approaches have been employed and they are briefly described in the following.

GEOMETRICAL METHOD

THE two couples of recorded images are first dewarped on the object plane by using the mapping function obtained from the calibration. Mapping the recorded images prior to processing them has the advantage of obtaining a constant and isotropic spatial resolution. By processing the mapped couples of images with a PIV algorithm, it is possible to evaluate both 2D displacement fields (u_c , v_c) on a common grid in the world coordinate system. In order to perform the mapping, it is needed to re-sample the images which can lead to a loss of image quality. It has to be noticed that if an image defor-

mation method (Astarita, 2007; Scarano, 2001) is used as a PIV algorithm, it is possible to insert the dewarping procedure directly inside the PIV algorithm without inducing any additional loss of quality (Scarano et al., 2005; Wieneke, 2005). The scheme of the adopted 3C displacement reconstruction procedure consists of the following steps:

- an iterative image deformation PIV process is computed on each couple of dewarped images: dewarping of images is computed by considering the real position of the measurement plane;
- a geometric reconstruction of the three-dimensional displacement field is obtained by means of the two 2C-vector fields (related to the two cameras) and of the local viewing angles $\alpha_1, \alpha_2, \beta_1,$ and β_2 (see Figure 2.7, α_c (β_c) is the angle between the viewing ray and the plane yz (xz) measured in the xz (yz) plane).

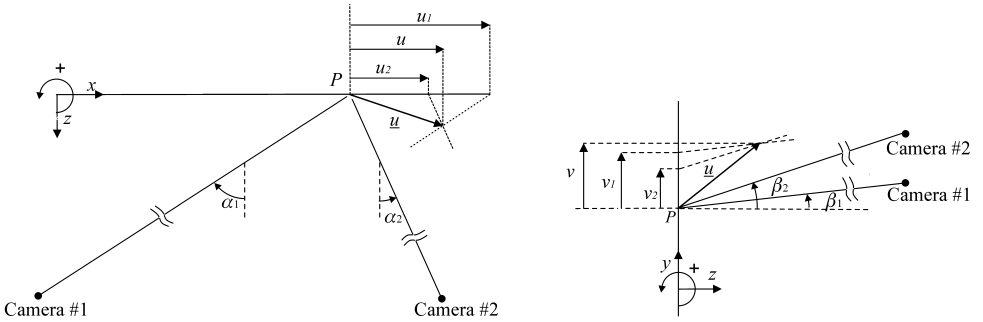


Figure 2.7: Geometrical reconstruction on the xz plane and yz plane. Image taken from Giordano and Astarita (2009).

In the case of small displacements (i.e. when the viewing rays are practically parallel), C. Willert, 1997 proposed the following formulas for the stereoscopic reconstruction of the 3C (u, v, w) velocity vector from the 2D components u_1, v_1 and u_2, v_2 (for $\beta_c \ll 1$):

$$u = \frac{u_1 \tan \alpha_2 - u_2 \tan \alpha_1}{\tan \alpha_2 - \tan \alpha_1} \quad (2.8a)$$

$$w = \frac{u_1 - u_2}{\tan \alpha_2 - \tan \alpha_1} \quad (2.8b)$$

$$v = \frac{v_1 \tan \beta_2 - v_2 \tan \beta_1}{\tan \beta_2 - \tan \beta_1} = \frac{v_1 + v_2}{2} + \frac{w}{2} (\tan \beta_1 + \tan \beta_2) \quad (2.8c)$$

The angles α_c and β_c are defined in Figure 2.7 and may be evaluated by measuring the relative distances:

$$\tan \alpha_c = \frac{x_c - x_p}{z_c - z_p}; \quad \tan \beta_c = \frac{y_c - y_p}{z_c - z_p} \quad (2.9)$$

where (x_p, y_p, z_p) and (x_c, y_c, z_c) are the coordinates in the object space of the measurement point P and of the pinhole of the generic camera c .

Following Giordano and Astarita, 2009 to determine the local viewing angle, one can

imagine an infinitesimal displacement vector $d\mathbf{x}$ along the viewing ray of the camera c (see Figure 2.8). Obviously, the correspondent displacement dX_c in the image plane is zero. Consequently, if one considers the Taylor series expansion of the mapping function:

$$d\mathbf{X}_c = \nabla \underline{F}^{(c)} \cdot d\mathbf{x} \quad (2.10a)$$

$$\begin{bmatrix} dX_c \\ dY_c \end{bmatrix} = \begin{bmatrix} X_x^{(c)} & X_y^{(c)} & X_z^{(c)} \\ Y_x^{(c)} & Y_y^{(c)} & Y_z^{(c)} \end{bmatrix} \cdot \begin{bmatrix} dx \\ dy \\ dz \end{bmatrix} \quad (2.10b)$$

where $X^{(c)}$ is the mapping function for the image coordinate X_c relative to the camera c and the subscript indicates derivation. The projection of Eq. (2.10b) along the viewing ray becomes:

$$\begin{bmatrix} X_x^{(c)} & X_y^{(c)} & X_z^{(c)} \\ Y_x^{(c)} & Y_y^{(c)} & Y_z^{(c)} \end{bmatrix} \cdot \begin{bmatrix} dx \\ dy \\ dz \end{bmatrix} = \underline{0} \quad (2.11)$$

As a result, the viewing angles α_c and β_c in a generic point P are found to be:

$$\tan \alpha_c = \left. \frac{dx}{dz} \right|_{dX_c=0} = \frac{Y_z^{(c)} X_y^{(c)} - Y_y^{(c)} X_z^{(c)}}{Y_y^{(c)} X_x^{(c)} - Y_x^{(c)} X_y^{(c)}} \quad (2.12a)$$

$$\tan \beta_c = \left. \frac{dy}{dz} \right|_{dX_c=0} = \frac{Y_z^{(c)} X_x^{(c)} - Y_x^{(c)} X_z^{(c)}}{Y_x^{(c)} X_y^{(c)} - Y_y^{(c)} X_x^{(c)}} \quad (2.12b)$$

The main advantage of the formulas proposed by Giordano and Astarita, 2009 is that

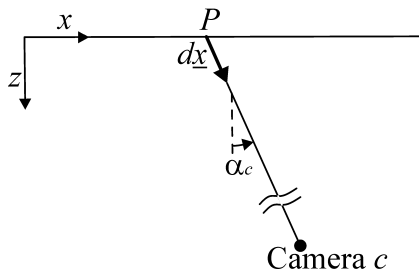


Figure 2.8: Sketch of a generic displacement along the viewing ray of the camera. Image taken from Giordano and Astarita (2009).

there is no need to measure any additional geometrical parameter of the experimental setup. Moreover, with these formulas it is possible to compute the viewing angles without any further computation in addition to the unavoidable calibration of the stereoscopic configuration. Lastly, Eq. (2.8a) to (2.8c) can also be written, for the generic camera c , in the following compact form:

$$\tan \alpha_c = \frac{u - u_c}{w}; \quad \tan \beta_c = \frac{v - v_c}{w} \quad (2.13)$$

By considering both cameras, Eq. (2.13) is a system of four linear equations in three unknowns velocity components (u , v , w) that can be easily solved in a least squares sense (Raffel et al., 2007). The general scheme of the geometrical approach for the 3C reconstruction procedure is reported in Figure 2.9.

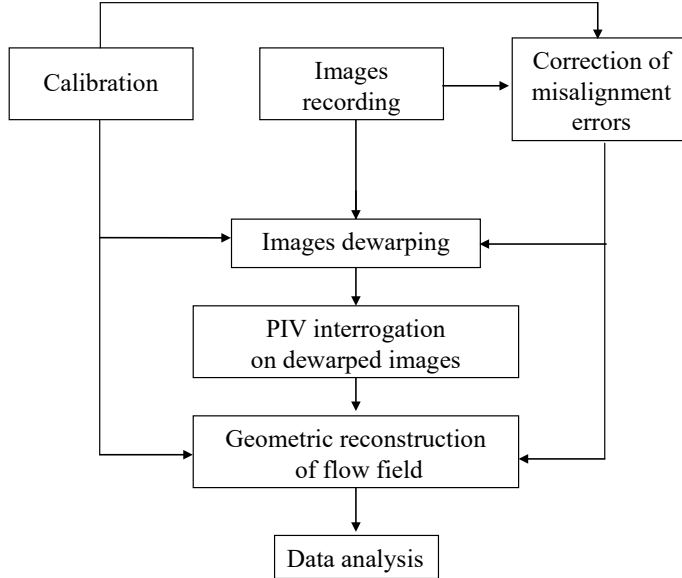


Figure 2.9: Scheme of the geometrical approach for the 3C reconstruction procedure.

GRADIENT BASED METHOD

As already mentioned, in the gradient based approach the 2D displacements fields are computed directly on the recorded images. In order to perform the stereoscopic reconstruction, the displacement vectors should be evaluated on a common grid, in the world coordinate system. Some authors report the possibility of evaluating the 2D displacements in the correct world position but this approach is of difficult application. The other possibility is to evaluate 2D displacements with a standard PIV on a structured rectangular grid in the image space and then to interpolate the vectors on a common grid in the world space. In this case the spatial resolution changes from point to point and this can have an influence on the Modulation Transfer Function (MTF) of the stereo PIV (Giordano & Astarita, 2009).

The stereoscopic reconstruction can be taken on in different ways. Calluaud and David, 2004 proposed to fix the tail of the displacement vector on a point in the world grid and then to map back the head of the vector from the two 2C measurements. From the difference between the positions of the head and tail, it is possible to reconstruct the velocity vector. This algorithm can be even improved by using a centered approach. The main flaw is that the solution of the nonlinear over-determined system can be difficult. The

most common gradient based approach is the one proposed by Soloff et al., 1997 which includes in one step the images dewarping and the 3C reconstruction. In particular, the 2D displacement of a particle in the image plane is:

$$d\underline{X}_c = \underline{F}^{(c)}(\underline{x} + d\underline{x}) - \underline{F}^{(c)}(\underline{x}) \quad (2.14)$$

where $d\underline{x}$ is the displacement in the object plane. By computing a Taylor series expansion of Eq. (2.14), a first-order relationship between the displacements in the image and object planes is:

$$d\underline{X}_c = \nabla \underline{F}^{(c)} \cdot d\underline{x} \quad (2.15a)$$

$$\begin{bmatrix} dX_1 \\ dY_1 \\ dX_2 \\ dY_2 \end{bmatrix} = \begin{bmatrix} X_x^{(1)} & X_y^{(1)} & X_z^{(1)} \\ Y_x^{(1)} & Y_y^{(1)} & Y_z^{(1)} \\ X_x^{(2)} & X_y^{(2)} & X_z^{(2)} \\ Y_x^{(2)} & Y_y^{(2)} & Y_z^{(2)} \end{bmatrix} \quad (2.15b)$$

Eq. (2.15a) (or (2.15b)) is a linear system with three unknowns and two equations for each camera. By combining the equations for the two cameras, it is possible to find a system with four equations and three unknowns, which can be easily solved in a least squares sense. Finally, the scheme of the whole procedure is drawn in Figure 2.10.

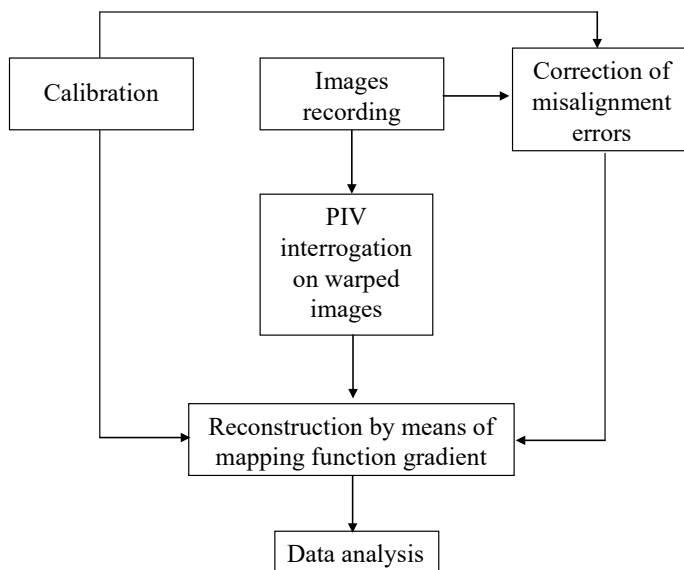


Figure 2.10: Scheme of the gradient based approach for the 3C reconstruction procedure.

3

FEASIBILITY TEST ON WINGTIP VORTICES ALLEVIATION

As already mentioned in the introduction section of the present thesis, the past researches performed a time-averaged analysis of the wake behavior studying the direct impact of blowing on the vortex dissipation by employing only a half-wing to generate one single wingtip vortex. As such, the author performed a feasibility test on the effectiveness of the synthetic jet actuation on wingtip vortices generated by a finite-span wing in order to preserve the mutual induction of the counter-rotating vortices during their evolution. Different blowing configurations have been investigated by varying the synthetic jet velocity and actuation frequency to analyze the effectiveness of the active flow control tuned also to the inherent instability frequencies of the vortices. In addition, a novel phase-locked analysis has been conducted to give clear insight of the development of the wingtip vortices under the synthetic jet actuation.

In the following, the experimental apparatus including the wind tunnel and S-PIV setup and the operating conditions are presented in section 3.1. The results are presented in section 3.2.1 and 3.2.2 related to the time-averaged and phase-averaged analysis respectively, while the conclusions are drawn in section 3.3.

3.1. EXPERIMENTAL APPARATUS AND OPERATING CONDITIONS

3.1.1. EXPERIMENTAL RIGS

THE experiments have been conducted in the open jet wind tunnel at the Department of Industrial Engineering of the Università degli Studi di Napoli “Federico II” shown in Figure 3.1. The flow is generated by a centrifugal fan and passes across a stagnation chamber; honeycomb screens are placed to ensure uniformity of the flow velocity over

Parts of this chapter have been published in *Experimental Thermal and Fluid Science*, 130, 110489 (2022), Zaccara et al., 2022.

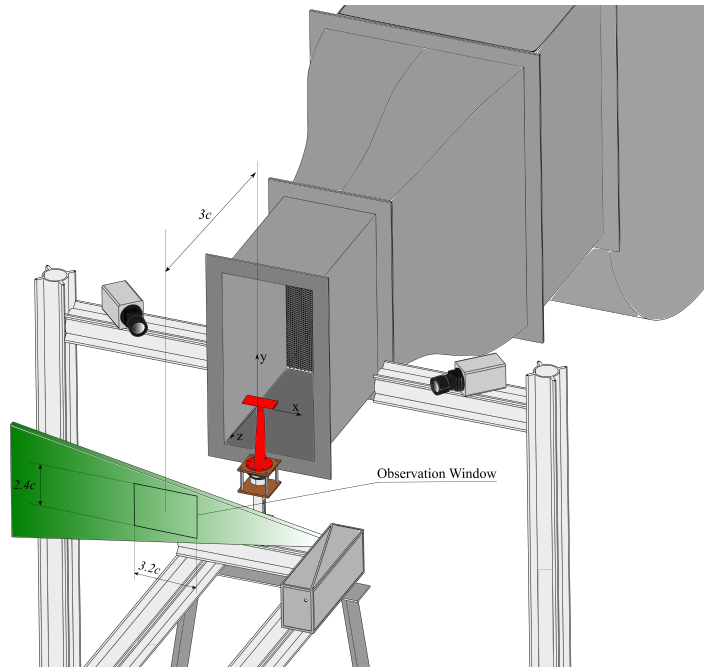


Figure 3.1: Experimental setup.

the cross section. Then, the flow develops across a convergent duct with a contraction ratio of 3.25 and a final 0.5 m-long rectangular duct with a constant cross sectional area of $0.30 \times 0.60 \text{ m}^2$. As shown in Figure 3.1, the reference frame $Oxyz$ is anchored to the wing trailing edge at the mid-span point with x , y , and z -axis aligned with the spanwise, crosswise, and streamwise directions respectively.

A sketch of the wing model employed for the present experiments is reported in Figure 3.2. It is a rectangular finite-span square-tipped wing equipped with a NACA 0024 airfoil section. The airfoil chord is $c = 0.05 \text{ m}$, the wingspan is $b = 0.1 \text{ m}$, resulting in an aspect ratio $\mathcal{R} = 2$. The wing sting support has a trapezoidal shape with a taper ratio of 1.6, root chord of 0.08 m, height of 0.208 m, and a NACA 0024 airfoil section. The wing is manufactured in PLA plastic by a high-resolution 3D printer at the Department of Industrial Engineering of the Università degli Studi di Napoli “Federico II”.

The synthetic jet is generated by using a loudspeaker as oscillating driver (Greco et al., 2013). At the basis of the wing support, a 50 W speaker (Ciare HW100) is attached. It is supplied with a sinusoidal input signal generated by a Digilent Analog Discovery™ USB Oscilloscope, coupled with a power amplifier (Kenwood KAC-6405). The duct for the supply of the synthetic jets runs throughout the wing span and the support. This chamber ends at the tips of the wing in two rectangular slots as shown in Figure 3.2. They are placed in the mid-plane of the wing based on the design from previous works (Dghim et al., 2018, 2020; Dghim et al., 2016; Heyes & Smith, 2004). The slots are $0.4c$ wide and positioned at $z/c = -0.20$. Following the findings of Margaris and Gursul, 2010, position-

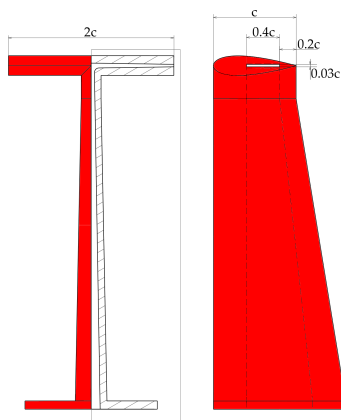


Figure 3.2: Front and side views of the finite-span wing model equipped with the internal synthetic actuator. The dashed lines display the slot running through the sting and the wing.

ing the jet further downstream leads to a higher jet velocity in the near wake and thus stronger jet vortices which could interact more with the wingtip vortices. The height of the slots of $0.03c$ is fixed by the minimum clearance of the 3D printer employed. The internal shape is similar to the airfoil section and then, in the wing, the duct turns to a rectangular one convergent to the slot at the wingtip with a contraction ratio equal to 2. For the Baseline Case (BC) with no control, the slots have been covered with tape to avoid passage of air inside the wing. Both the model and the loudspeaker are connected to an interface which can be oriented with respect to the streamwise direction with the aid of an inertial measurement unit.

3.1.2. STEREOSCOPIC PARTICLE IMAGE VELOCIMETRY SETUP

STEREOSCOPIC particle image velocimetry is used to measure the instantaneous three-component velocity and a schematic of the experimental setup is shown in Figure 3.1. The flow is seeded with olive oil particles having a mean diameter of $1\ \mu\text{m}$ and generated by a Laskin nozzle. They are spread through a seeding rake placed in front of the collector of the centrifugal fan. The seeding rake is made of 10 pipes (2 cm diameter) with 5 mm holes throughout their length and circumference. The centrifugal fan guarantees the mixing of the particles in the flow. Illumination is provided by the Quantel Evergreen laser, a low-speed double pulsed Nd:YAG laser (532 nm, 200 mJ per pulse, $<10\ \text{ns}$ pulse duration). The laser beam is shaped into a 2 mm thick light sheet. The time delay between the two laser pulses has been set to $10\ \mu\text{s}$. Images are acquired by two Andor Zyla sCMOS cameras (2160×2560 pixels, pixel pitch of $6\ \mu\text{m}$, intensity resolution 16 bit) in stereo configuration equipped with Tokina AT-X M100 PRO D lenses of 100 mm focal length. To compensate the different brightness conditions, the relative aperture is set at $f\# = 11$ for the camera in forward scattering configuration, whereas, at $f\# = 5.6$ for that in backward scattering. The angle between the optical axes of the two cameras is set at about 105° and Scheimpflug adapters are used in order to achieve good focus over the entire field of view. The present imaging produces a field of view of

$2.4c \times 3.2c$ with a spatial resolution of about 21 pixel/mm. In order to perform phase-locked measurements, an appropriate sampling frequency determined in accordance with the procedure of Greco et al., 2013 has been set for each investigated control case. The S-PIV measurements and the synthetic jet actuation were controlled by an external signal synchronizer. In particular, the S-PIV measurements were locked to the electrical signal driving the loudspeaker. Hence, the periodic phenomenon is sampled with a phase separation $\Delta\phi = 24^\circ$, leading to 15 phases per cycle. A total of 3750 image pairs, i.e. 250 snapshots per phase, are acquired to obtain a statistically reliable data. The quality of the image pairs is improved by subtracting a background intensity from the raw images obtained by computing the minimum intensity based on the entire ensemble of the image pairs. A multiple pass algorithm with image deformation is employed to compute the velocity field using Blackman weighting windows according to Astarita, 2006, 2007, 2008; Astarita and Cardone, 2005. The final interrogation area size is 64×64 pixels with an overlap of 87.5%, resulting in a measurement resolution L_m of 0.38 mm. Lastly, the maximum random error on the instantaneous velocity vectors is estimated to be 0.109 pixels (Bhattacharya et al., 2016), which leads to a vorticity uncertainty of about 1.7% of the maximum detected phase-averaged vorticity (Sciacchitano & Wieneke, 2016).

3.1.3. OPERATING CONDITIONS

ALL the experiments have been conducted at $Re_c = 8.16 \times 10^4$. The free-stream velocity U_∞ is 24.5 m/s with a turbulence level of 1.3% measured via hot-wire anemometry. The S-PIV measurement plane is placed at $z/c = 3$ for each test and the wing is mounted at an angle of attack of $\alpha = 5^\circ$ placed at a distance equal to one chord-length from the nozzle exit section.

The instantaneous velocity of the synthetic jet at both the tips is measured by means of a constant temperature anemometer system (Dantec-MiniCTA) equipped with a single-component hot wire of length 1.25 mm and diameter $5\mu\text{m}$ (55P11). To uniformly cool the active sensor, the wire was aligned with the direction of the long side of the slot and placed at the slot exit. The sampling frequency was fixed at $1000f_a$, where f_a is the synthetic jet actuation frequency. It is worth noting that the hot-wire sensor acquisitions were synchronized with the electrical signal sent to the loudspeaker. As a result, the phase shift between this electrical signal and the synthetic jet exit velocity was characterized in order to accurately identify the start of the cycle of the synthetic jet with respect to the sampled phases.

In order to analyze the effectiveness of the synthetic jet actuation, five different control cases (CCs) have been investigated. CC1 and CC2 are characterized by a $C_\mu = 0.2\%$ and $C_\mu = 0.04\%$ respectively, and by an f_a equal to the Crow instability frequency estimated to be 35 Hz according Eq. (1.16). CC3 is related to a $C_\mu = 0.04\%$ and by $f_a = 82$ Hz ($\lambda \sim 3b$) that is out of the range bounded by the Crow instability frequency as suggested by Bearman et al., 2005, 2007. CC4 is characterized by a $C_\mu = 0.04\%$ and by an f_a equal to the Widnall instability frequency estimated to be 272 Hz according Eq. (1.18). Lastly, CC5 is defined with a $C_\mu = 0.04\%$ and by an $f_a = 360$ Hz which corresponds to the fifth wake mode instability found by Edstrand et al., 2018. A summary of the control cases is reported in Table 3.1.

Table 3.1: Characteristic dimensionless parameters for the investigated configurations.

Control Case	α	Re_c	F^+	C_μ
BC	5°	8.16×10^4	-	-
CC1	5°	8.16×10^4	0.0714	0.2%
CC2	5°	8.16×10^4	0.0714	0.04%
CC3	5°	8.16×10^4	0.167	0.04%
CC4	5°	8.16×10^4	0.555	0.04%
CC5	5°	8.16×10^4	0.735	0.04%

3.2. RESULTS AND DISCUSSIONS

IN the present section, both the average results based on the entire ensemble of the instantaneous flow fields and the phase-averaged results are reported. The evaluation methods of each physical and geometrical quantity presented herein are detailed in Zaccara et al., 2022. As regards the notation employed, the symbols $\overline{(\cdot)}$ and $\langle \cdot \rangle$ represent a time-averaged and phase-average value respectively.

3.2.1. TIME-AVERAGED ANALYSIS

THE contour maps of the non-dimensional time-averaged streamwise vorticity $\overline{\zeta}_z c / U_\infty$ for all the investigated cases are reported in Figure 3.3. Here, the dashed black line represents the projection of the wing trailing edge onto the measurement plane. From the baseline case in Figure 3.3a, it is evident that at $z/c = 3$ the roll-up process is not completed yet (Ramaprian & Zheng, 1997). In fact, a region with lower vorticity than the wingtip vortices related to the shear-layer leaving the trailing edge is clearly discernible. In all the configurations reported in Figure 3.3, the vortices present an ellipsoidal shape which could be mainly attributed to the strong interaction with the shear-layer during the roll-up process and to the 3D vortices structure (Ramaprian & Zheng, 1997). Furthermore, the vortices centers do not coincide with the wingtips projections and they are drawn inboard of about $0.2c$. Under the control configuration CC1 tuned to the Crow instability frequency, the vortices appear to diffuse over a wider area, characterized by a smaller vorticity gradient too. Moreover, they appear to be stretched assuming an elongated ellipsoidal shape resulting in a strength reduction of 26% in terms of vorticity peak values with respect to the baseline case. By reducing the momentum coefficient of 80% at the same actuation frequency (CC2), the vortices characteristics do not substantially vary in terms of diffusion and vorticity peak which is slightly increased to 27% against the baseline case. This suggests that the momentum coefficient is not a crucial parameter for the investigated conditions of $F^+ = 0.0714$ and $z/c = 3$.

By fixing $C_\mu = 0.04\%$ and increasing the actuation frequency from CC3 to CC5, it is clear that the synthetic jet actuation results in a diffusion of the vortices which increases with F^+ . This is confirmed in Table 3.2 where the geometrical characteristics of the vortices are reported. In particular, the most pronounced diffusion is related to the CC4 and CC5 where a major axis increase of about 47% with respect to the baseline case is observed. As reported in Table 3.2, the aspect ratio and the inclination angle have a maximum in the

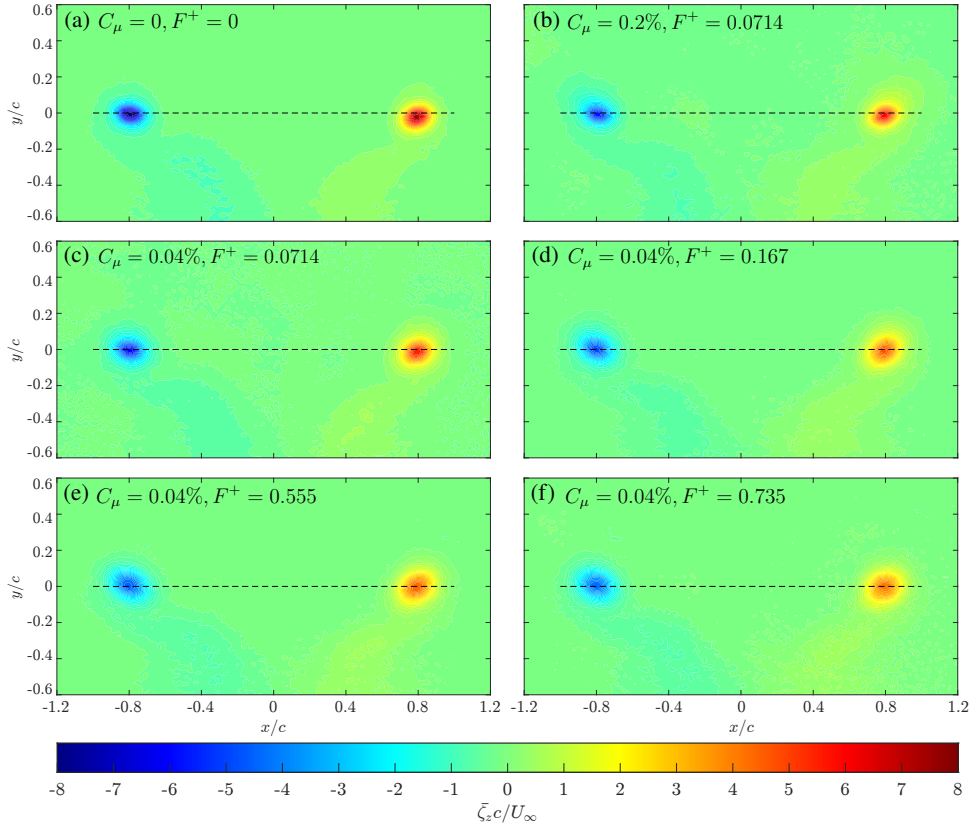


Figure 3.3: Time-averaged normalized streamwise vorticity contours at $z/c = 3$. a) BC, b) CC1, c) CC2, d) CC3, e) CC4, and f) CC5.

Table 3.2: Normalized streamwise vorticity peak value, circulation, vortex major axis, aspect ratio and inclination angle of the vortices for all the control cases. The BC value of $\bar{\zeta}_{z,max}c/U_\infty$ and $\bar{\Gamma}/(U_\infty c)$ are equal to 7.24 and 0.113 respectively.

Control Case	$\bar{\zeta}_{z,max}/\bar{\zeta}_{z,max}^{BC}$	$\bar{\Gamma}/\bar{\Gamma}^{BC}$	\bar{D}_{max}/c	$\bar{D}_{max}/\bar{D}_{min}$	$\bar{\Phi}$
BC	1.00	1.000	0.213	1.319	13.6°
CC1	0.745	1.233	0.223	1.353	26.2°
CC2	0.734	1.219	0.245	1.300	15.2°
CC3	0.595	1.292	0.280	1.261	26.1°
CC4	0.564	1.262	0.314	1.290	30.4°
CC5	0.538	1.240	0.310	1.208	19.5°

CC1 and CC4 respectively without showing any trend with the momentum coefficient and/or the actuation frequency. On the other hand, the vortices mean relative distance \bar{b}_0 appears to be not too affected by the SJ actuation. Lastly, in Table 3.2, the stream-

wise vorticity peak for the configurations investigated normalized with respect to the BC value is also reported. As it can be noted, a decrease of 41% and 44% is obtained for CC3 and CC4 (tuned to the Widnall instability frequency), while a major impact is achieved in the CC5 (-46%) which is representative of the fifth wake mode instability reported by Edstrand et al. Edstrand et al., 2018. It is worth noting that a huge reduction of the vorticity peak is registered for all the cases investigated. This effect could be related to the interaction between the SJ and the wingtip vortices which propagate downstream and/or to a change in the vorticity decay rate.

A crucial parameter to evaluate the synthetic jet actuation effectiveness on the wingtip vortices control is the time-averaged vortex circulation. It has been evaluated by analytically integrate the streamwise vorticity field as described by Zaccara et al., 2022. The results are displayed in Table 3.2.

Under the control case CC1, the effect of the actuation is to increase the average circulation of 23% with respect to the baseline case. The circulation seems to be not affected by the reduction of the momentum coefficient C_μ at the same actuation frequency (CC2). On the other hand, the circulation is increased by increasing the actuation frequency for the configuration CC3 of 29%, while an increase of 26% and 24% is registered for the configuration CC4 and CC5. It is important to recall that the increase of the circulation could be beneficial because the instability growth rate of the wingtip vortices is directly proportional to vortex circulation as reported in Eq. (1.15) (Lewke et al., 2016).

The synthetic jet effect is also observed in terms of the normalized circumferential velocity \bar{U}_θ/U_∞ reported in Figure 3.4. With reference to the baseline case, it is evident that the negative peaks are 26% higher than the positive ones. This behavior can be ascribed to the double induction caused by the vortex itself and by the neighboring one, both inducing a downward velocity. In the following, only the positive peaks are analyzed. Under the control case CC1, a striking effect of the SJ actuation is obtained with a smoother gradient and a peaks reduction of 29% with respect to the baseline case. By reducing the momentum coefficient (CC2), a weaker influence is registered with a decrease of 14% in the peaks values. However, the effect of higher C_μ is in agreement with the findings of Margaritis and Gursul Margaritis and Gursul, 2006 and Dghim et al. Dghim et al., 2018. As it can be noted in Figure 3.4, the control case CC1 is the most effective since a reduction of about 21%, 18%, and 20% has been obtained for the control case CC3, CC4, and CC5 respectively. In Dghim et al. Dghim et al., 2018, a decrease of the circumferential velocity peak value of about 7% and 18% is reported by increasing the momentum coefficient from $C_\mu = 0.1\%$ to $C_\mu = 1\%$ at the same $F^+ = 0.96$ which is a bit higher than the ones investigated in the present tests. They achieve the best performances with the lowest actuation frequency $F^+ = 0.29$ and $C_\mu = 1\%$ resulted in a peak reduction of 32% with respect to the natural vortex case. It is worth noting that in the present experiment for a similar $F^+ = 0.167$ and a $C_\mu = 0.04\%$ two order of magnitude lower (CC3), a reduction of 21% is achieved, confirming the possibility to obtain an effective control with a considerably less power.

3.2.2. PHASE-AVERAGED ANALYSIS

IN order to give more insights of the dynamics of the actuation effectiveness on vortices evolution, a phase-locked analysis of the phenomenon has been conducted. It

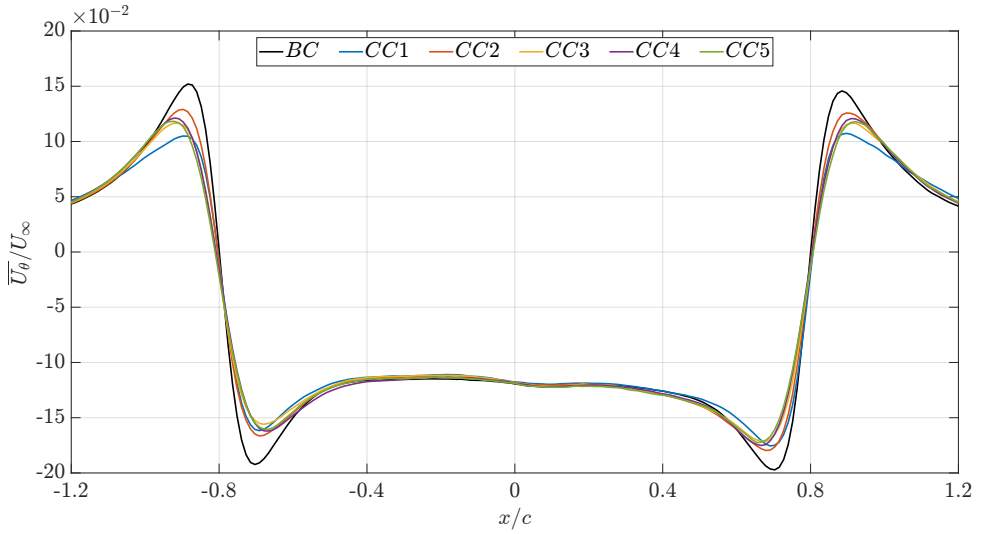


Figure 3.4: Normalized induced velocity profile across the vortices center for all the control cases.

has been assumed that the disturbance generated by the SJ propagates downstream at the free-stream velocity in the convective time $\tau = 3c/U_\infty$. Hereinafter, the phase $\phi = 0^\circ$ corresponds to the beginning of the blowing phase of the SJ. In Figure 3.5, the phase-evolution of the normalized streamwise vorticity field for the control case CC1 is reported. For the sake of brevity, the geometrical and physical characteristics of the vortices reported hereinafter are the average between the left and right vortex.

The main effects caused by the SJ actuation for the CC1 are the huge diffusion of the wingtip vortices which are barely visible in Figure 3.5d - 3.5g, and the displacement of the wingtip vortices themselves. In Figure 3.6, the phase-evolution of the vorticity peak is reported for all the control cases investigated normalized with respect to the time-averaged BC value. As such, the vorticity peak presents a sinusoidal phase-evolution, suggesting a direct correlation between the SJ phases and its effect on the wingtip vortices behavior. As it can be noted, the maximum vorticity peak reduction is relative to the Crow instability frequency with the higher C_μ (CC1) for which a decrease of 74% with respect to the baseline case is registered. On the other hand, this behavior is in contrast with the suction phase of the SJ where an increase of 54% is encountered at the end of the actuation period. A more effective control cases are the CC2 and CC3 with a reduced momentum coefficient and for which a 70% of peak vorticity reduction is obtained with an increase of only 13% and 6% during the suction phase. A completely different evolution is achieved for the control cases CC4 (Widnall instability) and CC5 (fifth wake mode instability (Edstrand et al., 2018)). Firstly, it appears that the phase-locked vorticity peak evolution is not correlated to the SJ blowing and suction phases. In fact, the maximum reduction of about 50% is immediately before the end of the suction phase. The observed decorrelation might be ascribed to several factors as the too low stroke length which causes the SJ to penetrate less in the wingtip vortex, and to the smaller actuation

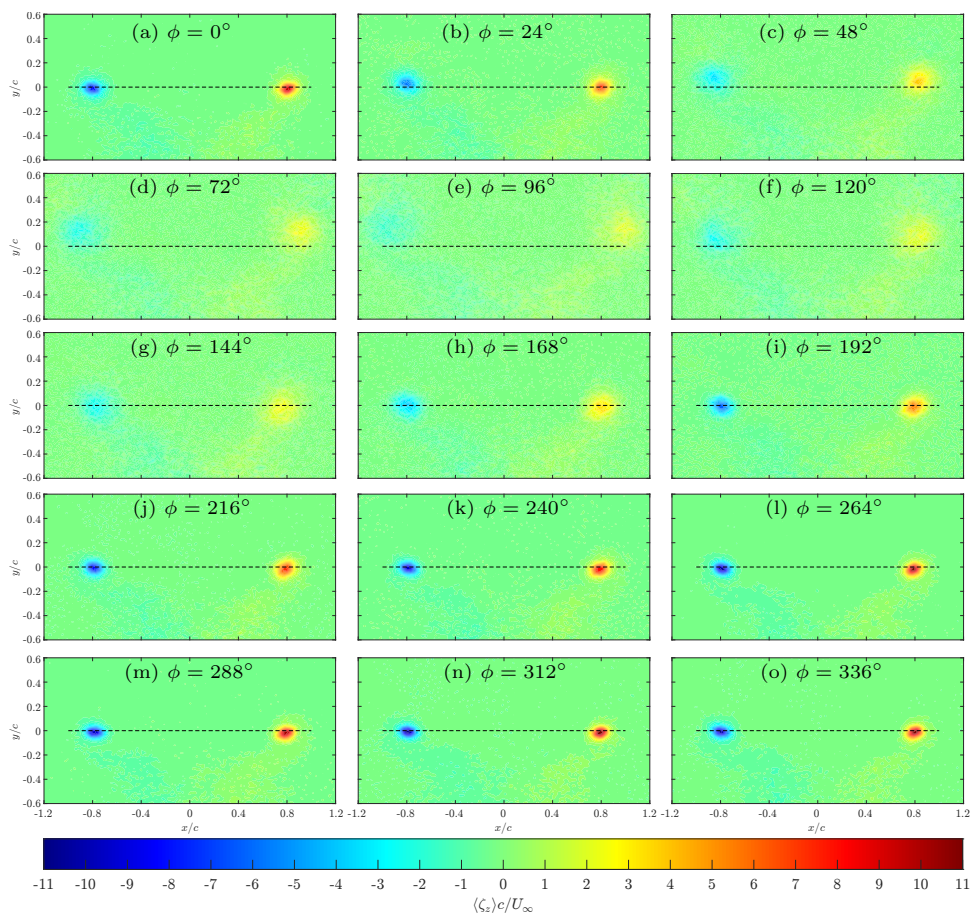


Figure 3.5: Phase-averaged normalized streamwise vorticity contours at $z/c = 3$ for the control case CC1.

period of CC4 and CC5 that is about half of the characteristic time τ needed for the vortex to travel downstream at $z/c = 3$ where S-PIV images are recorded. Finally, it is worth noting that the vorticity peak is at least 26% less than the baseline case for each phase of the SJ actuation only for the control cases CC4 and CC5, which can be considered the most effective ones according to the vortex diffusion metric.

In order to assess the variation of the vortex positions, a plot of the phase-evolution of the vortex centroids is reported in Figure 3.7 for the control case CC1. The black dashed line is again the projection of the trailing edge of the wing. As it can be noted, this configuration causes a periodic motion of the vortices at the Crow frequency along a direction inclined of 45° represented as plain gray lines, which could promote the Crow instability that is known to reveal and grow along these $\pm 45^\circ$ directions (Lewke et al., 2016). In particular, in both the crosswise and the spanwise direction, the maximum displacement of the vortex centroids with respect to the time-averaged position of the baseline

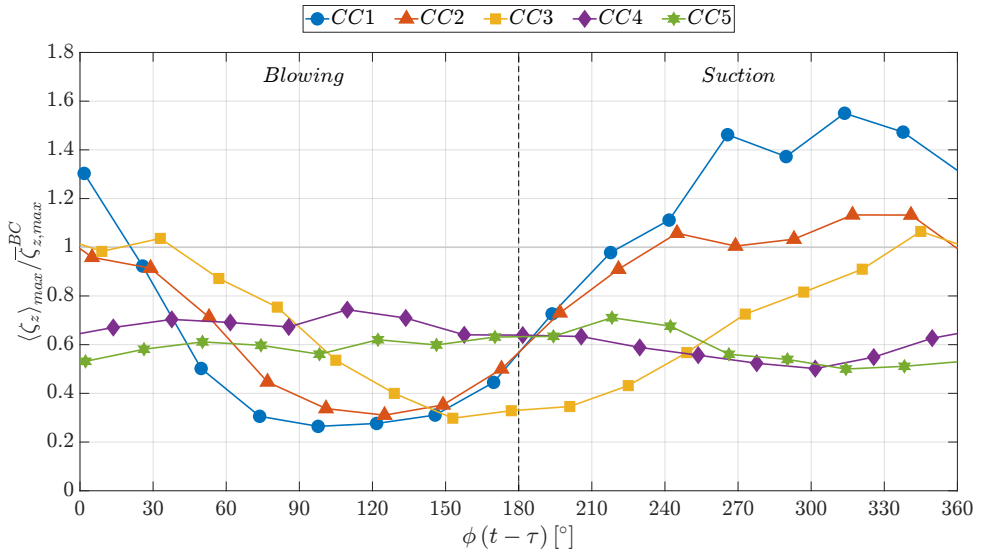


Figure 3.6: Normalized streamwise peak vorticity phase-evolution for all the control cases. The time-averaged BC value of $\overline{\zeta_z}_{max} c / U_\infty$ is equal to 7.24.

case is about $0.2c$. The remaining control cases are not reported herein because they do not cause a noticeable variation of the vortex centroids position due to their low momentum coefficients. This is confirmed by the phase-evolution of the vortex distance shown in Figure 3.8. Only for the control case CC1 an increase of 23% is obtained at the SJ blowing peak when the vortices are far displaced, while for the other configurations the maximum distance is below 6% more than the baseline case. With the exception of the CC4 and CC5 which are confirmed to be not correlated with the SJ ejection phases, during the suction phase the distance is kept practically constant and equal to the time-averaged baseline value. On the other hand, it is interesting to note that, for each configuration investigated, there is at least one phase in which the vortex distance is reduced of about 4% in respect to the baseline. This could be a very useful result because, moving further downstream, the amplitude of this motion is supposed to grow and this could lead to an early vortex linking with respect to the case with no SJ control.

As in the time-averaged analysis, useful information can be obtained from Figure 3.9, where the phase-locked evolution of the geometrical characteristics of the vortices has been shown. Since it is not possible to define a phase-evolution for the baseline case, only the time-averaged value is reported for comparison. It is evident that a synthetic jet blowing in the spanwise direction has a strong impact on altering the vortex size, promoting its premature dissipation. For each control case, the vortex major axis is higher than the baseline value, except for the SJ suction phase of the CC1, CC2, and CC3 where the value is almost constantly equal to the natural vortex value. CC1 appears to be the most effective configuration causing more than a doubling of the vortex size (+160%), with a slight reduction in the last part of the actuation period. As a matter, the CC2 and CC3 with a lower momentum coefficient, cause a maximum increase of about 116% dur-

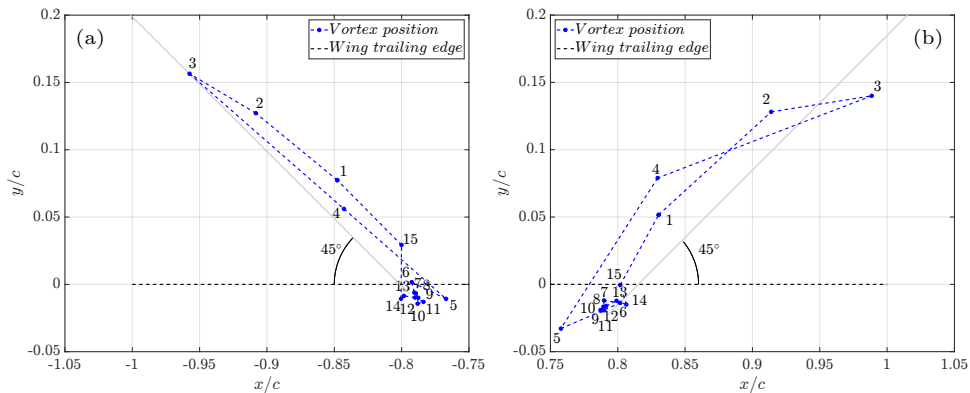


Figure 3.7: Phase-evolution of the (a) left vortex and (b) right vortex position for the control case CC1.

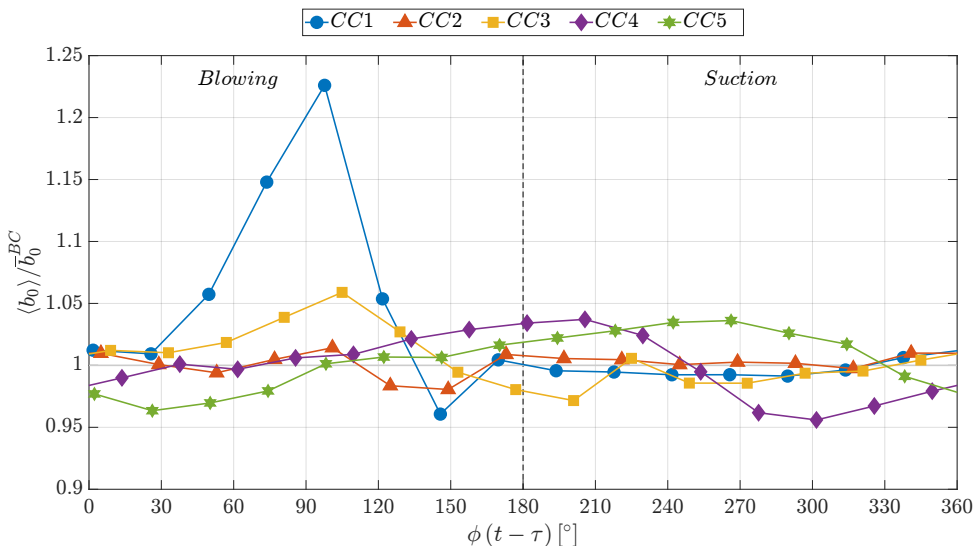


Figure 3.8: Normalized vortex distance phase-evolution for all the control cases. The time-averaged BC value of \bar{b}_0/b is equal to 0.794.

ing the SJ blowing phase and no variation during the SJ suction phase, suggesting that, in these conditions of F^+ and C_{μ} , the use of pulsed jet could be a useful alternative to be investigated. The control cases CC4 and CC5 at high F^+ , show a maximum and minimum increase of 60% and 30% with respect to the baseline case.

Phase-locked evolution of the normalized vortex circulation with respect to the time-averaged BC value is reported in Figure 3.10. As already stated for the time-averaged analysis, the circulation is increased with respect to the baseline case for each control case except for the last part of the actuation period for the CC1. This could promote a faster dissipation of the vortex, especially during the SJ blowing phase where a noticeable

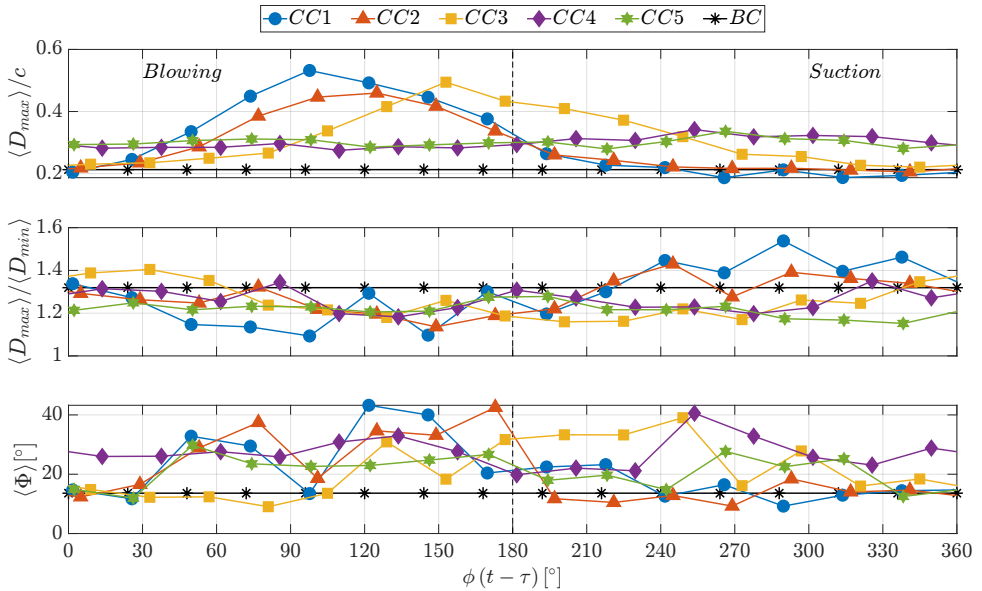


Figure 3.9: Normalized vortex major axis, aspect ratio and inclination angle phase-evolution for all the control cases.

rise is encountered of about 85%, 60%, and 65% for the CC1, CC2, and CC3 respectively. The quasi-sinusoidal evolution is confirmed for all the cases, with a slight demodulation between CC1 and CC2 and a phase delay for the CC4 and CC5 with respect to SJ actuation phases. The latter show a maximum increase of 38% and 53% with a small variation around the time-averaged value.

Lastly, the phase-locked evolution of the normalized induced velocity positive peak with respect to the time-averaged BC value is reported in Figure 3.11. It has been obtained in the analogous way described for the time-averaged analysis and by averaging the positive peak of the vortices. It is clear that the SJ actuation leads to a remarkable effect on the induced velocity and thus on the wake hazard metrics. The control configuration at low F^+ (CC1 to CC3) produces a huge decrease of about 36% at the SJ blowing phase peak with a slight increase in the last SJ phases. By increasing the actuation frequency, the CC4 and CC5 cause a small sinusoidal variation around the time-averaged value with a maximum reduction of 26% with respect to the baseline case.

3.3. CONCLUSIONS AND PERSPECTIVES

IN the present chapter, a parametric investigation on the synthetic jet actuation effectiveness on wingtip vortices control has been presented. Stereoscopic particle image velocimetry measurements have been performed in the near wake ($z/c = 3$) of a finite square-tipped rectangular wing with a NACA0024 airfoil section at a chord Reynolds number of 8.16×10^4 . The wing has been placed at an angle of attack of 5° , while the synthetic jets have been blown through rectangular slots at the wingtips. Five differ-

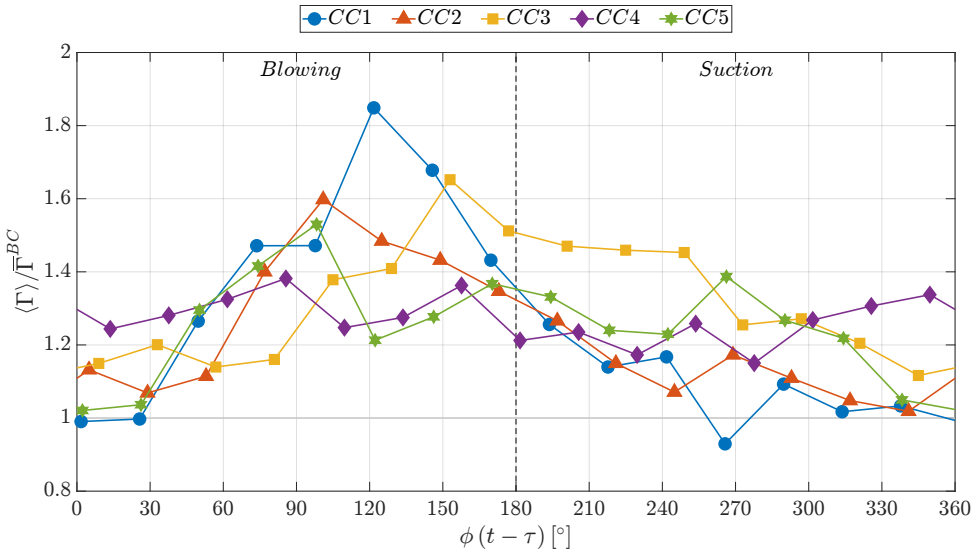


Figure 3.10: Normalized circulation phase-evolution for all the control cases. The time-averaged BC value of $\overline{\Gamma}/(U_\infty c)$ is equal to 0.113.

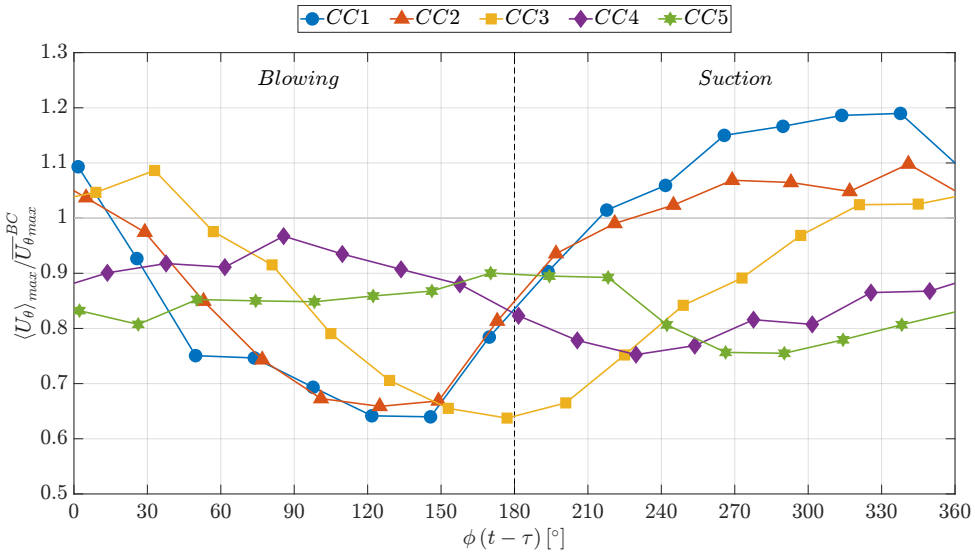


Figure 3.11: Phase-evolution of the normalized induced velocity positive peak for all the control cases. The time-averaged BC value of $\overline{U_\theta}_{max}/U_\infty$ is equal to 0.148.

ent control cases have been tested, tuned to the Crow instability (CC1 and CC2), to a frequency outside the range amplified by the Crow instability (CC3), to the Widnall instability (CC4), and to the fifth wake mode instability (CC5).

An evident impact of the actuation on the vortices development has been observed in the time-averaged analysis. The vortices are clearly stretched into an ellipsoidal shape and they present a diffusion which increases with the actuation frequency F^+ . The control cases CC4 and CC5 at the higher F^+ has the most significant effect causing a reduction of the vorticity peak and increase of the vortex diameter of about 44% and 47% respectively, leading to an intense vortex diffusion and vortex strength decrease. The vortex circulation appears to slightly increase with the actuation frequency although the maximum rise of 29% is obtained for $F^+ = 0.167$ (CC3). The most noteworthy time-averaged result has been achieved for the induced circumferential velocity for which a reduction of 29% (for both positive and negative peaks) is obtained with $C_\mu = 0.2\%$ and $F^+ = 0.0714$ (CC1), which is promising for a noticeable wake vortex hazard decrease.

Phase-locked analysis has allowed a deeper understanding of the phenomenon dynamics during the synthetic jet actuation. A clear relation between the synthetic jet blowing and suction phases and the periodic variation of the vortices geometrical and physical characteristics has been registered. The tuned Crow instability configurations report both a vorticity peak decrease with respect to the baseline case of 74% and 70% during the blowing phase, and an increase of 54% and 13% during the suction one. The CC3 configuration appears to outperform the others by decreasing the peak vorticity of about 70% with only a slight increase of 6% in the last part of the actuation period. A different behavior is registered for the CC4 and CC5 configurations which cause a vorticity reduction at each actuation phase with a minimum and maximum decrease of 26% and 50% respectively, being the less variable configurations as already stated for the time-averaged analysis. On the other hand, the most striking impact on the vortices dynamics has been obtained with the higher momentum coefficient (CC1). A huge diffusion of the vortices is encountered in correspondence of the SJ blowing peak together with a large displacement along the $\pm 45^\circ$ directions meaning that the SJ control could promote the Crow instability growth, which has not been found for the lower C_μ (CC2). In particular, the vortices diameter is more than doubled with respect to the baseline case, which could lead to an early linking and dissipation of the vortices further downstream. Lastly, the blowing peak causes an increase of 85% of the vortex circulation and a decrease of 36% of the circumferential velocity peak, confirming that this synthetic jet control configuration can represent a useful device to promote the vortex dissipation and reduce the wake vortex hazard.

Based on these findings, the author decided to focus the near and far-field experimental investigation of the present thesis only on two actuation frequencies tuned to the Crow and Widnall instability frequency, since the results of CC3 and CC5 at $F^+ = 0.167$ and $F^+ = 0.735$ have been demonstrated to be comparable with the CC1 and CC4. Since the most striking effectiveness has been detected for the CC1, the value of $C_\mu = 0.2\%$ has been taken as a reference for all the measurements conducted and discussed later in this thesis. However, the lower momentum coefficient $C_\mu = 0.04\%$ has been proven by the present feasibility tests to be fruitful as well, and thus it has been considered in the variable momentum coefficient investigation which has been carried out in the far-field experiments.

4

EXPERIMENTAL RIGS

THIS chapter describes the experimental rigs employed for the present thesis. As already mentioned, two different experimental campaigns have been conducted separately to investigate the effectiveness of the synthetic jet actuation both on the near and far-field wake. For each case, the wind tunnel features and operating conditions are presented and the wing models equipped with the SJ device are described in detail. Lastly, the S-PIV setup and the image processing parameters are discussed for the two different measurement campaigns.

4.1. NEAR-FIELD MEASUREMENTS SETUP

4.1.1. D3M WIND TUNNEL

THE near-field measurements were conducted in the closed-circuit subsonic wind tunnel “D3M” located in the “M. Panetti” laboratory of the Mechanical and Aerospace Engineering Department at Politecnico di Torino (Italy). The sketch of the wind tunnel is reported in Figure 4.1. The test chamber has a circular section with a diameter of 3 m and a length of 5 m, slightly divergent to compensate the growth of the boundary layer. The flow is set in motion by a fan placed immediately after the test chamber, consisting of 2 discs of 8 rotor blades each with variable pitch and 2 discs of stator blades, all with a diameter of 4 m. The installed power is 900 kW supplied by a direct current motor located outside the wind tunnel. The flow then circulates throughout the tunnel, with diverging sections and straightening vanes in the corners to guide their rotations, until reaching the convergent before the test chamber with a contraction ratio of 2.33. A series of grids and honeycomb screens are placed to ensure uniformity of the flow velocity over the cross section and to alleviate any residual fluctuation related to the fan. For the present investigation, the free-stream velocity has been set to $U_\infty = 12$ m/s, corresponding to a chord Reynolds number of $Re_c = 1.20 \times 10^5$.

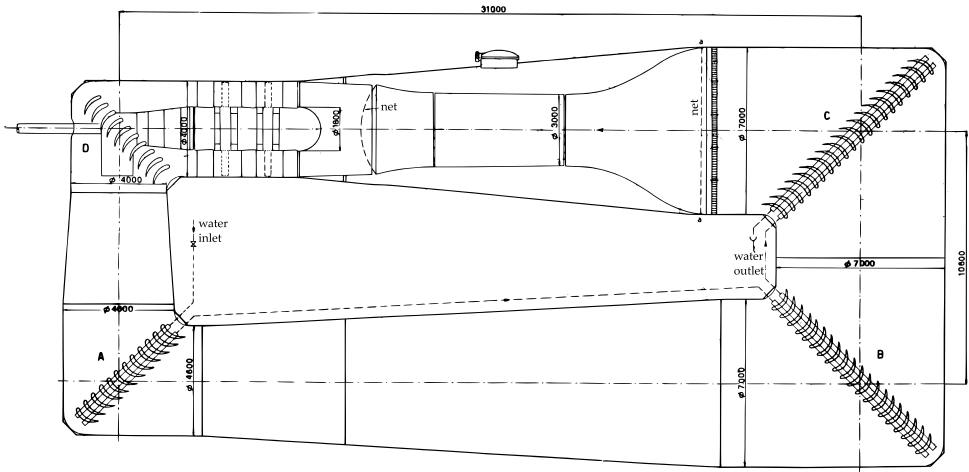


Figure 4.1: D3M wind tunnel sketch. Dimensions are in mm.

4.1.2. WING MODEL AND SYNTHETIC JET DEVICE

THE assembly employed for the near-wake measurements is shown in Figure 4.2. Starting from the bottom, the wing assembly is anchored to the wind tunnel through a 0.500 m squared iron base. In order to balance the wing, an angle regulation system has been designed based on three pillars with a threaded pivot ending with an axial ball joint. They are positioned at 120° around the axis passing through the $c/4$ point of the wing sting and they allow a $\pm 10^\circ$ pitch, and roll adjustment with an accuracy of $\approx 0.015^\circ$. The loudspeaker for the synthetic jet generation and its cavity of diameter 0.330 m and height 0.055 m are mounted directly on the basis of the wing sting which is attached to the pillars through an iron interface plate. In particular, the wing sting basis, made of carbon fibers with a 0.006 m of thickness, presents a buttonhole in correspondence to the each pillar to allow a $\pm 5^\circ$ yaw angle adjustment. The wing sting has a constant airfoil section NACA 0024, a chord of 0.149 m, and a span of 1.064 m. It is manufactured in carbon fibers with a 0.004 m of thickness to create a duct large enough for the synthetic jet. Finally, an interchangeable wing is mounted on the top by interference and the different wing models employed are shown in Figure 4.3. They are a rectangular finite-span square-tipped wings equipped with a NACA 0015 airfoil section. The airfoil chord is $c = 0.15$ m, the wingspan is $b = 2c = 0.30$ m, resulting in an aspect ratio $\mathcal{R} = 2$. The wings are manufactured in polyamide PA 2200 by a Selective Laser Sintering (SLS) 3D EOS printer. Then, the wings have been painted and their surface finish enhanced. As it can be seen in Figure 4.3, the angle of attack is fixed from the design to be equal at $\alpha = -5^\circ$. As a result, the wing assembly has been mounted in the wind tunnel by balancing the wing sting to be at 0° of yaw, pitch, and roll with respect to the streamwise direction with the aid of an inertial measurement unit. It has been chosen to use a negative angle of attack to avoid the possible influence of the wing sting wake on the wingtip vortices which will move inboard and upward going downstream.

Four different wing models have been tested in the present investigation: the reference wing (wing baseline “BCs”), and three models with a rectangular SJ exit section with the

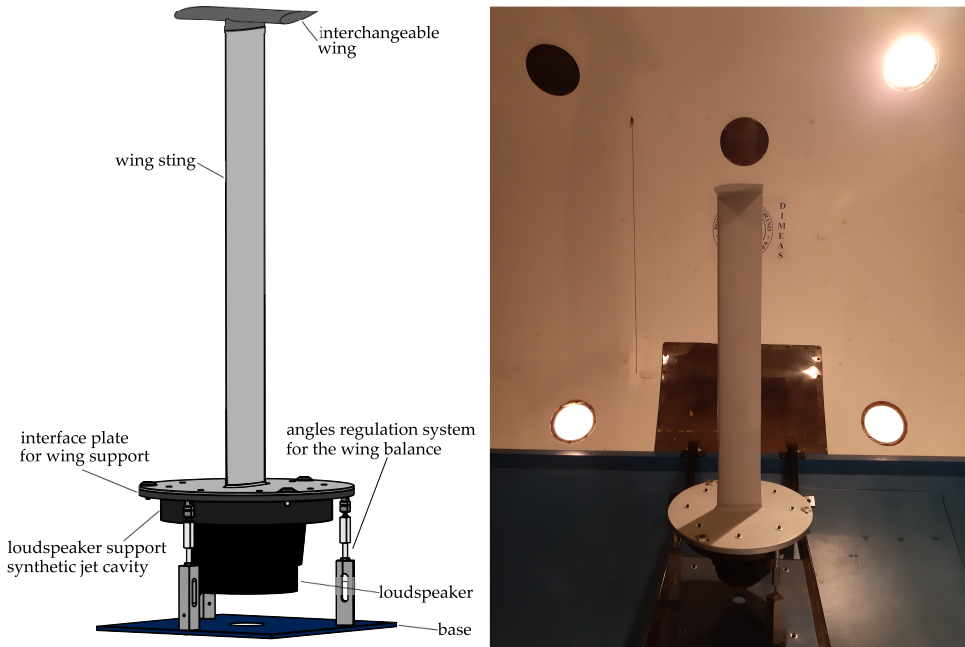


Figure 4.2: Wing assembly setup in the D3M wind tunnel.

same width of $0.6c$ and height of $0.01c$, $0.02c$, and $0.04c$ respectively. In each configuration, the slot is placed in the chord plane. Hereinafter, they will be referred to as “BCs” (Squared wing Baseline Case), “Ss01” (Squared wing with SJ slot height of 1% of the chord length), “Ss02” (Squared wing with SJ slot height of 2% of the chord length), and “Ss04” (Squared wing with SJ slot height of 4% of the chord length). Each wing is equipped with a pin $0.4c$ (0.060 m) long to be wedged in the wing sting by interference. The SJ runs throughout the wing sting and the wing pin, turning into a rectangular duct in the wing with a height of $0.054c$ (0.0081 m). It is important to note that both the width and the height of the SJ duct have been fixed by maximizing the flow area with respect to the minimum wall thickness of the 3D printer employed and by minimizing the head loss due to the flow area variation between the wing sting and the wing. Finally, the rectangular SJ chamber inside the wing ends at the tips with two rectangular ducts with the different heights described before and length equal to $L_e = 2D_e = 2 \cdot 4A_j / p_j$, being D_e the equivalent hydraulic diameter and p_j the perimeter of the SJ exit section. In this way, the SJ exit velocity profiles of the different models are self-similar. Furthermore, head losses and flow separation effects have been reduced with the aid of appropriate fillets shown in Figure 4.3.

As already mentioned, the synthetic jet is generated by using a 900 W, 12 in subwoofer (Alpine X-W12D4) as oscillating driver (Greco et al., 2013). It is supplied with a sinusoidal input signal generated by a Digilent Analog Discovery™ USB Oscilloscope, coupled with a power amplifier (Behringer NX6000D). The subwoofer has been mounted on the basis of the wing sting with an insulation sheath to avoid the transmission of the

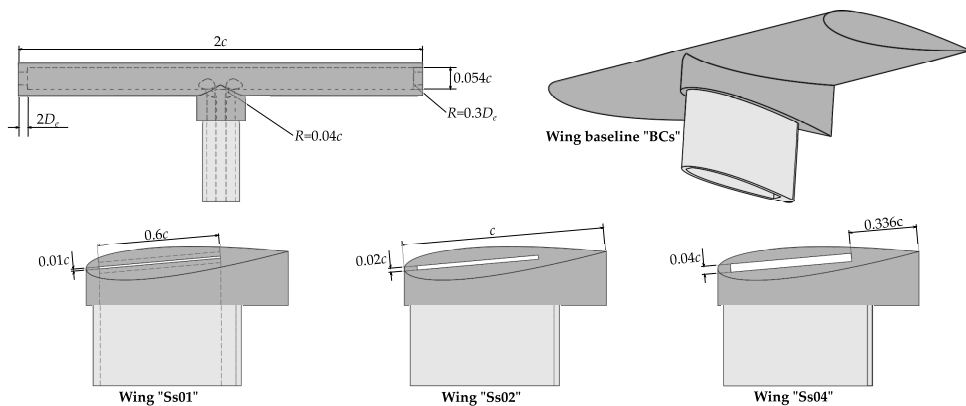


Figure 4.3: Sketch of the interchangeable wing with different synthetic jet exit sections.

vibrations to the wing and they are dampened also by the large mass of the wing assembly as shown in Figure 4.2. As a result, the possible effect of the vibration have been considered negligible especially in the low power range employed in the experimental tests. The resonance frequency of the system in all the configurations is experimentally determined by measuring the loudspeaker impedance (Greco et al., 2013), resulting in two resonance frequencies equal to about 8 Hz and 76 Hz as shown in Figure 4.4. As

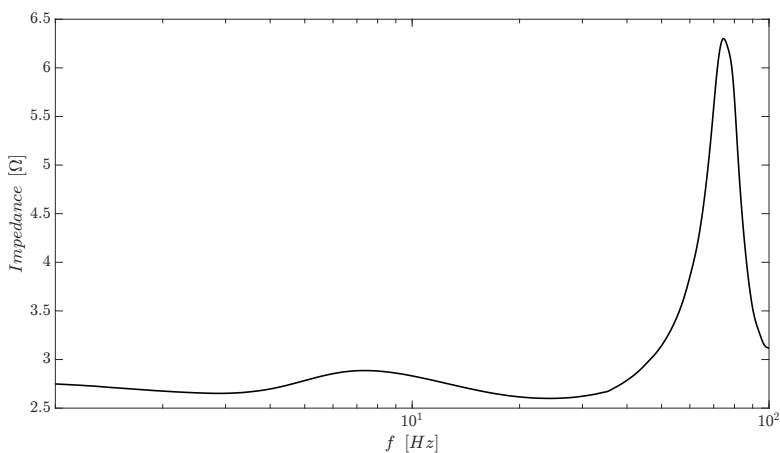


Figure 4.4: Impedance versus the input frequency for the Ss01 near-field configuration.

described in the introduction section, the SJ actuation frequencies have been tuned to the inherent vortices instabilities. As a result, the SJ device has not been operated at its proper resonance frequencies. By recalling Eq. (1.16) and Eq. (1.18) reporting the instability wavelengths of the Crow and Widnall instability respectively, being the free-stream

velocity set to $U_\infty = 12$ m/s, the following actuation frequencies have been employed:

$$f_{\text{Crow}} = \frac{U_\infty}{\lambda_{\text{Crow}}} \simeq 6 \text{ Hz} \implies F^+ = 0.071 \quad (4.1a)$$

$$f_{\text{Widnall}} = \frac{U_\infty}{\lambda_{\text{Widnall}}} \simeq 44 \text{ Hz} \implies F^+ = 0.55 . \quad (4.1b)$$

At these working frequencies the impedance of the three synthetic configurations differs of less than 4%.

In order to investigate the effect of SJ exit velocity U_0 on the wingtip vortices control, a constant momentum coefficient $C_\mu = 0.2\%$ (Eq. (1.19)) has been investigated for both frequencies. In fact, the tested models reported in Figure 4.3 present an increasing SJ exit section area from $0.006c^2$ (Ss01) to $0.024c^2$ (Ss04) which is four times higher. Since the C_μ is kept constant, the SJ velocity U_0 will result halved. As a matter, the input tension (i.e. electrical power) has been iteratively varied until the target SJ characteristic velocity U_0 obtained by solving Eq. (1.19) was reached. In Table 4.1, the SJ exit velocity and the root-mean-square electrical power needed to generate the SJ in each condition tested are reported. It is important to outline that the input electrical power is not indicative of the fluid dynamic power transferred to the fluid (Girfoglio et al., 2015). The instantaneous velocity of the synthetic jet at both the tips is measured by means of a constant temperature anemometer system (Dantec-MiniCTA) equipped with a single-component hot wire of length 1.25 mm and diameter $5\mu\text{m}$ (55P11). To uniformly cool the active sensor, the wire was aligned with the direction of the long side of the slot and placed at the slot exit. It is worth noting that the hot-wire sensor acquisitions, at a sampling frequency fixed to $1000f_a$, were synchronized with the electrical signal sent to the loudspeaker. As a result, the phase shift between this electrical signal and the synthetic jet exit velocity was characterized in order to accurately identify the start of the cycle of the synthetic jet with respect to the sampled phases.

Lastly, the near-wake investigation has been conducted at four different S-PIV measurement planes downstream the wing for each SJ configuration: $z/c = 0.1$, $z/c = 0.5$, $z/c = 1$, and $z/c = 2$. In the following, the S-PIV setup and the image processing are described in details.

Table 4.1: Synthetic jet characteristic velocity and electrical power for each configuration investigated.

$C_\mu = 0.2\%$		Ss01	Ss02	Ss04
$F^+ = 0.071$ $F^+ = 0.55$	U_0 [m/s]	6.93	4.90	3.47
$F^+ = 0.071$ $F^+ = 0.55$	P_j [W]	5.79	3.97	5.00
		16.9	42.78	138

4.1.3. S-PIV SETUP AND IMAGE PROCESSING

STEREOSCOPIC particle image velocimetry is used to measure the instantaneous two-dimensional three-component (2D-3C) velocity. A schematic of the experimental setup is shown in Figure 4.5. Particle images are acquired in the xy -plane with the origin on the trailing edge at the mid-span point, with the x , y , and z -axis aligned with the spanwise (inboard), crosswise (upward), and streamwise directions respectively. The flow is seeded using the Safex Fog Fluid “Extra Clean”, for PIV applications. It is nebulized by the smoke machine Martin Magnum 1200 which produces small particles having a mean diameter of $1 \mu\text{m}$, thus resulting in a Stokes number $St \ll 1$. The wind tunnel fan guarantees the mixing of the particles in the flow. Illumination is provided by the Quantel Evergreen laser, a low-speed double pulsed Nd:YAG laser (532 nm, 200 mJ per pulse, <10 ns pulse duration). The laser beam is shaped into a 2.2 mm thick light sheet. The time delay between the two laser pulses has been set to $20 \mu\text{s}$. Particle images are acquired by two Andor Zyla sCMOS cameras (2160×2560 pixels, pixel pitch of $6.5 \mu\text{m}$, intensity resolution 16 bit) in stereo configuration equipped with Nikon AF Micro-Nikkor 200mm f/4D IF-ED of 200 mm focal length. Both cameras are in side-scattering, with a relative aperture set at $f\# = 16$. The angle between the optical axes of the two cameras is set at about 86° and Scheimpflug adapters are used in order to achieve good focus over the entire field of view. The present imaging produces a field of view of $0.84c \times 0.90c$ with a spatial resolution of 15.8 pixel/mm. The optical camera calibration has been performed by using a target plate made of a regular Cartesian grid of white dots on a black background with a 10 mm spacing on both the front and back surfaces. Depending on what camera is going to calibrate, the front or the back surface of the target plate is aligned with the center plane of the laser sheet, and the images of the target plate are recorded at this initial location and when it is shifted 1 mm backward and forward along the positive and negative z direction (translation is performed with a translation micrometric stage). The mapping functions between the image planes and the measurement plane are determined using a pinhole camera model. The root mean square calibration error is lower than 1.4 pixels for both cameras.

In order to perform phase-locked measurements, the acquisition system is synchronized with the synthetic jet for each investigated control case by an external signal synchronizer. In particular, the S-PIV measurements were locked to the electrical signal driving the loudspeaker. Hence, the acquisition is performed at the frequency f_{acq} estimated following Greco et al., 2013:

$$f_{acq} = \frac{f_a}{\frac{1}{N_{Div}} + n_p} . \quad (4.2)$$

The phenomenon with frequency f_a is sampled every n_p periods of membrane oscillation with a phase shift of $360^\circ / N_{Div}$. For the present work, the phenomenon is sampled with a phase separation $\Delta\phi = 24^\circ$, leading to $N_{Div} = 15$ divisions (phases) per cycle. A total of 3750 image pairs, i.e. 250 snapshots per phase, are acquired to obtain statistically reliable data. The quality of the image pairs is improved by subtracting a background intensity from the raw images obtained by computing the historical minimum intensity based on the entire ensemble of the image pairs.

A multiple pass algorithm with image deformation is employed to compute the velocity field using Blackman weighting windows according to Astarita and Cardone, 2005

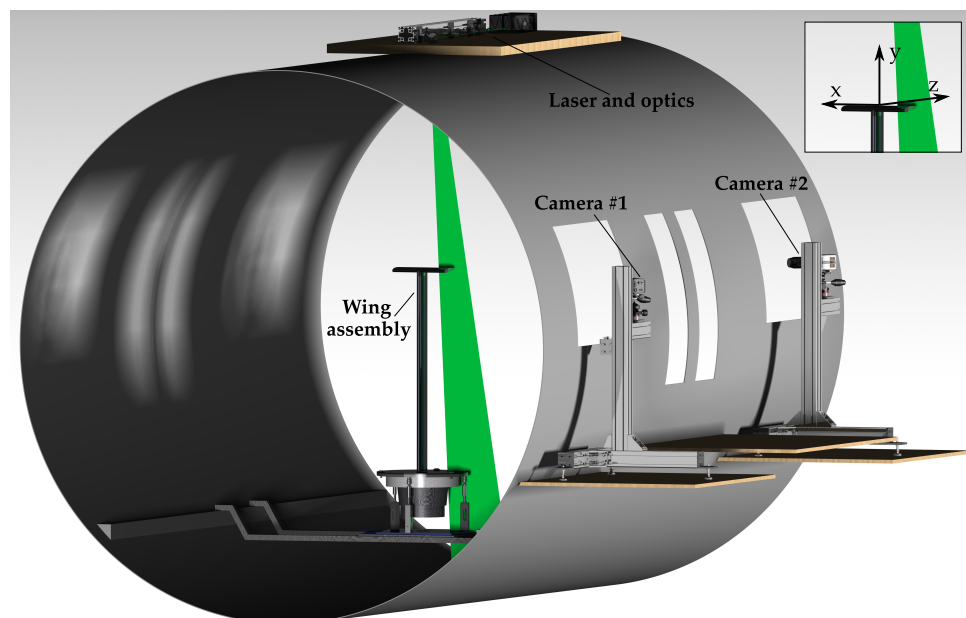


Figure 4.5: Experimental setup in the D3M wind tunnel.

and Astarita, 2006, 2007, 2008. The final interrogation area size is 96×96 pixels corresponding to an equivalent 48×48 top-hat interrogation window (Astarita, 2007), with an overlap of 66.7%, resulting in a measurement resolution L_m of about 3 mm. Lastly, the maximum random error on the instantaneous velocity vectors is estimated to be 0.106 pixels (Bhattacharya et al., 2016), which leads to a vorticity uncertainty of about 2.3% of the maximum detected phase-averaged vorticity (Sciacchitano & Wieneke, 2016).

4.2. FAR-FIELD MEASUREMENTS SETUP

4.2.1. LMFL BOUNDARY LAYER WIND TUNNEL

THE far-field measurements were conducted in the large boundary layer closed-loop wind tunnel of “Laboratoire de Mécanique des Fluides de Lille - Kampé de Fériet (LMFL)” (France). The test section of the wind tunnel is 20.6 m long with a vertical and transverse lengths of 1 m and 2 m, respectively. As the test section has an optical access from all sides along its complete length, high quality PIV measurements are possible. The sketch of the wind tunnel is reported in Figure 4.6. Incoming air to the plenum chamber passes through an air-water heat exchanger in order to provide an isothermal flow where efficiency is kept within $\pm 0.2^\circ C$. Subsequently, air through the guide vanes undergoes a relaminarization process via honeycomb screens and grids. Thereafter, a contraction of 5.4 is present. For the present investigation, the free-stream velocity has been set equal to $U_\infty = 8.6$ m/s ($Re_c = 2.87 \times 10^4$) at the entrance of the test section with a precision of $\pm 0.5\%$, while the free-stream turbulence is below 0.2% (Hasanuzzaman et al., 2020).

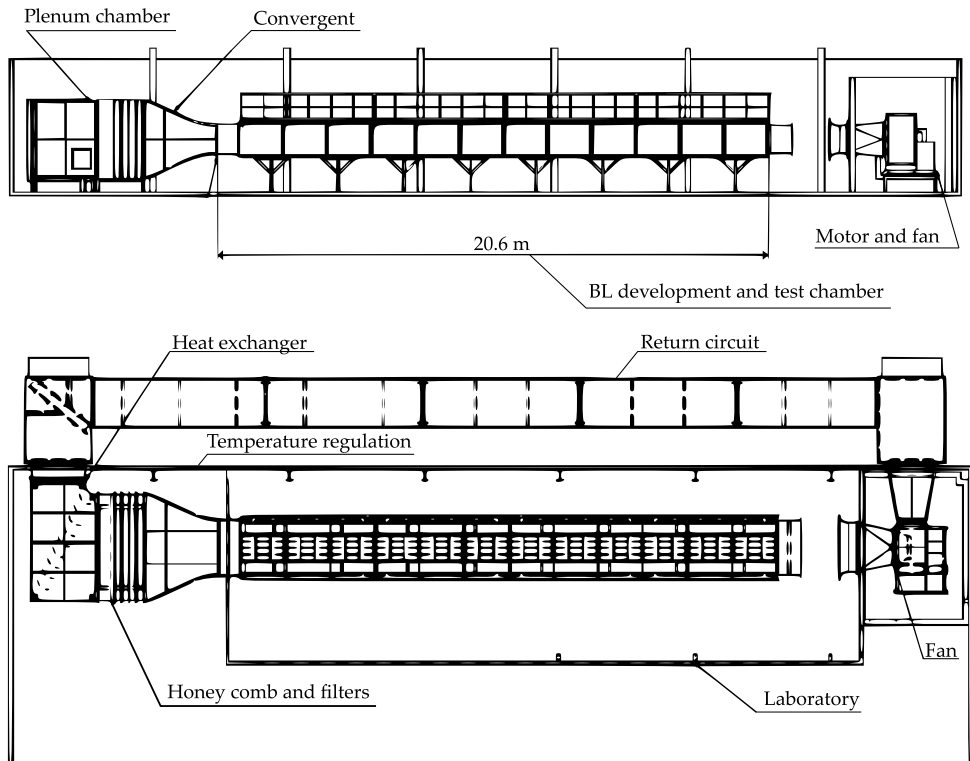


Figure 4.6: LMFL boundary layer wind tunnel sketch.

4.2.2. WING MODEL AND SYNTHETIC JET DEVICE

THE sketch and the photos of the wing assembly for the far-wake measurements in the LMFL boundary layer wind tunnel are shown in Figure 4.7 and Figure 4.8. The wing assembly is mounted on a system of bosch rexroth rails which are anchored on the top of the wind tunnel test section entrance. The fixed slewing ring of a crossed roller bearing is anchored through an iron interface plate to the bosch rails systems, while the rotating slewing ring is connected to a round iron plate which supports all the remaining wing assembly. With the use of both a micrometer head which tangentially pushes the plate and a recall spring, a fine regulation of the yaw angle is allowed up to $\pm 3^\circ$ with an accuracy of 0.005° . As in the near-wake setup, a pitch/roll regulation system has been designed based on three pillars with an axial ball joint fixed on the upper plate ending with a threaded pivot in the lower iron interface plate. They are positioned at 120° around the axis of the bearing and the upper plate, and when the pillars are rotated the lower plate moves allowing angles adjustment of $\pm 10^\circ$ with an accuracy of $\approx 0.03^\circ$. The loudspeaker for the synthetic jet generation is attached to the lower plate and its cavity of 0.100 m in diameter and 0.006 m in height is machined directly on the plate. The wing sting is fixed with a squared base of 0.110 m \times 0.110 m on the opposite side of the lower plate. It presents a NACA 0024 airfoil section, which is constant for 0.035 m to allow the



Figure 4.7: Wing assembly setup for the LMFL boundary layer wind tunnel.

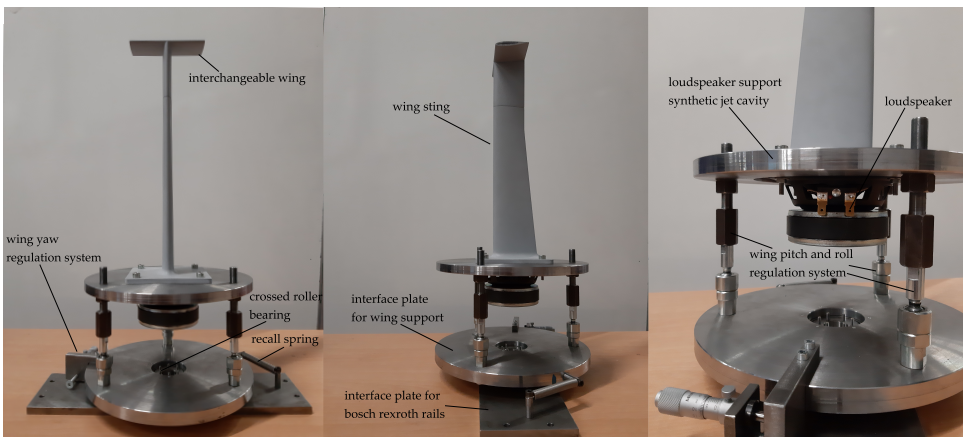


Figure 4.8: Photos of the wing assembly details.

interlocking with the wing. The remaining wing sting has a trapezoidal shape with a root chord of 0.080 m, taper ratio of 1.6, and height of 0.2025 m. The trapezoidal support has been conceived in order to strengthen the structure, together with the wall fillet at the basis. Finally, an interchangeable wing is mounted on the top by interference and the different wing models employed are shown in Figure 4.9 and Figure 4.10. Both the wing sting and the wing models are manufactured in Polyamide Multi Jet Fusion (MJF). Then, they have been painted and their surface finish enhanced.

The tested models are a rectangular finite-span square-tipped wings equipped with a NACA 0015 airfoil section. In order to investigate the far-field behavior of the wake which is scaled with the wingspan b as described in chapter 1, the wing dimensions have been reduced by a factor of 3 with respect to the ones employed for the near-wake measurements. As a result, the airfoil chord c and the wingspan b are 0.05 m and 0.10 m respectively. In this way, far-wake measurements could be carry out in a relatively short length of the wind tunnel test section to avoid the change in the free-stream velocity due to the boundary layer growth to be relevant. The wings are manufactured at a fixed angle of at-

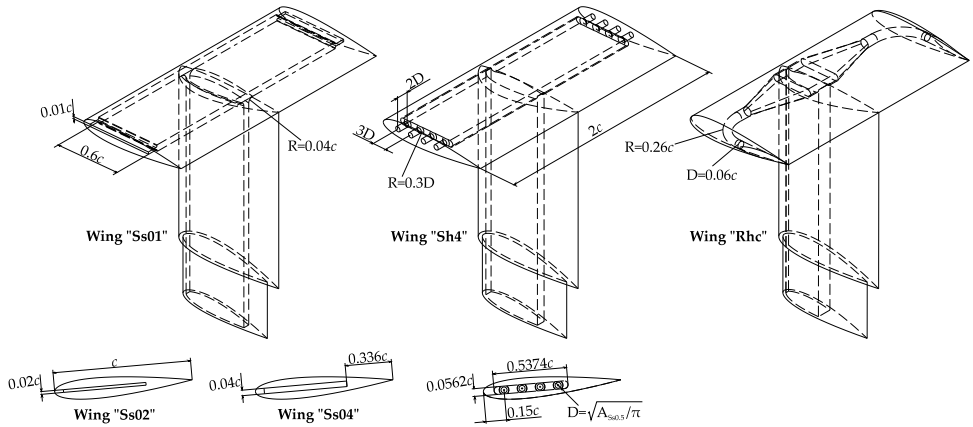


Figure 4.9: Sketch of the interchangeable wing with different synthetic jet exit sections.

tack of $\alpha = -5^\circ$ as shown in Figure 4.9 and Figure 4.10. Since the wing assembly has been mounted upside-down on the wind tunnel ceiling (see Figure 4.7 and Figure 4.13) and horizontally balanced with respect to the free-stream, the wing angle of attack results to be positive causing the wingtip vortices movement inboard and downward going downstream from the trailing edge.

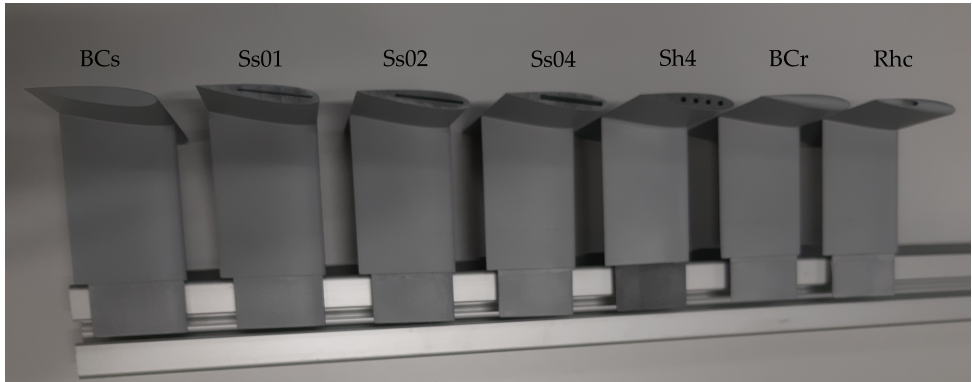


Figure 4.10: Photo of the interchangeable wings for the far-field measurements.

The far-field investigation has been conducted with the use of seven wing models with different synthetic jet exit section and/or direction including two reference wings "BCs" and "BCr" with a squared and rounded tip respectively. In order to study the effects of a variable synthetic jet exit section are A_j (i.e. SJ characteristic velocity U_0) at fixed momentum coefficient in similarity with the near-wake measurements, three models equipped with a rectangular SJ exit section aligned to the wing chord are employed with the same width of $0.06c$ and height of $0.01c$, $0.02c$, and $0.04c$ referred hereinafter to "Ss01", "Ss02", and "Ss04" respectively. The geometrical characteristics of the SJ duct inside the wing and the contraction at the tip are the same already described in sec-

tion 4.1.2. In order to investigate the effects of the SJ shape and direction, two additional models have been designed. In the first one, referred to as “Sh4”, the SJ comes out at the wing tip through four orifices positioned in the chord plane with a diameter equal to $0.0436c$ (0.00218 m) whose area is equivalent to the rectangular slot “Ss01” (0.5×30 mm²). According to Han and Leishman, 2004, a bundle of 4 turbulent vortlets co-rotating with the wingtip vortex are formed from the four pipes. As it can be seen from the schematic of the formation process in Figure 4.11, the vortlets easily roll-up around each other and penetrate the inner region of the vortex core, causing the inner laminar region to be dissolved and the turbulence promoted. Unlike all the other wing

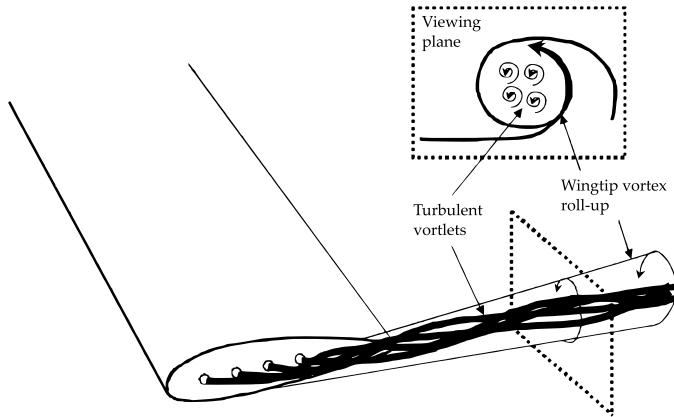


Figure 4.11: Schematic of the formation and evolution process of the turbulent vortlets generated at the slot exits. Adapted from Han and Leishman, 2004.

models, the “Rhc” configuration has a rounded tip with the SJ blowing through a circular pipe of $0.06c$ diameter in the chordwise direction inclined of 5° with respect to the free-stream direction, positioned in the chord plane tangential to the airfoil section in correspondence to the beginning of the trailing edge. As it can be noted in Figure 4.9, the SJ runs throughout the wing pin, turning into a rectangular chamber and reaching the exit through a convergent curved duct of radius $R = 0.26c = 0.013$ m. In particular, the rounded tip both for the baseline “BCr” and “Rhc” configuration has been realized with a half-revolution of the airfoil’s profile so that the wingspan measured between the points in correspondence to the maximum airfoil thickness is exactly equal to $b = 2c$. Finally, each wing is equipped with a pin $0.5c$ (0.025 m) long to be wedged in the wing sting by interference.

The synthetic jet is generated by using a 50 W woofer (Ciare HW100) as oscillating driver, supplied with a sinusoidal input signal generated by a Digilent Analog Discovery™, coupled with a power amplifier (Kenwood KAC-6405). As already pointed out for the near-field experimental setup in section 4.1.2, the vibrations of the loudspeaker are not transmitted to the wing since it is mounted through an insulation sheath on the basis of the iron lower plate of large mass as shown in Figure 4.7 and 4.8. The resonance frequency of the system in all the configurations has been experimentally determined to be equal to about 22 Hz by measuring the loudspeaker impedance (Greco et al., 2013), as shown

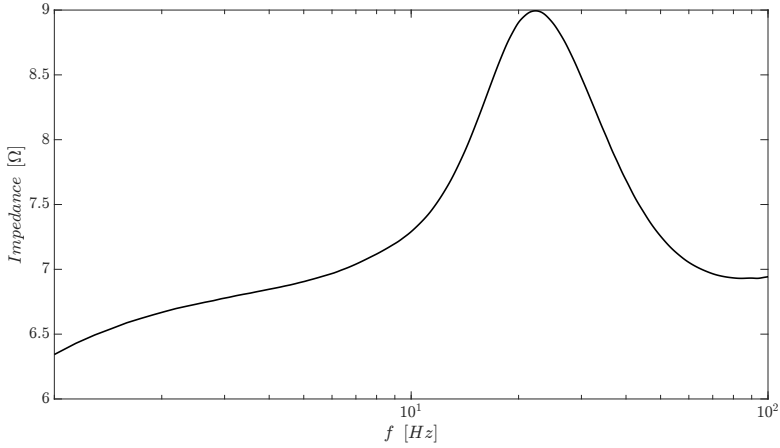


Figure 4.12: Impedance versus the input frequency for the Ss01 far-field configuration.

4

in Figure 4.12. As already described in section 4.1.2 for the near-wake investigation wing models, the SJ device is operated at its proper resonance frequency since it has been tuned to the Crow and Widnall instability frequencies. For the present case, being the free-stream velocity set to $U_\infty = 8.6$ m/s, the following actuation frequencies have been employed:

$$f_{\text{Crow}} = \frac{U_\infty}{\lambda_{\text{Crow}}} \simeq 12 \text{ Hz} \implies F^+ = 0.071 \quad (4.3a)$$

$$f_{\text{Widnall}} = \frac{U_\infty}{\lambda_{\text{Widnall}}} \simeq 96 \text{ Hz} \implies F^+ = 0.55 . \quad (4.3b)$$

At these working frequencies the impedance of the three synthetic configurations differs of less than 2.5%.

In order to make a comparison against the near-field measurements, for each wing configuration and frequency, a constant momentum coefficient $C_\mu = 0.2\%$ has been investigated while the effects of different momentum coefficients $C_\mu = 1\%$, 0.2% , 0.04% at both actuation frequencies has been analyzed by testing only the models “Ss01” and its equivalent “Sh4”. The corresponding SJ characteristic velocity has been obtained by iteratively varying the input tension and it has been measured by the same procedure described in section 4.1.2. Furthermore, for each of the above mentioned tests, an additional control case has been set by tuning the synthetic jet actuation signal $W(t)$ with a combination of the Crow and Widnall instabilities as follows:

$$W(t) = A_{\text{Crow}} \sin(2\pi f_{\text{Crow}} t) + A_{\text{Widnall}} \sin(2\pi f_{\text{Widnall}} t) \quad (4.4)$$

where A_{Crow} and A_{Widnall} are the signal amplitudes needed to generate the Crow and Widnall instability control case separately. In Table 4.1, the SJ exit velocity and the root-mean-square electrical power needed to generate the SJ in each condition tested are reported.

Table 4.2: Synthetic jet characteristic velocity and electrical power for each configuration investigated.

$C_\mu = 1\%$		Ss01	Ss02	Ss04	Sh4	Rhc
$F^+ = 0.071$ $F^+ = 0.55$	U_0 [m/s]	11.1	-	-	11.1	-
$F^+ = 0.071$ $F^+ = 0.55$	P_j [W]	5.44 19.0	- -	- -	6.50 27.5	- -
$C_\mu = 0.2\%$						
$F^+ = 0.071$ $F^+ = 0.55$	U_0 [m/s]	4.96	3.51	2.48	4.96	7.23
$F^+ = 0.071$ $F^+ = 0.55$	P_j [W]	0.459 2.86	0.515 6.33	1.28 19.6	0.541 3.97	2.17 8.35
$C_\mu = 0.04\%$						
$F^+ = 0.071$ $F^+ = 0.55$	U_0 [m/s]	2.22	-	-	2.22	-
$F^+ = 0.071$ $F^+ = 0.55$	P_j [W]	0.0731 0.585	- -	- -	0.0964 0.814	- -

Lastly, the far-wake investigation has been conducted at three different S-PIV measurement planes downstream the wing for each SJ configuration: $z/c = 26$, $z/c = 52$, and $z/c = 80$. In the following, the S-PIV setup and the image processing are described in details.

4.2.3. S-PIV SETUP AND IMAGE PROCESSING

STEREOSCOPIC particle image velocimetry is used to measure the 2D-3C velocity. A schematic of the experimental setup is shown in Figure 4.13. Particle images are acquired in the xy -plane with the origin on the trailing edge at the mid-span point, with the x , y , and z -axis aligned with the spanwise (inboard), crosswise (upward), and streamwise directions respectively. The flow is seeded with Poly-Ethylene Glycol particles nebulized by the Haze Base Classic fog machine in small particles with a mean diameter of $1 \mu\text{m}$. Illumination is provided by a double pulsed Nd:YAG Innolas laser (532 nm, 150 mJ per pulse). The laser beam is shaped into a 1.9 mm thick light sheets separated by 0.6 mm. The time delay between the two laser pulses has been set to $120 \mu\text{s}$, leading to about 13 pixels mean displacement. Images are acquired by two LaVision's Imager sC-MOS cameras (2160×2560 pixels, pixel pitch of $6.5 \mu\text{m}$, intensity resolution 16 bit) in

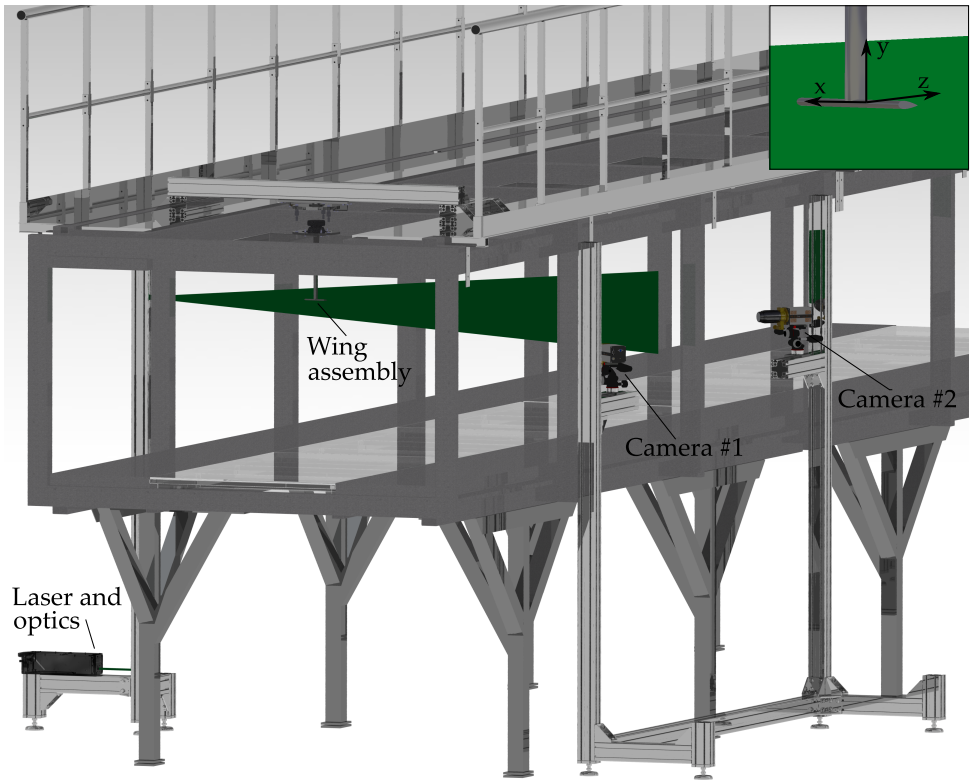


Figure 4.13: Experimental setup in the LMFL boundary layer wind tunnel test section.

forward scattering on one side of the wind tunnel, in stereo and scheinpflug configuration equipped with Nikon 135 mm lenses at $f\# = 11$ in order to obtain a large field and keep a good spatial resolution. The actual imaging produces a field of view of $3.3c \times 4.90c$ with a magnification of about 14 pixel/mm. The optical camera calibration has been conducted by using a target made of a regular Cartesian grid of black crosses on a transparent background with a $10 \text{ mm} \pm 0.1\%$ spacing. The target plate is aligned with the center plane of the laser sheet, and the images are recorded at this initial location and when it is translated $\pm 10 \text{ mm}$ backward and forward with a step of 0.5 mm along the positive and negative z direction by using an motorized translation micrometric stage. The reconstruction used is the one proposed by Soloff et al., 1997 and a self-calibration similar to Wieneke, 2005 was applied. The root mean square calibration error is lower than 0.3 pixels for both cameras.

In the present experimental campaign, the laser frequency (i.e acquisition frequency) is fixed to $f_{acq} = 10 \text{ Hz}$. As for the near-wake measurements, the phenomenon with frequency f_a is sampled with a phase separation $\Delta\phi = 24^\circ$, leading to $N_{Div} = 15$ divisions (phases) per cycle. As a matter, every $n_p = 5$ periods of membrane oscillation for both control cases, the same phases are acquired again. Since the number of division is fixed to 15 and only 5 different phases can be acquired temporarily, a time delay $\Delta\tau$ between

the acquisition system and the SJ signal is applied to divide the phase-locked measurements of each control case in three acquisition set. It is equal to:

$$\Delta\tau = \frac{\Delta t}{2} - i \left(\frac{1}{f_a} \frac{1}{N_{Div}} \right), \quad i = 0, 1, 2 \quad (4.5)$$

being Δt the time separation between two laser pulses, the shift is centered between the double exposure of the cameras. A total of 300 snapshots per phase, i.e 1500 image pairs for each set, are acquired to obtain statistically reliable data. Furthermore, the historical minimum intensity based on the entire ensemble of the image pairs has been subtracted to improve the quality of the image pairs.

A multi-grid multi-pass in-house algorithm of LMFL has been employed to compute the velocity field (Soria, 1996; C. E. Willert & Gharib, 1991). The final interrogation area size is 16×24 pixels with an overlap of 55%, resulting in a measurement resolution L_m of about 1.6 mm. Before the final pass, image deformation was also used to improve the quality of the data (Lecordier & Trinité, 2004; Scarano, 2001).

4.3. DATA PROCESSING AND METRICS

THE present section reports the main tools employed for the wingtip vortices description of both physical and geometrical characteristics. The discussion starts with the definition of the method adopted to identify the presence of the wingtip vortices in the instantaneous PIV snapshots, following by a novel vortex model to fit the vorticity field and extrapolate the vortices features. Lastly, a brief mathematical description of the metrics employed to analyze the wingtip vortices behavior is reported.

4.3.1. VORTEX IDENTIFICATION METHOD

THE location of the wingtip vortices should be determined in the PIV snapshot with a robust method. Different vortex identification methods have been proposed over the years such as the swirling strength scheme (Zhou et al., 1999), Q and λ_2 criteria (Jeong & Hussain, 1995), and the geometric center (Mula et al., 2013). Several reviews of the most common vortex identification techniques have been reported in the literature (Chakraborty et al., 2005; Cucitore et al., 1999). Although being widely employed, all the schemes listed above are based on the divergence of the velocity field and because of their mathematical formulation these methods suffer of sufficient accuracy in determining the physical location of the vortex center. As such, Graftieaux et al., 2001 proposed a more robust technique of identifying the vortex location in a flow by introducing a non-Galilean invariant approach. In particular, it is based on the evaluation of the scalar function $\Gamma_1(P)$ as follows:

$$\Gamma_1(P) = \frac{1}{N} \sum_S \frac{(PM \times u_M) \cdot \hat{e}_z}{|PM| |u_M|} \quad (4.6)$$

where PM is the vector from the center point P to a subregion point M in the region S , which may be of any arbitrary shape that encloses the point P for an estimate of $\Gamma_1(P)$. Furthermore, u_M is the total velocity vector at point M and \hat{e}_z is the unit vector normal

to the measurement plane. Finally, the vortex center corresponds then to the measurement point where the value of the scalar function Γ_1 is maximum. In particular, the Γ_1 function was developed such that the velocity fluctuations caused by large-scale vortices are separated from those related to small-scale turbulence (Graftieaux et al., 2001).

4.3.2. VORTEX MODEL

THE geometrical and physical characteristics of a single wingtip vortex has been accurately evaluated by fitting the experimental streamwise vorticity field to the two-dimensional elliptical Gaussian function expressed as

$$\zeta_z(x, y) = \zeta_{z,max} \exp \left[- \left(a(x - x_0)^2 + 2b(x - x_0)(y - y_0) + c(y - y_0)^2 \right) \right] \quad (4.7)$$

where the matrix

$$\begin{bmatrix} a & b \\ b & c \end{bmatrix} \quad (4.8)$$

is a positive-definite. In particular, $\zeta_{z,max}$ is the maximum streamwise vorticity value while (x_0, y_0) are the coordinates of the vortex center. By setting

$$a = \frac{\cos^2 \Phi}{2\sigma_x^2} + \frac{\sin^2 \Phi}{2\sigma_y^2}, \quad (4.9a)$$

$$b = -\frac{\sin 2\Phi}{4\sigma_x^2} + \frac{\sin 2\Phi}{4\sigma_y^2}, \quad (4.9b)$$

$$c = \frac{\sin^2 \Phi}{2\sigma_x^2} + \frac{\cos^2 \Phi}{2\sigma_y^2}, \quad (4.9c)$$

it is possible to obtain the rotation angle Φ and the standard deviations along the two directions x and y . In order to define the geometrical characteristics of the wingtip vortices, the following vortex model has been define from Eq. (4.7)

$$\zeta_z(x, y) = \zeta_{z,maxL} \exp \left[- \left(\frac{x_L'^2}{D_{maxL}^2/8} + \frac{y_L'^2}{D_{minL}^2/8} \right) \right] + \zeta_{z,maxR} \exp \left[- \left(\frac{x_R'^2}{D_{maxR}^2/8} + \frac{y_R'^2}{D_{minR}^2/8} \right) \right] \quad (4.10)$$

where D_{max} and D_{min} are the major and minor axes of the elliptical Gaussian function in the reference frame x', y' given by the rotation around the vortex center as

$$\begin{bmatrix} x' \\ y' \end{bmatrix} = \begin{bmatrix} \cos \Phi & \sin \Phi \\ -\sin \Phi & \cos \Phi \end{bmatrix} \begin{bmatrix} x - x_0 \\ y - y_0 \end{bmatrix} \quad (4.11)$$

The subscripts L and R indicate the left and right vortex respectively. As such, the geometrical characteristics of the vortex are completely described by the set of parameters D_{max} , D_{min} , and Φ . This approach has been preferred against the Lamb-Oseen vortex model (single Gaussian vorticity profile, Leweke et al., 2016) and all the other vortex models presented by Gerz et al., 2002 in order to increase the determination factor since the vortices can exhibit an ellipsoidal shape. In particular, according to the Eq. (4.10), the

mutual induction and the possible overlap of the two vortices is also taken into account. Furthermore, in case of only one vortex in the FOV, only the left vortex of Eq. (4.10) will be considered.

4.3.3. METRICS

IN the following, the metrics employed for the wingtip vortices description of both physical and geometrical characteristics in the near and far-field investigation are reported. It is important to outline that the metrics described hereinafter are applied for both the time-averaged and phase-averaged results reported in the chapters 5 and 6. The main characteristic of the wingtip vortices is represented by the strength of the streamwise vorticity, which is estimated using a second order central difference scheme as:

$$\zeta_z = \frac{\partial u}{\partial y} - \frac{\partial v}{\partial x} \approx \frac{u_{i+1,j} - u_{i-1,j}}{2\Delta y} - \frac{v_{i,j+1} - v_{i,j-1}}{2\Delta x} \quad (4.12)$$

where $i = 1, 2, \dots, m$, $j = 1, 2, \dots, n$, m and n are number of the measurements points along the y and x direction, and $\Delta y = \Delta x = L_m$ are the cross-stream spacing of the measurement grid.

Once the vorticity field has been correctly evaluated, the vortex circulation can be easily computed with the following expression

$$\Gamma = \int_{A_c} \zeta_z dA_c \quad (4.13)$$

where A_c is the area of the vortex core. In particular, the streamwise vorticity fitting model of Eq. (4.10) has been used to analytically integrate the Eq. (4.13).

Lastly, a key parameter for the evaluation of the SJ effectiveness in reducing the wake-hazard is represented by the circumferential velocity radial distribution across the wingtip vortices. Being u and v the measured spanwise and transverse velocities, they first interpolated in a polar mesh with linearly spaced r/c and θ , where r and θ are the radial and angular positions of the measurement points in a polar coordinate system centered at the vortex center. The circumferential velocity was then calculated as follows:

$$U_\theta = (v - v_c) \cos \theta - (u - u_c) \sin \theta \quad (4.14)$$

where u_c and v_c are the spanwise and transverse velocities of the vortex center, respectively. For each measurement plane, the interpolated values of U_θ are divided into two regions: one covering angles between $[270^\circ, 90^\circ]$ where radial positions were considered positive, and another region covering angles between $[90^\circ, 270^\circ]$ where radial positions were considered negative. Furthermore, values of U_θ at a given r/c are determined by averaging the values of the circumferential velocities, interpolated every 3.6 degrees, over each region.

5

TIME-AVERAGED RESULTS

IN this chapter, the results of the average based on the entire ensemble of the acquired instantaneous flow fields for each physical quantity will be presented and discussed. As regards the notation employed for velocity components, the small letters u , v , and w indicate the instantaneous velocity components while the symbol $\overline{(\cdot)}$ represents a time-averaged value.

5.1. NEAR-FIELD ANALYSIS

THE present section reports the time-averaged results of the near-field investigation in terms of the main physical characteristics of the wingtip vortex such as the streamwise vorticity fields, circumferential velocity, and circulation evaluated as described in section 4.3.3. As already described in section 4.1.2, the S-PIV measurement planes in the wing wake are placed at $z/c = 0.1, 0.5, 1$, and, 2 .

5.1.1. STREAMWISE VORTICITY AND GEOMETRICAL FEATURES

THE normalized time-averaged streamwise vorticity fields $\overline{\zeta}_z c/U_\infty$ for the baseline configuration BCs at $z/c = 0.1, 0.5, 1, 2$ are reported in Figure 5.1. Two different regions can be identified: the wake shear layer and the tip vortex. The former exhibits a spiral shape with relatively low vorticity levels, whereas the latter contains most of the vorticity within an area of a nearly circular shape. Outside the wake and the tip vortex regions, the vorticity is essentially zero. At $z/c = 0.1$, the peak value of the normalized streamwise vorticity at the center of the vortex core region is about 10. Half a chordlength downstream, the vorticity has rolled up into a coherent trailing vortex, which is also seen at the last measurement plane with no qualitative changes. However, the vortex moves inboard and upward going downstream due to the negative angle of attack, with a decreasing peak value up to 50% at $z/c = 2$. In order to obtain a good understanding of the effect of the SJ actuation with an increasing jet velocity, the contours of $\overline{\zeta}_z c/U_\infty$ for the

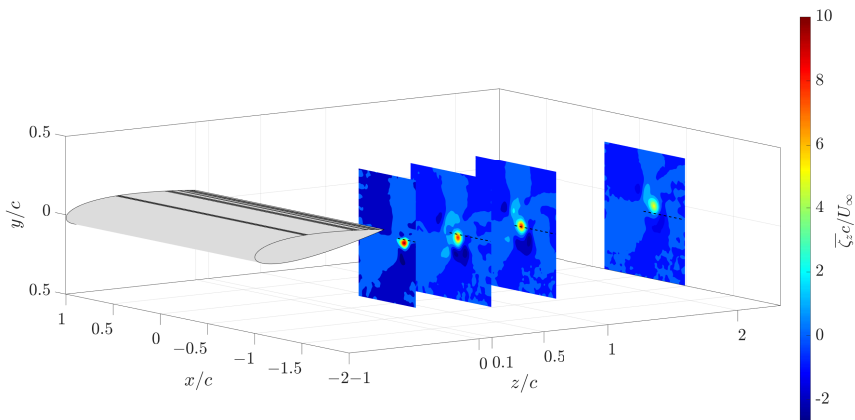


Figure 5.1: Time-averaged streamwise vorticity fields for the baseline configuration BCs. Measurement planes at $z/c = 0.1, 0.5, 1, 2$.

control case at $F^+ = 0.071$ and $F^+ = 0.55$ for the model Ss01 and Ss04 respectively are examined in Figure 5.2. The horizontal dashed black line represents the projection of the wing trailing edge. Under the control case at $C_{\mu} = 0.2\%$, $F^+ = 0.071$ for the wing model Ss01 (Figure 5.2a, 5.2b, 5.2c, and 5.2d), two main vortices are clearly visible, which are the wingtip vortex and the co-rotating jet vortex. The interaction between these two co-rotating vortices downstream of the trailing edge characterizes the near wake depending on their strengths and initial location. As it can be noted, the strength of the jet vortex is three times lower than the tip one and it is almost vanished at $z/c = 2$. The presence of the co-rotating jet vortex is in agreement with the findings of Margaris and Gursul, 2010. The effectiveness of the SJ is meaningful, leading a vortex strength reduction, with respect to the baseline case, of about 38%, 55%, 65%, and 53% at $z/c = 0.1, 0.5, 1, 2$ respectively. By decreasing the SJ exit velocity, the jet vortex has been found to be very weak and it completely disappears by increasing the actuation frequency to $F^+ = 0.55$ as shown in Figure 5.2e, 5.2f, 5.2g, and 5.2h. As a results, the upward displacement of the vortex is reduced with respect to the previous control case. However, a huge impact on the streamwise vorticity peak is registered as well with a maximum reduction of 50% at $z/c = 2$. Moreover, in both control cases the wingtip vortex appears to be more diffuse, hence covering a larger area around the mean vortex center moving downstream. This behavior is confirmed in Figure 5.3 where the geometrical characteristics of the vortex are reported for all the control cases tuned to the Crow ($F^+ = 0.071$) and Widnall ($F^+ = 0.55$) instability frequency. In particular, the most pronounced diffusion is related to the Ss02, $F^+ = 0.55$, where a major axis increase of about 82% with respect to the baseline case is observed at $z/c = 2$. As it can be noted in Figure 5.3a, the vortex aspect ratio in each control case is maximized at $z/c = 0.1$ and it is slightly higher than the baseline case, meaning that the SJ actuation does not give rise to a significant stretching whilst

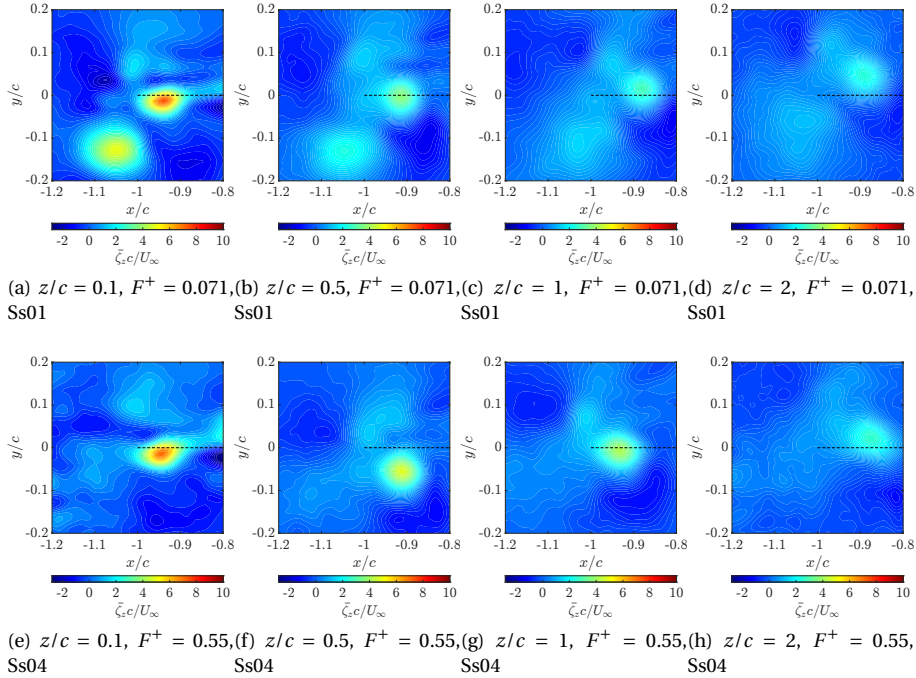


Figure 5.2: Contours of the normalized time-averaged streamwise vorticity fields for the control case at $F^+ = 0.071$ and $F^+ = 0.55$ for the model Ss01 and Ss04 at $C_{\mu} = 0.2\%$ respectively.

causing a mean rotation of the vortex principal axis since the inclination angle $\bar{\Phi}$ increases with the actuation and downstream distance. Lastly, in Table 5.1, the streamwise

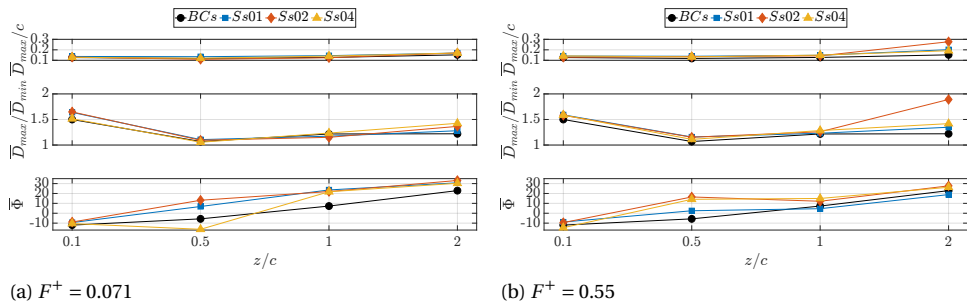


Figure 5.3: Normalized time-averaged vortex major axis, aspect ratio and inclination angle for all the configurations investigated at $C_{\mu} = 0.2\%$.

vorticity peak is compared against the baseline case for each measurement plane. As it can be noted, the SJ reveals to be a promising device to control the wingtip vortices since its strength is reduced at least of 25% in any of the configuration investigated. As a mat-

ter, blowing at high actuation frequency ($F^+ = 0.55$) turned out to be more effective than the configuration tuned to the Crow instability frequency ($F^+ = 0.071$) with a maximum vortex strength reduction up to 70% for the wing model Ss02 at $z/c = 2$.

The time-averaged analysis can be compared to the results achieved in the literature. As regards enhanced vorticity diffusion, at all control configurations both Dghim et al., 2018; Dghim et al., 2016 and Margaritis and Gursul, 2006 observe an increase in size of the region of concentrated vorticity. In the following, the momentum coefficient values reported in Dghim et al., 2018; Dghim et al., 2016 and Margaritis and Gursul, 2006 have been scaled by a factor of 4 and $\pi^2/2$ (Greco et al., 2016) respectively, due to the different definition of the SJ characteristic velocity of Eq. (1.19) employed for the present work. Particularly interesting is the result obtained by Margaritis and Gursul, 2006 at $z/c = 1$, whose best control configuration has a very low blowing coefficient, $C_\mu = 0.016\%$ and $F^+ = 0.75$. In this configuration, the jet is blown in spanwise direction from the slot placed near the upper part of the wing producing a clearly diffused vortex with significantly lower vorticity level of about 50% than the reference case which is in agreement with the present results, although the SJ exit section and its location are different. The streamwise vorticity peak reduction obtained in the present work is comparable to the one achieved by Dghim et al., 2018 at the downstream distance $z/c = 3$. With a momentum coefficient halved ($C_\mu = 0.1\%$) with respect to the control case of the present work, but with higher frequency ($F^+ = 0.96$), they obtained a decrease of the axial vorticity peak of 22% with respect to the baseline case against the reduction of at least 50% obtained for the present work at $z/c = 2$. Dghim et al., 2018 demonstrated a similar streamwise vorticity peak reduction of 60% compared to the natural vortex case only with a higher $C_\mu = 1\%$ against the momentum coefficient of the present work equal to $C_\mu = 0.2\%$, suggesting that a minor amount of power to generate the actuation would be sufficient to produce an equally effective control which is noticeable.

Table 5.1: Normalized time-averaged streamwise vorticity peak comparison with respect to the BCs for each configuration investigated at $C_\mu = 0.2\%$.

	$\frac{\bar{\zeta}_{z,max}^{BCs}}{U_\infty}$	$\frac{\bar{\zeta}_{z,max}}{\bar{\zeta}_{z,max}^{BCs}}$					
		Ss01		Ss02		Ss04	
		$F^+ = 0.071$	$F^+ = 0.55$	$F^+ = 0.071$	$F^+ = 0.55$	$F^+ = 0.071$	$F^+ = 0.55$
$z/c = 0.1$	10.5	0.716	0.641	0.674	0.616	0.732	0.694
$z/c = 0.5$	8.31	0.450	0.536	0.739	0.475	0.589	0.587
$z/c = 1$	8.26	0.350	0.573	0.614	0.491	0.518	0.511
$z/c = 2$	5.34	0.468	0.456	0.450	0.302	0.527	0.502

5.1.2. CIRCUMFERENTIAL VELOCITY

THE effect of the SJ actuation frequency on the wingtip vortices may be further quantified by evaluating the radial profiles of the mean circumferential velocity which is a crucial parameter for the induced rolling moment in a wake hazard. The distribution of the normalized time-averaged circumferential velocity, \bar{U}_θ/U_∞ , against r/c for all the investigated control configurations are shown in Figure 5.4. It is important to note that at

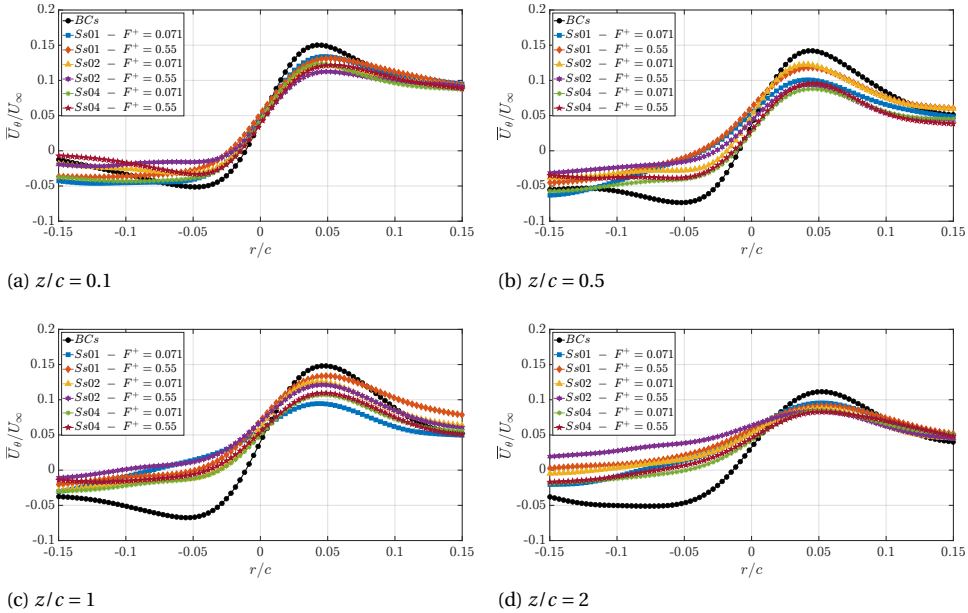


Figure 5.4: Time-averaged radial distribution of the normalized circumferential velocity at different downstream positions for all the configuration investigated at $C_\mu = 0.2\%$.

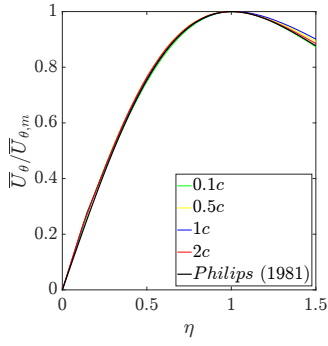
all measurement planes, the circumferential velocity exhibits positive peaks with magnitudes that are at least 50% higher than that of the negative peaks. This behavior can be ascribed to the double induction caused by the vortex itself and by the neighboring one, both inducing an upward velocity. In the following, only the positive peaks are analyzed. In Figure 5.4, the distribution of \bar{U}_θ/U_∞ reached a peak value before slowly decreasing to a nearly asymptotic value. The region between the ensemble-averaged vortex location ($r/c = 0$) and the radial location at which the peak value occurs is often referred to as the inner vortex region. For the case BCs at $z/c = 0.1$, a dimensionless circumferential velocity peak value of 0.15 is reached at a normalized radial location of about 0.043. Moving downstream up to $z/c = 2$, the peak is displaced to larger radial location ($r/c = 0.053$) reaching a value 26% lower that may be attributed to the increased roll-up of the shear layer with increased streamwise distance. With the actuation, the gradient of \bar{U}_θ/U_∞ across the vortex center is decreased of about 30% for each control case, which is the result of a more diffuse vortex. This is confirmed also by the degree of asymmetry which becomes more pronounced with the SJ blowing going downstream. This decrease

in the core velocity gradient is accompanied by a remarkable decrease in the peak value of at least 10% for each control case and downstream distance, with a maximum drop of about 38% for the configuration of Ss04, $F^+ = 0.071$ at $z/c = 0.5$. In particular, the higher actuation frequency $F^+ = 0.55$ (i.e. Widnall instability frequency) generally outperforms the lower one in any test case with the only exception of the wing model Ss01 at $z/c = 0.5, 1$ in which the tuned Crow instability has a 7% better performance. Finally, blowing through a larger exit section (Ss04) leads to a striking reduction of the \bar{U}_θ/U_∞ of 19%, 32%, 27%, and 26% (Ss04, $F^+ = 0.55$) at $z/c = 0.1, 0.5, 1, 2$ respectively, which is promising. The effectiveness of the SJ actuation in promoting vortex diffusion is in agreement with the literature. Margaris and Gursul, 2006 and Dghim et al., 2020 investigated a similar C_μ (0.016% and 0.025%) with almost the same $F^+ = 0.075$, finding a normalized circumferential peak reduction of about 10% which increase up to 15% and 40% at higher F^+ of 0.75 and 0.3 respectively, being the higher actuation frequency more impactful. The same behavior has been found by the author in the feasibility tests reported in chapter 3, where the control case tuned to the Widnall instability reduced the circumferential velocity peak of about 20%.

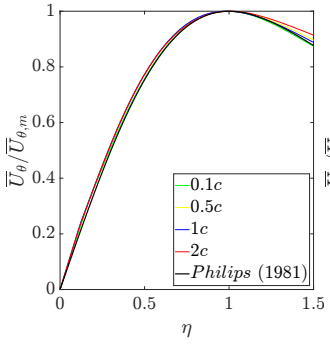
Although very crucial three-dimensional effects dominate the genesis of vortex roll-up and formation, Phillips, 1981 reported that the circumferential velocity profiles in the core of a wingtip vortex adopt a self-similar behavior, when \bar{U}_θ and r are normalized by the peak value, $\bar{U}_{\theta,m}$, and the corresponding radial location, r_c , respectively. The normalized radial positions are denoted with the self-similar variable, $\eta = r/r_c$. The profiles of the normalized circumferential velocities fit the following model equation:

$$\frac{\bar{U}_\theta}{\bar{U}_{\theta,m}} = \left(1 + \frac{1}{2\chi}\right) \frac{1}{\eta} \left(1 - e^{-\chi\eta^2}\right) \quad (5.1)$$

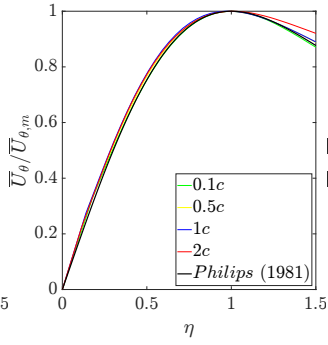
where χ is defined by $e^\chi = 1 + 2\chi$, yielding $\chi \approx 1.256$. The vortex model of Eq. (5.1) along with the experimental measurements are shown in Figure 5.5. Starting from the baseline configuration BCs, a good collapse with the theoretical fit inside the vortex core ($\eta \leq 1.2$) is clearly visible at $z/c = 0.1$. For larger downstream distances $z/c \geq 0.5$, the profiles of the normalized circumferential velocity collapse fairly well with the curve fit proposed by Phillips, 1981, indicating a self-similar vortex structure. It may be inferred that the roll-up process is almost completed at $z/c = 2$ and the vortex core has evolved asymptotically to reach a nearly axisymmetric distribution. However, a not negligible variance of the radial profiles $\bar{U}_\theta/\bar{U}_{\theta,m}$ from the theoretical model is present outside the vortex core ($\eta \geq 1.2$). As suggested by Saffman, 1993, the lack of collapse can be caused by the gradual transition between the viscous core region and the outer region dominated by the irrotational flow of the rolling vortex sheet. Under the control case tuned to the Crow instability frequency (Figure 5.5b, 5.5c, 5.5d), the SJ actuation seems to not modify the structure of the vortex core as the $\bar{U}_\theta/\bar{U}_{\theta,m}$ continues to exhibit a reasonable collapse with the theoretical fit at all downstream locations, suggesting an asymptotic state. Actually, in the outer region, a larger departure from the model with respect to the BCs case is registered. This behavior is representative of the SJ actuation effects on the region around the vortex core where high-turbulence mixing alleviates the velocity gradients and thus increases the outward diffusion of vorticity. On the other hand, under the con-



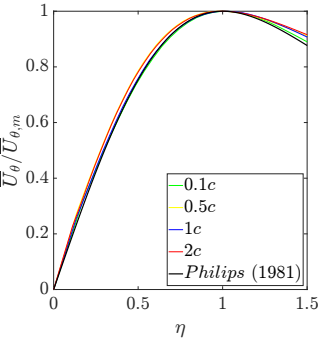
(a) BCs



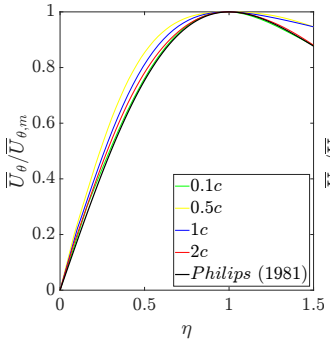
(b) $F^+ = 0.071$, Ss01



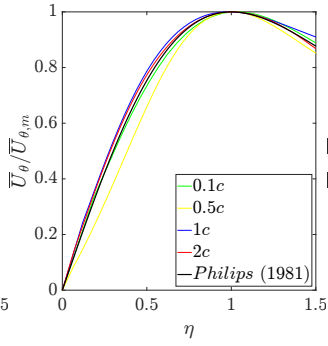
(c) $F^+ = 0.071$, Ss02



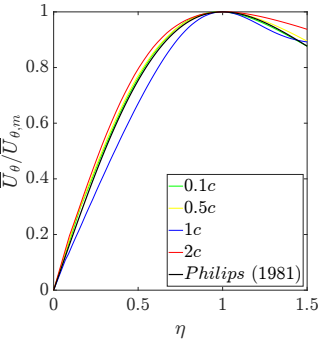
(d) $F^+ = 0.071$, Ss04



(e) $F^+ = 0.55$, Ss01



(f) $F^+ = 0.55$, Ss02



(g) $F^+ = 0.55$, Ss04

Figure 5.5: Time-averaged radial profiles of the normalized circumferential velocity in a self-similar coordinates system at $C_\mu = 0.2\%$ and different downstream positions.

tro case tuned to the Widnall instability frequency (Figure 5.5e, 5.5f, 5.5g), it is clear that the wingtip vortex does not exhibit a self-similar behavior. In fact, the vortex core structure is deeply modified by the Widnall instability as already described in section 1.2. The slight upward departure from the theoretical model was observed in previous studies (Dghim et al., 2018, 2020). On the contrary, the actuation at higher F^+ appears to not follow the theoretical vortex model, as it can be noted in Figure 5.5b, 5.5c, 5.5d. This atypical trend may be ascribed to the smoothing of the velocity gradients and to the large turbulence levels around the vortex generated by the SJ blowing which may lead to a higher spreading rate along the radial direction, requiring larger downstream distances to achieve a self-similar state.

5.1.3. CIRCULATION

TIME averaged vortex circulation represents a key parameter to evaluate the effect of the synthetic jet actuation on the wingtip vortices features and development. The results are displayed in Figure 5.6. As expected from the streamwise vorticity results, the SJ

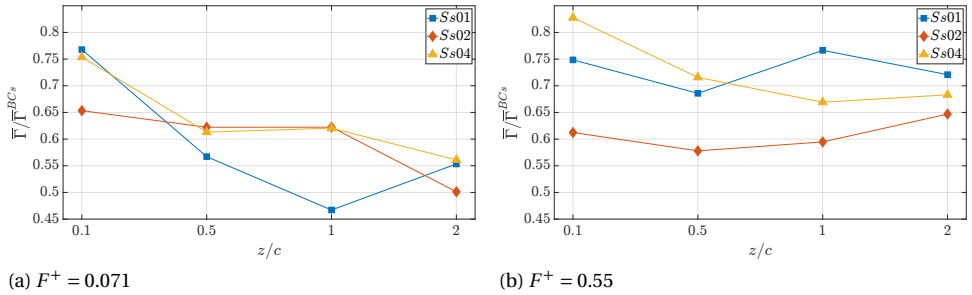


Figure 5.6: Normalized time-averaged vortex circulation comparison with respect to the BCs for each configuration investigated at $C_\mu = 0.2\%$. The BCs values of $\bar{\Gamma}^{BC_s} / cU_\infty$ are equal to 0.0443, 0.0424, 0.0433, 0.0404 at $z/c = 0.1, 0.5, 1, 2$ respectively.

greatly affects the time-averaged vortex circulation causing a relevant reduction in each condition investigated which is at least of about 25% with respect to the baseline configuration BCs. The maximum SJ influence is registered for the wing configuration Ss01 at $z/c = 1$ for the Crow instability frequency ($F^+ = 0.071$) which leads to a striking reduction of the circulation of 52% which corresponds to the maximum vortex diffusion as shown in Table 5.1. According to this metrics, higher SJ velocity can be more beneficial in the wingtip vortices alleviations. On the other hand, by increasing the actuation frequency ($F^+ = 0.55$), the intermediate wing model Ss02 has been found to be the best configuration which reduces the circulation more than 35% at each measurement plane. However, these results are in contrast with the findings of the present author reported in chapter 3 (Zaccara et al., 2022) at $z/c = 3$, where an increase of the vortex circulation up to 29% has been demonstrated, which could be beneficial as well because the instability growth rate of the wingtip vortices is proportional to $\Gamma / 2\pi b$ as reported in Eq. (1.15). Margaritis and Gursul, 2006 evaluates the circulation over a rectangle, defined as the area including all the vorticity above 5% of the streamwise vorticity peak value. They did not demonstrate

a noticeable effect of the synthetic jet actuation on the total circulation which remains constant with the actuation frequency and at most 2% higher than the reference value, while Dghim et al., 2018 evaluated only the radial distribution of the circulation at $z/c = 3$ finding a circulation decrease inside the vortex core due to the reduced vorticity, and an increase of around 10% outside the core region due to the vorticity diffusion over a larger area.

As already demonstrated for the circumferential velocity, the effect of the SJ actuation control on the wingtip vortex core structure can be examined from the radial distribution of the normalized circulation, $\bar{\Gamma}/\bar{\Gamma}_c$, plotted against the similarity variable, η , for different downstream positions as illustrated in Figure 5.7. Hoffmann and Joubert, 1963 suggested an empirical curve fitting relationship to analyze the circulation behavior within the inner core and the logarithmic regions of the vortex according the following expressions:

$$\frac{\bar{\Gamma}(\eta)}{\bar{\Gamma}_c} = A\eta^2 \quad \text{for } \eta < 0.4 \quad (5.2)$$

$$\frac{\bar{\Gamma}(\eta)}{\bar{\Gamma}_c} = 1 + B \log(\eta) \quad \text{for } 0.5 < \eta < 1.4 \quad (5.3)$$

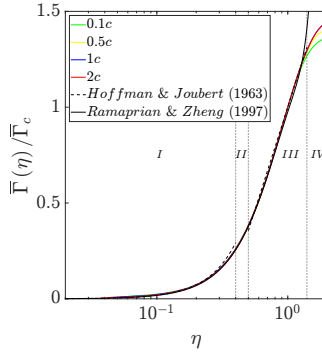
where the constants A and B are 1.83 and 0.93, respectively. As it can be noted in Figure 5.7a, the baseline configuration BCs shows a reasonable agreement with the curve fit equations (5.2) and (5.3). However, a departure is evident in the logarithmic and outer regions (III and IV), suggesting that the vortex has not reached a self-similar state yet and thus a perfectly complete roll-up. A better agreement has been noticed with the sixth-order polynomial suggested by Ramaprian and Zheng, 1997 and Birch et al., 2004 following the expression

$$\frac{\bar{\Gamma}(\eta)}{\bar{\Gamma}_c} = a_0\eta^2 + a_1\eta^4 + a_2\eta^6 \quad (5.4)$$

where the constants a_0 , a_1 , and a_2 are 1.756, -1.044, and 0.263, respectively. The excellent agreement of both the baseline and control cases self-similar circulation profiles with the curve fit in the inner core region (I) indicates that this region is mainly dominated by the viscous effect where the vortex core has an approximately rigid-body rotation (Devenport et al., 1996; Hoffmann & Joubert, 1963). The lack of collapse in the outer region (IV) is present also for the controlled cases. In particular, when increasing the actuation frequency at $F^+ = 0.55$, the departure among the curves at different measurement plane increases, meaning that the vortex core will require larger downstream distances to reach an asymptotic state due to outward diffusion caused by the SJ momentum injection.

5.2. FAR-FIELD ANALYSIS

THE present section reports the time-averaged results of the far-field investigation in terms of the main physical characteristics and metrics employed to analyze the wingtip vortices behavior in the near-field discussed in the previous section 5.1. As already described in section 4.2.2, the S-PIV measurement planes in the wing wake are



(a) BCs

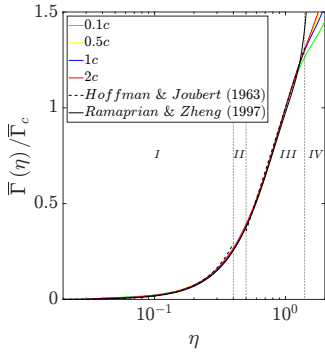
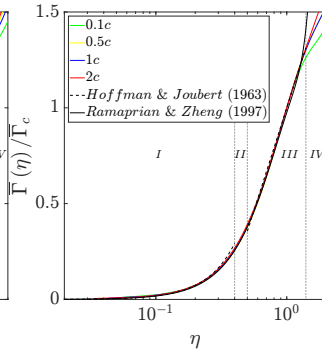
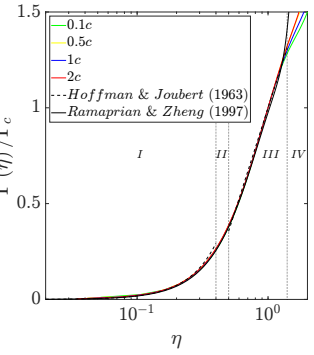
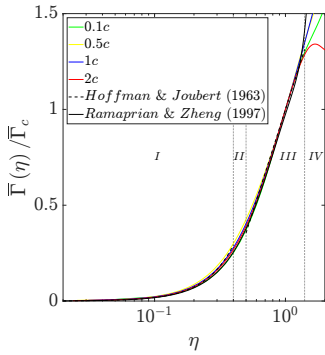
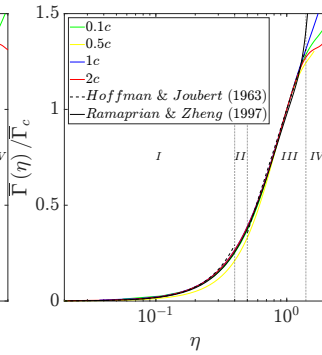
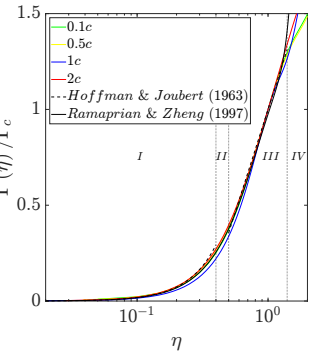
(b) $F^+ = 0.071$, Ss01(c) $F^+ = 0.071$, Ss02(d) $F^+ = 0.071$, Ss04(e) $F^+ = 0.55$, Ss01(f) $F^+ = 0.55$, Ss02(g) $F^+ = 0.55$, Ss04

Figure 5.7: Time-averaged self-similar circulation profiles of the inner region at $C_\mu = 0.2\%$ and different downstream positions: I, inner core; II, buffer region; III, logarithmic region; IV, outer region.

placed at $z/c = 26, 52,$ and 80 . If not different declared, the geometrical and physical characteristics of the vortices reported hereinafter are the average between the left and right vortex.

5.2.1. STREAMWISE VORTICITY AND GEOMETRICAL FEATURES

IN the following, the streamwise vorticity evaluated as in section 4.3.3 is analyzed. The normalized streamwise vorticity fields $\bar{\zeta}_z c/U_\infty$ for the baseline configuration BC are reported in Figure 5.8. At $z/c = 26$, the vorticity is clearly concentrated only in the

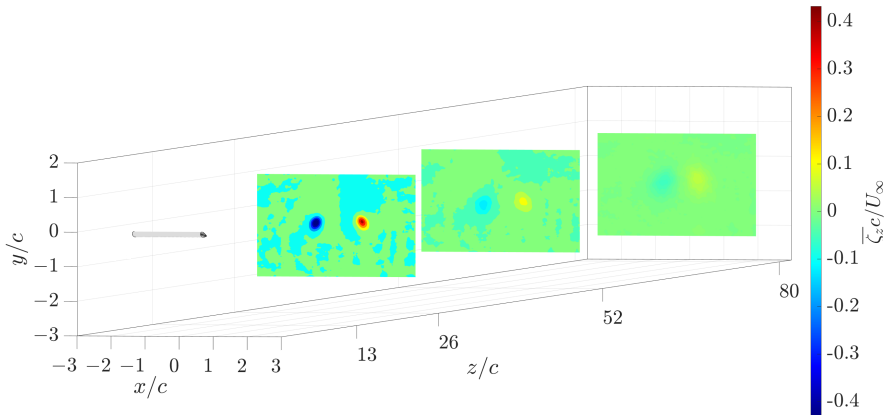


Figure 5.8: Time-averaged normalized streamwise vorticity fields for the baseline configuration BCs. Measurement planes at $z/c = 26, 52, 80$.

wingtip vortices, while outside is essentially zero, since the roll-up is completed. The peak value of the normalized streamwise vorticity at the center of vortices core region is about 0.45, which is more than 95% less than the initial value at $z/c = 0.1$. It is evident that the vortices are going to vanish by looking at the vorticity fields at larger downstream distances where they are barely visible, with a peak value of $\bar{\zeta}_z c/U_\infty$ of 0.12 and 0.06 at $z/c = 52$ and $z/c = 80$ respectively. Due to the mutual induction and the growing of the inherent instabilities, the vortices are displaced both inboard up to the 50% of their initial relative distance b (wing span) and downward up to about $0.70c$ since the angle of attack is positive.

In order to understand the effect of the SJ actuation and its exit velocity, direction, and exit section shape, by comparing the results with near-field analysis, the momentum coefficient is fixed to $C_\mu = 0.2\%$ and all the wing configurations have been tested for each measurement plane at both the chosen actuation frequencies (i.e. the Crow and Widnall instability frequencies) and their combination. The peak values of the normalized streamwise vorticity with respect to the BC peak value is reported in Figure 5.9. As for the near-field investigation, the impact of the SJ actuation on the vortices strength is confirmed also at large downstream distance from the wing. The maximum vorticity

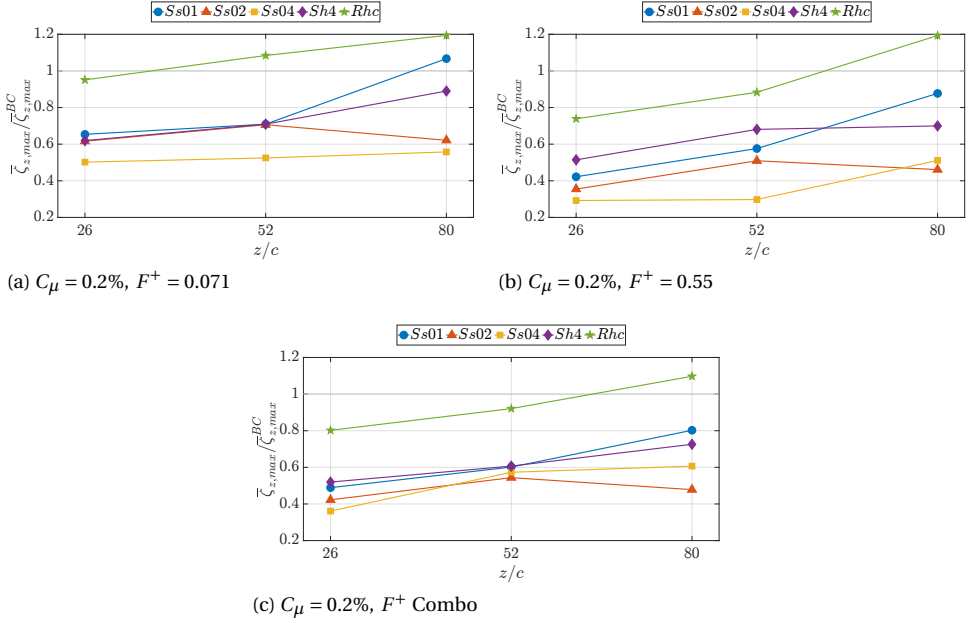


Figure 5.9: Normalized time-averaged streamwise vorticity peak at $C_\mu = 0.2\%$ for all the measurement planes. The BCs and BCr values of $\bar{\zeta}_{z,max}^{BC}/U_\infty$ are equal to 0.531 and 0.467, 0.136 and 0.115, 0.0579 and 0.0402 at $z/c = 26, 52, 80$ respectively.

peak reduction is registered for the wing model at high SJ exit section area (Ss04) tuned to the Widnall instability frequency $F^+ = 0.55$ (see Figure 5.9b). In fact, a 70% of decrease is measured at $z/c = 26$ and $z/c = 52$, with a slight increase at the last station to 45%. As a matter, blowing at low SJ velocity seems to outperform every configuration also at lower actuation frequency of $F^+ = 0.071$ where a $\bar{\zeta}_{z,max}$ reduction of 45% is reported as shown in Figure 5.9a. Increasing the SJ velocity, the wing model Ss02 and Ss01 revealed to be less effective and their influence decreases with the downstream distance at both actuation frequency. Furthermore, the SJ exit section shape does not appear to be a crucial parameter. In fact, the results between the wing model Sh4 and Ss01 at the same SJ exit section area are comparable, with a slight better performance of the rectangular slot at $F^+ = 0.55$. Lastly, it is clear that changing the SJ blowing direction to the chordwise one (Rhc model) leads to a severe decrease of the SJ effectiveness. In particular, the streamwise SJ seems to strengthen the wingtip vortices ($\bar{\zeta}_{z,max}^{BC}/\bar{\zeta}_{z,max} > 1$) going downstream. This behavior has been demonstrated for both SJ actuation frequency, as shown in Figure 5.9. As a whole, blowing with a combination of the Crow and Widnall instability frequencies appears to not outperform the single control cases, confirming all the trend already presented. Actually, the values of the normalized streamwise vorticity peaks are almost the average between the Crow and Widnall instability cases, meaning that a good compromise could be reached with this configuration. According to the streamwise vorticity peak metric, the best control configuration in reducing the vortex strength is represented

by the Ss04 at $F^+ = 0.55$, which means blowing through large exit section area at low velocity and tuning the actuation to the Widnall instability frequency. This configuration has been demonstrated to outperform the others also in the near-field investigation (i.e. Ss04), with the only drawback related to the electrical power needed to generate the synthetic jet which is more than 20 times higher than the one needed at lower F^+ . However, it is worth recalling that the SJ device of the present work has not been designed to be optimized at the actuation frequency selected for the active flow control.

In Figure 5.10, the contours of $\bar{\zeta}_z c / U_\infty$ for the control case at $F^+ = 0.071$ and $F^+ = 0.55$ for the model Ss01 and Ss04 respectively are examined, together with the combo control case for the model Ss04. The BCs fields have been reported too for comparison purposes. As expected from the near-field results, the jet vortex is completely disappeared at large downstream distance, also in case the SJ velocity is maximum for the model Ss01. Looking at the vorticity fields of the measurement plane $z/c = 80$, there is a vertical cut at the right and left of the left and right vortex respectively. This means that the vortices start to overlap each other, canceling the opposite sign vorticity, demonstrating that at this downstream distance a strong interaction with linking between the vortices occurs and, as a consequence, vortex rings are formed. For each case, the wingtip vortices undergo a rapid and increasing outward diffusion, which causes the vorticity weakening and the diameter increasing as shown in Figure 5.11 where the geometrical characteristics of the vortices are reported. The vortices relative distance and their locations at different measurement planes seem to not be affected by the SJ actuation. As already found by the author in the feasibility test described in chapter 3, the vortices present an ellipsoidal shape which can be attributed to a 3D structure of the core, which further justify the use of the vortex fitting model of Eq. (4.10). As far as regards the Crow instability tuned configurations in Figure 5.11a, the maximum diameter doubles its value from $z/c = 26$ ($\bar{D}_{max}/c = 0.42$) to $z/c = 80$ ($\bar{D}_{max}/c = 0.83$), without any relevant change with respect to the BC cases. The vortices aspect ratio $\bar{D}_{max}/\bar{D}_{min}$ results to be reduced being the shape more circular while the inclination angle $\bar{\Phi}$ does not show any particular trend.

On the other hand, an opposite behavior is registered for the control cases tuned to the higher $F^+ = 0.55$. As it can be noted in Figure 5.10g, 5.10h, and 5.10i, the core structure of both vortices is dramatically modified resulting in an elongated shape outward and a larger diffusion with respect to the lower actuation frequency. In fact, the maximum diameter results higher than the BCs in each configuration with a maximum value three times larger for the Ss04. Furthermore, the vortices appear to be more stretched than the BC being the aspect ratio $\bar{D}_{max}/\bar{D}_{min}$ risen up although it decreases with the downstream distance. By combining the actuation frequencies related to the Crow and Widnall instability, the streamwise vorticity fields appear to be an exact compromise between the single control cases (Figure 5.10j, 5.10k, and 5.10l). As a matter, the vortices strength is reduced as well up to 64% with respect to the BCs case, and the geometrical characteristics are very similar to the configuration at low F^+ . In fact, the shape is more circular than the configuration at higher F^+ , with a diameter increasing with the downstream distance (see Figure 5.11c) up to a double value of the baseline case, a vortices aspect ratio $\bar{D}_{max}/\bar{D}_{min}$ almost constant as for the Crow tuned configuration, and an inclination angle decreasing with the downstream with the only exception of the model Ss01.

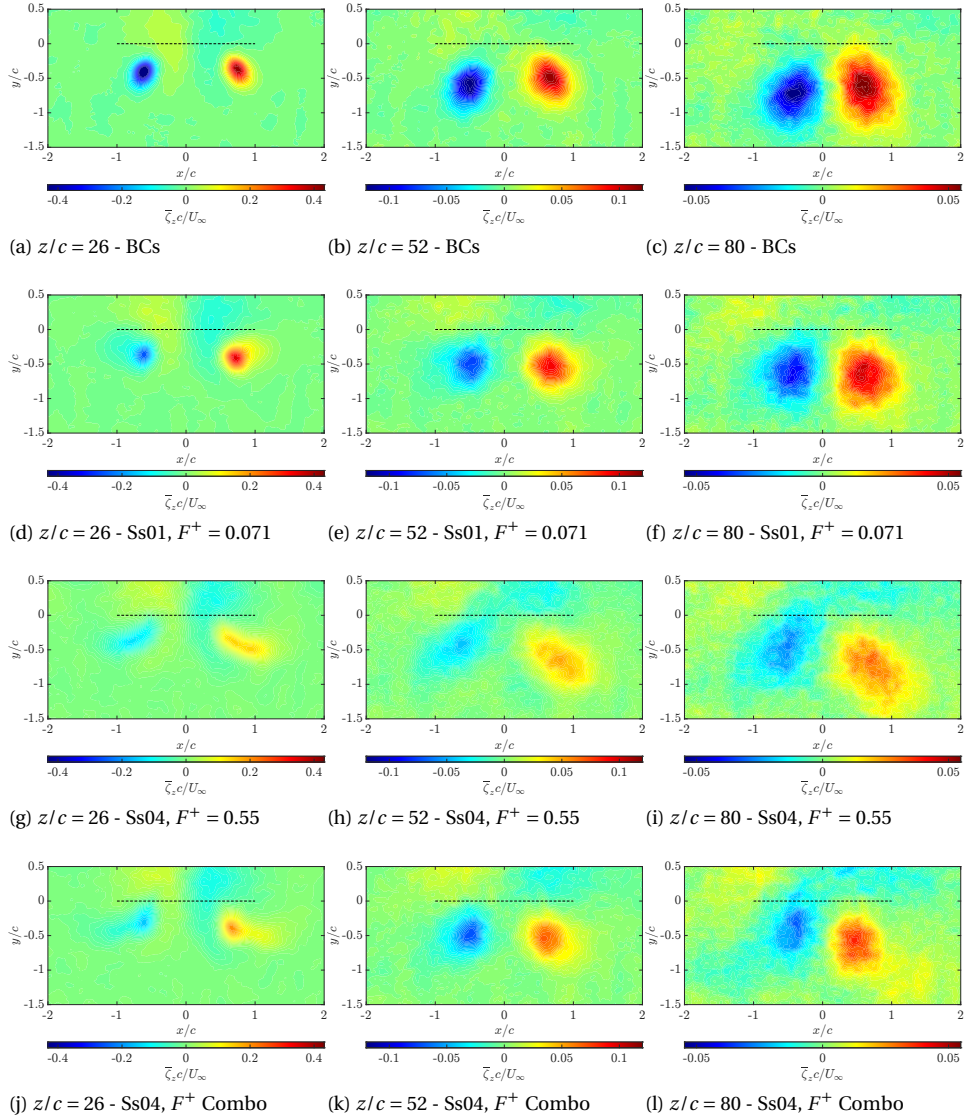


Figure 5.10: Normalized time-averaged streamwise vorticity fields at $C_\mu = 0.2\%$ for all the measurement planes for the wing model Ss01 and Ss04.

In order to investigate the effects of different momentum rate ejected from the SJ, the model Ss01 with the lower exit section area has been taken as a reference, together with the equivalent model Sh4. For each measurement plane and actuation frequency, three momentum coefficients of $C_\mu = 1\%$, $C_\mu = 0.2\%$, and $C_\mu = 0.04\%$ have been tested. The results in terms of normalized streamwise vorticity peak are reported in Figure 5.12. With

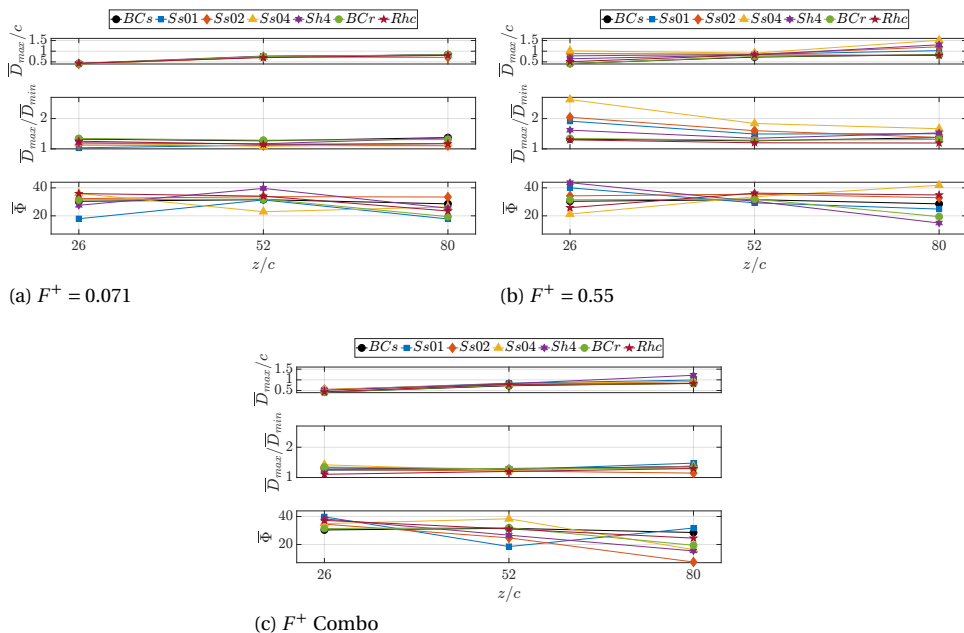


Figure 5.11: Normalized time-averaged vortex major axis, aspect ratio and inclination angle at $C_\mu = 0.2\%$ for all the wing configurations and measurement planes investigated.

only exception of the outliers point at $z/c = 80$, the wingtip vortices are weakened in each configuration. As expected, the higher momentum coefficient $C_\mu = 1\%$ has a striking impact reducing the vorticity peak up to 50%, 74%, and 70% for the $F^+ = 0.071$, $F^+ = 0.55$, and their combination respectively at $z/c = 26$. On the other hand, with a momentum coefficient 25 times lower ($C_\mu = 0.04\%$, meaning the SJ velocity 5 times lower), a reasonable effect of the SJ actuation is encountered with a $\bar{\zeta}_{z,max}/\bar{\zeta}_{z,max}^{BC}$ reduction of at least 10% except the control case at $F^+ = 0.55$ for Ss01 in which the BC value is recovered at $z/c = 80$. These results are promising for the possibility to obtain an effective control with a considerably less power. In fact, the SJ velocity for $C_\mu = 1\%$ is equal to $U_0 = 1.29U_\infty$, which could be not feasible when scaled to a real aircraft wing. As already stated above, the change in the exit section shape from a rectangular slot to four circular nozzles does not play a crucial role, being the results comparable.

Lastly, in Figure 5.13, the geometrical characteristics of the vortices related to the wing model Ss01 are reported. The findings related to the momentum coefficient $C_\mu = 0.2\%$ are confirmed and scaled for the higher and lower value. In fact, the vortex diameter and the vortex aspect ratio are deeply affected only at the higher $F^+ = 0.55$, with the $C_\mu = 1\%$ curve larger than the other ones, confirming that injecting more momentum increases the vortex diffusion.

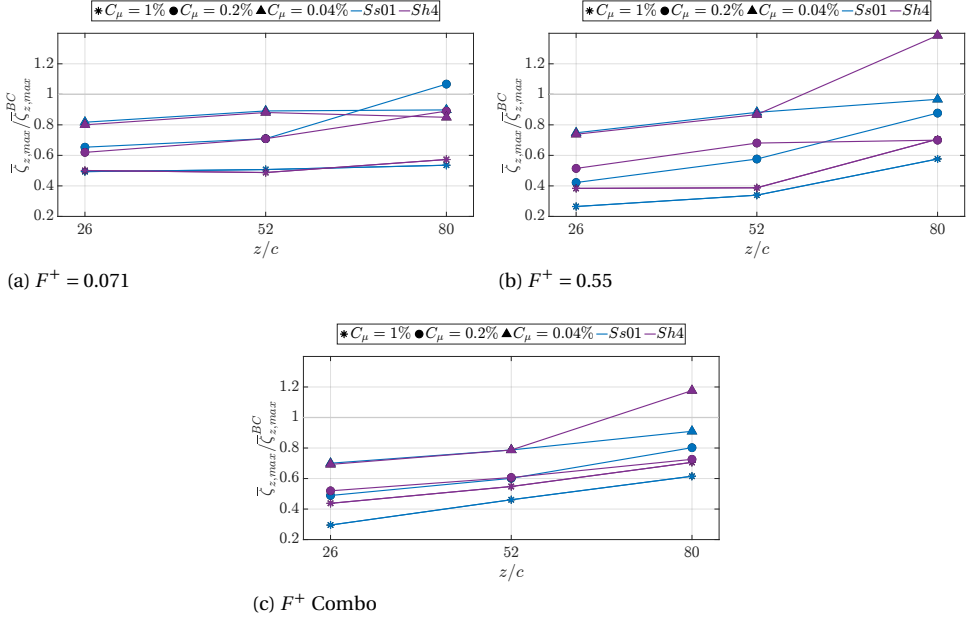


Figure 5.12: Normalized time-averaged streamwise vorticity peak at different momentum coefficient C_μ for all the measurement planes for the wing model Ss01 and Sh4. The BCs values of $\zeta_{z,max}^{BC} c / U_\infty$ are equal to 0.531, 0.136, and 0.0579 at $z/c = 26, 52, 80$ respectively.

5.2.2. CIRCUMFERENTIAL VELOCITY

THE present section reports the time-averaged circumferential velocity profiles which are crucial for the wake-hazard metric since a possible encounter can occur in the far-wake of the leading aircraft. They are evaluated as described in section 4.3.3 for each vortex by considering the influence of the neighborhood one. The distribution of the normalized mean circumferential velocity, $\bar{U}_\theta / U_\infty$, against x/c for the control configurations at $C_\mu = 0.2\%$ for all the measurement planes and actuation frequencies are shown in Figure 5.14. In the following, all the comments are referred on the positive peak if not differently declared. As already stated for near-field analysis, the circumferential velocity exhibits negative peaks with magnitudes that are at least 38% higher than that of the positive peaks due to the double induction caused by the vortex itself and by the neighboring one, both inducing a downwash velocity since the angle of attack is positive. Starting from the baseline cases, a peak value of $\bar{U}_\theta / U_\infty = 0.0197$ is registered at $z/c = 26$, which is only the 13% of the peak value at $z/c = 0.1$. Going further downstream, the circumferential velocity peak is located at slightly higher distance from the vortex center and the peak is equal to 0.00835 and 0.00453 at $z/c = 52$ and $z/c = 80$ respectively. Furthermore, the negative peak is increased as well, meaning that the induced downwash is reducing and thus the velocity gradient across the vortices is reduced too. As a result, the wingtip vortices are going to vanish and the probability of a dangerous wake-hazard are dramatically diminished being the induced rolling moment on the following aircraft

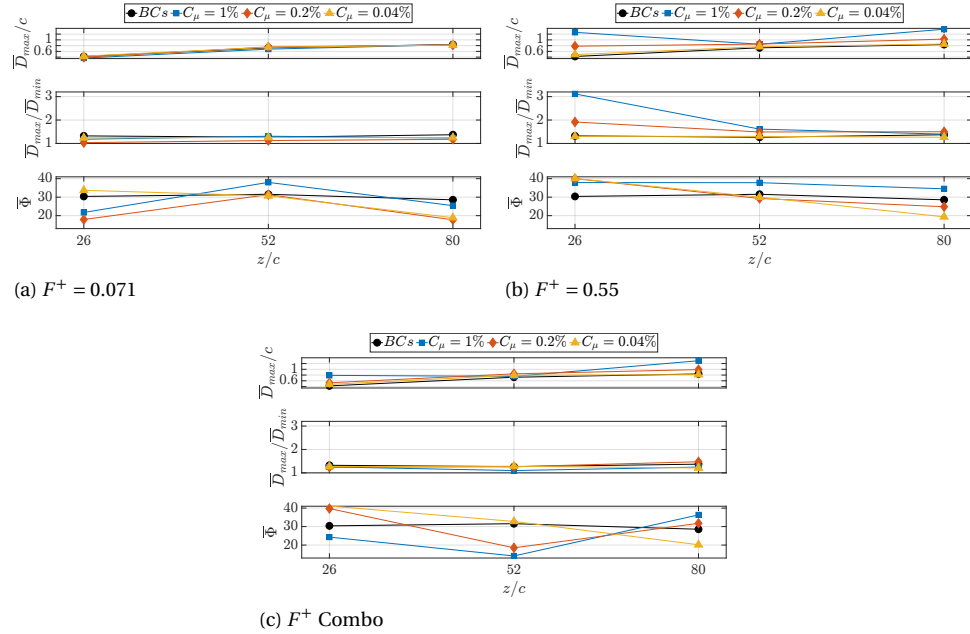


Figure 5.13: Normalized time-averaged vortex major axis, aspect ratio and inclination angle at different momentum coefficient C_μ for all the measurement planes for the wing model Ss01.

strictly related to the circumferential velocity profiles.

Under the synthetic jet actuation, the peak value of the normalized circumferential velocity is prominently reduced at $z/c = 26$, where a maximum decrease of about 72%, 66%, and 73% are found for the wing model Ss04 at $F^+ = 0.071$, $F^+ = 0.55$, and their combination respectively. At this downstream distance, a second peak around at the mid-span of the wing is present, as expected by the lifting-line theory Anderson, 2007. This means that the wingtip vortices are far enough from each other to start a strong interaction. Going downstream at $z/c = 52$, a flat profile is recorded in between the two vortices and at $z/c = 80$ the negative peaks of the two vortices are joined together. The latter characteristics are representative of the vortices linking and overlap, which is preliminary of an immediate start of vortices decay. As it can be noted from Figure 5.15b and 5.15c, the effectiveness of the SJ actuation is less pronounced, with a maximum normalized circumferential velocity decrease of about 50%, 46%, and 45% at $z/c = 52$, 28%, 30%, and 50% at $z/c = 80$, for the actuation $F^+ = 0.071$, $F^+ = 0.55$, and their combination respectively, which are referred again to the wing model Ss04. By considering the average between the left and the right vortex, for each measurement plane has been demonstrated that increasing the SJ exit section area from the wing model Ss01 to Ss04 leads to a better performance, which is in agreement with the previous results on the stream-wise vorticity fields. Furthermore, the Ss04 configuration outperforms all the other one at each actuation frequency, meaning that a SJ device for active control of the circumferential velocity should be designed by maximizing the SJ exit section area. Contrary

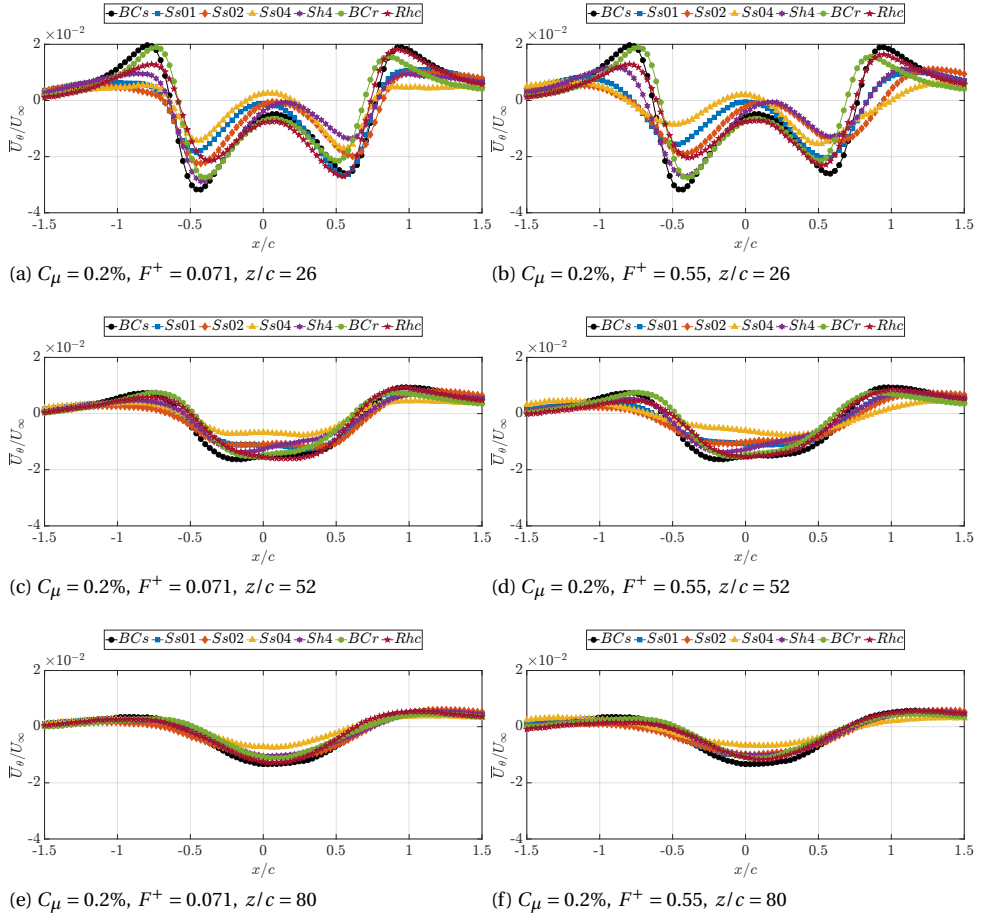


Figure 5.14: Time-averaged radial distribution of the normalized circumferential velocity at $C_\mu = 0.2\%$ for all the measurement planes.

to the statements of the previous section 5.2.1 and according to the metric of $\overline{U}_\theta/U_\infty$, it appears that using a rectangular slot instead of four circular nozzle promotes a larger effectiveness. On the other hand, the use of Rhc, and thus blowing in the chordwise direction inclined of 5° with respect to the streamwise one, revealed to be the less effective configuration although it generates a not negligible $\overline{U}_\theta/U_\infty$ reduction up to 20%. Lastly, from Figure 5.14, it is hard to identify the best SJ actuation frequency, since the effects of F^+ seems to be leveled and comparable, although the $F^+ = 0.55$ tuned to the Widnall instability frequency outperforms the lower $F^+ = 0.071$ and the combo F^+ especially at the furthest measurement planes of $z/c = 52$ and $z/c = 80$, which is promising to anticipate the vortex linking.

The normalized circumferential velocity distribution for different momentum coefficient C_μ for each measurement plane and SJ actuation frequency is reported in Figure

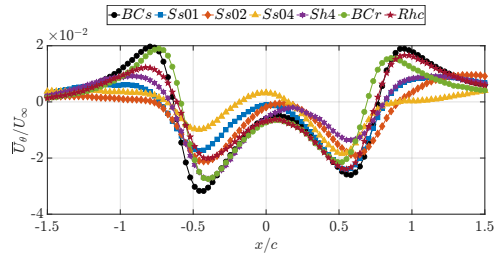
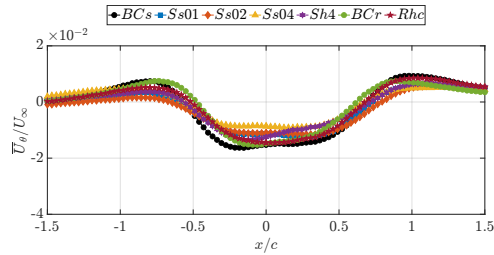
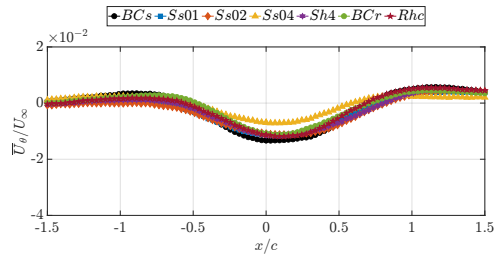
(a) $C_\mu = 0.2\%$, F^+ Combo, $z/c = 26$ (b) $C_\mu = 0.2\%$, F^+ Combo, $z/c = 52$ (c) $C_\mu = 0.2\%$, F^+ Combo, $z/c = 80$

Figure 5.15: Time-averaged radial distribution of the normalized circumferential velocity at $C_\mu = 0.2\%$ with the F^+ Combo configuration for all the measurement planes.

5.16. For the sake of brevity, only the results related to the wing model Ss01 are shown. As expected from the streamwise vorticity behavior described in section 5.2.1, the effect of the actuation at $C_\mu = 1\%$ is impressive. The wingtip vortices are really weak and largely diffused going downstream, causing a nearly null value of the positive peak at $z/c = 52$ and $z/c = 80$ for the configuration tuned to the Crow instability. As shown in Figure 5.16b and 5.16c, only a small amount of downwash in correspondence of the mid-span region of the wing is present, meaning the possibility to completely avoid any wake-hazard issues. However, the practical problem of implementing this control configuration on a real-scaled wing remains open. Increasing the SJ frequency at $F^+ = 0.55$ for $C_\mu = 1\%$ results in a less effective configuration since a positive distribution of \bar{U}_θ/U_∞ is still present for $x/c > |1|$. The same behavior has been registered for the combo F^+ . By decreasing the momentum coefficient at $C_\mu = 0.04\%$ which corresponds to a SJ exit

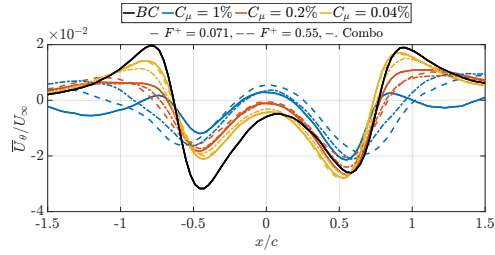
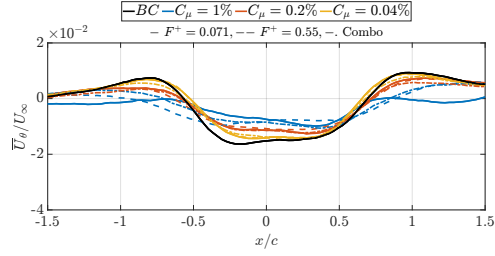
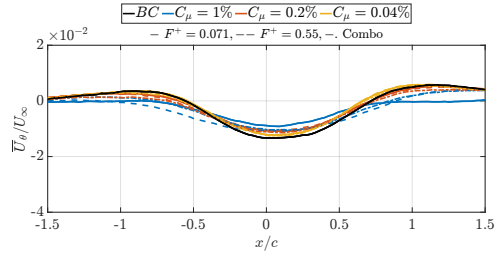
(a) $z/c = 26$ (b) $z/c = 52$ (c) $z/c = 80$

Figure 5.16: Time-averaged radial distribution of the normalized circumferential velocity at different momentum coefficient C_μ for all the measurement planes for the wing model Ss01.

velocity of $U_0 = 0.29U_\infty$, a significant effect is registered only at $z/c = 26$ where a \bar{U}_θ/U_∞ decrease of 19% is present. Going further downstream, this control configuration loses its effectiveness and the BCs curve is recovered. As it can be noted, the actuation frequency does not show a relevant effects being the plain and the dashed curves perfectly coincident for both momentum coefficient of $C_\mu = 0.2\%$ and $C_\mu = 0.04\%$.

In conclusion, blowing at relatively low SJ velocity ($C_\mu = 0.04\%$) revealed to be not effective in the very far-wake of the wing, while the highest momentum coefficient $C_\mu = 1\%$ is not feasible from a realistic point of view although its effect is astonishing. As a matter, the intermediate $C_\mu = 0.2\%$ represents a good compromise for future investigations and design of more appropriate and optimized SJ devices.

5.2.3. CIRCULATION

THE last metric for the far-field investigation is represented by the time-averaged circulation around the wingtip vortices. It has been evaluated by integrating the vorticity fields as explained in section 4.3.3 and the results referred to the intermediate momentum coefficient $C_\mu = 0.2\%$ are shown in Figure 5.17. Under the synthetic jet actua-

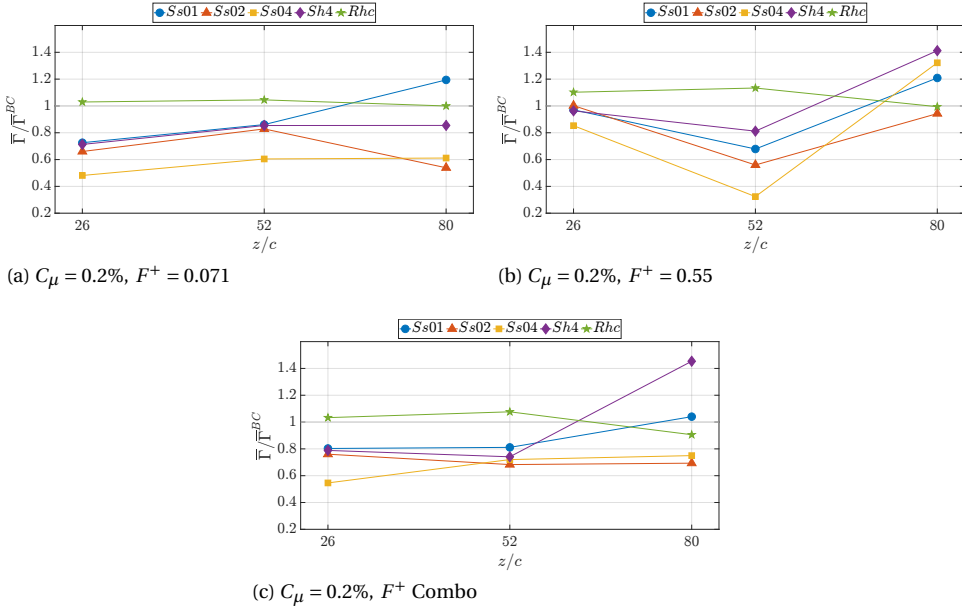


Figure 5.17: Normalized time-averaged vortex circulation at $C_\mu = 0.2\%$ for all the measurement planes. The BCs and BCr values of $\bar{\Gamma}^{BC}/cU_\infty$ are equal to 0.0282 and 0.0240, 0.0220 and 0.0195, 0.0117 and 0.0104 at $z/c = 26, 52, 80$ respectively.

tion at $F^+ = 0.071$, a huge reduction of about 52% of the normalized vortices circulation is obtained for the wing model Ss04 at $z/c = 26$ in correspondence with the maximum vorticity field weakening. Increasing the downstream distance, this configuration with low SJ velocity (i.e. maximum SJ exit section area) outperforms the other ones although the $\bar{\Gamma}/\bar{\Gamma}^{BC}$ increases to 0.59. This result is in contrast with the findings of the near-wake investigation where the best performance are registered for the model with the highest SJ velocity at the same momentum coefficient $C_\mu = 0.2\%$. However, decreasing the SJ exit section area with the models Ss02 and Ss01, the time-averaged circulation remains deeply affected and below the baseline reference value with the only outlier at $z/c = 80$ for Ss01 where the $\bar{\Gamma}/\bar{\Gamma}^{BC}$ is equal to 1.2 which was surprising. Actually, this behavior has been found also for the control configurations at higher $F^+ = 0.55$ and the combo F^+ as reported in Figure 5.17b and 5.18c. As expected from the streamwise vorticity results of section 5.2.1, the maximum SJ effectiveness is achieved at $z/c = 52$ and $z/c = 26$ where the vortices circulation is reduced up to 68% and 45% respectively. Nevertheless, a clear increasing circulation trend is identified for each configuration going further down-

stream at $z/c = 80$ where it turns out to be higher than the BC value up to 40%. By recalling the Eq. (1.15) and (1.18), an increase of $\bar{\Gamma}/\bar{\Gamma}^{BC} > 1$ can be beneficial also since the instability growth rate of the wingtip vortices is directly proportional to the circulation. Since this behavior is registered at the furthest downstream distance of $z/c = 80$, this is promising to accelerate the vortex decay which, as already stated, is already started. It is also possible to notice from Figure 5.17 that blowing in the chordwise direction with the wing model Rhc could be an interesting SJ configuration according to this metric, since the vortices circulation results to be larger than the baseline for each actuation frequency and measurement planes investigated.

The results of the normalized vortices circulation for different momentum coefficient C_μ are reported in Figure 5.18. With the exception of furthest measurement plane at

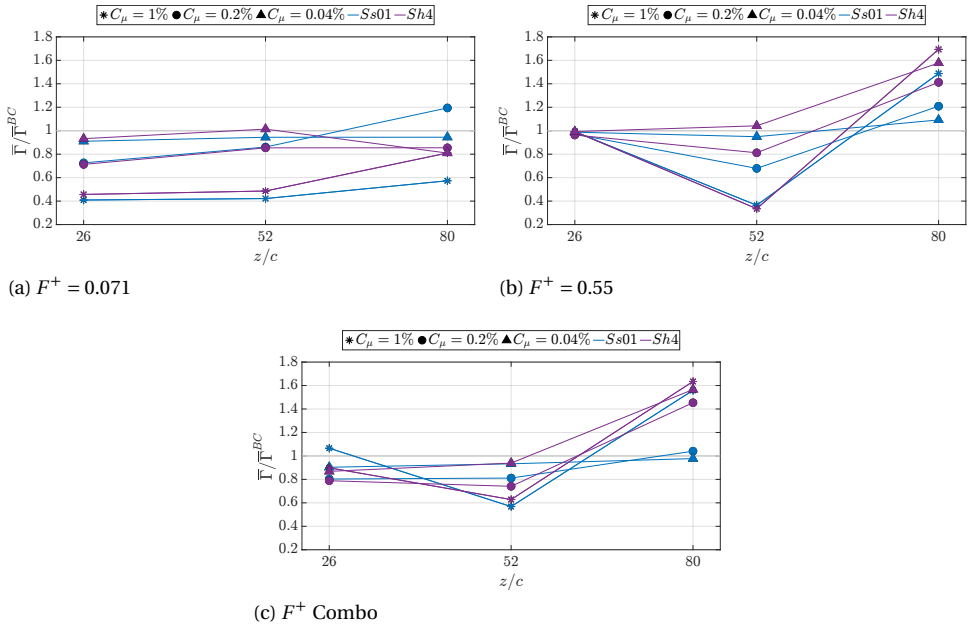


Figure 5.18: Normalized time-averaged vortex circulation at different momentum coefficient C_μ for all the measurement planes for the wing model Ss01 and Sh4. The BCs values of $\bar{\Gamma}^{BC}/cU_\infty$ are equal to 0.0282, 0.0220, and 0.0117 at $z/c = 26, 52, 80$ respectively.

$z/c = 80$ at $F^+ = 0.071$, there is no significant difference between the two exit section geometries of a rectangular slot and four circular nozzle since the results are reasonably comparable. With the SJ actuation tuned to the Crow instability frequency, blowing at high momentum coefficient $C_\mu = 1\%$ allows one to achieve the best performance with a normalized vortices circulation reduction of about 56% at $z/c = 26$. It is noteworthy that, at the same measurement plane, the same circulation decrease has been obtained with the model Ss04 and a value of $C_\mu = 0.2\%$, but with a SJ characteristic velocity 78% lower. The same result has been obtained at the higher $F^+ = 0.55$, where a maximum reduction of 67% is reported at $z/c = 52$ for $C_\mu = 1\%$ which is the same reported in Figure

5.17b. It has also been found that the momentum coefficient does not change the trend of increasing the vortices circulation going downstream at $z/c = 80$ under the actuation at $F^+ = 0.55$, which means the crucial parameter is represented by the actuation frequency. Blowing with a combination of the Crow and Widnall instability frequencies (Figure 5.18c), leads to a maximum reduction of vortices circulation of about 40% at $z/c = 52$ for the higher momentum coefficient $C_\mu = 1\%$. This combined actuation represents a good compromise especially at $z/c = 26$ where the circulation is reduced up to 20% contrary to the Widnall tuned configuration ($F^+ = 0.55$) for which the BCs value is recovered at this downstream distance. As expected, going downstream at $z/c = 80$ the vortices circulation increases as found for the control cases at $F^+ = 0.071$ and $F^+ = 0.55$, being the combined actuation a sort of intermediate configuration between them. Furthermore, it is evident from Figure 5.18 that blowing with a very low SJ exit velocity and through a low exit section area as well is not an useful device in altering the vortices circulation. Finally, a conclusion can be drawn. Based on the results obtained herein, it is expected that increasing both the momentum coefficient and the SJ exit section area could represent the most effective configuration at the actuation frequency tuned to the Widnall instability.

6

PHASE-AVERAGED RESULTS

THE phase-locked measurement results of the wingtip vortices are discussed in details in the present chapter in order to analyze the dynamics of the SJ actuation effectiveness on the vortices evolution from the near to the far field state. It is important to recall that the disturbance generated by the SJ has been assumed to propagate downstream at the free-stream velocity in the convective time $\tau = 3c/U_\infty$. As already pointed out for the phase-averaged analysis of the previous tests presented in section 3.2.2, the phase $\phi = 0^\circ$ corresponds to the beginning of the blowing phase of the SJ. In the following, the symbol $\langle \cdot \rangle$ represents a phase-averaged value.

6.1. NEAR-FIELD ANALYSIS

As already presented in section 5.1 for the time-averaged discussion, the phase-evolution of the physical and geometrical characteristics of the vortices such as the streamwise vorticity, vortex position, circumferential velocity, and vortex circulation are analyzed in the near-field at $z/c = 0.1, 0.5, 1,$ and $2,$ and they are presented hereinafter.

6.1.1. STREAMWISE VORTICITY AND GEOMETRICAL FEATURES

As already pointed out in the time-averaged analysis, the characteristics of the vorticity fields represent a key parameters to evaluate the synthetic jet effectiveness on wingtip vortex control. The phase-evolution of the normalized streamwise vorticity peak is reported in Figure 6.1 for each control configuration investigated at different downstream positions. It is important to recall that the synthetic jet is generated from a sinusoidal signal input to the loudspeaker and the exit velocity exhibits the same wave-shape. As such, at both actuation frequencies, the vorticity peak presents a sinusoidal behavior too, suggesting a strict correlation between the SJ phases and its effect on the wingtip vortices as already found in the feasibility test shown in section 3.2.2. When the SJ is tuned to the Crow instability frequency at low $F^+ = 0.071$ (Figure 6.1a, 6.1c, 6.1e, 6.1g), it is evident that the SJ is largely impactful during the blowing phase, with the only

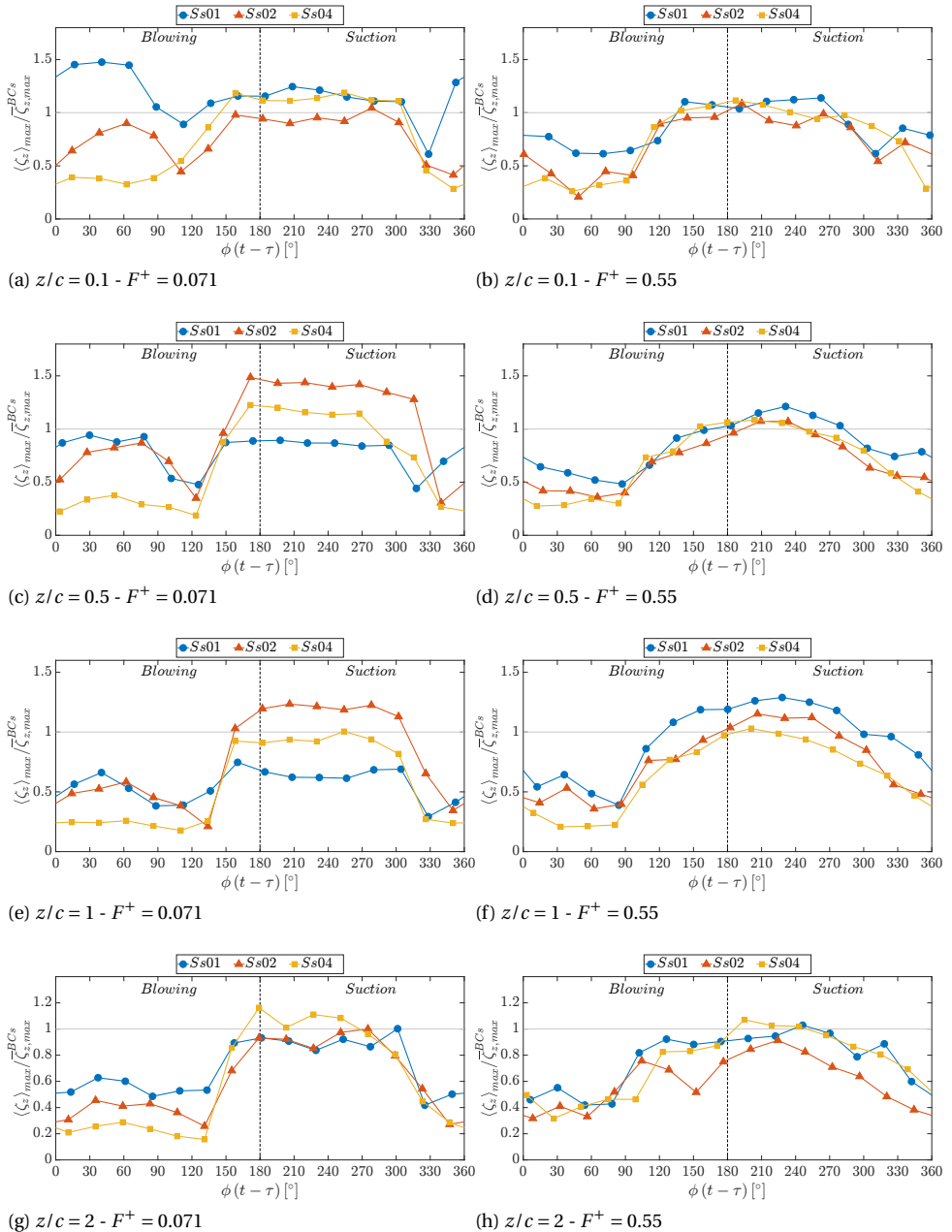


Figure 6.1: Normalized phase-averaged streamwise vorticity peak at different downstream positions for all the configuration investigated. The time-averaged BCs values of $\bar{\zeta}_{z,max}^{BCs} c/U_\infty$ are equal to 10.5, 8.31, 8.26, 5.34 at $z/c = 0.1, 0.5, 1, 2$ respectively.

exception represented by the wing model Ss01 at $z/c = 0.1$. In this case, the jet vortex has its maximum strength and the wingtip core vorticity is increased, being the two vortices overlapped and co-rotating. This effect is weakened going downstream, since the vorticity peak results to be less than the baseline value up to 50% at $z/c = 2$. On the contrary, the suction phase of the SJ actuation has an opposite behavior with respect to the blowing phase, being the streamwise vorticity higher than the BC value especially at $z/c = 0.1$ and $z/c = 0.5$ with a maximum increase of about 20% and 40% for the wing model Ss01 and Ss02 respectively. As it will be shown later in this section, the wingtip vortices are pushed outward during the SJ blowing phase and they move back on the suction phase. As a result, the low pressure side is increased, and the vortices interact more with the shear-layer leaving the trailing edge which could cause the vorticity enhancement. However, it is possible to note that at each downstream location of the measurement plane, increasing the SJ exit section area from the wing model Ss01 to a 4 times higher value of the wing model Ss04 leads to an even better performance in terms of streamwise vorticity peak reduction with respect to the baseline configuration from 40% to 80% at $z/c = 2$. In particular, the wing model Ss04 with the higher SJ exit section area (i.e lower SJ exit velocity) outperforms the others with a streamwise vorticity peak reduction up of at least 60% during the SJ blowing phase at each downstream distance, which is promising. As a result, it is possible to state that blowing through a large area allows the jets to interact more with the wingtip vortices resulting in a better performance of the synthetic jet active control. Actually, this behavior is confirmed in Figure 6.1b, 6.1d, 6.1f, and 6.1h where the normalized streamwise vorticity peak of the SJ configurations tuned to the Widnall instability frequency ($F^+ = 0.55$) are reported. Here, the sinusoidal phase-evolution is more evident, with a more efficiency during the SJ blowing phase with a maximum peak reduction around 80% for the wing model Ss04 as in the previous configurations. As a matter, during the SJ suction phase the streamwise vorticity peak recovers the baseline value or it is slightly higher up to 30% for the wing model Ss01 at $z/c = 1$, confirming the time-averaged results for which the maximum SJ effectiveness on wingtip vortices control is achieved by blowing at high actuation frequency according the vorticity strength metric.

In order to have a better and visual understanding of the SJ actuation effectiveness, the phase-averaged contours of the normalized streamwise vorticity $\langle \zeta \rangle c/U_\infty$ are reported in Figure 6.2 and 6.3 for the control configurations at $F^+ = 0.071$ and $F^+ = 0.55$ for the model Ss01 and Ss04 respectively at $z/c = 0.1$. The horizontal dashed black line represents the wing trailing edge projection on the measurement plane. Since in Figure 6.1 it is possible to notice different phases in which the behavior of the streamwise vorticity peak is very similar, for the sake of clarity, only half of the phase-averaged contour maps are presented. At the lower actuation frequency $F^+ = 0.071$, the vortex appears reinforced and overlapped to the jet vortex during the first part of the SJ blowing phase, then it loses its strength during the SJ suction phase being very close to the baseline configuration. The vortex shape is almost circular and it is diffused over a larger area in correspondence of the SJ maximum blowing with respect to SJ suction phase where the SJ seems to be less effective since the baseline characteristics are restored. This is confirmed in Figure 6.4 where the geometrical characteristics of the vortex are reported for all the configurations investigated at $F^+ = 0.071$. Since the baseline configuration

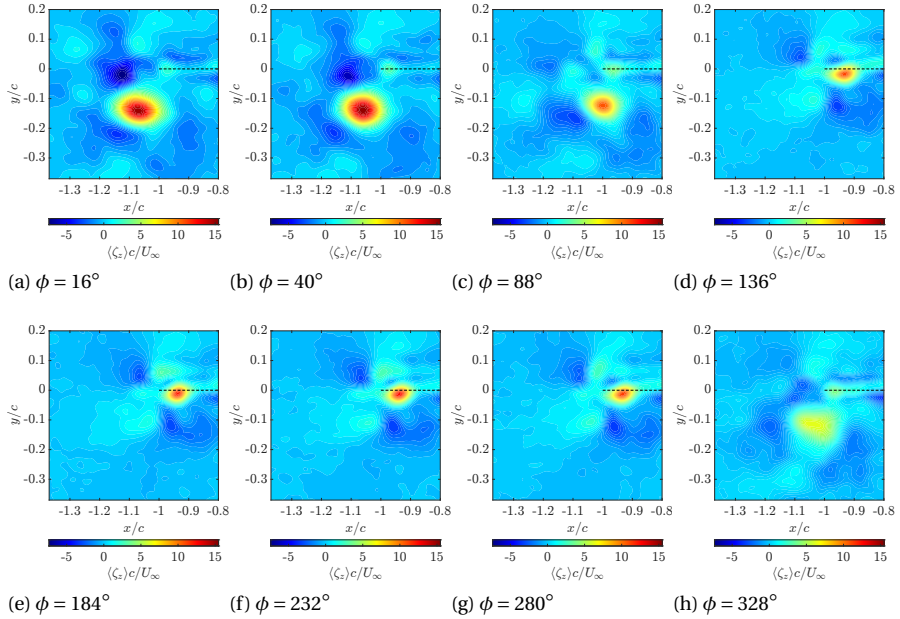


Figure 6.2: Normalized phase-averaged streamwise vorticity fields at $z/c = 0.1$ for the wing model Ss01 at $F^+ = 0.071$.

can not be analyzed in a phase-averaged approach, only the time-averaged value is reported for comparison. The synthetic jet impact on altering the vortex size is evident during the blowing phase, while a flat behavior close to the baseline value is registered for the suction phase. The vortex diffusion due to the SJ actuation is revealed for each wing configuration with a maximum increase in vortex diameter more than three times of the BC value for the Ss04 as expected, since the streamwise vorticity peak has its minimum in this configuration, meaning that the vortex is spread over a wide area. On the other hand, the actuation causes a slight reduction of the vortex aspect ratio in almost each phase and wing configuration being the vortex far from a clear ellipsoidal shape. A more sinusoidal evolution is achieved for the vortex inclination angle evolution, where is still confirmed that the vortex is rotated due to the SJ actuation only during the blowing phase. However, the effect of an increasing SJ exit section area is visible also from the geometrical features, being the wingtip vortex more diffused and stretched by decreasing the SJ exit velocity from the wing model Ss01 to Ss04 (blue to yellow curves in Figure 6.4). Finally, from Figure 6.2 is possible to notice that a further effect of the synthetic jet control is represented by the movement of the vortex from the baseline position which is located in correspondence of the wing trailing edge projection and about $0.07c$ inboard. The phase-evolution of the vortex centroids during the actuation is shown in Figure 6.5. The black dashed line is again the projection of the trailing edge of the wing. It is possible to notice in Figure 6.5a that the synthetic jet actuation causes a periodic motion of the vortex at the Crow instability frequency configuration, moving the vortex about $0.14c$

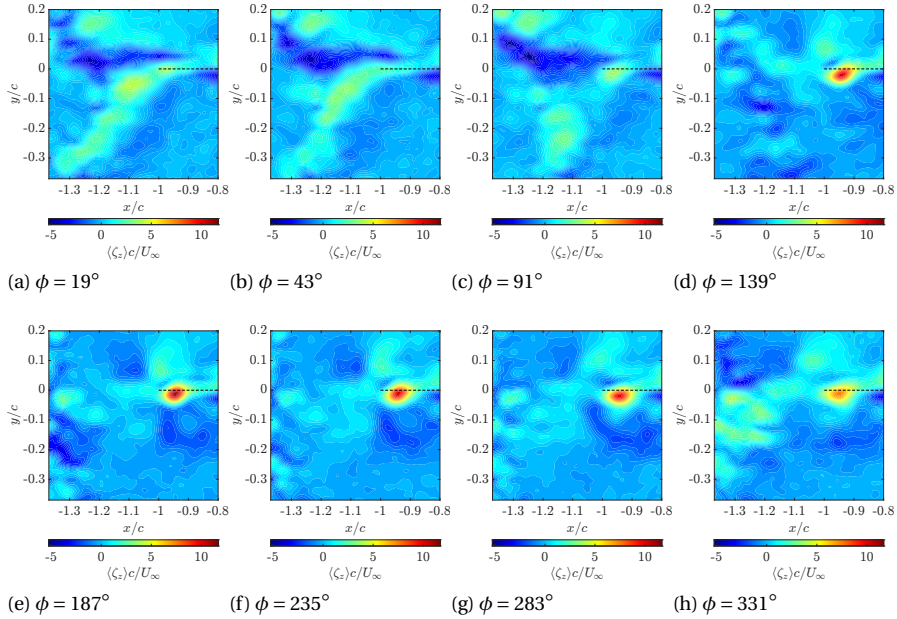


Figure 6.3: Normalized phase-averaged streamwise vorticity fields at $z/c = 0.1$ for the wing model Ss04 at $F^+ = 0.55$.

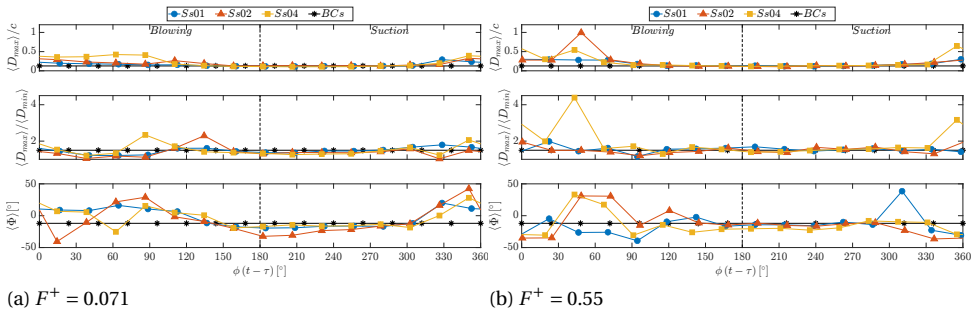


Figure 6.4: Normalized phase-averaged vortex major axis, aspect ratio, and inclination angle at $z/c = 0.1$ positions for all the configuration investigated.

both outboard and downward. In particular, the motion turns out to be concentrated along a direction inclined of 45° represented as plain gray line, which could promote the Crow instability as shown in Figure 1.8. The same periodic behavior is obtained also for the tuned configuration at the Widnall instability frequency for the wing model Ss04 as reported in Figure 6.5b. At higher F^+ , the vortex is pushed more outward up to $0.24c$ and $0.1c$ downward, being the motion direction less inclined with respect to the previous case. This is clearly visible from the streamwise contour maps shown in Figure 6.3. As

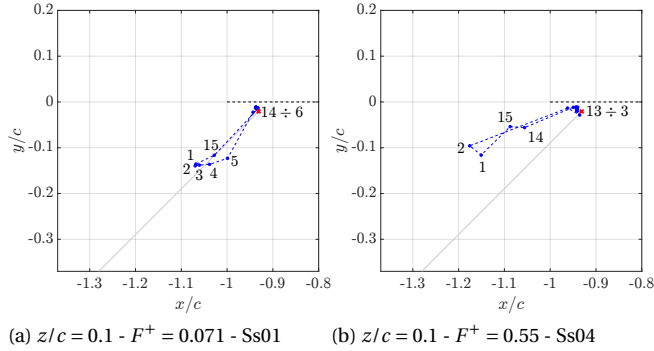


Figure 6.5: Phase-averaged vortex center position at $z/c = 0.1$ for the wing model Ss01 and Ss04 at $F^+ = 0.071$ and $F^+ = 0.55$. The time-averaged BC position is marked with a red cross, while the gray line represent the 45° direction.

already stated, the impact of the control configuration Ss04 at high actuation frequency is striking on reducing the wingtip vortex strength. In fact, during the SJ blowing phase, the vortex starts to lose its coherence being largely diffused with a very low value of the vorticity peak. The vortex diameter is increased up to 4 times the baseline value and it is highly stretched as reported in Figure 6.4b, which could cause a premature dissipation. However, the SJ is confirmed to be less effective during the suction phase also for the configuration at high actuation frequency, since the vortex recovers the vorticity distribution, the geometrical characteristics, and the position of the BC reference case.

Going downstream at $z/c = 0.5$, the vorticity field contours reported in Figure 6.6 for the wing model Ss01 at $F^+ = 0.071$ confirms the phase-evolution started at the previous station. In fact, the vortex assumes a more circular shape with a minimum intensity in correspondence of the maximum SJ blowing velocity and in the last part of suction phase. As reported in Figure 6.8, the vortex increases his major diameter of 20% with respect to the $z/c = 0.1$ measurement plane, while the vortex aspect ratio starts to be higher than the baseline value, but still very close to unity. However, the synthetic jet effectiveness is demonstrated only in the SJ blowing phase also in terms of the vortex position evolution (Figure 6.9) reaching a maximum displacement of about $0.15c$ both outboard and downward along a 45° direction, confirming the possibility of an early trigger of the Crow instability.

Blowing at higher actuation frequency, the synthetic jet penetrates more in the wingtip vortex leading to a very weak vorticity distribution in the first part of the blowing period as shown in the contour maps in Figure 6.7. The vortex continues losing his coherence due to the largely distributed turbulence injected through the high SJ exit section (Ss04) and it is barely recognizable. Both the vortex diameter and his aspect ratio are more than doubled with respect to the BC value with a peak value in correspondence of the maximum blowing velocity of the synthetic jet (Figure 6.8b). Differently to the previous case, the tuned configuration to the Widnall instability causes a larger displacement of the vortex up to $0.4c$ outboard and $0.22c$ downward parallel to a 45° direction contrary to the previous station. On the other hand, the vorticity fields and the vortex features revealed

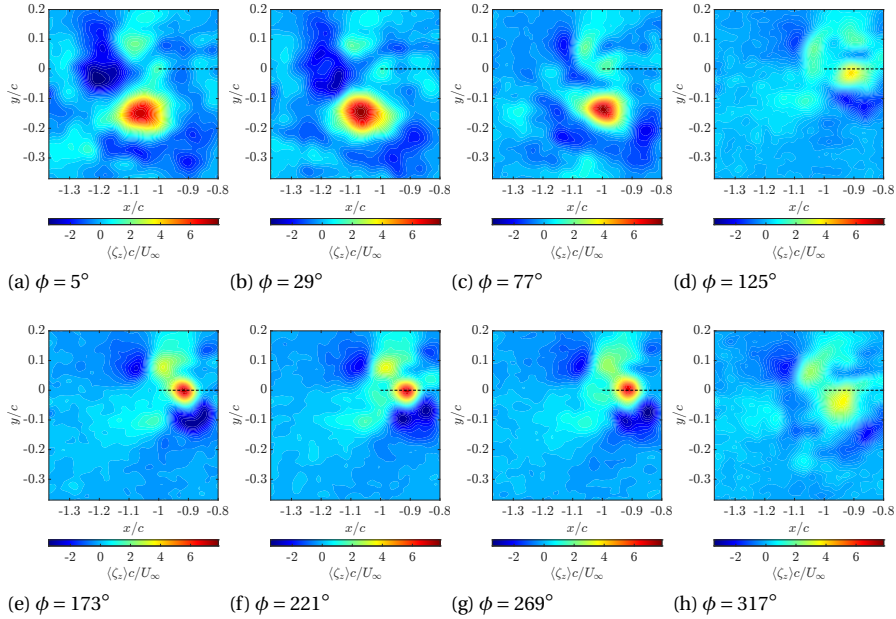


Figure 6.6: Normalized phase-averaged streamwise vorticity fields at $z/c = 0.5$ for the wing model Ss01 at $F^+ = 0.071$.

to be very similar to the baseline configuration during the suction phase, confirming the effectiveness reduction of the synthetic jet. Finally, from the geometrical characteristics reported in Figure 6.8, it is worth underlining that blowing with a low SJ velocity through a larger exit section area leads to a more effective device, causing a considerable diffusion of the vortex more than two times the value of the model with the lowest SJ area, corresponding also to a noticeable vorticity strength reduction.

For the sake of brevity, the phase-averaged vorticity results related to the downstream measurement plane at $z/c = 1$ are not reported herein, since the vortex features are very close to the normalized vorticity contour maps at $z/c = 2$ shown in Figure 6.10 and 6.11 for the wing model Ss01 and Ss04 at $F^+ = 0.071$ and $F^+ = 0.55$ respectively. Under the first control configuration, the wingtip vortex is noticeably weakened during the synthetic jet blowing phase with respect to the same period at $z/c = 0.1$, and it is distributed over a wide area. During the suction phase, the vortex moves back around the baseline position which is located above the wing trailing edge projection due to the upwash induced by the couple of wingtip vortices generated with the negative lift of the wing. In particular, the baseline vorticity field is recovered also in this case and the presence of the jet vortex is clearly discernible from Figure 6.10d ÷ 6.10g. On the other hand, the synthetic jet configuration of the wing model Ss04 at higher $F^+ = 0.55$ is demonstrated to be strongly effective as shown in the normalized vorticity fields reported in Figure 6.11. In correspondence to the maximum blowing state of the synthetic jet, the wingtip vortex appears divided in different weak sub-vortices which then merge together during

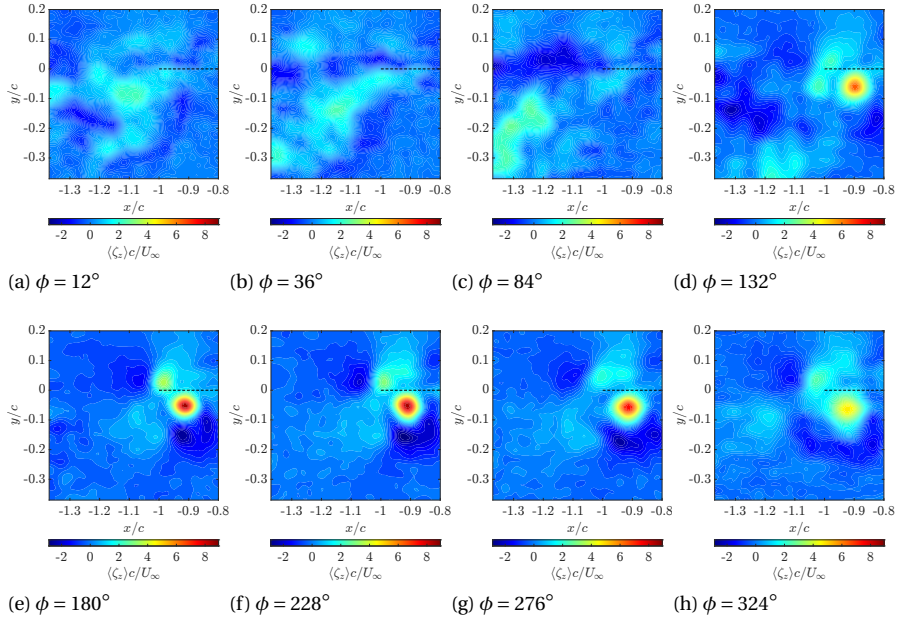
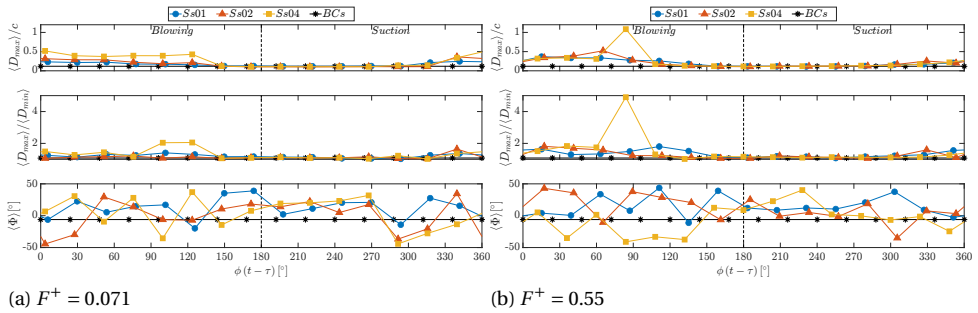


Figure 6.7: Normalized phase-averaged streamwise vorticity fields at $z/c = 0.5$ for the wing model Ss04 at $F^+ = 0.55$.



(a) $F^+ = 0.071$

(b) $F^+ = 0.55$

Figure 6.8: Normalized phase-averaged vortex major axis, aspect ratio, and inclination angle at $z/c = 0.5$ positions for all the configuration investigated.

the suction phase where a clearly coherent structure is visible. The geometrical characteristics of each tested control case at $z/c = 2$ are reported in Figure 6.12. As already discussed for the previous downstream results, the synthetic jet effectiveness appears to be concentrated on its blowing phase. The lower actuation frequency at $F^+ = 0.071$ causes a very large diffusion of the vortex which increases by decreasing the synthetic jet exit velocity from the wing model Ss01 to Ss04. The maximum value of the vortex major diameter is registered for the Ss04 configuration in correspondence to the SJ velocity

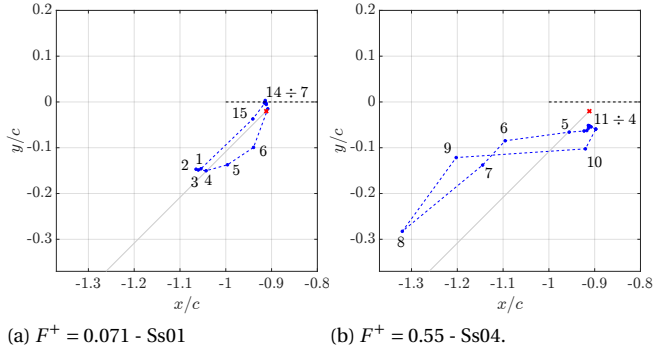


Figure 6.9: Phase-averaged vortex center position at $z/c = 0.5$ for the wing model Ss01 and Ss04 at $F^+ = 0.071$ and $F^+ = 0.55$. The time-averaged BC position is marked with a red cross, while the gray line represent the 45° direction.

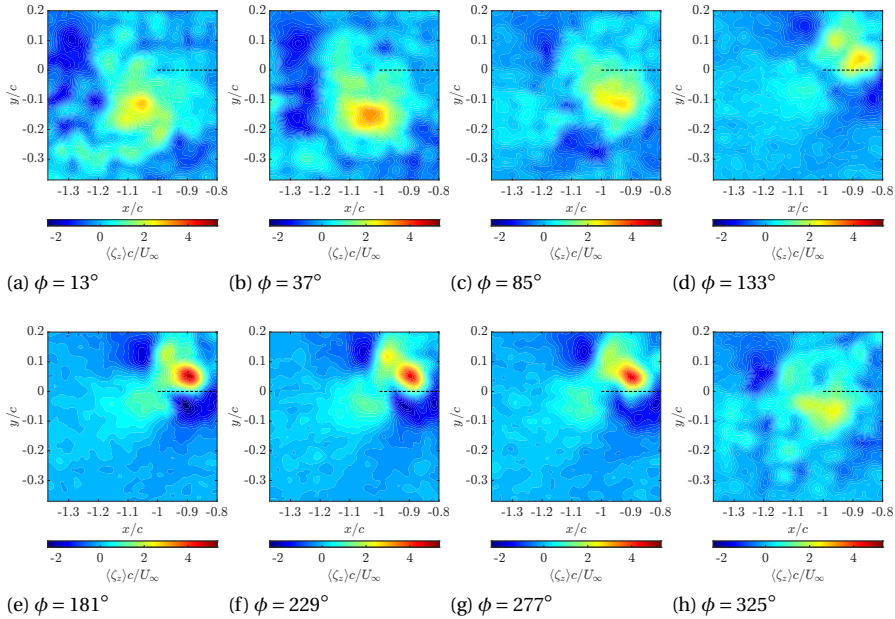


Figure 6.10: Normalized phase-averaged streamwise vorticity fields at $z/c = 2$ for the wing model Ss01 at $F^+ = 0.071$.

peak and it is equal to 5 times the baseline case, together with a double value of the vortex aspect ratio. By increasing the actuation frequency, none of the configurations clearly outperforms the other and no particular trend could be easily identified. However, the vortex diameter is increased only of 2.8 times the BC value, leading to a minor diffusion with respect to the tuned Crow instability configuration which is in line with the

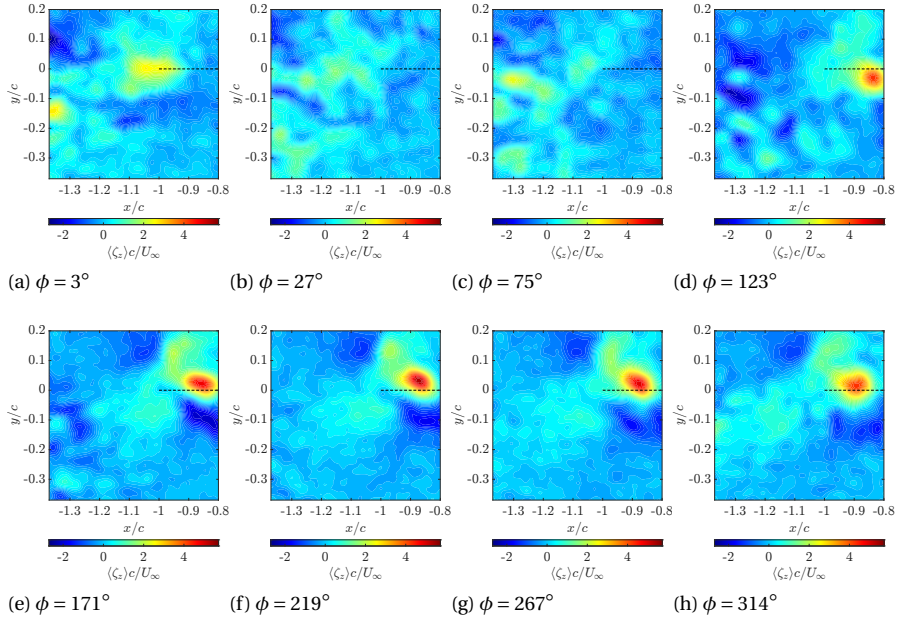


Figure 6.11: Normalized phase-averaged streamwise vorticity fields at $z/c = 2$ for the wing model Ss04 at $F^+ = 0.55$.

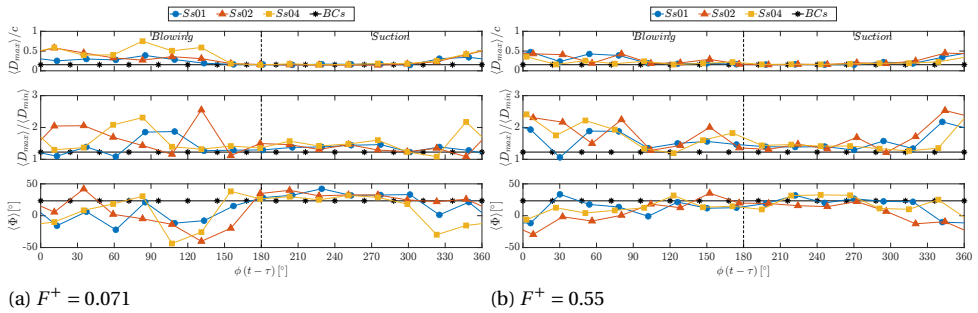


Figure 6.12: Normalized phase-averaged vortex major axis, aspect ratio, and inclination angle at $z/c = 2$ for all the configuration investigated.

findings of Figure 6.1 where the streamwise vorticity slightly increases with the higher actuation frequency. Lastly, in order to assess the variation of the vortex positions, a plot of the phase-evolution of the vortex centroids is reported in Figure 6.13. Due to the upwash caused by the mutual induction of the couple of wingtip vortices generated by the finite wing, the majority of the phase-average positions are located above the wing trailing edge projection and they correspond to the synthetic jet suction phases. During the blowing phase, it is evident that the vortex is pushed downward and outboard of about

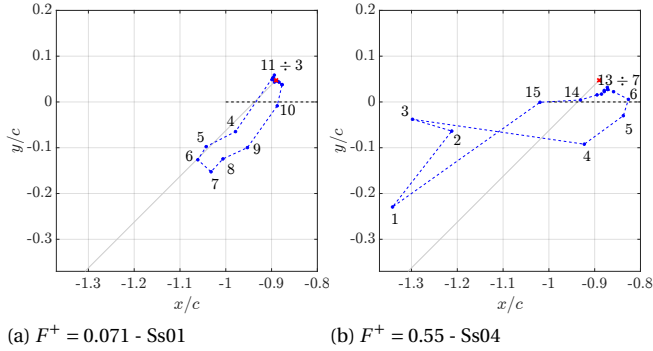


Figure 6.13: Phase-averaged vortex center position at $z/c = 2$ for the wing model Ss01 and Ss04 at $F^+ = 0.071$ and $F^+ = 0.55$. The time-averaged BC position is marked with a red cross, while the gray line represent the 45° direction.

$0.2c$ and $0.55c$ for the configuration of Ss01 at $F^+ = 0.071$ and Ss04 at $F^+ = 0.55$ respectively. The periodic motion already found at the nearer measurement planes discussed before is confirmed at $z/c = 2$. In particular, it can be noticed that going downstream the vortex displacement increases especially by blowing at the Widnall instability frequency. This is an encouraging result, since the inherent instability of the wingtip vortices seems to be amplified by means of the synthetic actuation and this could lead to a premature vortex linking and their dissipation, reducing the probability and the danger of a wake-hazard encounter.

Finally, a conclusion can be drawn. According to the streamwise vorticity metric and the analysis of the geometrical characteristics of the wingtip vortex, the best control configuration is represented by the wing model with the highest synthetic jet exit section area (Ss04) at the higher actuation frequency tuned to the Widnall instability frequency ($F^+ = 0.55$). Moreover, the synthetic jet actuation has been demonstrated to reach the maximum effectiveness only during the blowing phase, while the baseline configuration features are restored during the suction phase. As such, the use of a pulsed jet could be a useful alternative to be investigated, but losing the advantage of a zero-net-mass-flux device, so the problem of harvesting the mass injected remains open.

6.1.2. CIRCUMFERENTIAL VELOCITY

IN order to have a clearer insights on the parameter which regulates the danger of a possible wake-hazard, the phase-locked evolution of the normalized circumferential velocity with respect to the time-averaged baseline value is reported in Figure 6.14 for each control configuration investigated at different downstream distances. Under the SJ actuation at low $F^+ = 0.071$, the sinusoidal evolution found in the preliminary test reported in section 3.2.2 is not registered in any measurement plane. As expected from the phase-averaged results of the vorticity peaks instead, it is possible to notice that the SJ blowing and suction phases have different effects. Starting from the nearest downstream distance at $z/c = 0.1$, the SJ blowing causes a noticeable increase of the circumferential

velocity peak which is even higher as the SJ exit velocity increase from the wing model Ss01 to Ss04. On the other hand, during the suction phase of the synthetic jet, the value of $\langle U_\theta \rangle_{max} / \overline{U_{\theta,max}}^{BCs}$ oscillates around the unity, meaning that baseline configuration is recovered and the SJ is not impactful. By recalling the time-averaged results shown in Figure 5.4a, the same control configuration (Ss01 - $F^+ = 0.071$ - $z/c = 0.1$) presents a reduction of the circumferential velocity peak of about 10%, which is in contrast with the results of Figure 6.14a. This mismatch is related to the noticeable vortex displacement obtained with the actuation shown in Figure 6.5. In particular, the time-average is a classical “Eulerian” average process according to which each spatial point is averaged over the time, while the phase-average process is carried out in a “Lagrangian” way by tracking the vortex behavior. Although the time-averaged results give to the reader an immediate and whole interpretation of the phenomenon and they could be at the base of several numerical simulations, they could be misleading and not enough extensive to draw a general physical conclusion. As a results, in the very near-wake of the wing the use of the synthetic jet actuation control tuned to the Crow instability frequency at high SJ exit velocity is counter-productive in reducing the wake-hazard since the value of $\langle U_\theta \rangle_{max}$ is larger than the baseline case. However, by halving the SJ velocity at the same C_μ and F^+ , a more effective configuration is obtained with a noteworthy reduction of 45% in correspondence of the maximum SJ blowing whilst an increase of only 20% is achieved at the beginning. By fixing the actuation frequency and moving downstream, the wing equipped with the larger SJ exit section area is confirmed to be the best control configuration with a striking reduction of the normalized circumferential velocity peak up to 50%, with each phase being less than unity, which is encouraging in the possibility of reducing the wake vortex hazard by means of the SJ active flow control. The only exception is represented by the last measurement plane at $z/c = 2$, where a slight increase of the $\langle U_\theta \rangle_{max}$ with respect to the BC value is obtained for each wing model which, however, present a comparable behavior.

When the synthetic jet is operated at higher actuation frequency of $F^+ = 0.55$, a remarkable difference with the previous case can be noticed from Figure 6.14b, 6.14d, 6.14f, and 6.14h. At $z/c = 0.1$, the same mismatch with the time-averaged results has been found for the model Ss01, but with a peak value of $\langle U_\theta \rangle_{max} / \overline{U_{\theta,max}}^{BCs}$ 40% less than the case at lower $F^+ = 0.071$. More generally, the higher actuation frequency results in a phase-evolution of the circumferential velocity peak which is below the baseline case basically for the all the configurations investigated, with the only exception for the wing model Ss01 at $z/c = 1$. As it has been stated for the streamwise vorticity metric, the most effective synthetic jet configuration is represented by the wing model equipped with the higher SJ exit section area blowing at the Widnall instability frequency ($F^+ = 0.55$) by which the circumferential velocity peak is entirely reduced with respect to the baseline case up to 50% which is extremely favorable to reduce the wake-hazard.

6.1.3. CIRCULATION

THE last metric for the analysis of the wingtip vortices evolution is represented by the vortex circulation which is the main parameter representative of its strength and it is directly related to the vortex instability growth rate and the main vortex adverse effect as the induced drag (see Eq. (1.8)). The phase-evolution of the normalized cir-

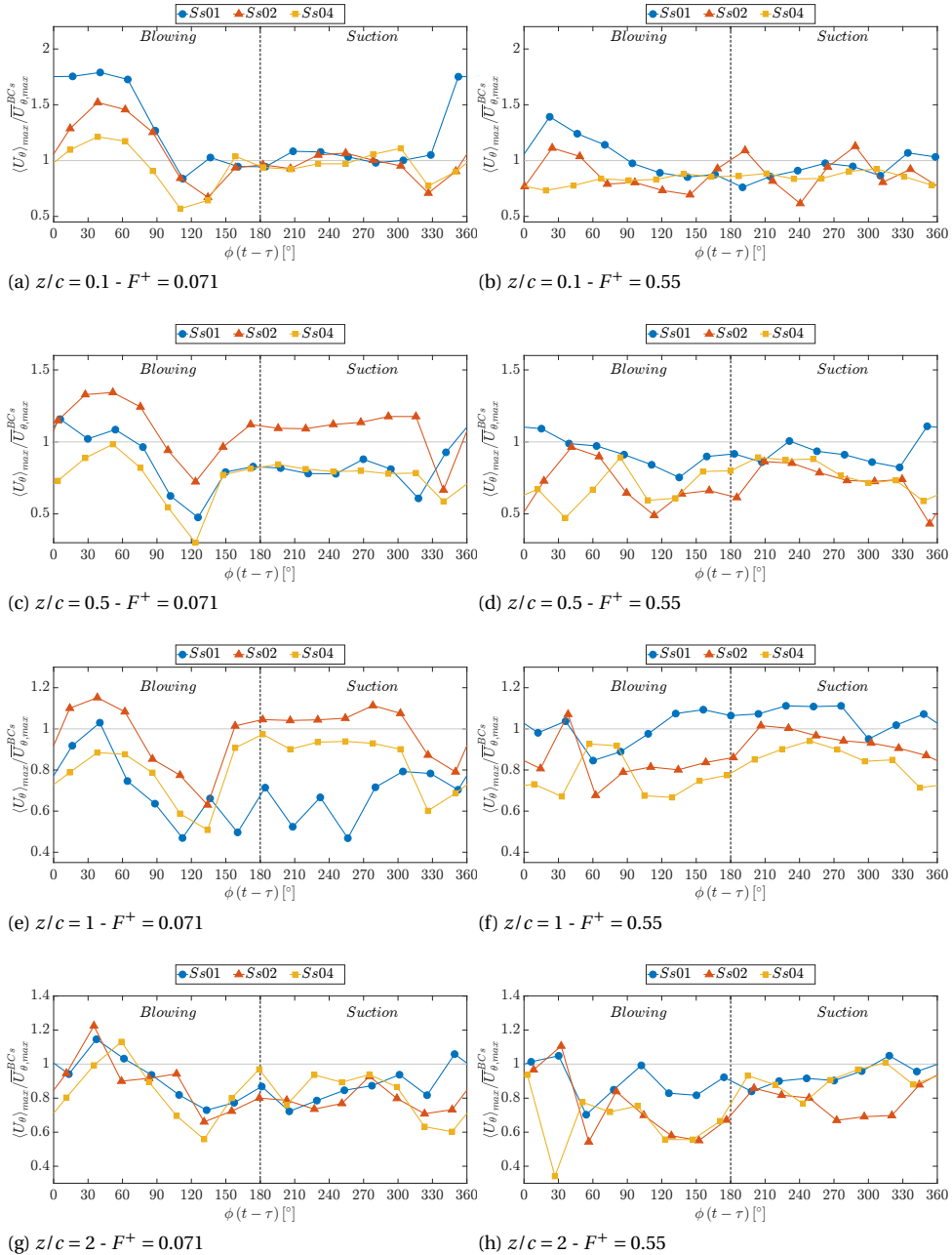


Figure 6.14: Normalized phase-averaged circumferential velocity peak at different downstream positions for all the configuration investigated. The time-averaged BCs values of $\bar{U}_{\theta,max}^{BCs}/U_{\infty}$ are equal to 0.150, 0.142, 0.148, 0.111 at $z/c = 0.1, 0.5, 1, 2$ respectively.

ulation with respect to the baseline case is reported in Figure 6.15 for each actuation configuration investigated at different downstream planes. As already pointed out for the circumferential velocity peak results in the previous section 6.1.2, a mismatch with the time-averaged results presented in Figure 5.6 is present. In fact, according to the latter, the vortex circulation is reduced with respect to the BC for each configuration and downstream distance, meaning that the vortex should be highly weakened and thus the induced drag decreased too, which is beneficial. On the contrary, the phase-averaged evolution revealed a huge increase of the circulation, with a peak value of $\langle \Gamma \rangle$ between 2 and 4.5 time the baseline. As a result, during the SJ blowing phase the circulation increase causes a larger induced downwash, which can be menacing for a small aircraft encountering the wake of an heavy one leading to a possible loss of lift, altitude, and climb rate (Breitsamter, 2011). On the other hand, the higher the vortex circulation, the more amplified the inherent instability growth rate, which coexists with a noteworthy reduction of the streamwise vorticity distribution on a wider area, so an early development of the Crow and Widnall instabilities is achievable. From Figure 6.15, it is possible to notice that the SJ suction phase presents an opposite evolution with respect to the blowing part. One should state that the SJ loses his effectiveness since the circulation is almost constant around the baseline value, but at $z/c = 2$ it is decreased up to 30% for the wing model Ss01 and Ss02 as shown in Figure 6.15g and 6.15h. In particular, this behavior is registered for both the actuation frequencies adopted without any relevant different in the absolute value and trend, meaning that at these downstream distances the frequency dependent disturbances are entrained to the flow but they need a further development to generate different results. Lastly, a compromise needs to be reached. At the lower actuation frequency tuned to the Crow instability, the wing model Ss02 with an intermediate SJ exit section area could allow to achieve higher instability growth rate in the far-field and also a less hazardous vortex going downstream with a reduced circulation in the suction period, while blowing at the Widnall instability with a very low SJ velocity (Ss04) leads to a lower values of $\langle \Gamma \rangle$ which can be more beneficial on average. However, the following far-field evidence is needed to draw a more exhaustive conclusion.

6.2. FAR-FIELD ANALYSIS

IN this section, the phase-locked evolution of the wingtip vortices up to 80 chord lengths downstream of the wing is presented. In addition to the physical and geometrical characteristics analyzed in the near-field investigation (section 5.2), the evolution of the vortices position and their relative distance are reported. Differently from the time-averaged analysis, the results related to the synthetic jet configuration at a combined frequency of the Crow and Widnall instability one is not presented hereinafter since it is not possible to define a proper phase evolution for a signal sum of two different sine waves. Finally, the geometrical and physical characteristics of the vortices reported in the following are the average between the left and right vortex if not different declared.

6.2.1. STREAMWISE VORTICITY AND GEOMETRICAL FEATURES

IN the present section, the phase-evolution far-wake streamwise vorticity fields and the geometrical characteristics of the wingtip vortices as vortex size, shape, positions

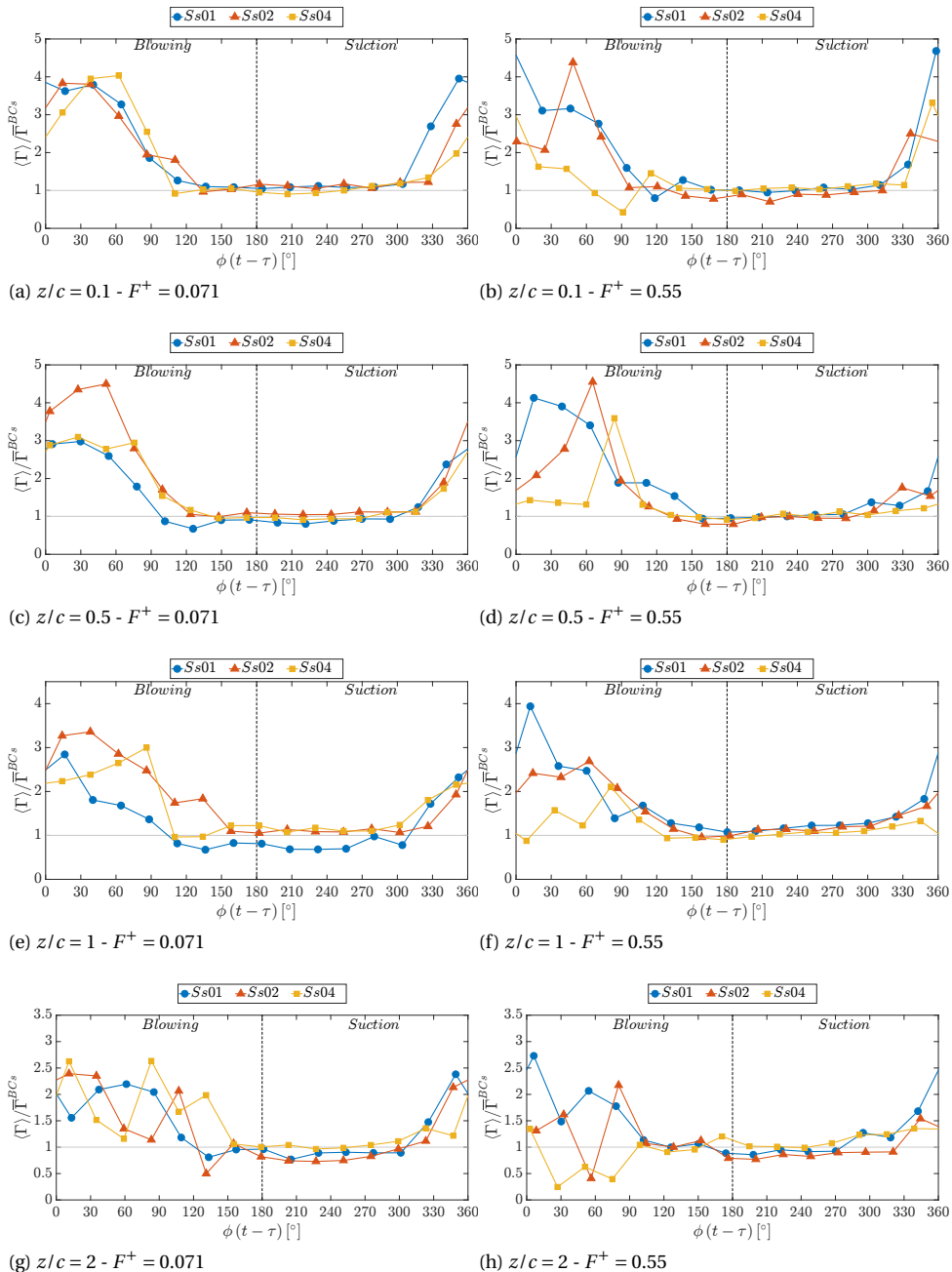


Figure 16.15: Normalized phase-averaged vortex circulation at different downstream positions for all the configuration investigated. The time-averaged BCs values of $\bar{\Gamma}^{BCs}/cU_\infty$ are equal to 0.0443, 0.0424, 0.0433, 0.0404 at $z/c = 0.1, 0.5, 1, 2$ respectively.

and relative distance are analyzed to deeply understand their dynamics under the synthetic jet actuation control. For the sake of brevity, the phase-averaged results related to the measurement plane at $z/c = 52$ are not presented hereinafter since the physical and geometrical features of the wingtip vortices are very close to the ones at $z/c = 26$.

MEASUREMENT PLANE AT $z/c = 26$

THE phase-average development of the normalized streamwise vorticity peak $\langle \zeta_z \rangle_{max} / \bar{\zeta}_{z,max}^{BC}$ for the measurement plane located at $z/c = 26$ downstream of the wing is reported in Figure 6.16 for all the synthetic jet configuration employed at $C_\mu = 0.2\%$.

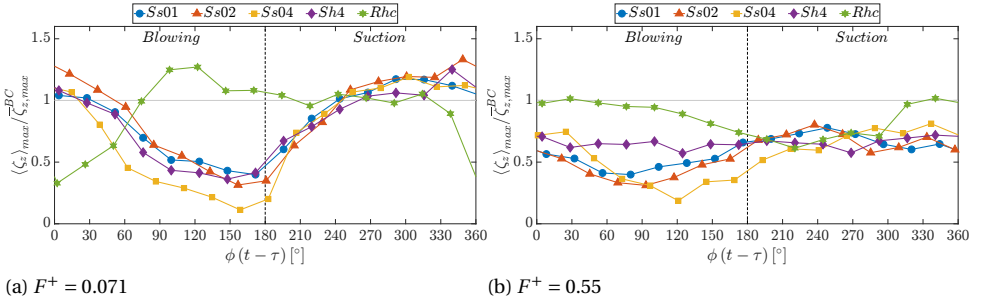


Figure 6.16: Normalized phase-averaged streamwise vorticity peak at $z/c = 26$ for all the configuration investigated at $C_\mu = 0.2\%$. The time-averaged BCs and BCr values of $\bar{\zeta}_{z,max}^{BC} c / U_\infty$ are equal to 0.531 and 0.467 respectively.

As already found out for the near-field investigation, the vorticity peak presents a sinusoidal development over the synthetic jet period at both actuation frequencies, confirming that the sinusoidal disturbances introduced to the flow have been absorbed by the wingtip vortices and convected far downstream. At the lower actuation frequency $F^+ = 0.071$ tuned to the Crow instability, the SJ control reaches the maximum effectiveness during its blowing phase, where a striking reduction from 60% (Ss01) up to about 90% (Ss04) of the streamwise vorticity peak is achieved. On the other hand, the values of $\langle \zeta_z \rangle_{max} / \bar{\zeta}_{z,max}^{BC}$ rise over unity up to 20% for each wing model during the SJ suction phase as observed also for the near-field phase-evolution measurements shown in Figure 6.1. A completely different evolution is registered for the rounded wing model Rhc in which the synthetic jet is blown in the chordwise inclined of 5° with respect to the free-stream direction, which appears to be phase-shifted of about 90° with respect to the other configurations, although a huge vorticity reduction of about 60% is achieved as well, the SJ seems to lose its effectiveness during the suction phases, making this wing model not the preferred device. Moreover, the exit section geometry does not play a crucial role when the SJ is operated at low actuation frequency. In fact, the use of equally spaced circular nozzles (Sh4) or an equivalent rectangular slot (Ss01) is basically analogous with a slight better performance for the former as shown in Figure 6.16a. Lastly, the far-field measurements at $F^+ = 0.071$ confirm that injecting turbulence into the wingtip vortices through a larger SJ exit section area is high-performance, since the

vorticity peak is reduced more and more by reducing the SJ exit velocity from the wing model Ss01, Ss02, and Ss04. Actually, the same trend has been obtained by increasing the SJ frequency to $F^+ = 0.55$ as it can be noted in Figure 6.16b. In fact, the streamwise vorticity peak is hugely reduced of about 60%, 70%, and 80% for the wing configuration Ss01, Ss02, and Ss04 respectively. In particular, the sinusoidal evolution has been obtained also at higher F^+ although it is less pronounced than the previous case in Figure 6.16a. As it has been already found for the near-field measurements at $z/c = 3$ of the preliminary test in Figure 3.6, also in the far-wake the vorticity peak is reduced for each phase over the entire SJ actuation period with a decrease of at least 20% in the SJ suction phases, which is noteworthy. This particular characteristic is verified only by blowing in the spanwise direction. In fact, the rounded wing model Rhc with the SJ directed in the chordwise direction seems to be in phase opposition with respect to the other curves with a maximum vorticity peak decrease of 39% in correspondence of the suction phase of the synthetic jet, while the evolution continues reaching the baseline reference value. As it can be noted in Figure 6.16b, with the SJ tuned to the Widnall instability frequency, blowing through a rectangular slot (Ss01) turns into a more effective device than blowing through a series of four circular equivalent nozzles (Sh4).

In order to better investigate the structure of the wingtip vortices, the phase-averaged normalized streamwise vorticity field contours are reported in Figure 6.17 and 6.19 for the fixed momentum coefficient $C_\mu = 0.2\%$ at $F^+ = 0.071$ and $F^+ = 0.55$ respectively. For the sake of brevity, only the most interesting phases are displayed in correspondence of the maximum synthetic jet effectiveness according to the streamwise vorticity metric for the wing model Ss04 with the maximum SJ exit section area. As for the near-field phase-averaged results in section 6.1, the SJ actuation at $F^+ = 0.071$ causes a displacement of

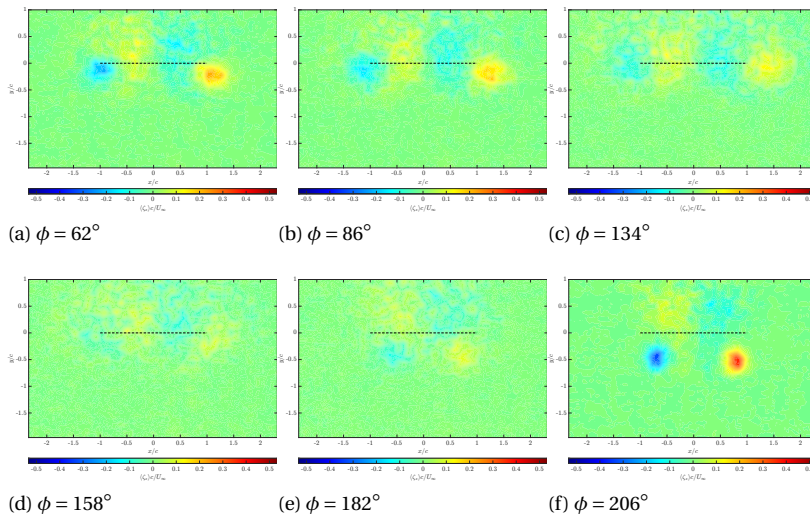


Figure 6.17: Normalized phase-averaged streamwise vorticity fields at $C_\mu = 0.2\%$, for the wing model Ss04 at $F^+ = 0.071$ and $z/c = 26$.

the vortices during the blowing phase. Until the SJ blowing velocity peak is reached (Figure 6.17d), the vorticity of the wingtip vortices appears to be concentrated in two almost circular regions, while two vorticity distribution of opposite sign each other are located in between. These structures can be related to the corner vortices formed at the junction between the wing and the sting support of the model (see Figure 4.7) since they are present in each vorticity field acquired. When the vortices are hugely weakened and pushed outboard and upward by the synthetic jet (Figure 6.17b and 6.17c), the corner vortices become more visible and they appears to be stationary and really weak. In correspondence to the maximum SJ blowing velocity phase, the wingtip vortices are almost dissipated as they are barely visible and they are positioned on the projection of the tips of the wing. Then, the wingtip vortices move back and start regaining more strength during the SJ suction phases as shown in Figure 6.17e and 6.17f.

The phase-evolution of the geometrical characteristics of the vortices as their major axis, aspect ratio, and inclination angle are displayed in Figure 6.18 for each SJ configuration investigated at $C_{\mu} = 0.2\%$. At the lower actuation frequency $F^+ = 0.071$, the vortex ma-

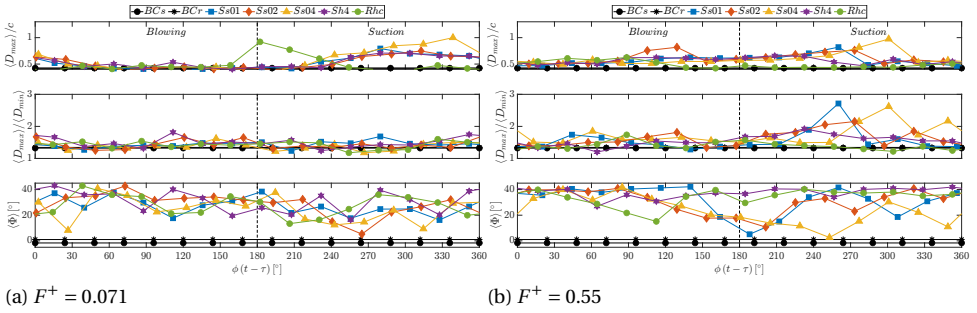


Figure 6.18: Normalized phase-averaged vortex major axis, aspect ratio, and inclination angle at $z/c = 26$ for all the configuration investigated at $C_{\mu} = 0.2\%$.

ajor axis D_{max} presents a sinusoidal evolution with a minimum at the SJ blowing peak ($\phi = 158^\circ$) where a reduction of 15% is registered against the BC value for the most interesting wing model Ss04, and a maximum during the suction phases up to 2.5 times the baseline case. On the other hand, the vortex aspect ratio shows an opposite behavior with any relevant trend, and thus the SJ actuation at this frequency does not affect the wingtip vortices shape which remain a bit more elliptical. On the contrary, the vortices inclination angle Φ is highly increased with respect to the BC case, demonstrating a noteworthy interaction with the synthetic jet which rotates major axis of the vortices. With the only exception of the wing model Rhc which confirms to be phase-shifted, all the wing models tested present the same trend described for the Ss04 configuration. Although the vorticity strength is higher during the suction period, the corresponding increasing diameter could be beneficial as well with the possibility of an early vortex linking. By increasing the actuation frequency at $F^+ = 0.55$, the geometrical features of the wingtip vortices appear to be more affected as it can be noted in Figure 6.18b. As already pointed out for the previous case, the different wing models present the same evolution of the Ss04 configuration which is considered as a reference, being only the Rhc model

phase-shifted. As such, the vortex diameter results to be higher than the baseline case during the entire SJ actuation period, with a continue increasing trend reaching a maximum equal to about $1c$ which is double with respect to the BC value. On the other hand, the tuned configuration to the Widnall instability causes a deep changes also in the vortices aspect ratio, since it is supposed to directly modify the vortices core structure. Under the SJ actuation, the vortices result in a more remarkable ellipsoidal shape which is more relevant during the SJ suction phases with a maximum two times larger than the BC value for both the wing model Ss01 and Ss04. This is confirmed by the normalized streamwise vorticity distribution reported in Figure 6.19. Differently to the previously

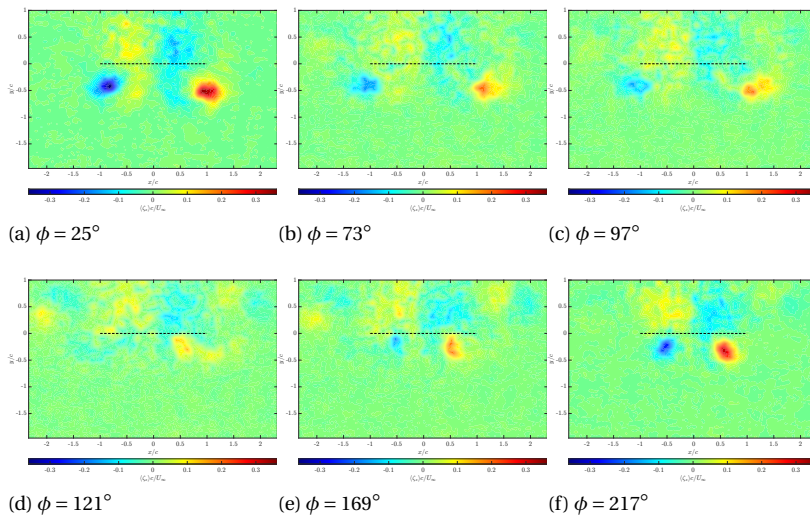


Figure 6.19: Normalized phase-averaged streamwise vorticity fields at $C_\mu = 0.2\%$, for the wing model Ss04 at $F^+ = 0.55$ and $z/c = 26$.

described configuration at lower F^+ , the vortices appear more elongated in the crosswise direction and they are less intense and, in fact, the corner vortices are clearly discernible. When reaching the maximum SJ blowing velocity, the wingtip vortices do not show a coherent structure but result highly stretched with different sub-vortices surrounding them near the upper corners of the measured field (see Figure 6.19d and 6.19e). Since they are not detected at the beginning of the blowing and suction phases (Figure 6.19a and 6.19f), these secondary structures could be ascribed as the development of the jet vortex already found in the near-field measurements. However, they have not been detected in the vorticity fields reported in Figure 6.17 for the same wing model Ss04 at lower actuation frequency. This mismatch could be explained by analyzing the Figure 6.20 and 6.21 in which the phase-evolution of the wingtip vortices centroids is reported for the wing models Ss01, Ss02, and Ss04 with a SJ configuration tuned to $F^+ = 0.071$ and $F^+ = 0.55$ respectively, at the same $C_\mu = 0.2\%$. The black dotted line represents the wing trailing edge projection. In fact, when operated at the Crow instability frequency and through a large exit section area, the SJ causes a noteworthy displacement outboard and upward

of the vortices upon reaching the wing trailing edge projection at about $y/c = 0$. In this way, they interact and cancel the secondary vorticity distribution previously described for the case at $F^+ = 0.55$. Moreover, by increasing the actuation frequency to the Widnall instability at $F^+ = 0.55$, the vortices are displaced in the opposite direction downward, and thus they are farther from the jet vortex structures. This particular behavior was not found in the near-field investigation, where the vortex motion followed the same direction and orientation. On the contrary, at both actuation frequencies, the vortices

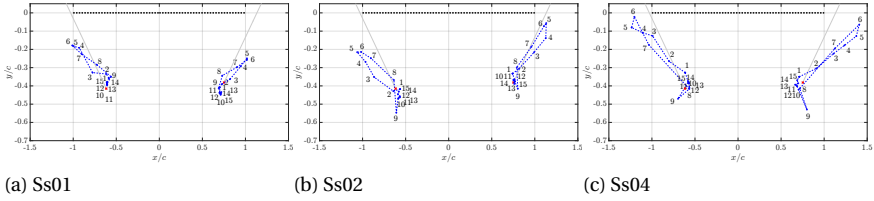


Figure 6.20: Phase-averaged evolution of the vortices position for the wing model Ss01, Ss02, and Ss04 at $F^+ = 0.071$ and $C_{\mu} = 0.2\%$ at $z/c = 26$. The time-averaged BC position is marked with a red cross, while the gray lines represent the $\pm 45^\circ$ directions.

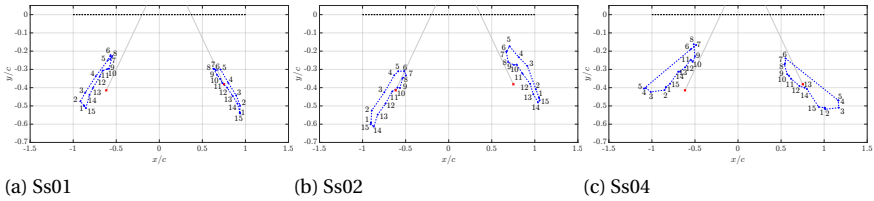


Figure 6.21: Phase-averaged evolution of the vortices position for the wing model Ss01, Ss02, and Ss04 at $F^+ = 0.55$ and $C_{\mu} = 0.2\%$ at $z/c = 26$. The time-averaged BC position is marked with a red cross, while the gray lines represent the $\pm 45^\circ$ directions.

6

motion has been confirmed to develop along a $\pm 45^\circ$ directions as described in the instability theory. At the Crow instability frequency, a key role is played by the synthetic jet exit velocity which diminishes from the wing model Ss01 to Ss04 since the momentum coefficient $C_{\mu} = 0.2\%$ is constant. As it can be noted in Figure 6.20, the wingtip vortices motion is magnified from Ss01 to Ss04 which corresponds to the minimum SJ velocity and the maximum SJ exit section area. In this case, the vortices are pushed upward of $0.5c$ and outboard of about $0.7c$ which means that the inherent vortices instability can be prematurely triggered and more amplified by injecting turbulence through a SJ exit section as large as possible. When the SJ actuation frequency is increased to $F^+ = 0.55$, the vortices motion is more regular with a maximum displacement downward and outboard of about $0.3c$ and $0.5c$ respectively for each configuration reported in Figure 6.21. It is interesting to note that, increasing the SJ exit section area, the external branch of the vortices trajectories remains almost unvaried while the internal are drawn inboard and the elliptical trajectory is enlarged. In this way, the vortices relative distance is reduced

and an early vortices linking could happen. For the sake of brevity, the scatter plot of the vortices position for the remaining configurations are not reported herein being very close to the ones discussed above, while the phase-evolution vortex relative distance is shown in Figure 6.22. For each phase, the value of $\langle b_0 \rangle$ has been normalized by the time-

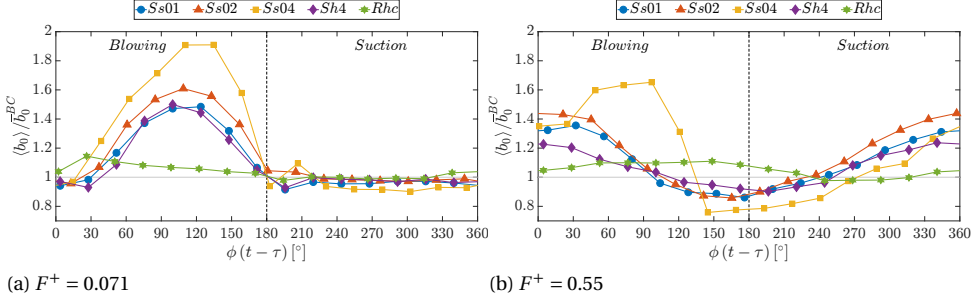


Figure 6.22: Normalized phase-averaged vortices distance at $z/c = 26$ for all the configuration investigated at $C_\mu = 0.2\%$. The time-averaged BCs and BCr values of \bar{b}_0^{BC}/b are equal to 0.684 and 0.621 respectively.

averaged baseline value \bar{b}_0^{BC} . At the lower actuation frequency $F^+ = 0.071$, the SJ blowing has been demonstrated to drastically move the vortices and their relative distance is increased up to 1.9 times the baseline value \bar{b}_0^{BC} for the wing model Ss04. The peak value of $\langle b_0 \rangle$ is reduced by increasing the SJ exit velocity as already seen in Figure 6.20 and the use of the Sh4 model is perfectly equivalent to the rectangular slot of Ss01. During the suction phases, all the SJ configurations investigated regain the BC value, with the exception of the Ss04 where the vortices relative distance is reduced of about 10%. This is an interesting result, since the vortices diameter is increased as well and thus this SJ device could lead to a premature vortices linking and their dissipation. By increasing the F^+ , an opposite phase-evolution is registered as expected from the Figure 6.21. The curves appear more regular characterized by a sinusoidal tendency with a throat in correspondence to the maximum vorticity reduction at $\phi \approx 150^\circ$ which is slightly shifted from the maximum SJ blowing velocity. However, the wing model equipped with the maximum SJ exit section area is demonstrated again to be the most useful device causing a reduction of the vortices relative distance of about 25% with respect to the baseline case which is noteworthy. Lastly, the rounded wing model Rhc does not considerably affect the vortices position, demonstrating that blowing in the streamwise direction does not represent a useful configuration.

At the same downstream distance $z/c = 26$, the effects of a variable momentum coefficient on the streamwise vorticity peak are reported in Figure 6.23 for the wing models Ss01 and Sh4 at $F^+ = 0.071$ and $F^+ = 0.55$. At both the Crow and Widnall instability frequency, a variable momentum coefficient does not modify the general features of the vorticity peak phase-averaged evolution. In fact, at $F^+ = 0.071$, the maximum $\langle \zeta_z \rangle_{max} / \bar{\zeta}_{z,max}^{BC}$ reduction of about 80% is achieved in proximity of the SJ blowing velocity peak for the wing model Sh4, while the vorticity is increased with respect to the baseline case up to 25% during the SJ suction phase. By reducing the SJ exit velocity

of 5 times at $C_\mu = 0.04\%$ a noteworthy maximum vorticity peak weakening of 48% and 58% is obtained for Ss01 and Sh4 respectively, while the results during the suction phase are comparable to the higher momentum coefficient. As a result, if one is interested only in reducing the vorticity absolute value, the SJ actuation has been demonstrated to be effective in the far-wake also with a low power consumption. At higher frequency $F^+ = 0.55$, the sinusoidal evolution is less pronounced but it is clear that also at very low momentum coefficient $C_\mu = 0.04\%$ the wingtip vortices are mitigated during the entire synthetic jet actuation period of at least 10% with respect to the BC. However, the SJ blowing phase remains the most effective period where a $\langle \zeta_z \rangle_{max} / \bar{\zeta}_{z,max}^{BC}$ decrease of 35% to 75% is achieved increasing the momentum coefficient from $C_\mu = 0.04\%$ to $C_\mu = 1\%$ for the wing model equipped with the rectangular slot Ss01. Since the high momentum coefficient $C_\mu = 1\%$ is clearly the most effective SJ configuration, the normalized streamwise vorticity fields at $F^+ = 0.071$ for the model Sh4 are reported in Figure 6.24 only for the most relevant SJ phases. As already described for the lower C_μ , the two symmetrical vorticity distributions around the mid-span location represent the corner vortices generated at the wing junction and they are stationary and present at each measured phase. Due to the high SJ characteristic velocity $U_0 = 1.29U_\infty$, the four circular nozzles generate four turbulent vortlets which are wrapped around the wingtip vortices. The latter are positioned at the corners of the field of view in Figure

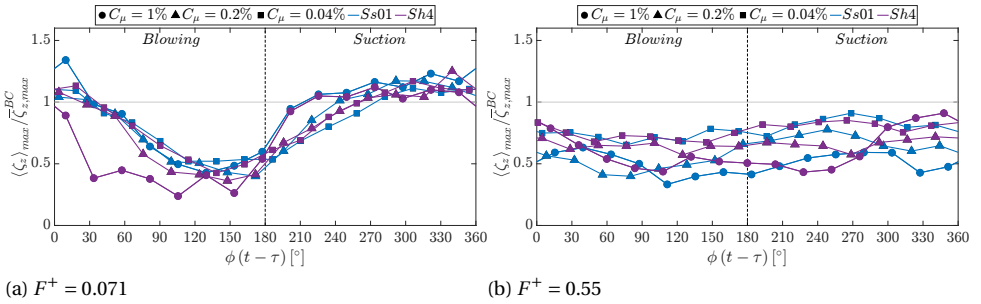


Figure 6.23: Normalized phase-averaged streamwise vorticity peak at $z/c = 26$ for the wing models Ss01 and Sh4 at variable momentum coefficients. The time-averaged BCs value of $\bar{\zeta}_{z,max}^{BC} / U_\infty$ is equal to 0.531.

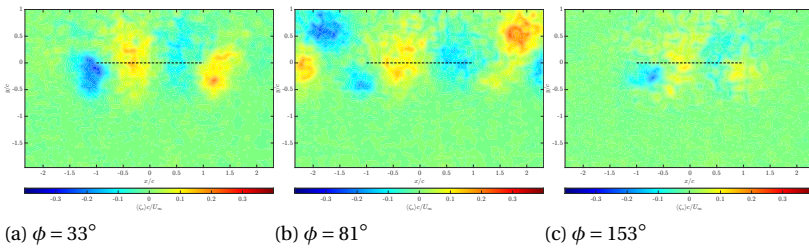


Figure 6.24: Normalized phase-averaged streamwise vorticity fields at $C_\mu = 1\%$, for the wing model Sh4 at $F^+ = 0.071$ and $z/c = 26$.

6.24b, while two jet vortices of opposite vorticity sign each other are detected below of each wingtip vortices. They are hugely weakened due to this interaction as visible in Figure 6.24c which represents the final phase of the SJ blowing. Furthermore, the effects of the high momentum coefficient are not so much considerable on the wingtip vortices geometrical characteristics at $F^+ = 0.071$ as shown in Figure 6.25a. In fact, during the SJ

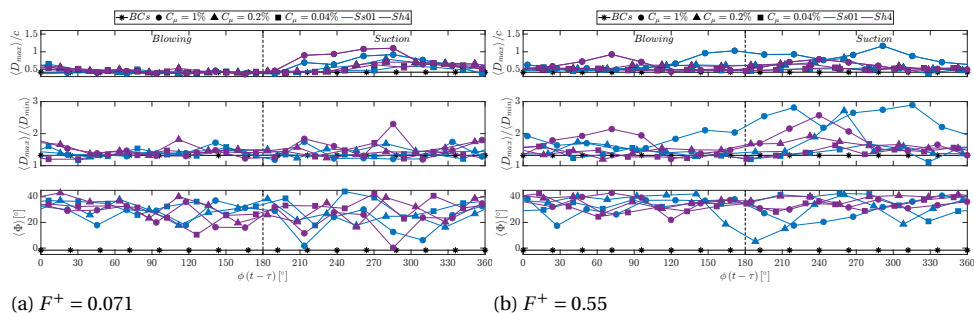


Figure 6.25: Normalized phase-averaged vortex major axis, aspect ratio, and inclination angle at $z/c = 26$ for the wing models Ss01 and Sh4 at variable momentum coefficients.

blowing phases the vortices diameter does not vary with the change in the C_μ remaining very close to the baseline value. During the SJ suction phase, a considerably high synthetic jet velocity allows to enlarge the wingtip vortices size up to 2.6 times the baseline value for the Sh4 wing model, whilst an increase of 1.6 and 1.5 times is registered for the lower momentum coefficients $C_\mu = 0.2\%$ and $C_\mu = 0.04\%$. Both the vortices aspect ratio and inclination angle result in a not recognizable trend. On the contrary, when the SJ is operated at $F^+ = 0.55$, the geometrical features are deeply modified when blowing at $C_\mu = 1\%$. By considering the most interesting configuration for the wing model Ss01, the vortices diameter is more than doubled with respect to the baseline case both at the SJ blowing and suction phases, with a vortex aspect ratio 1.6 times higher than the reference. As it can be noted from the normalized streamwise vorticity fields in Figure 6.26, the wingtip vortices are clearly stretched and elongated in the downward direction. In this case, the corner vortices appear more visible since the wingtip vortices are displaced and not overlapped to them. Furthermore, it is worth noting that also for a rectangular slot and higher actuation frequency, the high SJ velocity causes the formation of secondary vorticity structures due to the synthetic jet in cross-flow which are visible at the corners of the Figure 6.26. As expected, their intensity decreases from Figure 6.26a to 6.26c which corresponds to the end of the SJ blowing period. However, the interaction with the wingtip vortices is less remarkable than the case at lower actuation frequency since they are periodically displaced in the opposite direction downward as displayed in Figure 6.27. With the exception of the configuration at $C_\mu = 0.04\%$, the vortices trajectory develops parallel to a $\pm 45^\circ$ represented as gray lines, with an increasing amplitude with the momentum coefficient. At $C_\mu = 1\%$, the vortices periodic motion is established outboard the BC position and they are drawn inboard and downward of about $0.6c$ which is noteworthy. By reducing the momentum coefficient at $C_\mu = 0.2\%$, the vortices trajectory develops near the BC value with an amplitude of $0.3c$ downward and $0.4c$ inboard,

which are reduced to $0.1c$ at $C_\mu = 0.04\%$ which is highly less effective. The same behavior is obtained also at $F^+ = 0.071$, as shown in Figure 6.28 for the wing model Sh4. As already pointed out, the SJ tuned to the Crow instability frequency causes a symmetrical trajectory with respect to the Widnall one, being the wingtip vortices displaced outboard and upward, but still along a $\pm 45^\circ$ directions. At $C_\mu = 1\%$, the SJ actuation remarkably pushes the vortices up to $0.7c$ above the wing trailing edge projection and up to $2c$ outboard, while the oscillations are deeply reduced at $0.3c$ and $0.1c$ at $C_\mu = 0.2\%$ and $C_\mu = 0.04\%$ respectively. It is important to note that, at $F^+ = 0.071$, the vortices are subjected to a large movement only during the synthetic jet blowing phases as shown in Figure 6.29a where the normalized vortices relative distance with respect to the baseline value is reported. It is clear that the higher the SJ characteristic velocity, the higher the distance between the vortices which is counterproductive if the main goal of the actuation is to

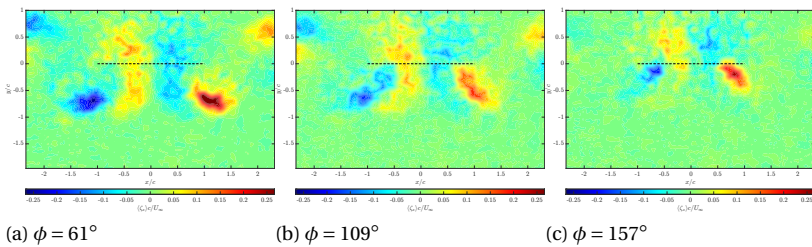


Figure 6.26: Normalized phase-averaged streamwise vorticity fields at $C_\mu = 1\%$, for the wing model Ss01 at $F^+ = 0.55$ and $z/c = 26$.

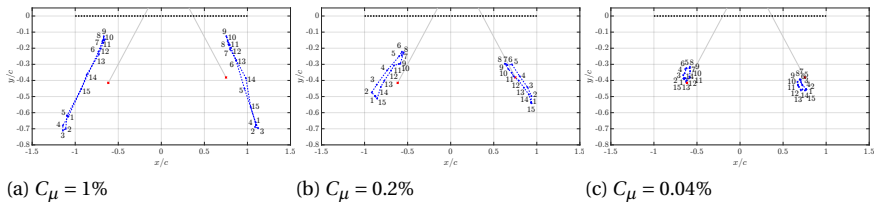


Figure 6.27: Phase-averaged evolution of the vortices position for the wing model Ss01 at $F^+ = 0.55$ at $z/c = 26$ and variable momentum coefficient. The time-averaged BC position is marked with a red cross.

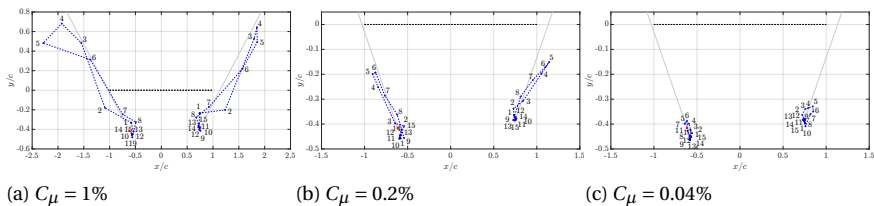


Figure 6.28: Phase-averaged evolution of the vortices position for the wing model Sh4 at $F^+ = 0.071$ at $z/c = 26$ and variable momentum coefficient. The time-averaged BC position is marked with a red cross.

anticipate the vortices linking. Furthermore, reaching a SJ velocity like $U_0 = 1.29U_\infty$ is unfeasible on a realistic application due to the massive power needed. As such, the use of an intermediate momentum coefficient $C_\mu = 0.2\%$ seems to be a reasonable compromise, since a lower value of 0.04% is really low fruitful. Although the maximum vortices relative distance is halved at higher actuation frequency ($F^+ = 0.55$ in Figure 6.29b), the wing model tested Ss01 and Sh4 are even less effective since the value of $\langle b_0 \rangle$ is increased over the baseline value also during the suction phase for the $C_\mu = 1\%$ and $C_\mu = 0.2\%$, while the configuration at $C_\mu = 0.04\%$ is practically comparable to the BC.

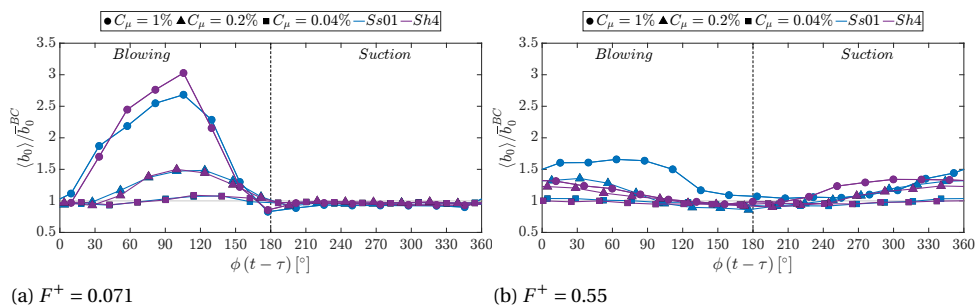


Figure 6.29: Normalized phase-averaged streamwise vorticity peak at $z/c = 26$ for the wing models Ss01 and Sh4 at variable momentum coefficients. The time-averaged BCs value of $\overline{b_0}^{BC}/b$ is equal to 0.684 .

MEASUREMENT PLANE AT $z/c = 80$

IN this section, the streamwise vorticity and geometrical features of the vortices are presented for the farthest measurement plane positioned at 80 chordlengths downstream of the wing. In Figure 6.30, the normalized streamwise vorticity peak with respect to the baseline case is reported for each SJ configuration investigated at fixed momentum coefficient equal to 0.02% . As for the nearest measurement plane at $z/c = 26$, at

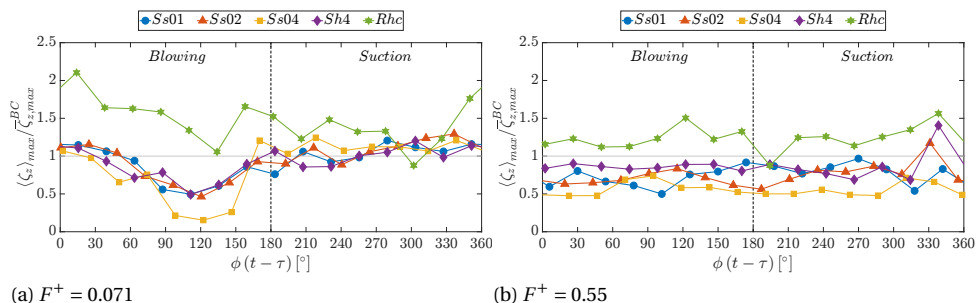


Figure 6.30: Normalized phase-averaged streamwise vorticity peak at $z/c = 80$ for all the configuration investigated at $C_\mu = 0.02\%$. The time-averaged BCs and BCR values of $\zeta_{z,max}^{BC}c/U_\infty$ are equal to 0.0579 and 0.0402 respectively.

$F^+ = 0.071$ the $\langle \zeta_z \rangle_{max} / \overline{\zeta_{z,max}^{BC}}$ presents a similar sinusoidal phase-evolution with the throat in proximity of the SJ blowing peak and the maximum over the SJ suction phases. The most high-performance device is again the wing model equipped with the higher SJ exit section area Ss04, which causes a vorticity peak reduction of 85%, against the 54% registered for the Ss01, Ss02, and Sh4, while the actuation leads to a vorticity level higher than the baseline case of about 25% during the SJ suction phases as already found at $z/c = 26$. It is also confirmed that analogous results in the far-wake are obtained by blowing at $F^+ = 0.071$ through a rectangular slot (Ss01, blue curve) or four equivalent circular nozzle (Sh4, purple curve). On the contrary, at this far distance from the wing, the rounded wing model Rhc with the SJ blowing in the chordwise direction inclined of 5° with respect to the free-stream direction has been demonstrated to be not effective since the streamwise vorticity peak results higher than the baseline case in each phase of the SJ actuation period. This is verified also at higher $F^+ = 0.55$ as shown in Figure 6.30b. At the Widnall instability frequency, the vorticity phase-evolution of the other configurations lose the sinusoidal characteristics being almost constant around their mean value. However, with the only exception of the last suction phase of the Sh4 and Ss02 models, the values of $\langle \zeta_z \rangle_{max} / \overline{\zeta_{z,max}^{BC}}$ remain below unity and the wing model Ss04 with the lower SJ exit velocity at $C_\mu = 0.2\%$ outperforms the different devices with a maximum vorticity reduction up to 50% against the BC. Lastly, at high actuation frequencies, employing a rectangular slot as SJ exit section geometry turns out to be more effective than using 4 circular equivalent jets.

It is worth noting that although the relative reduction is the same at the downstream distance $z/c = 26$, the absolute value of the baseline normalized streamwise vorticity is reduced from 0.531 to 0.0579, meaning that the wingtip vortices are very close to be completely dissipated. This hypothesis is confirmed in Figure 6.31 where the most interesting SJ blowing phases are reported for the wing model Ss04 at $F^+ = 0.071$. It is immediately evident that at this far downstream distance the wingtip vortices are very close to each other and starts losing their coherence under the SJ actuation. As already pointed out for the nearest measurement plane $z/c = 26$, at the Crow instability frequency they undergo to a large periodic motion as visible from Figure 6.31a to 6.31c in which the vortices are pushed upward and outboard. The latter represents the maximum SJ blowing velocity phase and, as a result, they are strikingly weakened and barely visible. However, the attention of the reader should be captured by the Figure 6.31d. Here, the wingtip vortices are not recognizable, meaning that they are completely dissipated or they are so weak to not be detected anymore from the high-resolution S-PIV process. It is worth recalling that each vorticity field presented in Figure 6.31 are the average of 300 snapshots, and thus statistically reliable enough to state that the configuration of the wing model Ss04 with the largest SJ exit section at $F^+ = 0.071$ and $C_\mu = 0.2\%$ allows to prematurely trigger the inherent vortices instabilities causing an early vortices linking and their dissipation already at $z/c = 80$. In fact, in the following phase in Figure 6.31e near the end of the SJ blowing, the wingtip vortices are linked together and this strong interaction leads to their dissipation. These features have been observed only for this configuration, meaning that it can represent the most high-performance device to be further investigate to continue increasing its effectiveness. On the other hand, during the suction SJ phase, the vortices regain the baseline vorticity level and they are again separated. Lastly,

at this downstream distance the corner vortices generated at the wing junction seems to be incorporated in the wingtip vorticity distribution or naturally dissipated since they are very weak.

The development of the geometrical features of the wingtip vortices at the downstream distance of $z/c = 80$ are reported in Figure 6.32 for the momentum coefficient $C_\mu = 0.2\%$ at $F^+ = 0.071$ and $F^+ = 0.55$ respectively.

When the SJ is operated at the Crow instability frequency (Figure 6.32a), the vortices size appears to be not affected by the actuation with the normalized \overline{D}_{max}/c value for the baseline case increasing from 0.423 ($z/c = 26$) to 0.837 ($z/c = 80$). The SJ effects at $F^+ = 0.071$ are recognizable only during the suction phase, where the vortices diameter

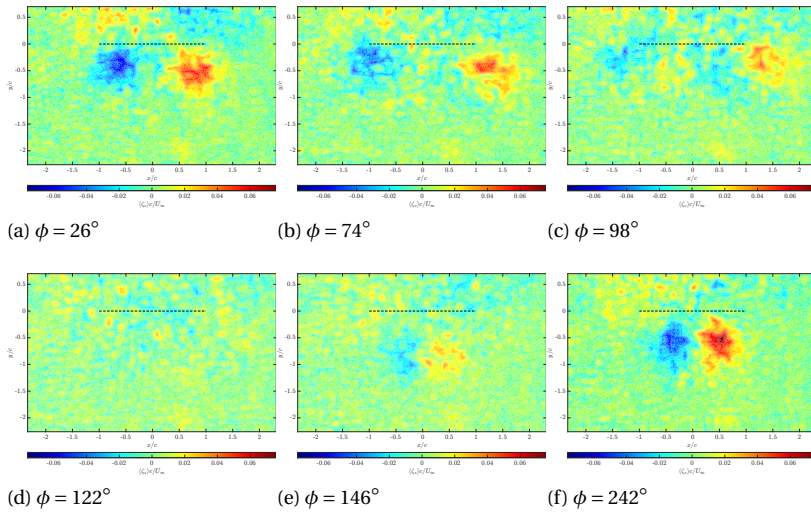


Figure 6.31: Normalized time-averaged streamwise vorticity fields at $C_\mu = 0.2\%$, for the wing model Ss04 at $F^+ = 0.071$ and $z/c = 80$.

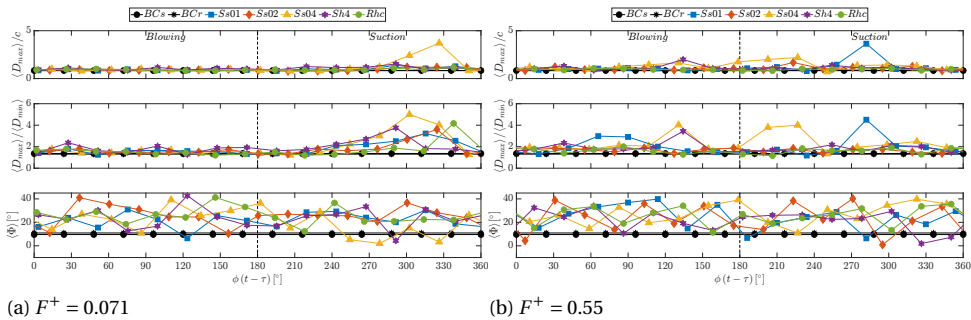


Figure 6.32: Normalized phase-averaged vortex major axis, aspect ratio, and inclination angle at $z/c = 80$ for all the configuration investigated at $C_\mu = 0.2\%$.

results up to 4.47 times higher than the BC value for the model Ss04, while the vortices aspect ratio is increased for each tested wing model with a maximum of 3.65 times the BC value for the Ss04 configuration. In this case, the vortices aspect ratio $\overline{D}_{max}/\overline{D}_{min}$ for the baseline case does not significantly vary with the downstream distance slightly increasing from 1.32 ($z/c = 26$) to 1.37 ($z/c = 80$). As already described for the nearest measurement plane at $z/c = 26$, at higher $F^+ = 0.55$ tuned to the Widnall instability, the SJ actuation modifies the core structure of the vortices, with a doubled vortex major axis during the SJ blowing phases (i.e. Ss04) and a generally higher value with respect to the baseline case during the suction phases where the maximum variation is reached with the wing model at the higher SJ exit velocity Ss01 ($\langle D \rangle_{max} = 3.65 \overline{D}_{max}^{BC}$). As expected, also in the far-wake the SJ actuation causes a remarkably changes in the vortices aspect ratio at high actuation frequency, remodeling the vortices in a more accentuate ellipsoidal shape as displayed in Figure 6.33 where the phase-averaged normalized vorticity fields for the model Ss04 at $C_\mu = 0.2\%$ and $F^+ = 0.55$ are reported. Again, only the most interesting phases are taken into account for the sake of brevity.

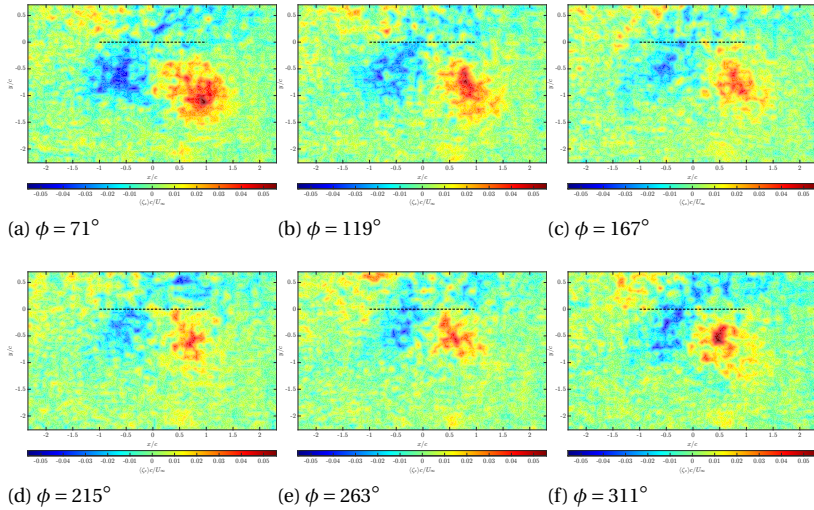


Figure 6.33: Normalized time-averaged streamwise vorticity fields at $C_\mu = 0.2\%$, for the wing model Ss04 at $F^+ = 0.55$ and $z/c = 80$.

The first difference to be highlighted with respect to the vorticity distribution at lower F^+ is that the vortices size is much higher over the entire SJ actuation period and their are closer each other, resulting in a definitely larger interaction. Furthermore, their shape is more elliptical since they appear elongated and stretched outboard and downward which is the direction of the periodic motion at which they undergo under the SJ actuation at $F^+ = 0.55$ as already shown in Figure 6.21 at $z/c = 26$. Although the wing configuration with the larger SJ exit section area Ss04 has been demonstrated to be the most effective one, at the $C_\mu = 0.2\%$ and $F^+ = 0.55$ the wingtip vortices have proven to be not completely dissipated as for the case at $F^+ = 0.071$ since they are clearly visible at each

phase over the SJ actuation period.

As it is possible to notice from both the Figure 6.31 and 6.33, the wingtip vortices undergo to a large diffusion over a wide area, overlapping each other, and presenting a less coherent core structure with respect the nearest downstream measurement plane $z/c = 26$ described herein above. As a result, the uncertainty in the identification of the vortices centroids is estimated to be $\approx 0.2c$ and thus it is not possible to track and show a reliable trajectory as discussed for the previous case at $z/c = 26$. On the other hand, the phase-evolution of the vortices relative distance $\langle b_0 \rangle$ continues to keep a physical meaning since its uncertainty is much smaller. It has been reported in Figure 6.34 normalized against the time-averaged baseline value at the same downstream distance $z/c = 80$.

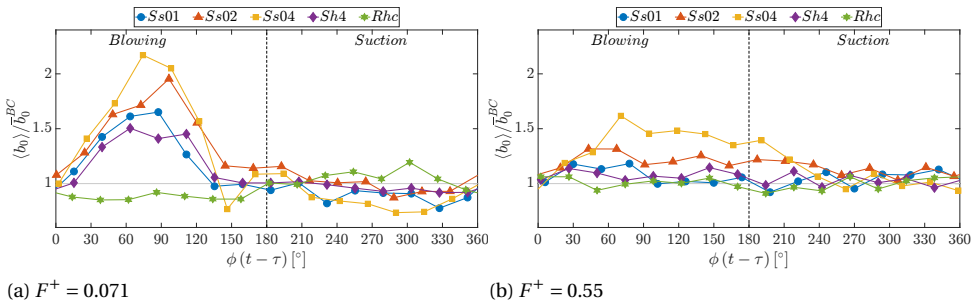


Figure 6.34: Normalized phase-averaged vortices distance at $z/c = 80$ for all the configuration investigated at $C_\mu = 0.2\%$. The time-averaged BCs and BCr values of $\overline{b_0}^{BC}/b$ are equal to 0.511 and 0.468 respectively.

At the Crow instability frequency $F^+ = 0.071$, the SJ actuation has been proven to displace the wingtip vortices upward and outboard during the blowing phases, with a maximum relative distance of about 2.2 times the BC value for the model Ss04. By reducing the SJ exit section area (i.e. increasing the SJ velocity) the value of $\langle b_0 \rangle / \overline{b_0}^{BC}$ is reduced to 1.95 and 1.65 for the model Ss02 and Ss01 while the use of the model Sh4 gives comparable results to the Ss01. As for the nearest downstream plane at $z/c = 26$, during the SJ suction phase an opposite behavior is registered where the vortices relative distance is reduced against the baseline case. Again, the wing model with the larger SJ exit section Ss04 outperforms the remaining configurations with a maximum drop of 27% (see Figure 6.31f). This feature is coupled with the increase in the vortex diameter during the suction phase, making this synthetic jet configuration the most high-performance device which leads to a anticipated vortices linking and their consequent dissipation. Lastly, the rounded wing model Rhc has been confirmed to be phase-shifted with respect the others with a favorable peak-to-valley difference as shown in Figure 6.34a. However, it can not be considered a useful device so far due to the strengthening of the vortices described in Figure 6.30. A completely different results are obtained at $F^+ = 0.55$ (Figure 6.34b), where the phase-evolution does not show a sinusoidal trend identified at the previous downstream measurement plane. Furthermore, the SJ actuation seems to be counter-productive according this metric, since the vortices are pushed far from each other more than the baseline case ($\langle b_0 \rangle / \overline{b_0}^{BC} > 1$) for each phase over almost the entire

actuation period.

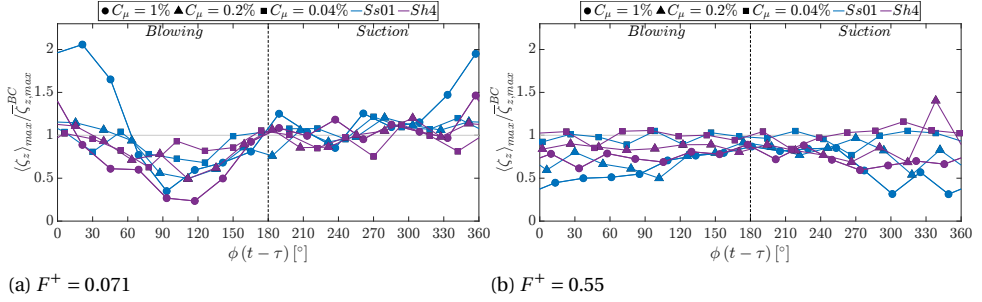


Figure 6.35: Normalized phase-averaged streamwise vorticity peak at $z/c = 80$ for the wing models Ss01 and Sh4 at variable momentum coefficients. The time-averaged BCs value of $\overline{\zeta_{z,max}^{BC}}/U_\infty$ is equal to 0.0579.

By fixing the synthetic jet exit section for the two equivalent model Ss01 and Sh4, the effects of a variable SJ characteristic velocity on the normalized streamwise vorticity peak are reported in Figure 6.35 for the momentum coefficients equal to 1%, 0.2%, and 0.04% at $F^+ = 0.071$ and $F^+ = 0.55$. At both actuation frequencies, the phase-evolution of $\langle \zeta_z \rangle_{max} / \overline{\zeta_{z,max}^{BC}}$ appears similar and scaled with respect to the ones presented in Figure 6.23 for the measurement plane at $z/c = 26$. At $F^+ = 0.071$, the higher momentum coefficient $C_\mu = 1\%$ results in a massive vorticity alleviation up to 75% for both the model Ss01 and Sh4 in correspondence of the SJ blowing. As already highlighted, by diminishing the SJ Characteristic velocity U_0 from 11.1 m/s ($C_\mu = 1\%$) to 4.96 m/s ($C_\mu = 0.2\%$) and 2.22 m/s ($C_\mu = 0.04\%$), the SJ effectiveness is reduced but the $\langle \zeta_z \rangle_{max} / \overline{\zeta_{z,max}^{BC}}$ maximum drops are equal to 50% and 32% respectively. As such, a noteworthy vorticity alleviation can be achieved with a considerably low amount of power by designing the control device optimized in the blowing phase like a pulsed jet. In fact, during the SJ suction phase, the evolution of each configuration oscillates around the baseline value without any particular trend to be identified. On the other hand, at the higher $F^+ = 0.55$ the sinusoidal phase-evolution is less relevant while the effectiveness of the different momentum coefficient is clearer. In fact, at the lower value $C_\mu = 0.04\%$ the streamwise vorticity peak is oscillating near the BC value over almost the entire SJ actuation period with a maximum reduction of 23% on the suction phase. By increasing the momentum coefficient, the curves are shifted below to lower values of $\langle \zeta_z \rangle_{max} / \overline{\zeta_{z,max}^{BC}}$ with a peak of 0.90 between the blowing and suction phases and a minimum equal to about 0.50 and 0.31 for the $C_\mu = 0.2\%$ and $C_\mu = 1\%$ respectively for both wing models Ss01 and Sh4. As already pointed out for the analysis conducted at fixed $C_\mu = 0.2\%$, at this far downstream distance a high value of $C_\mu = 1\%$ leads to the the same relative alleviation of the normalized streamwise vorticity of the measurement plane at $z/c = 26$, but with a baseline value reduced of more than 85%, resulting in an almost completely dissipated wingtip vortices as shown in Figure 6.36. Here, the normalized streamwise vorticity fields of the SJ blowing phases for the most effective device Ss01 at $F^+ = 0.071$ and $C_\mu = 1\%$ are reported. At the first phases, the wingtip vortices are strengthened, present a notewor-

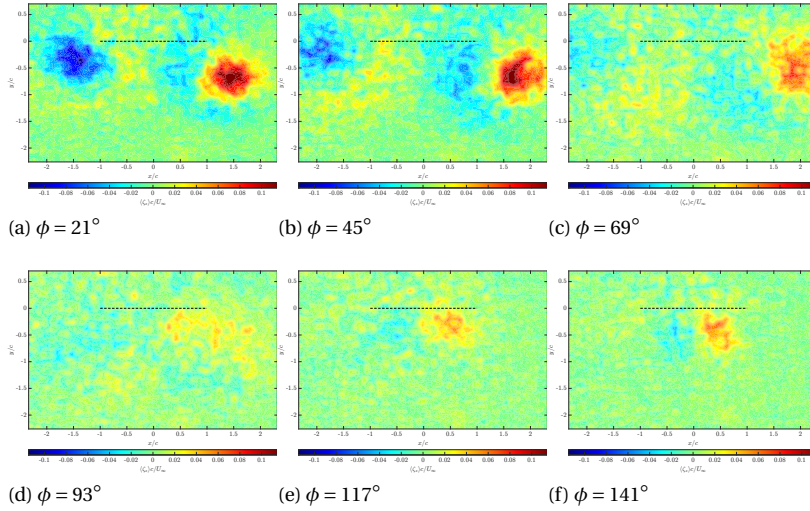


Figure 6.36: Normalized time-averaged streamwise vorticity fields at $C_\mu = 1\%$, for the wing model Ss01 at $F^+ = 0.071$ and $z/c = 80$.

thy increased size, and they are pushed outboard in the spanwise direction up to $\pm 2c$ at $\phi = 69^\circ$ as visible in Figure 6.36c. Then, in correspondence to the maximum SJ blowing, the vortices are not recognizable anymore, being dissipated and/or divided in several weaker small vorticity structures which, however, are less hazardous of a single, diffused, and weak vortex. Furthermore, the effectiveness of the actual SJ configuration can be noted also in Figure 6.36e and 6.36f, where the vortices remain alleviated in a continue interaction since they are overlapped, canceling the opposite vorticity sign and leading to a premature natural vortex linking.

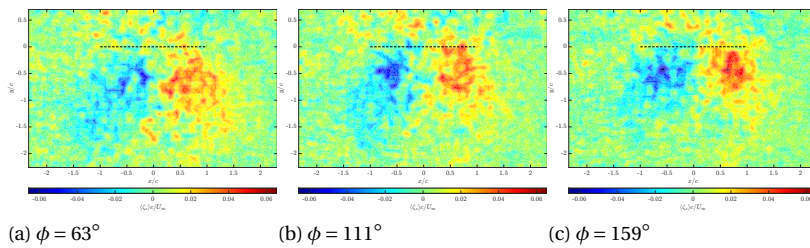


Figure 6.37: Normalized time-averaged streamwise vorticity fields at $C_\mu = 1\%$, for the wing model Ss01 at $F^+ = 0.55$ and $z/c = 80$.

Increasing the actuation frequency to $F^+ = 0.55$ for the same wing model Ss01 and momentum coefficient $C_\mu = 1\%$, at $z/c = 80$ the wingtip vortices presents a larger diameter up to $1c$, but with a lack of coherence and a really low vorticity strength as shown in Figure 6.37 where only the most interesting three blowing phases are reported. In fact, it

has been seen that the vorticity fields during the actuation period at high SJ frequency present similar features as already discussed for the phase-evolution of the vorticity peak in Figure 6.35b. In particular, the secondary vorticity structures generated by the synthetic jet in cross-flow are already dissipated since only the concentrated wingtip vorticity are discernible. The elongation and stretching of the vortices are amplified at this downstream distance with respect to the findings at $z/c = 26$ while their periodic motion is confirmed to be outboard and downward although the centroids identification is really difficult to define. The irregularity of the vorticity fields reported in Figure 6.37 leads also to a not negligible uncertainty in the correct evaluation of the geometrical characteristics which are presented herein.

Finally, the phase-evolution of the relative vortices distance $\langle b_0 \rangle$ normalized with the time-averaged baseline value $\overline{b_0}^{BC}$ is reported in Figure 6.38. As expected by the inspection of Figure 6.36, during the synthetic jet blowing phase at $F^+ = 0.071$ and $C_\mu = 1\%$ the wingtip vortices are largely displaced far from each other with respect to the baseline position ($\langle b_0 \rangle / \overline{b_0}^{BC} \approx 4$), which in turn is regained during the suction phase. At lower momentum coefficients, the periodic motion of the vortices is alleviated and the maximum normalized relative distance is reduced to 1.6 at $C_\mu = 0.02\%$, while the lower value of $C_\mu = 0.04\%$ does not affect the vortices position being constantly equal to the reference value. It is worth recalling that although a high SJ characteristic velocity U_0 causes a large motion of the wingtip vortices along a $\pm 45^\circ$ and thus amplifies the Crow instability, the power consumption needed for a full scale aircraft wing will be unaffordable. When the SJ is operated at $F^+ = 0.55$, the increase in the momentum coefficient for both the wing model Ss01 and Sh4 is confirmed to be counter-productive in reducing the vortices distance since the value of $\langle b_0 \rangle / \overline{b_0}^{BC}$ is over unity for the entire actuation period in each configuration investigated.

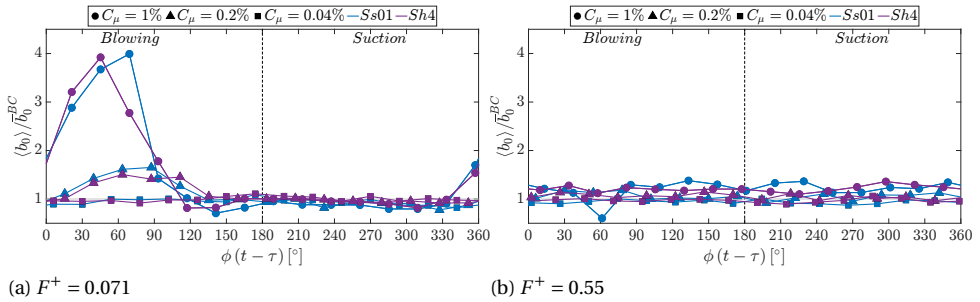


Figure 6.38: Normalized phase-averaged streamwise vorticity peak at $z/c = 80$ for the wing models Ss01 and Sh4 at variable momentum coefficients. The time-averaged BCs value of $\overline{b_0}^{BC}/b$ is equal to 0.511.

In conclusion, the phase-averaged results of the vorticity and geometrical features metric revealed that the effects of a variable momentum coefficient is less relevant of the SJ exit section area variation, being the wing model Ss04 the most effective configuration investigated at $F^+ = 0.071$ and $C_\mu = 0.2\%$.

6.2.2. CIRCUMFERENTIAL VELOCITY

As of crucial importance for the wake-hazard metric, the far-wake phase-averaged evolution of the circumferential velocity peak normalized by the time-averaged value is reported in Figure 6.39 for the fixed momentum coefficient $C_\mu = 0.02\%$ and both actuation frequencies $F^+ = 0.071$ and $F^+ = 0.55$ for each measurement plane investigated. Contrary to the near-field results, the phase-evolution of $\langle U_\theta \rangle_{max} / \overline{U}_{\theta,max}^{BC}$ at $F^+ = 0.071$ presents a sinusoidal trend with opposite characteristics between the synthetic jet blowing and suction phases. Starting from the downstream distance at $z/c = 26$, the circumferential velocity peak is continuously decreasing with a minimum near the end of the SJ blowing of -50% and -58% for the wing model Ss01 and its equivalent Sh4 which is slightly more efficient. By increasing the SJ exit section area, the control effectiveness increases being the $\langle U_\theta \rangle_{max} / \overline{U}_{\theta,max}^{BC}$ values reduced to about 0.44 and 0.22 for the Ss02 and Ss04 configurations respectively. These findings are in agreement with the vorticity results of the previous section 6.2.1 where the vortices have been demonstrated to be hugely weakened in correspondence to the same SJ phases which is encouraging for the wake-hazard alleviation. As already pointed out in Figure 6.16, the rounded wing model is phase-shifted backward with respect to the other configurations since the minimum value of the normalized circumferential velocity peak is registered at the beginning of the SJ blowing and it increases up to +20% around $\phi \approx 90^\circ$. As for the phase-evolution of $\langle U_\theta \rangle_{max} / \overline{U}_{\theta,max}^{BC}$ in the near-field, during the suction phase the SJ control effectiveness is reduced. In fact, for each configuration, the wingtip vortices regain their strength, increase their diameter, and the circumferential velocity peak is raised as well reaching the baseline value and overcoming it after the SJ suction blowing with a maximum of +27% for the Ss02 model. However, the SJ configuration with the lowest characteristic velocity U_0 remains the most high-performance one also during the suction phases causing the minimum oscillation around the BC value.

Going far downstream at the Crow instability frequency, the normalized circumferential velocity peak preserves the same phase-evolution profile with a slight shift-up and scaling since the maximum drop registered is 40%, 53%, and 73% at $z/c = 52$, and 37%, 45%, and 58% at $z/c = 80$ for the wing model Ss01, Ss02, and Ss04 respectively. It is worth noting that despite the relative variation with respect to the baseline case is slightly reduced moving in the very far wake, the BC circumferential peak is reduced as well of about 74% from $z/c = 26$ to $z/c = 80$, so a reduction of 58% turns into an almost vanished danger for a possible following aircraft encounter. Although during the suction phases the SJ is even less impactful going downstream being the value of $\langle U_\theta \rangle_{max} / \overline{U}_{\theta,max}^{BC}$ over unity for each phase, spreading the SJ jet on a large area represents the most useful device to be employed in reducing the wake-vortex hazard. As reported in Table 4.2, the main drawback of this configuration is the high power consumption needed which is about 2.78 times higher than the Ss01. It is important to recall, however, that the synthetic jet configuration have not been designed with a power optimization goal.

When the synthetic jet is operated at $F^+ = 0.55$, an evident different phase-evolution of the circumferential velocity peak is detected. As shown in Figure 6.39b, a sinusoidal behavior is still present at $z/c = 26$ with a minimum and maximum of $\langle U_\theta \rangle_{max} / \overline{U}_{\theta,max}^{BC}$ located in proximity of the SJ blowing peak and at the beginning of the SJ suction respec-

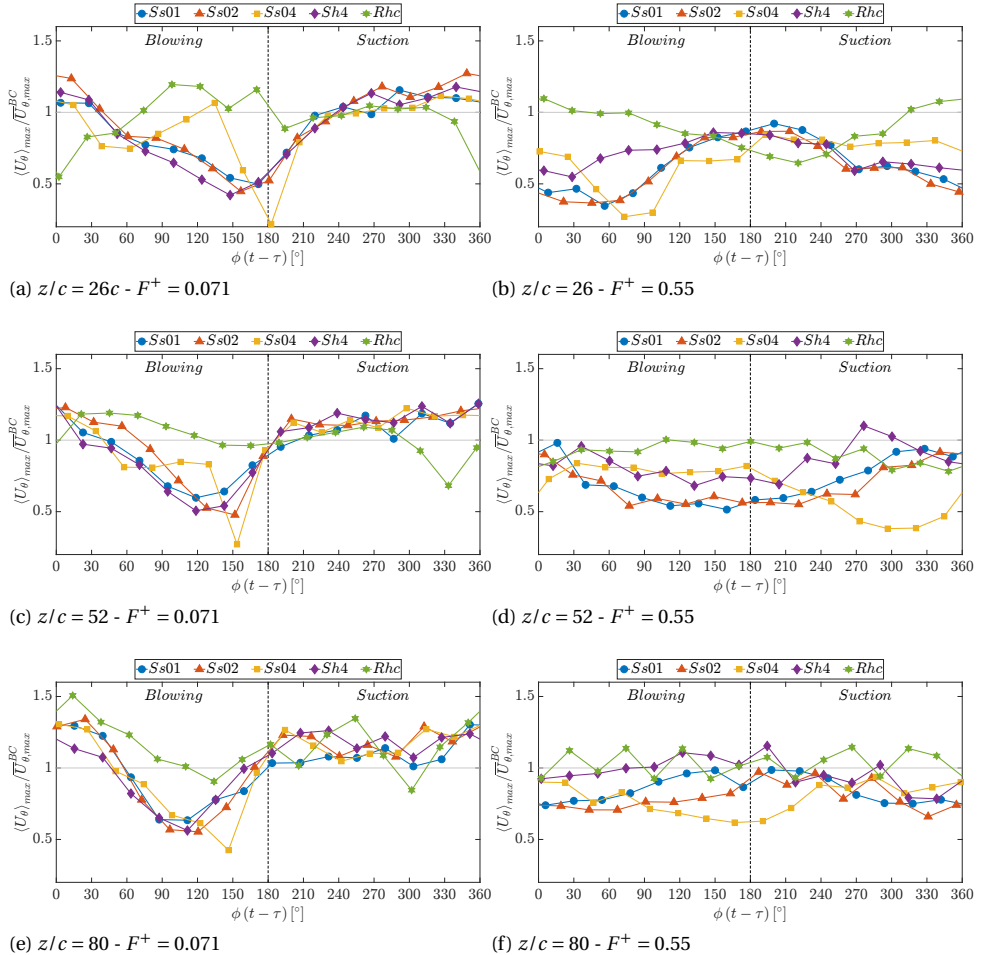


Figure 6.39: Normalized phase-averaged circumferential velocity peak at different downstream positions for all the configuration investigated at $C_\mu = 0.2\%$. The time-averaged BCs and BCr values of $\overline{U}_{\theta, \max}^{BC}/U_\infty$ are equal to 0.0195 and 0.0173, 0.00846 and 0.00749, 0.00466 and 0.00382 at $z/c = 26, 52, 80$ respectively.

tively. Differently to the case at $F^+ = 0.071$, the SJ actuation leads to a reduction of the circumferential velocity at each phase with the only exception of the Rhc model which is phase-shifted and less effective. On the other hand, increasing the SJ exit section area at fixed C_μ is confirmed the best control strategy during the blowing phases since the maximum circumferential velocity peak reduction is reduction of -73% is achieved for the wing model Ss04, although the Ss01 and Ss02 outperform it in the suction period. At the higher frequency, the use of a rectangular slot (Ss01) should be preferred to the equivalent four circular nozzles (Sh4) since the values of $\langle U_\theta \rangle_{\max} / \overline{U}_{\theta, \max}^{BC}$ drop up to 0.35 and 0.55 respectively. At the further distance $z/c = 52$, the wing model Ss04 causes the maxi-

imum circumferential velocity peak reduction of 62% during the SJ suction phase which is in opposition to the previous findings at $z/c = 26$ at both actuation frequency. The same phase-shift has been found also at the last measurement plane at $z/c = 80$, where the synthetic jet effectiveness appears to be reduced. In particular, the wing model Sh4 and Rhc present an oscillation around the baseline value, while the rectangular slots show a circumferential velocity alleviation in each phase of the synthetic jet actuation period with a maximum drop of about 38% for the Ss04 as expected.

The effects of a variable momentum coefficient C_μ on the normalized phase-evolution of the circumferential velocity peak for the fixed synthetic jet geometries Ss01 and Sh4 at $F^+ = 0.071$ and $F^+ = 0.55$ are displayed in Figure 6.40. It is possible to notice that the trend of the curves are exactly the same shown in Figure 6.39, meaning that the crucial parameter is represented only by the synthetic jet actuation frequency. At $z/c = 26$ and $F^+ = 0.071$, the higher momentum coefficient $C_\mu = 1\%$ leads to a reinforcement of the circumferential velocity peak during the blowing phase up to +55% while a reduction of 46% and 65% has been reached immediately before the suction phases for the Ss01 and Sh4 respectively. It is interesting to note that with a momentum coefficient 25 times lower ($C_\mu = 0.04\%$), the synthetic jet blowing revealed to be fruitful as well attenuating the $\langle U_\theta \rangle_{max}$ of 35% which is noteworthy. However, the effects of a very low momentum coefficients tend to vanish going downstream at $z/c = 52$ and $z/c = 80$ where the values of $\langle U_\theta \rangle_{max} / \overline{U}_{\theta,max}^{BC}$ are below unity only for a few phases, but not enough to be the base for a future control strategy. On the contrary, blowing at $C_\mu = 1\%$ remains impactful also at larger downstream distances with a huge decrease up to 50% and 70% at $z/c = 52$ and 75% and 63% at $z/c = 80$ for the model Ss01 and Sh4 respectively, so a best configuration can not be easily identified. However, the intermediate momentum coefficient $C_\mu = 0.2\%$ is confirmed to be the feasible compromise for a possible control based wing design due to the circumferential velocity peak drop of about 50% obtained at each downstream position investigated with a relatively low power consumption. The same conclusion can be drawn by analyzing the phase-evolution of $\langle U_\theta \rangle_{max} / \overline{U}_{\theta,max}^{BC}$ reported in Figure 6.40b, 6.40d, and 6.40f referred to the test cases at $F^+ = 0.55$. Firstly, the rectangular slot Ss01 is much more fruitful than the wing model equipped with the equivalent four circular jets as it can be noted from the purple curves which are higher than the blue ones at each C_μ . By considering only the Ss01 configuration, the higher actuation frequency turns out to be most efficacious than the lower one since the normalized circumferential velocity phase-evolution is entirely below unity for each measurement plane and momentum coefficient investigated, with the only exception for the $C_\mu = 0.04\%$ at $z/c = 80$ where the baseline value is almost constantly regained as shown in Figure 6.40f. In fact, as already found out for the time-averaged results in section 5.2.2, the lowest momentum coefficient is impactful only at $z/c = 26$ where a minimum and maximum drop of 6% and 30% are obtained. However, if one would like to design a SJ actuator working at the Widnall instability frequency, it should be optimized for the operating condition at $C_\mu = 1\%$ by which an almost constant $\langle U_\theta \rangle_{max} / \overline{U}_{\theta,max}^{BC}$ decrease of about 67%, 57%, and 58% has been achieved at least in the SJ blowing phases at $z/c = 26$, 52, and 80 respectively. As already mentioned above, the intermediate value of $C_\mu = 0.2\%$ should be considered for a future SJ based control strategy tuned to the Widnall instability since the danger of the wake-vortex hazard is deeply alleviated up to 65%,

49%, and 27% for the wing model Ss01 at the different downstream distance analyzed, without requiring a massive power.

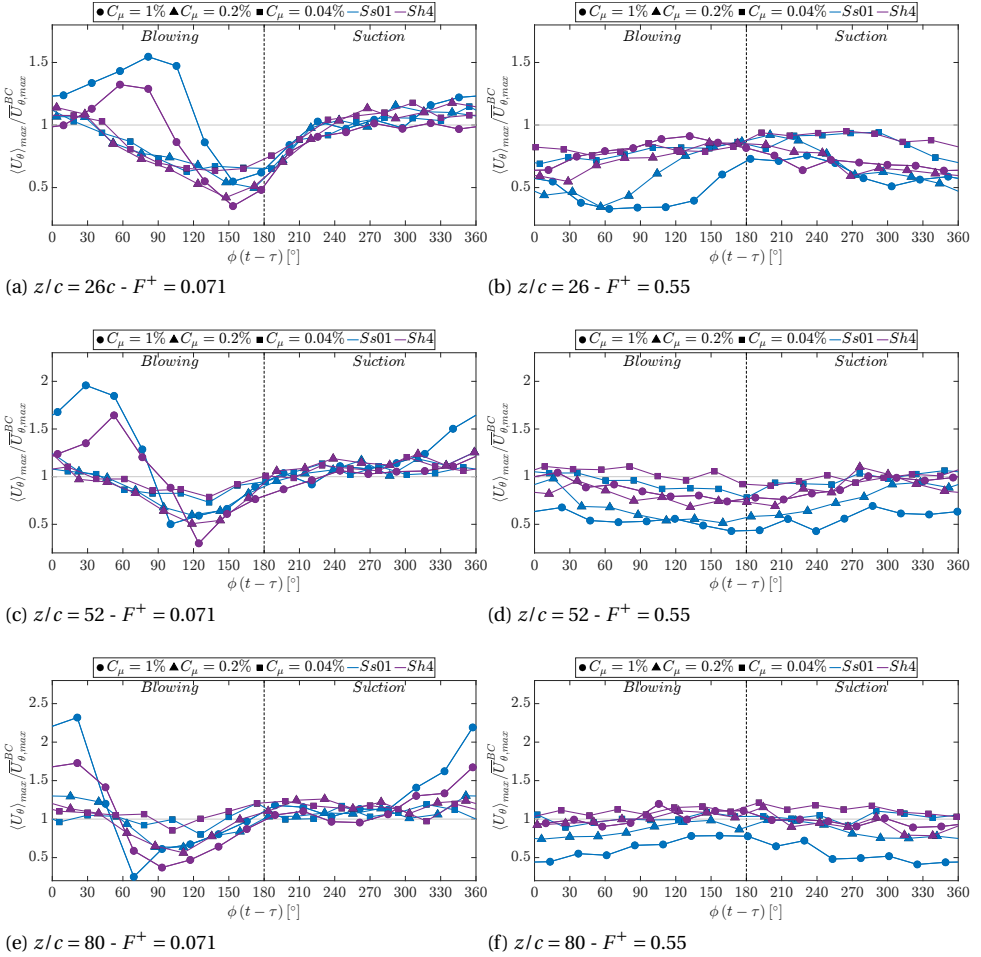


Figure 6.40: Normalized phase-averaged circumferential velocity peak at different downstream positions for the wing models Ss01 and Sh4 at variable momentum coefficients. The time-averaged values of $\overline{U}_{\theta,max}^{BC}/U_{\infty}$ are equal to 0.0195, 0.00846, and 0.00466 at $z/c = 26, 52, 80$ respectively.

6.2.3. CIRCULATION

To conclude the phase-average analysis of the wingtip vortices in the far-wake, the evolution of the normalized circulation with respect to the baseline case is reported in Figure 6.41 for each wing model tested at $C_{\mu} = 0.2\%$ and both actuation frequencies $F^+ = 0.071$ and $F^+ = 0.55$. Firstly, it is worth noting that the mean value of the curves presented is different from the corresponding time-averaged value reported in Figure

5.17 as already explained in section 6.1.2. In fact, according to the time-averaged results, the normalized wingtip vortices circulation is hugely reduced with the synthetic jet control except for the downstream plane $z/c = 80$ in which values higher than unity can be reached at both actuation frequencies and their combination. On the contrary, at $F^+ = 0.071$ and $z/c = 26, 52$, the phase-averaged evolution shows a maximum increase between 1.2 and 1.45 during the blowing phase which turns into an increase downwash and a consequent more dangerous wake hazard, although the instability growth rate would be increased as well. However, in proximity to the end of the SJ blowing phase and in correspondence of the maximum vorticity peak reduction shown in Figure 6.16,

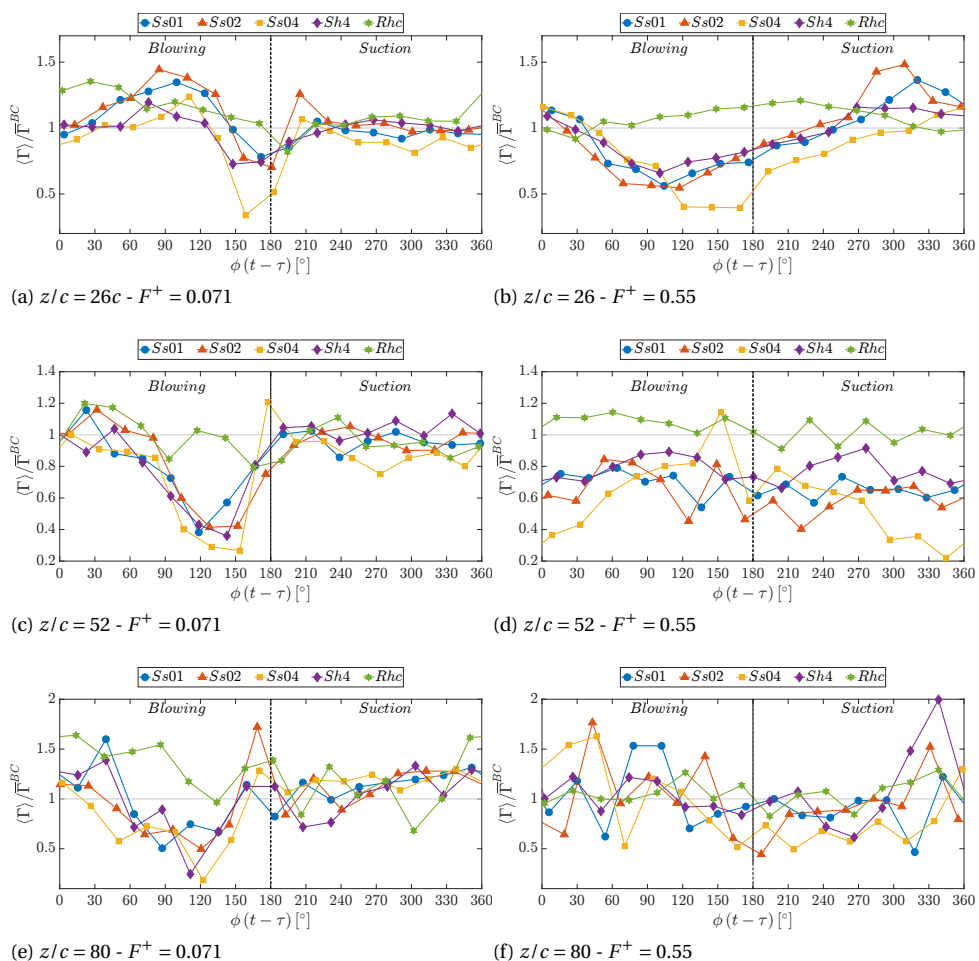


Figure 6.41: Normalized phase-averaged vortices circulation at different downstream positions for all the configuration investigated at $C_\mu = 0.2\%$. The BCs and BCr values of $\bar{\Gamma}^{BC}/cU_\infty$ are equal to 0.0282 and 0.0240, 0.0220 and 0.0195, 0.0117 and 0.0104 at $z/c = 26, 52, 80$ respectively.

at $z/c = 26$ the vortices circulation is decreased from 22% to 64% increasing the SJ exit section area from the model Ss01 to a 4 times higher one for the wing Ss04. Going far downstream at $z/c = 52$, each SJ configuration appears to be more effective in alleviating the vortices circulation since the reduction of the curves is steeper during the blowing period and the maximum $\langle \Gamma \rangle / \bar{\Gamma}^{BC}$ is registered to be in between 57% (Sh4) and 73% (Ss04) for each wing model, except the rounded Rhc which is shifted upward as already noted for the previous metrics discussed. On the other hand, the exit section geometry shape (Ss01 and Sh4) seems to be not a crucial parameter since the blue and purple curves are comparable. At the furthest measurement plane located at $z/c = 80$, the most fruitful configuration is again the wing equipped with the large SJ exit section area Ss04 which shows a striking drop of the normalized vortices circulation of about 72% where the vortices are practically vanished due to the premature vortex linking already discussed and displayed in Figure 6.31. As already found for the phase-averaged results in the near-field measurements in section 6.1.3, during the SJ suction phase the wingtip vortices circulation tends to regain the corresponding baseline reference value which is in agreement with the evolution of both the vorticity distribution and the vortices size. However, with the aim of reducing the wake-hazard and thus the vortices strength which is directly related to their circulation, the active control strategy should be based on injecting turbulence through a cross-section as large as possible since the wing model Ss04 is demonstrated to drop the $\langle \Gamma \rangle / \bar{\Gamma}^{BC}$ value up to 19% and 25% also during the SJ suction phases at $z/c = 26$ and $z/c = 56$ respectively. On the other hand, a slight increase is achieved at $z/c = 80$ which can be beneficial too to promote the growth of the Crow instability, although the uncertainty related to these curves is larger and this is confirmed by the oscillating behavior registered also for the remaining wing configuration.

A more regular and sinusoidal trend is obtained when the SJ is operated at the Widnall instability frequency as shown in Figure 6.41b at $z/c = 26$ for the same fixed $C_{\mu} = 0.2\%$. In this condition, the SJ blowing is again more effective with the wing model Ss04 which leads to a maximum drop of the normalized circulation of about 60% while the curve increases upon reaching a $\langle \Gamma \rangle / \bar{\Gamma}^{BC} > 1$ at the end of the suction phase. By increasing the synthetic jet characteristic velocity for the wing model Ss02 and Ss01, the curves are moved up to a maximum decrease of 46% and increase of 48% during the suction phase, while the Sh4 presents the same efficacy and the Rhc a completely opposite evolution being the controlled vortices circulation above the BC value over almost the entire actuation period, which result has been obtained for the further measurement plane at $z/c = 52$ and $z/c = 80$. At the former (Figure 6.42d), the wing configurations with the SJ blowing in the spanwise direction reach the maximum effectiveness in terms of wake-hazard alleviation since the vortices circulation is reduced over the entire period with a minimum and maximum drop of $\langle \Gamma \rangle / \bar{\Gamma}^{BC}$ of 10% (Sh4) and 78% (Ss04) respectively, which is promising. Finally, as already mentioned for the lower actuation frequency, at $z/c = 80$ it is difficult to identify a specific trend and/or a preferred SJ operating condition since an oscillating behavior is obtained for each wing configuration due to the strong vortices interaction detected at this downstream distance since the vortices are really weak, not coherent, and overlapped each other.

As reported for the other physical characteristics discussed herein above, the effects of a

variable momentum coefficient ($C_\mu = 1\%$, 0.2% , 0.04%) on the phase-evolution wingtip vortices circulation is displayed in Figure 6.42 for both actuation frequency. Firstly, the use of four circular nozzle is confirmed to be exactly equivalent to the rectangular slot as already anticipated in the time-averaged analysis. Blowing at $C_\mu = 1\%$ and $F^+ = 0.071$ causes a striking increase of the circulation up to almost 3 times the baseline reference value in correspondence to the SJ blowing peak where the vortices reach their maximum strength. This is verified at both downstream distances of $z/c = 26$ and $z/c = 52$. Then, a drop of about 50% and 70% are obtained in proximity to the beginning of the suction phases, where the time-averaged BC value is recovered for each momentum coefficient

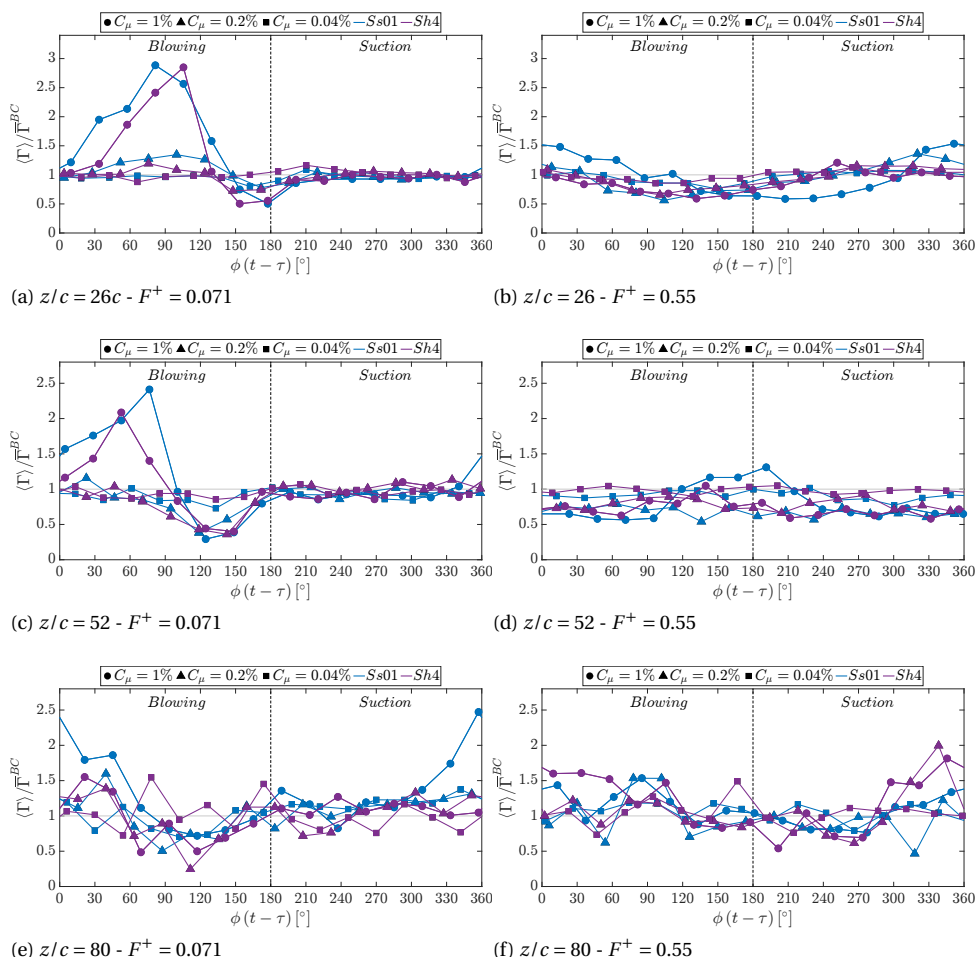


Figure 6.42: Normalized phase-averaged vortices circulation at different downstream positions for the wing models Ss01 and Sh4 at variable momentum coefficients. The BCs and BCr values of $\bar{\Gamma}^{BC}/cU_\infty$ are equal to 0.0282, 0.0220, and 0.0117 at $z/c = 26, 52, 80$ respectively.

investigated. The most interesting finding to be highlighted is that the same effective results are obtained with the SJ configuration at $C_\mu = 0.2\%$ and the wing model Ss04, with a SJ characteristic velocity U_0 78% lower, although the electrical power consumption is comparable. By reducing the momentum coefficient to 0.2% for the wing model Ss01, the wingtip vortices are less strengthened during the SJ blowing with a maximum $\langle \Gamma \rangle / \bar{\Gamma}^{BC}$ value of 1.34 and 1.15 against the decrease of 25% and 37% at $z/c = 26$ and $z/c = 52$ respectively, which are comparable to the findings at higher momentum coefficient $C_\mu = 1\%$ especially at $F^+ = 0.55$. On the other hand, the results related to the lowest $C_\mu = 0.04\%$ are in agreement with the findings of the streamwise vorticity and circumferential velocity peaks. Despite the $\langle \Gamma \rangle / \bar{\Gamma}^{BC}$ alleviation is the same of the one related to $C_\mu = 0.2\%$ at $z/c = 26$, the effectiveness is reduced going downstream with only a -27% detected on the SJ blowing velocity peak. At the furthest distance $z/c = 80$, the same oscillating evolution already found in Figure 6.41e and 6.41f is obtained also for the $C_\mu = 1\%$ and $C_\mu = 0.04\%$ at both $F^+ = 0.071$ and $F^+ = 0.55$. Although a clear trend is not easily recognizable, it is possible to state that in the very far field of the wing wake, the actuation loses its effectiveness on the vortices circulation since it is increased on average with respect to the baseline case but, at the same time, it is worth recalling that the absolute value of $\bar{\Gamma}^{BC}$ is really low and thus also a small relative reduction can lead to a complete attenuation of the wingtip vortices and their dangerous hazard. However, at the nearer measurement planes of $z/c = 26$ and $z/c = 52$ in Figure 6.42b and 6.42f, it can be noted that the variable momentum coefficient is not a crucial parameter. In fact, the $C_\mu = 0.2\%$ and 1% presents the same maximum drop of about 44% and 46%, while the lower value of $C_\mu = 0.04\%$ is not effective due to the low U_0 as already stated for the time-averaged analysis.

On the base of the metrics discussed in this section, a concluding remark is necessary. The phase-averaged results confirms that the synthetic jet exit section is a more relevant parameter than the characteristic velocity U_0 , being the effect of a high momentum coefficient with a low value of SJ area (Ss01) less effective or at least comparable to the same results obtained for the wing model Ss04 but with a 5 times lower C_μ . Furthermore, the configuration Ss01 - $C_\mu = 0.04\%$ and Ss04 - $C_\mu = 0.2\%$ have the same SJ characteristic velocity, but the first has been demonstrated to be low effective, while the second represents the most impactful device. In fact, with the latter configuration at $F^+ = 0.071$, the far field measurements at $z/c = 80$ have shown that the vortices interact more, the opposite vorticity sign is canceled, the vortex linking is amplified, and the vortex rings are supposed to be generated early with respect to the baseline case, which was the main goal of this thesis.

7

CONCLUSIONS AND OUTLOOKS

THIS thesis has addressed the experimental investigation of the effectiveness of synthetic jet actuation control on the wingtip vortices and their wake hazard generated by an unswept, low aspect ratio, rectangular wing in order to preserve the mutual induction of the counter-rotating vortices during their evolution. In particular, the active control has been designed to trigger the inherent instabilities of Crow and Widnall at different momentum coefficient C_μ with the goal to reduce the vortices strength, the induced circumferential velocity, and to obtain an early vortices linking and the consequent dissipation. Steroscopic Particle Image Velocimetry has been extensively employed as measurement technique for the 2D-3C velocity evaluation.

A first experimental campaign has been presented in chapter 3 conducted on a single measurement plane at $z/c = 3$ downstream of a finite squared-tipped rectangular wing to study the feasibility of a synthetic jet actuation control through a rectangular slot on a couple of counter-rotating wingtip vortices based on different momentum coefficients and dimensionless frequencies including the Crow and Widnall instability. The time-averaged analysis suggested that the synthetic jet actuation greatly affects the wingtip vorticity distribution causing an outward diffusion which increases with the actuation frequency, with a maximum reduction of 46% on the peak value. On the other hand, when the synthetic jet is operated at the Crow instability frequency, the wingtip circumferential velocity peak shows its maximum decrease equal to 29% with respect to the baseline case, which is crucial for the danger related to a possible wake-hazard. A novel phase-locked analysis revealed a clear relation between the synthetic jet blowing and suction phases and the periodic variation of the vortices features. In correspondence to the blowing phase, the wingtip vortices undergo a huge diffusion and they are characterized by a larger diameter, higher circulation, and lower induced velocity.

Based on the preliminary findings, a proper near and far-field experimental rigs described in chapter 4 have been designed based only on the actuation frequencies tuned to the Crow and Widnall instabilities. A fixed reference momentum coefficient of $C_\mu = 0.2\%$ has been considered for the near-field investigation at the downstream distances

from the wing trailing edge of $z/c = 0.1, 0.5, 1, \text{ and } 2$. In addition to the baseline wing with a plain wing tip and no synthetic jet actuation, three squared-tipped wing models equipped with a SJ rectangular slot $0.6c$ long with an increasing height of $0.01c, 0.02c, \text{ and } 0.04c$ (namely Ss01, Ss02, and Ss04) have been tested to analyze the effects of a variable SJ characteristic velocity U_0 at both actuation frequencies of $F^+ = 0.071$ and $F^+ = 0.55$ at fixed C_μ . For the far-field investigation, the wing dimensions are scaled by a factor of 3 to carry out the measurements at the downstream distances from the wing trailing edge of $z/c = 26, 52, \text{ and } 80$ in a relatively short length of the wind tunnel test section. The SJ slot dimensions have been scaled as well so that the effects of the variation of U_0 is studied in a similar way also in the far wake. The effects of a different synthetic jet exit section shape with four circular nozzles (Sh4), oriented in the spanwise direction, and of equivalent area of the rectangular slot Ss01 has been investigated. Furthermore, the effect of the SJ blowing direction has been taken into account in the Rhc model equipped with a rounded tip with the SJ blowing through a circular pipe oriented in the chordwise direction, and positioned in the chord plane tangential to the airfoil section in correspondence to the beginning of the trailing edge. For a comparison purpose with the near-field measurements, for each wing configuration and frequency, a constant momentum coefficient $C_\mu = 0.2\%$ has been investigated while the effects of a variable $C_\mu = 1\%, 0.2\%, 0.04\%$ at both actuation frequencies have been analyzed by testing only the models Ss01 and its equivalent Sh4.

The near-field results reported in chapter 5 confirm the striking effectiveness of the synthetic jet actuation in alleviating the wingtip vortices, since a time-averaged reduction of the streamwise vorticity of at least 25% is obtained at each downstream distance for each wing model tested at both actuation frequencies. However, a control strategy based on blowing through a large SJ exit section area leads to a more impactful wingtip vortices alleviation as confirmed by the phase-averaged results reported in 6. The higher A_j , the larger the vorticity drop as shown i.e. for the $z/c = 2$ measurements at $F^+ = 0.071$ where a 40% and 80% of $\langle \zeta_z \rangle_{max} / \bar{\zeta}_{z,max}^{BC}$ decrease is obtained for the Ss01 and Ss04 wing models respectively. Furthermore, the phase-evolution of the circumferential velocity peak confirms that the SJ configuration Ss04 (maximum A_j) is high-performance to reduce the wake-hazard dangers since the value of $\langle U_\theta \rangle_{max}$ is reduced up to 50% which is noteworthy. The latter result is obtained at the $F^+ = 0.55$ tuned to the Widnall instability frequency, which represents the second ingredient for obtaining the most useful SJ device for the active control of the wingtip vortices in the near-field. In fact, increasing the actuation frequency, the Ss04 configuration allows to reach the minimum vorticity level, the maximum vortex diffusion with an increased diameter up to 3 times the baseline reference value, and low values of the vortex circulation. In addition, the periodic motion along a $\pm 45^\circ$ direction at which the vortex undergo with the synthetic jet blowing is amplified at higher F^+ , which can be beneficial for avoiding the blade-vortex-interaction noise in a rotor and for a premature instability development in the aircraft wake.

As already mentioned, a wider parametric study has been conducted on the far-field measurements since they are more representative of the adverse effects of the wingtip vortices. Firstly, the use of a rectangular slot instead of a series of four circular nozzles of equivalent cross-section area (i.e. easier to machine) has been demonstrated to be more effective especially at $F^+ = 0.55$. On the other hand, blowing in the chordwise

direction (wing model “Rhc”) revealed to be much less fruitful than the other configuration with the synthetic jet oriented in the spanwise direction. Although at $z/c = 26$ a relevant reduction of the streamwise vorticity and circumferential velocity peak is detected, it turns out to be substantially not effective going downstream up to $z/c = 80$ and increasing the actuation frequency too. According to the time-averaged results of chapter 5, the effects of the synthetic jet exit section area is crucial also in the far wake. The wing model Ss04 is confirmed to be the most high-performance device with the larger A_j , outperforming the other configuration in each metric considered such as streamwise vorticity, circumferential velocity, and circulation reduction. This has been proven by the phase-averaged analysis reported in chapter 6 where an impressive variation has been detected in the streamwise vorticity alleviation between the model Ss01 and Ss04 such as -60% and -90% ($z/c = 26$) and -54% and -85% ($z/c = 80$) at $F^+ = 0.071$ during the SJ blowing phases which is confirmed to be more effective than the suction ones. Increasing the actuation frequency to $F^+ = 0.55$, the overall effectiveness is slightly reduced, the blowing and suction effects are comparable especially going far downstream, but the wing model Ss04 is demonstrated to be again the most impactful device in reducing the vortices strength, their circulation, and their wake-hazard. Interestingly, a key role is played by the A_j variation in the periodic motion along a $\pm 45^\circ$ directions at which the wingtip vortices undergo which has been already found in the near-field analysis. At both actuation frequencies, the wingtip vortices displacement is magnified from Ss01 to Ss04 which corresponds to the minimum U_0 and the maximum A_j . In particular, at $F^+ = 0.071$ and $z/c = 26$, the vortices are pushed upward of $0.5c$ and outboard of about $0.7c$ which means that the inherent vortices instability can be prematurely triggered and more amplified by blowing through a SJ exit section as large as possible. As a matter, this statement has been verified by the measurements at $z/c = 80$ where, in correspondence of the synthetic jet blowing peak, the wingtip vortices are not recognizable anymore and they completely dissipated. As shown in the subsequent suction phases, an early vortices linking has therefore obtained, the opposite vorticity is canceled, and the vortex rings are supposed to be generated early with respect to the baseline case, which was the main goal of this thesis.

By fixing the A_j of the wing configuration Ss01, blowing at really high SJ velocity with a momentum coefficient $C_\mu = 1\%$ allows to achieve a huge impact in the streamwise vorticity, circumferential velocity, and vortices circulation reduction at $z/c = 26$ up to 80%, 46%, and 50% respectively. By reducing the C_μ to 0.04% with extremely lower power needed, the SJ active control is still fruitful in terms of $\zeta_{z,max}$ and $U_{\theta,max}$ decrease up to 35% in the blowing phases, while its effects vanish during the suction ones and going far downstream. On the other hand, the same circulation alleviation of the higher $C_\mu = 0.2\%$ has been achieved at $F^+ = 0.071$, while at $F^+ = 0.55$ the results of $C_\mu = 1\%$ are comparable to $C_\mu = 0.2\%$, and thus the effects of a variable momentum coefficient are not so relevant in each vortices metric. Finally, it is worth noting that using a high value of the momentum coefficient ($C_\mu = 1\%$) with a low A_j (Ss01) at fixed actuation frequency, does not allow to outperform the wingtip vortices alleviation obtained with the configuration Ss04 at $C_\mu = 0.2\%$, meaning that the crucial parameter is represented by the synthetic jet exit section area A_j rather than its characteristic velocity U_0 .

Although an intensive study has been carried out in this thesis, much room for future

works is left. A possible route in this regard could be the design of the synthetic jet actuator equipped with a rectangular slot as large as possible optimized to work at the characteristic resonant frequencies to minimize the power needed also for an intermediate momentum coefficient which revealed to be a reasonable compromise. Since the suction phase has been demonstrated to not be impactful at large downstream distance, a pulse jet could be used instead, but the problem of harvesting the mass injected remains open. A possible and innovative solution to avoid bleeding air from the engine could be represented by the twin synthetic jets, in which a single actuator generates two single jets in phase opposition with a zero net mass flux. Lastly, a complete reconstruction of the whole wing wake is needed to deeply analyze the vortices dynamics development together with their inherent instability growth, which challenging experiment could be conducted in a towing tank where the possible boundary layer influence on the wingtip vortices is canceled.

BIBLIOGRAPHY

- Adrian, R. J., & Yao, C. S. (1985). Pulsed laser technique application to liquid and gaseous flows and the scattering power of seed materials. *24*(1), 44. <https://doi.org/10.1364/ao.24.000044>
- Anderson, J. D. (2007). *Fundamentals of aerodynamics* (4th ed.). McGraw-Hill.
- Asnaghi, A., Svennberg, U., Gustafsson, R., & Bensow, R. E. (2021). Propeller tip vortex mitigation by roughness application. *Applied Ocean Research*, *106*, 102449. <https://doi.org/10.1016/j.apor.2020.102449>
- Astarita, T. (2006). Analysis of interpolation schemes for image deformation methods in PIV: Effect of noise on the accuracy and spatial resolution. *Experiments in Fluids*, *40*(6), 977–987. <https://doi.org/10.1007/s00348-006-0139-4>
- Astarita, T. (2007). Analysis of weighting windows for image deformation methods in PIV. *Experiments in Fluids*, *43*(6), 859–872. <https://doi.org/10.1007/s00348-007-0314-2>
- Astarita, T. (2008). Analysis of velocity interpolation schemes for image deformation methods in PIV. *Experiments in Fluids*, *45*(2), 257–266. <https://doi.org/10.1007/s00348-008-0475-7>
- Astarita, T., & Cardone, G. (2005). Analysis of interpolation schemes for image deformation methods in PIV. *Experiments in Fluids*, *38*(2), 233–243. <https://doi.org/10.1007/s00348-004-0902-3>
- Bailey, S. C. C., & Tavoularis, S. (2008). Measurements of the velocity field of a wing-tip vortex, wandering in grid turbulence. *Journal of Fluid Mechanics*, *601*, 281–315. <https://doi.org/10.1017/s0022112008000694>
- Barber, M. R., & Tymczyszyn, J. (1980). *Wake vortex attenuation flight tests* (tech. rep.). NASA CP-2170. Federal Aviation Administration Los Angeles, CA, United States.
- Bearman, P., Heyes, A., Lear, C., & Smith, D. (2005). Natural and forced evolution of a counter rotating vortex pair. *Experiments in Fluids*, *40*(1), 98–105. <https://doi.org/10.1007/s00348-005-0051-3>
- Bearman, P., Heyes, A., Lear, C., & Smith, D. (2007). Evolution of a forced counter rotating vortex pair for two selected forcing frequencies. *Experiments in Fluids*, *43*(4), 501–507. <https://doi.org/10.1007/s00348-007-0312-4>
- Bertin, J. J., & Cummings, R. M. (2021). *Aerodynamics for engineers*. Cambridge University Press. <https://doi.org/10.1017/9781009105842>
- Betz, A. (1932). *Behavior of vortex systems* (tech. rep. NACA-TM-713).
- Bhagwat, M., Franke, M., Martin, P., & Leishman, J. (1999). Flow visualisation and measurement in the wake of a rotor with a subwing tip. *55th annual forum of the American Helicopter Society*.

- Bhattacharya, S., Charonko, J. J., & Vlachos, P. P. (2016). Stereo-particle image velocimetry uncertainty quantification. *Measurement Science and Technology*, 28(1), 015301. <https://doi.org/10.1088/1361-6501/28/1/015301>
- Bilanin, A., & Widnall, S. (1973). Aircraft wake dissipation by sinusoidal instability and vortex breakdown. *11th Aerospace Sciences Meeting*. <https://doi.org/10.2514/6.1973-107>
- Birch, D., Lee, T., Mokhtarian, E., & Kafyeke, F. (2004). Structure and induced drag of a tip vortex. *Journal of Aircraft*, 41(5), 1138–1145. <https://doi.org/10.2514/1.2707>
- Breitsamter, C. (2011). Wake vortex characteristics of transport aircraft. *Progress in Aerospace Sciences*, 47(2), 89–134. <https://doi.org/10.1016/j.paerosci.2010.09.002>
- Brocklehurst, A., & Barakos, G. (2013). A review of helicopter rotor blade tip shapes. *Progress in Aerospace Sciences*, 56, 35–74. <https://doi.org/10.1016/j.paerosci.2012.06.003>
- Brocklehurst, A., & Pike, A. Reduction of bvi noise using a vane tip. In: *Ahs specialists' conference on aerodynamics, dynamics and acoustics*. San Francisco, 1994.
- Calluau, D., & David, L. (2004). Stereoscopic particle image velocimetry measurements of the flow around a surface-mounted block. *Experiments in Fluids*, 36(1), 53–61. <https://doi.org/10.1007/s00348-003-0628-7>
- Cater, J. E., & Soria, J. (2002). The evolution of round zero-net-mass-flux jets. *Journal of Fluid Mechanics*, 472, 167–200. <https://doi.org/10.1017/s0022112002002264>
- Cattafesta, L. N., & Sheplak, M. (2011). Actuators for active flow control. *Annual Review of Fluid Mechanics*, 43(1), 247–272. <https://doi.org/10.1146/annurev-fluid-122109-160634>
- Chae, S., Yee, K., Yang, C., Aoyama, T., Jeong, S., & Obayashi, S. (2010). Helicopter rotor shape optimization for the improvement of aeroacoustic performance in hover. *Journal of Aircraft*, 47(5), 1770–1783. <https://doi.org/10.2514/1.c000283>
- Chakraborty, P., Balachandar, S., & Adrian, R. J. (2005). On the relationships between local vortex identification schemes. *Journal of Fluid Mechanics*, 535, 189–214. <https://doi.org/10.1017/s0022112005004726>
- Chevalier, H. (1973). Flight test studies of the formation and dissipation of trailing vortices. *Journal of Aircraft*, 10(1), 14–18. <https://doi.org/10.2514/3.60193>
- Coe, D., Allen, M., Trautman, M., & Glezer, A. (1994). Micromachined jets for manipulation of macro flows. *Solid-State Sensors and Actuators Workshop*, 243–247.
- Corsiglia, V. R., & Dunham, R. E. (1977). Aircraft wake-vortex minimization by use of flaps.
- Coudert, S. J. M., & Schon, J.-P. (2001). Back-projection algorithm with misalignment corrections for 2d3c stereoscopic PIV. *Measurement Science and Technology*, 12(9), 1371–1381. <https://doi.org/10.1088/0957-0233/12/9/301>
- Croom, D. R. (1977). Evaluation of flight spoilers for vortex alleviation. *Journal of Aircraft*, 14(8), 823–825. <https://doi.org/10.2514/3.44620>
- Crow, S. C. (1970). Stability theory for a pair of trailing vortices. *AIAA Journal*, 8(12), 2172–2179. <https://doi.org/10.2514/3.6083>
- Crow, S. C., & Bate, E. R. (1976). Lifespan of trailing vortices in a turbulent atmosphere. *Journal of Aircraft*, 13(7), 476–482. <https://doi.org/10.2514/3.44537>

- Cucitore, R., Quadrio, M., & Baron, A. (1999). On the effectiveness and limitations of local criteria for the identification of a vortex. *European Journal of Mechanics - B/Fluids*, 18(2), 261–282. [https://doi.org/10.1016/s0997-7546\(99\)80026-0](https://doi.org/10.1016/s0997-7546(99)80026-0)
- Devenport, W. J., Rife, M. C., Liapis, S. I., & Follin, G. J. (1996). The structure and development of a wing-tip vortex. *Journal of Fluid Mechanics*, 312, 67–106. <https://doi.org/10.1017/s0022112096001929>
- Dghim, M., Ferchichi, M., & Fellouah, H. (2018). Mid-wake wing tip vortex dynamics with active flow control. *Experimental Thermal and Fluid Science*, 98, 38–55. <https://doi.org/10.1016/j.exptthermflusci.2018.05.011>
- Dghim, M., Ferchichi, M., & Fellouah, H. (2020). On the effect of active flow control on the meandering of a wing-tip vortex. *Journal of Fluid Mechanics*, 896. <https://doi.org/10.1017/jfm.2020.343>
- Dghim, M., Ferchichi, M., Perez, R. E., & BenChiekh, M. (2016). Near wake development of a wing tip vortex under the effect of synthetic jet actuation. *Aerospace Science and Technology*, 54, 88–107. <https://doi.org/10.1016/j.ast.2016.04.008>
- Donaldson, C. (1971). *A brief review of the aircraft trailing vortex problem* (tech. rep.). Defense Technical Information Center. <https://doi.org/10.21236/ad0748271>
- Edstrand, A. M., & Cattafesta, L. N. (2015). Topology of a trailing vortex flow field with steady circulation control blowing. *53rd AIAA Aerospace Sciences Meeting*. <https://doi.org/10.2514/6.2015-1706>
- Edstrand, A. M., Schmid, P. J., Taira, K., & Cattafesta, L. N. (2018). A parallel stability analysis of a trailing vortex wake. *Journal of Fluid Mechanics*, 837, 858–895. <https://doi.org/10.1017/jfm.2017.866>
- García-Ortiz, J. H., Blanco-Rodríguez, F. J., Parras, L., & del Pino, C. (2020). Experimental observations of the effects of spanwise blowing on the wingtip vortex evolution at low Reynolds numbers. *European Journal of Mechanics - B/Fluids*, 80, 133–145. <https://doi.org/10.1016/j.euromechflu.2019.12.007>
- Gerz, T., Holzäpfel, F., & Darracq, D. (2002). Commercial aircraft wake vortices. *Progress in Aerospace Sciences*, 38(3), 181–208. [https://doi.org/10.1016/s0376-0421\(02\)00004-0](https://doi.org/10.1016/s0376-0421(02)00004-0)
- Gharib, M., Rambod, E., & Shariff, K. (1998). A universal time scale for vortex ring formation. *Journal of Fluid Mechanics*, 360, 121–140. <https://doi.org/10.1017/s0022112097008410>
- Giordano, R., & Astarita, T. (2009). Spatial resolution of the stereo PIV technique. *Experiments in Fluids*, 46(4), 643–658. <https://doi.org/10.1007/s00348-008-0589-y>
- Girfoglio, M., Greco, C. S., Chiatto, M., & de Luca, L. (2015). Modelling of efficiency of synthetic jet actuators. *Sensors and Actuators A: Physical*, 233, 512–521. <https://doi.org/10.1016/j.sna.2015.07.030>
- Glauert, H. (1983). *The elements of aerofoil and airscrew theory*. Cambridge University Press. <https://doi.org/10.1017/cbo9780511574481>
- Graftieaux, L., Michard, M., & Grosjean, N. (2001). Combining PIV, POD and vortex identification algorithms for the study of unsteady turbulent swirling flows. *Measurement Science and Technology*, 12(9), 1422–1429. <https://doi.org/10.1088/0957-0233/12/9/307>

- Graham, W. R., Park, S. W., & Nickels, T. B. (2003). Trailing vortices from a wing with a notched lift distribution. *AIAA Journal*, 41(9), 1835–1838. <https://doi.org/10.2514/2.7305>
- Greco, C. S., Cardone, G., & Soria, J. (2016). On the behaviour of impinging zero-net-mass-flux jets. *Journal of Fluid Mechanics*, 810, 25–59. <https://doi.org/10.1017/jfm.2016.703>
- Greco, C. S., Ianiro, A., Astarita, T., & Cardone, G. (2013). On the near field of single and twin circular synthetic air jets. *International Journal of Heat and Fluid Flow*, 44, 41–52. <https://doi.org/10.1016/j.ijheatfluidflow.2013.03.018>
- Green, S. I. (1995). Wing tip vortices. *Fluid mechanics and its applications* (pp. 427–469). Springer Netherlands. https://doi.org/10.1007/978-94-011-0249-0_10
- Han, Y. O., & Leishman, J. G. (2004). Investigation of helicopter rotor-blade-tip-vortex alleviation using a slotted tip. *AIAA Journal*, 42(3), 524–535. <https://doi.org/10.2514/1.3254>
- Hasanuzzaman, G., Merbold, S., Cuvier, C., Motuz, V., Foucaut, J.-M., & Egbers, C. (2020). Experimental investigation of turbulent boundary layers at high Reynolds number with uniform blowing, part i: Statistics. *Journal of Turbulence*, 21(3), 129–165. <https://doi.org/10.1080/14685248.2020.1740239>
- Haverkamp, S., Neuwerth, G., & Jacob, D. (2005). Active and passive vortex wake mitigation using control surfaces. *Aerospace Science and Technology*, 9(1), 5–18. <https://doi.org/10.1016/j.ast.2004.08.005>
- Heyes, A. L., & Smith, D. A. R. (2004). Spatial perturbation of a wing-tip vortex using pulsed span-wise jets. *Experiments in Fluids*, 37(1), 120–127. <https://doi.org/10.1007/s00348-004-0791-5>
- Hoad, D. (1980). Helicopter model scale results of blade-vortex interaction impulsive noise as affected by tip modification. *36th annual forum of the American Helicopter Society*.
- Hoffmann, E. R., & Joubert, P. N. (1963). Turbulent line vortices. *Journal of Fluid Mechanics*, 16(03), 395. <https://doi.org/10.1017/s0022112063000859>
- Holman, R., Utturkar, Y., Mittal, R., Smith, B. L., & Cattafesta, L. (2005). Formation criterion for synthetic jets. *AIAA Journal*, 43(10), 2110–2116. <https://doi.org/10.2514/1.12033>
- Jacquin, L., Fabre, D., Sipp, D., Theofilis, V., & Vollmers, H. (2003). Instability and unsteadiness of aircraft wake vortices. *Aerospace Science and Technology*, 7(8), 577–593. <https://doi.org/10.1016/j.ast.2003.06.001>
- Jeong, J., & Hussain, F. (1995). On the identification of a vortex. *Journal of Fluid Mechanics*, 285, 69–94. <https://doi.org/10.1017/s0022112095000462>
- Jordan, F. L. J. (1983). *Flow visualization of the wake of a transport aircraft model with lateral-control oscillations* (tech. rep.). NASA TM-84623. NASA Langley Research Center Hampton, VA, United States.
- Kerswell, R. R. (2002). Elliptical instability. *Annual Review of Fluid Mechanics*, 34(1), 83–113. <https://doi.org/10.1146/annurev.fluid.34.081701.171829>
- Klein, R., Majda, A. J., & Damodar, K. (1995). Simplified equations for the interaction of nearly parallel vortex filaments. *Journal of Fluid Mechanics*, 288, 201–248. <https://doi.org/10.1017/s0022112095001121>

- Kroo, I. (2001). Drag due to lift: Concepts for prediction and reduction. *Annual Review of Fluid Mechanics*, 33(1), 587–617. <https://doi.org/10.1146/annurev.fluid.33.1.587>
- Lasance, C. J., & Aarts, R. M. (2008). Synthetic jet cooling part i: Overview of heat transfer and acoustics. *2008 Twenty-fourth Annual IEEE Semiconductor Thermal Measurement and Management Symposium*. <https://doi.org/10.1109/stherm.2008.4509360>
- Lecordier, B., & Trinité, M. (2004). Advanced piv algorithms with image distortion validation and comparison using synthetic images of turbulent flow. In M. Stanislas, J. Westerweel, & J. Kompenhans (Eds.), *Particle image velocimetry: Recent improvements* (pp. 115–132). Springer Berlin Heidelberg.
- Lee, C. S., Ahn, B. K., Han, J. M., & Kim, J. H. (2017). Propeller tip vortex cavitation control and induced noise suppression by water injection. *Journal of Marine Science and Technology*, 23(3), 453–463. <https://doi.org/10.1007/s00773-017-0484-4>
- Leishman, J. (2000). *Principles of helicopter aerodynamics*. Cambridge University Press.
- Lessen, M., & Paillet, F. (1974). The stability of a trailing line vortex. part 2. viscous theory. *Journal of Fluid Mechanics*, 65(4), 769–779. <https://doi.org/10.1017/s0022112074001649>
- Lessen, M., Singh, P. J., & Paillet, F. (1974). The stability of a trailing line vortex. part 1. inviscid theory. *Journal of Fluid Mechanics*, 63(4), 753–763. <https://doi.org/10.1017/s0022112074002175>
- Leweke, T., Dizès, S. L., & Williamson, C. H. (2016). Dynamics and instabilities of vortex pairs. *Annual Review of Fluid Mechanics*, 48(1), 507–541. <https://doi.org/10.1146/annurev-fluid-122414-034558>
- Liu, Z., Zheng, Y., Jia, L., Jiao, J., & Zhang, Q. (2006). Stereoscopic PIV studies on the swirling flow structure in a gas cyclone. *61(13)*, 4252–4261. <https://doi.org/10.1016/j.ces.2006.01.024>
- Liu, Z., Sankar, L., & Hassan, A. (1999). Alteration of the tip vortex structure of a hovering rotor by blowing. *37th Aerospace Sciences Meeting and Exhibit*. <https://doi.org/10.2514/6.1999-906>
- Liu, Z., Sankar, L., & Hassan, A. (2000). Alteration of the tip vortex structure of a hovering rotor using oscillatory jet excitation. *38th Aerospace Sciences Meeting and Exhibit*. <https://doi.org/10.2514/6.2000-259>
- Margaris, P., & Gursul, I. (2006). Wing tip vortex control using synthetic jets. *The Aeronautical Journal*, 110(1112), 673–681. <https://doi.org/10.1017/s0001924000001536>
- Margaris, P., & Gursul, I. (2010). Vortex topology of wing tip blowing. *Aerospace Science and Technology*, 14(3), 143–160. <https://doi.org/10.1016/j.ast.2009.11.008>
- Matalanis, C. G., & Eaton, J. K. (2007). Wake vortex control using static segmented gurney flaps. *AIAA Journal*, 45(2), 321–328. <https://doi.org/10.2514/1.25956>
- McAlister, K., Tung, C., & Heinech, J. (2001). Forced diffusion of trailing vorticity from a hovering rotor. *57th annual forum of the American Helicopter Society*.
- McGuinn, A., Farrelly, R., Persoons, T., & Murray, D. B. (2013). Flow regime characterisation of an impinging axisymmetric synthetic jet. *Experimental Thermal and Fluid Science*, 47, 241–251. <https://doi.org/10.1016/j.expthermflusci.2013.02.003>

- Moore, D. W., & Saffman, P. G. (1973). Axial flow in laminar trailing vortices. *Proceedings of the Royal Society of London. A. Mathematical and Physical Sciences*, 333(1595), 491–508. <https://doi.org/10.1098/rspa.1973.0075>
- Mula, S. M., Stephenson, J. H., Tinney, C. E., & Sirohi, J. (2013). Dynamical characteristics of the tip vortex from a four-bladed rotor in hover. *Experiments in Fluids*, 54(10). <https://doi.org/10.1007/s00348-013-1600-9>
- Ortega, J. M., Bristol, R. L., & Savas, O. (2002). Wake alleviation properties of triangular-flapped wings. *AIAA Journal*, 40(4), 709–721. <https://doi.org/10.2514/2.1703>
- Ortega, J. M., Bristol, R. L., & Sava, Ö. (2003). Experimental study of the instability of unequal-strength counter-rotating vortex pairs. *Journal of Fluid Mechanics*, 474, 35–84. <https://doi.org/10.1017/s0022112002002446>
- Ota, T., Hashiguchi, Y., & Tsukahara, T. Bvi noise reduction research with canard blade tip. In: *27th european rotorcraft forum*. Moscow, 2001, 23.1–11.
- Ozger, E., Schell, I., & Jacob, D. (2001). On the structure and attenuation of an aircraft wake. *Journal of Aircraft*, 38(5), 878–887. <https://doi.org/10.2514/2.2847>
- Patterson, J. C. (1975). Vortex attenuation obtained in the langley vortex research facility. *Journal of Aircraft*, 12(9), 745–749. <https://doi.org/10.2514/3.59865>
- Phillips, W. R. C. (1981). The turbulent trailing vortex during roll-up. *Journal of Fluid Mechanics*, 105(-1), 451. <https://doi.org/10.1017/s0022112081003285>
- Prasad, A. K. (2000). Stereoscopic particle image velocimetry. *Experiments in Fluids*, 29(2), 103–116. <https://doi.org/10.1007/s003480000143>
- Raffel, M., Willert, C. E., Wereley, S. T., & Kompenhans, J. (2007). *Particle image velocimetry*. Springer Berlin Heidelberg. <https://doi.org/10.1007/978-3-540-72308-0>
- Ramaprian, B. R., & Zheng, Y. (1997). Measurements in rollup region of the tip vortex from a rectangular wing. *AIAA Journal*, 35(12), 1837–1843. <https://doi.org/10.2514/2.59>
- Reed, A. M., & Milgram, J. H. (2002). Ship wakes and their radar images. *Annual Review of Fluid Mechanics*, 34(1), 469–502. <https://doi.org/10.1146/annurev.fluid.34.090101.190252>
- Rossow, V. J. (1975). Theoretical study of lift-generated vortex wakes designed to avoid rollup. *AIAA Journal*, 13(4), 476–484. <https://doi.org/10.2514/3.49734>
- Rossow, V. J. (1978). Effect of wing fins on lift-generated wakes. *Journal of Aircraft*, 15(3), 160–167. <https://doi.org/10.2514/3.58335>
- Rossow, V. J. (1986). Wake hazard alleviation associated with roll oscillations of wake-generating aircraft. *Journal of Aircraft*, 23(6), 484–491. <https://doi.org/10.2514/3.45333>
- Saffman, P. G. (1993). *Vortex dynamics*. Cambridge University Press. <https://doi.org/10.1017/cbo9780511624063>
- Scarano, F. (2001). Iterative image deformation methods in PIV. *Measurement Science and Technology*, 13(1), R1–R19. <https://doi.org/10.1088/0957-0233/13/1/201>
- Scarano, F., David, L., Bsibsi, M., & Calluau, D. (2005). S-PIV comparative assessment: Image dewarping + misalignment correction and pinhole + geometric back projection. *Experiments in Fluids*, 39(2), 257–266. <https://doi.org/10.1007/s00348-005-1000-x>

- Schell, I., Özger, E., & Jacob, D. (2000). Influence of different flap settings on the wake-vortex structure of a rectangular wing with flaps and means of alleviation with wing fins. *Aerospace Science and Technology*, 4(2), 79–90. [https://doi.org/10.1016/s1270-9638\(00\)00120-6](https://doi.org/10.1016/s1270-9638(00)00120-6)
- Schmitz, F. H. (1991). Rotor noise. *Aeroacoustics of Flight Vehicles: Theory and Practice. Volume 1: Noise Sources, I*, 65–149.
- Schöll, R., Buxel, C., & Neuwerth, G. (2006). Influence of spanwise loading and fins on extended near-field vortex wake. *44th AIAA Aerospace Sciences Meeting and Exhibit*. <https://doi.org/10.2514/6.2006-62>
- Sciacchitano, A., & Wieneke, B. (2016). PIV uncertainty propagation. *Measurement Science and Technology*, 27(8), 084006. <https://doi.org/10.1088/0957-0233/27/8/084006>
- Sezen, S., & Bal, S. (2020). Computational and empirical investigation of propeller tip vortex cavitation noise. *China Ocean Engineering*, 34(2), 232–244. <https://doi.org/10.1007/s13344-020-0022-8>
- Shuster, J. M., & Smith, D. R. (2007). Experimental study of the formation and scaling of a round synthetic jet. *Physics of Fluids*, 19(4), 045109. <https://doi.org/10.1063/1.2711481>
- Sipp, D., & Jacquin, L. (2003). Widnall instabilities in vortex pairs. *Physics of Fluids*, 15(7), 1861–1874. <https://doi.org/10.1063/1.1575752>
- Smith, B. L., & Glezer, A. (1998). The formation and evolution of synthetic jets. *Physics of Fluids*, 10(9), 2281–2297. <https://doi.org/10.1063/1.869828>
- Soloff, S. M., Adrian, R. J., & Liu, Z.-C. (1997). Distortion compensation for generalized stereoscopic particle image velocimetry. *Measurement Science and Technology*, 8(12), 1441–1454. <https://doi.org/10.1088/0957-0233/8/12/008>
- Soria, J. (1996). An investigation of the near wake of a circular cylinder using a video-based digital cross-correlation particle image velocimetry technique. *Experimental Thermal and Fluid Science*, 12(2), 221–233. [https://doi.org/10.1016/0894-1777\(95\)00086-0](https://doi.org/10.1016/0894-1777(95)00086-0)
- Spalart, P. R. (1998). Airplane trailing vortices. *Annual Review of Fluid Mechanics*, 30(1), 107–138. <https://doi.org/10.1146/annurev.fluid.30.1.107>
- Spreiter, J. R., & Sacks, A. H. (1951). The rolling up of the trailing vortex sheet and its effect on the downwash behind wings. *Journal of the Aeronautical Sciences*, 18(1), 21–32. <https://doi.org/10.2514/8.1830>
- Stumpf, E. (2004). Numerical study of four-vortex aircraft wakes and layout of corresponding high-lift configurations. *42nd AIAA Aerospace Sciences Meeting and Exhibit*. <https://doi.org/10.2514/6.2004-1067>
- Tangler, J. (1975). The design and testing of a tip to reduce blade slap. *31st annual forum of the American Helicopter Society*.
- Thomas, P. J., & Auerbach, D. (1994). The observation of the simultaneous development of a long- and a short-wave instability mode on a vortex pair. *Journal of Fluid Mechanics*, 265, 289–302. <https://doi.org/10.1017/s0022112094000844>
- Traub, L. W., Mani, S., Galls, S. F., & Rediniotis, O. K. (1998). Application of the vortex breakdown phenomenon in the attenuation of trailing vortices. *The Aeronautical Journal (1968)*, 102(1018), 439–444. <https://doi.org/10.1017/S0001924000027676>

- Tsai, C. Y., & Widnall, S. E. (1976). The stability of short waves on a straight vortex filament in a weak externally imposed strain field. *Journal of Fluid Mechanics*, 73(4), 721–733. <https://doi.org/10.1017/s0022112076001584>
- Unser, M. (1999). Splines: A perfect fit for signal and image processing. *IEEE Signal Processing Magazine*, 16(6), 22–38. <https://doi.org/10.1109/79.799930>
- Unser, M., Aldroubi, A., & Eden, M. (1993a). B-spline signal processing. i. theory. *IEEE Transactions on Signal Processing*, 41(2), 821–833. <https://doi.org/10.1109/78.193220>
- Unser, M., Aldroubi, A., & Eden, M. (1993b). B-spline signal processing. II. efficiency design and applications. *IEEE Transactions on Signal Processing*, 41(2), 834–848. <https://doi.org/10.1109/78.193221>
- Vasilescu, R., & Dancila, S. (2006). Rotor wake modifications in hover using unsteady spanwise blowing. *44th AIAA Aerospace Sciences Meeting and Exhibit*. <https://doi.org/10.2514/6.2006-1065>
- Westerweel, J., Dabiri, D., & Gharib, M. (1997). The effect of a discrete window offset on the accuracy of cross-correlation analysis of digital PIV recordings. 23(1), 20–28. <https://doi.org/10.1007/s003480050082>
- Whitcomb, R. T. (1976). *A design approach and selected wind tunnel results at high subsonic speeds for wing-tip mounted winglets* (tech. rep. NASA-TN-D-8260). <https://ntrs.nasa.gov/search.jsp?R=19760019075>
- Widnall, S. E., Bliss, D., & Zalay, A. (1971). Theoretical and experimental study of the stability of a vortex pair. In J. H. Olsen, A. Goldburg, & M. Rogers (Eds.), *Aircraft wake turbulence and its detection* (pp. 305–338). Springer US.
- Widnall, S. E. (1975). The structure and dynamics of vortex filaments. *Annual Review of Fluid Mechanics*, 7(1), 141–165. <https://doi.org/10.1146/annurev.fl.07.010175.001041>
- Widnall, S. E., Bliss, D. B., & Tsai, C. Y. (1974). The instability of short waves on a vortex ring. *Journal of Fluid Mechanics*, 66(1), 35–47. <https://doi.org/10.1017/s0022112074000048>
- Wieneke, B. (2005). Stereo-PIV using self-calibration on particle images. 39(2), 267–280. <https://doi.org/10.1007/s00348-005-0962-z>
- Willert, C. E., & Gharib, M. (1991). Digital particle image velocimetry. *Experiments in Fluids*, 10(4), 181–193. <https://doi.org/10.1007/bf00190388>
- Willert, C. (1997). Stereoscopic digital particle image velocimetry for application in wind tunnel flows. 8(12), 1465–1479. <https://doi.org/10.1088/0957-0233/8/12/010>
- Wren, G. G. (1997). Detection of submerged vessels using remote sensing techniques. *Australian Defence Force Journal*, 9–15.
- Yu, Y. H. (2000). Rotor blade-vortex interaction noise. *Progress in Aerospace Sciences*, 36(2), 97–115. [https://doi.org/10.1016/s0376-0421\(99\)00012-3](https://doi.org/10.1016/s0376-0421(99)00012-3)
- Zaccara, M., Paolillo, G., Greco, C. S., Astarita, T., & Cardone, G. (2022). Flow control of wingtip vortices through synthetic jets. *Experimental Thermal and Fluid Science*, 130, 110489. <https://doi.org/10.1016/j.expthermflusci.2021.110489>
- Zhou, J., Adrian, R. J., Balachandar, S., & Kendall, T. M. (1999). Mechanisms for generating coherent packets of hairpin vortices in channel flow. *Journal of Fluid Mechanics*, 387, 353–396. <https://doi.org/10.1017/s002211209900467x>

LIST OF PUBLICATIONS

JOURNAL ARTICLES

1. M. Contino, **Zaccara, M.**, Montanaro, A., Allocca, L., & Cardone, G., *Dynamic Thermal Behavior of a GDI Spray Impacting on a Heated Thin Foil by Phase-Averaged Infrared Thermography*, SAE International Journal of Advances and Current Practices in Mobility 2(2):512-519, 2020.
2. **Zaccara, M.**, Edelman, J.B., & Cardone, G., *A general procedure for infrared thermography heat transfer measurements in hypersonic wind tunnels*, International Journal of Heat and Mass Transfer, Elsevier BV, 2020, 163, 120419.
3. **Zaccara, M.**, Paolillo, G., Greco, C.S., Astarita, T., & Cardone, G., *Flow control of wingtip vortices through synthetic jets*, Experimental Thermal and Fluid Science, Elsevier BV, 2022, 130, 110489.
4. Running, C. L., Rataczak, J. A., **Zaccara, M.**, Cardone, G., & Juliano, T. J., *A wrap-film technique for infrared thermography heat-transfer measurements in high-speed wind tunnels*, Experimental Thermal and Fluid Science, Elsevier BV, 2022, 110604.
5. Carvallo, C., **Zaccara, M.**, Montanaro, A., Allocca, L., & Cardone, G., *Heat transfer measurements of impinging spray by time history infrared thermography*, under submission to Experimental Thermal and Fluid Science, Elsevier BV, 2022.
6. **Zaccara, M.**, Cafiero, G., Greco, C.S., Astarita, T., Iuso, G., & Cardone, G., *Experimental investigation of wingtip vortices control with synthetic jets actuation - Part 1: near-field analysis*, to be submitted to Aerospace Science and Technology.
7. **Zaccara, M.**, Bragança, P., Cuvier, C., Greco, C.S., Astarita, T., Cardone, G., & Foucaut, J.M., *Experimental investigation of wingtip vortices control with synthetic jets actuation - Part 2: far-field analysis*, to be submitted to Aerospace Science and Technology.

BOOK CONTRIBUTIONS

1. **Zaccara, M.**, Cerasuolo, S., Edelman, J.B., Cardone, G., & Schneider, S.P., (2020). Chapter 13 - Infrared Thermography Data Reduction Technique for Heat Flux Measurements in the Boeing/AFOSR Mach-6 Quiet Tunnel, in: *Hypersonic Boundary-Layer Transition Prediction*, NATO Technical Report RDP, STO-TR-AVT-240, ISBN 978-92-837-2227-4.

CONFERENCE CONTRIBUTIONS

1. **Zaccara, M.**, Cerasuolo, S., Cardone, G., Edelman, J.B., & Schneider, S.P., *Infrared thermography data reduction technique for heat transfer measurements in the Boeing/AFOSR Mach-6 quiet tunnel*, AIAA Scitech 2019 Forum, American Institute of Aeronautics and Astronautics, 2019, doi: 10.2514/6.2019-0894.
2. M. Contino, **Zaccara, M.**, Montanaro, A., Allocca, L., & Cardone, G., *Dynamic Thermal Behavior of a GDI Spray Impacting on a Heated Thin Foil by Phase-Averaged Infrared Thermography*, SAE 14th International Conference on Engines and Vehicles, ICE 2019, Capri, Italy.
3. **Zaccara, M.**, Contino, M., Montanaro, A., Allocca, L., & Cardone, G., *Thermal analysis of a GDI multi-hole spray footprint dynamics by phase-averaged Infrared thermography*, 15th International Conference on Fluid Control, Measurements and Visualization, 2019; Naples, Italy.
4. Piccolo, A., **Zaccara, M.**, Paolillo, G., & Greco, C. S., *Wing-tip vortex control with synthetic jet technology*, 15th International Conference on Fluid Control, Measurements and Visualization, 2019; Naples, Italy.
5. Greco, C.S., Piccolo, A., **Zaccara, M.**, Paolillo, G., Astarita T., & Cardone G., *Synthetic jet-based control of wing tip vortices*, APS Division of Fluid Dynamics (Fall) 2019, abstract id.L26.006; C, Seattle, USA.

ACKNOWLEDGEMENTS

“Mirko, you desidered a PhD, you managed it, and you finally did it!”. This is my thought while writing this difficult paragraph. I finally reached this important goal of my personal and professional career, it was a long and bendy way, I felt like on a roller-coaster of emotions every day, but what an amazing journey! An important chapter of my life is ending, and it is time to reap the rewards of the hard work, my best and worst choices, sweat and tears, perseverance, satisfactions, and “nothing-is-working” moments. The last but not the least, this is the right moment to thank all the people I met during this experience. Thanks to your teachings, advice, and emotions you let me feel which made me what I am at the end of this step.

The first person I would like to thank is my supervisor Prof. Gennaro Cardone. I still remember your email some months before joining the PhD program, where you suggested me to follow my instinct and passion for the academia, like yours. Thank you for the several opportunities you gave to me. You trusted me since the MSc thesis project in the United States of America, you have always instilled your enthusiasm in me tackling the ever-present challenges of work, and I am very grateful to you. I have always tried to learn the most from your impressive knowledge on the fluid-dynamics and your passion in designing and assembling experimental apparatuses in the most feasible way. However, I have never seen you like a boss, rather like a second father. Thank you for your humility and for the thousands of advice you gave to me.

Worthy of acknowledgments is my second supervisor Prof. Carlo Salvatore Greco. I have always admired you for your immense patience and dedication. Thank you for all the support in the wingtip vortices research activity you proposed me from the beginning, thank you for having ever said yes to the never-ending meeting on analyzing the measurements results which made us crazy.

I am thankful to my colleague Gerardo of the “*Gas Lab*”, who never refused to help me in any situation, from the experiments to the bureaucracy, especially if there was some math to do although the Navier-Stokes equations were not necessary after all. I really esteem your love for the science and research, you should be an example for all the future PhD students. I thank you also for all the coffee we made each other without asking, and for every telling-off “*comm è bell a perder u tiemp!*”.

Many thanks also to Prof. Tommaso Astarita, who is my idea of what a genius is. Thank you for your 24/7 availability for my countless questions and doubts about PIV and your impressive software. I really appreciated your frankness in highlighting the stupid mistakes I made and your as fast as efficient solutions.

Heartfelt thanks to the emeritus Prof. Giovanni Maria Carlomagno. I always defined him as a “walking encyclopedia”, I tried to learn as much as possible from his limitless experience and his life lessons of inestimable value, especially when the conversation

started with “*Ai miei tempi*”. I was honored to be one of your students during your last lesson before the retirement and I will never forget your last speech “*I am not really retiring, I remain at my office and I will continue working for the academia and for you, because the students will be the future*”. I hope to represent your idea of future.

I would like to thank Peppe, the “*Gas Lab*” technician, who has more phone numbers than the UniNA rector! Thank you for your daily willingness and patient support in manufacturing parts of the experimental setup and for having solved tons of administrative issues thanks to your endless *conoscenze*. I will miss the tasty bread you prepared every morning (actually, the machine does), with the entire laboratory smelling of *casatiello*. You have always taken care of me as a lovely father, and I really appreciated it.

I kindly acknowledge Prof. Gaetano Iuso and Prof. Gioacchino Cafiero who hosted me for three months at *Politecnico di Torino* for carrying out the near-field measurements of the present thesis. I really appreciated your support in managing the incredible challenges we bumped into while tuning the experimental setup.

The results reached in the present thesis would not have been possible without the support of Prof. Jean-Marc Foucaut, Prof. Christophe Cuvier, and Dr. Pierre Bragança from the *Laboratoire de Mécanique des Fluides de Lille - Kampé de Fériet (LMFL)*. I thank you for having hosted me in Lille (France) and giving me the opportunity of working in a facility unique as the LMFL Boundary Layer Wind Tunnel is.

I warmly thank “my person” Stefania, for being a certainty in my life. You have always stood behind me, and there was no exception. I am grateful to you for being a tireless sink of my complaints, for your infinite perseverance and love. Thank you for celebrating my victories and sharing my worries, keeping me grounded and reminding me of what is important in real life. Thank you for fielding an enormous number of phone calls, most of them ending up fighting, but with the faith of being there for each other the day after, forever and ever. I shall try to live up to your expectations and I hope you will get a lot back in return. I do not forget our promises.

Deepest thanks go to Gianluca and Giusy, for your lifetime friendship. Thank you for your limitless loyalty, for giving me the strength to go on and rise again after the falls, for calming me down when I feel the ground give way under my feet. Thank you for telling me that I am awesome even when I didn’t feel that way. If I look back, there is just future with you, no matter how far from each other our lives takes us.

I would like to thank also Roberta, Felice, Giada, Giusy C., Antonello, Stefano, Rocco, Milena, Cekka and all the others for all the enjoyable time that we have since we met at the kindergarten. Thanks to Giovanni and Gennaro, for being my second family in Naples, you will be always a place to be.

Special thanks to Raffaella, Claudia, Peppe, and the *Volley con ghiaccio* people for being teammates on and off the pitch. Thank you for giving me moments of amusement and lightheartedness during my most stressful period.

Lastly, my family deserves endless gratitude. Your constant love and support keep me motivated and confident every day. I learned from you the meaning of the unconditional love, daily sacrifices, humility, and politeness, which are the cornerstones of my life. My accomplishments and success are because you believe in me respecting my decisions. I love you all.

Mirko Zaccara